



**STATIK UND DYNAMIK  
DER TRAGWERKE**



# Development of Scaled Boundary Polygon Elements for Coupled Thermoelastic Fracture Modeling

Der Fakultät für Ingenieurwissenschaften, Abteilung Bauwissenschaften  
der Universität Duisburg-Essen zur Erlangung des akademischen Grades eines  
Doktors der Ingenieurwissenschaften (Dr.-Ing.)  
vorgelegte Dissertation von  
**Muhammad Danish Iqbal, M. Sc.**



# Kurzfassung

Die Modellierung thermoelastischer Bruchvorgänge ist aufgrund ihrer Relevanz für zahlreiche technische Anwendungen ein unverzichtbares Forschungsgebiet. Bei thermoelastischen Problemen führt die Kopplung von Temperatur- und Verschiebungsfeldern zu thermischen Spannungen, die im Falle eines Bruchs singulär werden können. Spezielle Werkstoffe, wie z.B. funktional gradierte Materialien (FGMs), werden entwickelt, um den Auswirkungen hoher thermischer Spannungen entgegenzuwirken. In den meisten realen Anwendungen werden seit Jahrzehnten numerische Methoden wie die etablierte Finite-Elemente-Methode (FEM) zur Analyse des thermoelastischen Bruchs eingesetzt. Sie erfordert jedoch aufgrund ihrer polynomialen Basisinterpolationsfunktionen eine spezielle Behandlung zur Modellierung der singulären Spannungen. Es wurden zahlreiche andere numerische Methoden vorgeschlagen, um die Einschränkungen der FEM-Methode zu überwinden. Die Modellierung thermisch-induzierter Bruchvorgänge ist jedoch nach wie vor ein aktives Forschungsfeld.

In dieser Arbeit wird ein numerisches Verfahren zur Modellierung thermisch-induzierter Rissausbreitung mit Hilfe der Scaled-Boundary-Finite-Elemente-Methode (SBFEM) entwickelt. Die SBFEM ist eine semi-analytische Methode, bei der nur der Rand des Berechnungsgebiets diskretisiert und eine analytische Lösung in radialer Richtung konstruiert wird. Bei einer auf der SBFEM basierenden Simulation wird das Gebiet in sternförmig Polygone mit beliebig vielen Seiten unterteilt, die Risse auf natürliche Weise durch offene Polygonelemente darstellen können. Polygonelemente erleichtern auch die Vernetzung und das Neuvernetzen komplexer Gebiete im Falle einer diskreten Rissausbreitungsmodellierung. Im Gegensatz zu den polynomialen Basisinterpolationsfunktionen der FEM führt die semi-analytische Diskretisierung der SBFEM zu Potenzfunktionen der Radialkoordinate als Interpolationsfunktionen. Eines der Hauptmerkmale der SBFEM-Lösung ist die direkte Darstellung der singulären Spannungen, ohne dass eine zusätzliche Nachbearbeitung erforderlich ist. Mit der Fähigkeit, komplexe Geometrien zu vernetzen und neu zu vernetzen, und der eingebauten Fähigkeit, singuläre Spannungen zu erfassen, ist die SBFEM eine attraktive Wahl für die Modellierung von Rissausbreitungsvorgängen.

In dieser Arbeit wird zunächst die geometrische Transformation eines Berechnungsgebiets von kartesischen in "scaled boundary" koordinaten beschrieben. Dann wird die SBFEM-Modellierung der Laplace-Gleichung und des linearen Elastizitätsproblems diskutiert. Anschließend wird die Verschiebung aufgrund eines bekannten Temperaturfeldes semi-analytisch für den Fall der Elastostatik ermittelt, wobei eine unidirektionale Kopplung der Temperatur- und Verschiebungsfelder angenommen wird. Ein vorhandenes Temperaturfeld führt zu einem Lastvektor in der SBFE-Gleichung der Verschiebung, die dann zu einer inhomogenen Differentialgleichung wird. Die spezielle Lösung des inhomogenen Terms wird mit Hilfe von Integralen in radialer Richtung ausgedrückt, die für Temperaturänderungen, die als radiale Potenzfunktionen variieren, analytisch ausgewertet werden. Anschließend werden die zusätzlichen "scaled boundary" Formfunktionen ebenfalls aus der speziellen Lösung der nicht-homogenen SBFE-Gleichung für die Verschiebung gewonnen, ohne dass eine vorherige Lösung des Temperaturfeldes erforderlich ist, wodurch der Weg für die Modellierung vollständig gekoppelter Temperatur- und Verschiebungsfelder geebnet wird. Die Gleichungen der vollständig gekoppelten Thermoelastizität werden dann mit den SBFE-Formfunktionen diskretisiert, die mit zusätzlichen Formfunktionen angereichert sind.

Für die SBFEM-Modellierung von FGMs wird die räumliche Variation der Materialeigenschaften mit Polynomen approximiert. Die neuartige semi-analytische Integration von thermoelastischen Materialkoeffizientenmatrizen für FGMs wird vorgestellt. Darüber hinaus werden verallgemein-

erte Spannungsintensitätsfaktoren (SIFs) unter Verwendung des direkten und effizienten SBFEM-Ansatzes zur Erfassung singulärer Spannungen vorgestellt. Ein lokalisierter Algorithmus zur Neuvernetzung mit Polygonelementen wird implementiert, um diskrete Rissausbreitungsprobleme zu modellieren. Physikalische Größen werden mit Hilfe der SBFEM-Formfunktionen abgebildet, und es wird ein neuartiges Abbildungsverfahren für die Hilfsvariablen vorgestellt, die den zusätzlichen Formfunktionen entsprechen. Schließlich wird die entwickelte SBFEM für gekoppelten thermoelastischen Bruch durch verschiedene Benchmark-Beispiele validiert. Es werden unidirektionale und vollständig gekoppelte Fälle betrachtet, und es werden Beispiele für thermoelastischen Bruch in allgemeinen und funktional graduierten Materialien behandelt. Darüber hinaus wird die Modellierung von diskreten Rissausbreitungsproblemen bei unidirektonaler und vollständiger Kopplung untersucht.

# Abstract

Thermoelastic fracture modeling is an indispensable field of research due to its relevance in numerous engineering applications. In thermoelastic problems, coupling temperature and displacement fields leads to thermal stress, which can become singular in case of fracture. Special purpose materials, such as functionally graded materials (FGMs), are engineered to counter the effects of high thermal stress. In most real-world applications, numerical methods such as the standard finite element method (FEM) have been employed to analyze thermoelastic fracture for decades. However, it requires special treatments to model the singular stress due to its polynomial base interpolation functions. Plenty of other numerical methods have been proposed to overcome the limitations of the standard finite element method, yet thermoelastic fracture modeling is still an active field of research.

This thesis develops a numerical technique to model thermoelastic fracture using the scaled boundary finite element method (SBFEM). The SBFEM is a semi-analytical method in which only the boundary of the computational domain is discretized, and an analytical solution is constructed in the radial direction. In a simulation based on SBFEM, the domain is divided into arbitrary-sided star-convex polygons that can represent cracks naturally using open polygon elements. Polygon elements also facilitate the meshing and re-meshing of complex domains in the case of discrete crack propagation modeling. Contrary to the polynomial base interpolation functions of the FEM, the semi-analytical discretization of the SBFEM leads to power functions of its radial coordinate as the interpolation functions. One of the key features of the SBFEM solution is the direct representation of singular stress without the need for additional post-processing. With the capabilities to mesh and re-mesh complex geometries and the built-in capacity to capture singular stress, the SBFEM is an attractive choice to model fracture.

The work presented in this thesis first outlines the geometric transformation of a computational domain from Cartesian to the scaled boundary coordinates. Then, the SBFEM modeling of Laplace's equation and linear elasticity problem is discussed. Next, the displacement due to a known temperature field is obtained semi-analytically for elastostatics, assuming uni-directional coupling of the temperature and displacement fields. A temperature field leads to a load vector in the SBFE equation in displacement, which then becomes a non-homogeneous differential equation. The non-homogeneous term's particular solution is expressed as integrals in the radial direction, which are evaluated analytically for temperature changes varying as power functions of radial coordinate. Then, the supplementary scaled boundary shape functions are also obtained from the particular solution of the non-homogenous SBFE equation in displacement but without needing a prior solution of temperature field, thus paving the way for modeling fully coupled temperature and displacement fields. The equations of fully coupled thermoelasticity are then discretized using the SBFE shape functions enriched with supplementary shape functions.

For the SBFEM modeling of FGMs, the spatial variation of material properties is approximated by polynomial functions. The novel semi-analytical integration of thermoelastic material coefficient matrices for FGMs is presented. Furthermore, the generalized stress intensity factors (SIFs) are evaluated using the direct and efficient SBFE approach to capture singular stress. A localized re-meshing algorithm using polygon elements is implemented to model discrete crack propagation problems. Physical quantities are mapped using the SBFEM shape functions, and a novel mapping procedure is presented for the auxiliary variables corresponding to supplementary shape functions. Finally, the developed SBFEM for coupled thermoelastic fracture is validated through various benchmark examples. Uni-directional and full coupling cases are considered, and examples of

thermoelastic fracture in standard and functionally graded materials are addressed. Moreover, the modeling of discrete crack propagation problems in uni-directional and full coupling is verified.

# Contents

|   |           |
|---|-----------|
| <b>Nomenclature</b> . . . . .   | <b>IX</b> |
| <b>1 Introduction</b> . . . . .                                       | <b>1</b>  |
| 1.1 Motivation . . . . .  | 1         |
| 1.2 State of the Art . . . . .  | 2         |
| 1.3 Objectives and Outline . . . . .                                  | 6         |
| <b>2 Theoretical Framework</b> . . . . .                              | <b>9</b>  |
| 2.1 Kinematics . . . . .  | 9         |
| 2.2 Strain and Stress Measure . . . . .                               | 11        |
| 2.3 Balance Laws . . . . .  | 13        |
| 2.3.1 Conservation of Mass . . . . .                                  | 13        |
| 2.3.2 Conservation of Momentum . . . . .                              | 13        |
| 2.3.3 Conservation of Energy . . . . .                                | 14        |
| 2.3.4 Entropy Inequality . . . . .                                    | 14        |
| 2.4 Linear Thermoelasticity . . . . .                                 | 15        |
| 2.4.1 Constitutive Model . . . . .                                    | 16        |
| 2.4.2 Governing Equations of Linear Thermoelasticity . . . . .        | 17        |
| 2.5 Linear Elastic Fracture Mechanics . . . . .                       | 18        |
| 2.5.1 Fracture Modelling of Brittle Materials . . . . .               | 19        |
| 2.5.2 Stress Intensity Factors . . . . .                              | 20        |
| 2.5.3 Prediction of Crack Path Based on SIFs . . . . .                | 21        |
| <b>3 Scaled Boundary Finite Element Method</b> . . . . .              | <b>23</b> |
| 3.1 Description of Geometry in SBFEM . . . . .                        | 23        |
| 3.1.1 Modeling of Bounded Domains . . . . .                           | 24        |
| 3.1.2 Transformation of Coordinates . . . . .                         | 26        |
| 3.2 SBFEM for Laplace Equation . . . . .                              | 29        |
| 3.2.1 Derivation of SBFE Equation in Temperature Change . . . . .     | 30        |
| 3.2.2 Solution of SBFE Equation by Eigenvalue Decomposition . . . . . | 34        |
| 3.3 SBFEM for Elastostatics . . . . .                                 | 36        |
| 3.3.1 Derivation of SBFE Equation in Displacement . . . . .           | 37        |
| 3.3.2 Solution of SBFE Equation by Schur Decomposition . . . . .      | 39        |
| 3.4 Shape Functions of Polygon Elements . . . . .                     | 41        |
| <b>4 SBFEM for Thermoelasticity</b> . . . . .                         | <b>43</b> |
| 4.1 Thermal Stress Analogous to Load . . . . .                        | 43        |
| 4.2 Thermal Load as Power Functions of Coordinates . . . . .          | 47        |
| 4.3 Supplementary Shape Functions . . . . .                           | 49        |
| 4.4 Discretization of Coupled Thermoelastic Equations . . . . .       | 53        |
| <b>5 Modeling of Functionally Graded Materials in SBFEM</b> . . . . . | <b>57</b> |
| 5.1 Fundamentals of FGMs . . . . .                                    | 57        |
| 5.2 Representation of FGMs in Local Coordinates . . . . .             | 58        |
| 5.3 Integration of Coefficient Matrices . . . . .                     | 60        |

|   |            |
|---|------------|
| <b>6 Fracture Modeling Using SBFEM . . . . .</b>                          | <b>63</b>  |
| 6.1 Evaluation of Fracture Parameters . . . . .                           | 63         |
| 6.1.1 Capturing of Singular Stress . . . . .                              | 63         |
| 6.1.2 Convergence of Singular Modes . . . . .                             | 65         |
| 6.1.3 Calculation of Generalized SIFs . . . . .                           | 66         |
| 6.2 Meshing and Re-meshing of Polygon Elements . . . . .                  | 69         |
| 6.2.1 Generation of Polygon Mesh . . . . .                                | 69         |
| 6.2.2 Localized Re-meshing Technique . . . . .                            | 71         |
| 6.2.3 Mapping of Re-meshed System . . . . .                               | 73         |
| <b>7 Numerical Examples Part-I: Uni-directional Coupling . . . . .</b>    | <b>77</b>  |
| 7.1 Validation of Stress Intensity Factors . . . . .                      | 77         |
| 7.1.1 Mode-I Fracture – Plate with Edge Crack . . . . .                   | 78         |
| 7.1.2 Mode-II Fracture – Plate with Center Crack . . . . .                | 79         |
| 7.1.3 Mixed-mode Fracture – Plate with Inclined Center Crack . . . . .    | 81         |
| 7.2 Stress Intensity Factors in FGMs . . . . .                            | 82         |
| 7.2.1 Plate with Linearly Varying Material Properties . . . . .           | 82         |
| 7.2.2 Plate with Hyperbolic Tangent Material Gradient . . . . .           | 84         |
| 7.2.3 Orthotropic Plate with Power-law Material Gradient . . . . .        | 87         |
| 7.3 Quasi-Static Crack Propagation . . . . .                              | 89         |
| 7.3.1 Corner Crack in Cruciform Panel . . . . .                           | 89         |
| 7.3.2 Edge Crack in Perforated Plate . . . . .                            | 91         |
| 7.3.3 Multiple Cracks Emanating from Perforation . . . . .                | 94         |
| <b>8 Numerical Examples Part-II: Transient Coupling . . . . .</b>         | <b>97</b>  |
| 8.1 Validation of Transient Stress Intensity Factors . . . . .            | 97         |
| 8.1.1 Mode-I Fracture – Temperature Shock . . . . .                       | 97         |
| 8.1.2 Mode-II Fracture – Temperature Shock . . . . .                      | 100        |
| 8.1.3 Mixed-mode Fracture – Flux Shock on Inclined Crack . . . . .        | 102        |
| 8.2 Dynamic Stress Intensity Factors in FGMs . . . . .                    | 103        |
| 8.2.1 Exponential Material Gradient Parallel to Crack . . . . .           | 104        |
| 8.2.2 Plate with Inclined Crack and Power-law Material Gradient . . . . . | 106        |
| 8.2.3 Orthotropic Plate with Exponential Material Gradient . . . . .      | 110        |
| 8.3 Fully Coupled Dynamic Crack Propagation . . . . .                     | 113        |
| 8.3.1 Temperature Shock in Notched Plate with Three Holes . . . . .       | 113        |
| 8.3.2 Temperature Shock in Hollow Disk with Multiple Cracks . . . . .     | 118        |
| <b>9 Concluding Remarks . . . . .</b>                                     | <b>123</b> |
| <b>Bibliography . . . . .</b>   | <b>125</b> |
| <b>List of Figures . . . . .</b>  | <b>133</b> |
| <b>List of Tables . . . . .</b>   | <b>137</b> |

# Nomenclature

## Roman Letters

|                                   |  |
|-----------------------------------|--|
| $\Delta a$                        | User-defined crack increment/accumulation length                       |
| $\Delta a_e$                      | Crack extension length at each time step                               |
| $b_1, b_2$                        | Component matrices of elastic problem                                  |
| $\bar{b}_1, \bar{b}_2$            | Component matrices of thermal problem                                  |
| $B$                               | Strain-displacement transformation matrix                              |
| $\bar{B}$                         | Flux-temperature transformation matrix                                 |
| $B_1, B_2$                        | Components of shape functions and their derivatives of elastic problem |
| $\bar{B}_1, \bar{B}_2$            | Components of shape functions and their derivatives of thermal problem |
| $\underline{\underline{B}}$       | Left Cauchy-Green tensor   |
| $c$                               | Specific heat capacity at constant strain                              |
| $c_R, c_d, c_s$                   | Rayleigh, dilatational, and shear wave speeds                          |
| $\mathbf{c}$                      | Integration constants of elastic problem                               |
| $\bar{\mathbf{c}}$                | Integration constants of thermal problem                               |
| $\underline{\underline{C}}$       | Right Cauchy-Green tensor  |
| $\underline{\underline{d}}$       | Symmetric part of spatial velocity gradient                            |
| $D$                               | Elasticity matrix  |
| $\underline{\underline{D}}$       | Elasticity tensor  |
| $\underline{\underline{e}}$       | Euler-Almansi strain tensor  |
| $E$                               | Young's modulus  |
| $E_0, E_1, E_2$                   | SBFEM coefficient matrix of elastic problem                            |
| $\bar{E}_0, \bar{E}_1, \bar{E}_2$ | SBFEM coefficient matrix of thermal problem                            |
| $\underline{\underline{E}}$       | Green-Lagrange strain tensor   |
| $F$                               | Non-homogeneous term of SBFE equation in displacement                  |
| $\bar{F}$                         | Non-homogeneous term of SBFE equation in temperature                   |

|                         |  |
|-------------------------|--|
| <u>F</u>                | Deformation gradient tensor              |
| <u>g</u>                | Generalized coordinate functions         |
| <u>G</u>                | Shear modulus                            |
| $h_S$                   | Production of entropy in the bulk        |
| $H$                     | Heat supply in bulk                      |
| <u>H</u>                | Displacement gradient                    |
| $J$                     | Jacobian                                 |
| <b>J</b>                | Jacobian matrix                          |
| $k_1, k_2$              | Crack velocity functions                 |
| <b>K</b>                | Stress intensity factors                 |
| $\mathbf{K}^{dyn}$      | Dynamic stress intensity factors         |
| $\hat{\mathbf{K}}$      | Stiffness matrix of elastic problem      |
| $\overline{\mathbf{K}}$ | Stiffness-like matrix of thermal problem |
| <u>L</u>                | Spatial velocity gradient                |
| $m$                     | Mass                                     |
| <u>M</u>                | Thermo-stress module                     |
| $\overline{\mathbf{N}}$ | Vector of shape function                 |
| $\mathbf{N}$            | Matrix of shape function                 |
| $O$                     | Scaling center                           |
| $\mathbf{p}$            | Body forces                              |
| <u>P</u>                | First Piola-Kirchhoff stress tensor      |
| $\mathbf{q}$            | Heat flux                                |
| $\mathbf{R}^F$          | Nodal thermal load vector                |
| <u>R</u>                | Proper orthogonal tensor                 |
| $s^*$                   | Specific heat supply per unit mass       |
| <b>S</b>                | Matrix of eigenvalues in Schur form      |
| $\mathbf{S}^{(s)}$      | Schur block of singular modes            |
| $S^e$                   | Subdomain                                |
| <u>S</u>                | Second Piola-Kirchhoff stress tensor     |
| $t$                     | Time                                     |
| X                       |  |

|                      |   |
|----------------------|---|
| <b>u</b>             | Displacement vector                                   |
| $\mathbf{u}_b$       | Nodal displacements                                   |
| $\hat{\mathbf{u}}_b$ | Vector of nodal displacements with auxiliary DOFs     |
| <b>U</b>             | Right stretch tensor                                  |
| $v$                  | Crack propagation velocity                            |
| <b>V</b>             | Schur vectors   |
| <b>V</b>             | Left stretch tensor                                   |
| <b>w</b>             | Skew-symmetric part of spatial velocity gradient      |
| $\mathbf{x}$         | Position of material point in current configuration   |
| <b>X</b>             | Position of material point in reference configuration |
| <b>Z</b>             | SBFEM Z-matrix of elastic problem                     |
| $\bar{\mathbf{Z}}$   | SBFEM Z-matrix of thermal problem                     |

## Greek Letters

|  |  |
|--|--|
| $\alpha$                                 | Thermal expansion                        |
| $\beta$                                  | Vector of thermal expansion coefficients |
| <b><math>\beta</math></b>                | Tensor of thermal expansion coefficients |
| $\Gamma$                                 | Boundary of computational domain         |
| $\epsilon$                               | Infinitesimal strain vector              |
| $\epsilon_0$                             | Initial thermal strain vector            |
| <b><math>\underline{\epsilon}</math></b> | Infinitesimal strain tensor              |
| $\eta$                                   | Local coordinate                         |
| $\theta$                                 | Temperature change                       |
| $\bar{\theta}$                           | Absolute temperature                     |
| $\theta_0$                               | Reference temperature                    |
| $\kappa$                                 | Heat conduction vector                   |
| <b><math>\kappa</math></b>               | Heat conduction tensor                   |
| $\lambda$                                | Eigenvalues                              |
| $\nu$                                    | Poisson's ratio                          |
| $\xi$                                    | Scaling direction                        |

|                      |  |
|----------------------|--|
| $\rho$               | Density  |
| $\sigma$             | Cauchy stress vector   |
| $\sigma_0$           | Initial thermal stress vector                                    |
| $\sigma^{(s)}$       | Singular stress vector   |
| $\underline{\sigma}$ | Cauchy stress tensor   |
| $\tau$               | Surface traction   |
| $\varphi$            | Crack angle  |
| $\varphi_p$          | Crack propagation angle  |
| $\varphi$            | Non-linear mapping from reference to current configuration       |
| $\Phi$               | Eigenvectors   |
| $\chi$               | SBFEM shape functions of displacement field                      |
| $\bar{\chi}$         | SBFEM shape functions of temperature field                       |
| $\hat{\chi}$         | SBFEM matrix of displacement and supplementary shape functions   |
| $\psi$               | Helmholtz free energy  |
| $\Psi$               | Accumulated transformation matrix of Schur block diagonalization |
| $\Omega$             | Computational domain   |

## Special Letters

|                 |  |
|-----------------|--|
| $\mathcal{D}$   | Dissipation inequality                 |
| $\mathcal{E}_e$ | Strain energy                          |
| $\mathcal{E}_s$ | Surface energy                         |
| $\mathcal{H}$   | Heat supply                            |
| $\mathcal{K}$   | Kinetic energy                         |
| $\mathcal{P}$   | Potential energy                       |
| $\mathcal{S}^*$ | Entropy density per unit mass          |
| $\mathcal{U}$   | Internal energy                        |
| $\mathcal{U}^*$ | Specific internal energy per unit mass |
| $\mathcal{V}_0$ | Reference configuration                |
| $\mathcal{V}_c$ | Current configuration                  |
| $\mathcal{V}_t$ | Control volume                         |

|     |                                     |
|-----|-------------------------------------|
| $W$ | Rate of work of the external forces |
|-----|-------------------------------------|

## Abbreviations

|         |  |
|---------|--|
| BEM     | Boundary Element Method  |
| CTE     | Crack Tip Element  |
| DBEM    | Dual Boundary Element Method                                       |
| DOF     | Degrees of freedom   |
| EFEM    | Embedded Finite Element Method                                     |
| EFGM    | Element-Free Galerkin Method                                       |
| EPFM    | Elastic-Plastic Fracture Mechanics                                 |
| ES-FEM  | Edge-Based Smoothed Finite Element Method                          |
| ES-XFEM | Edge-Based Smoothed Extended Finite Element Method                 |
| FEM     | Finite Element Method  |
| FGM     | Functionally Graded Material                                       |
| LEFM    | Linear Elastic Fracture Mechanics                                  |
| MERR    | Maximum Energy Release Rate  |
| MLPGM   | Meshless Local Petrov-Galerkin Method                              |
| MM      | Meshless Method  |
| MTS     | Maximum Tangential Stress  |
| NMM     | Numerical Manifold Method  |
| NURBS   | Non-Uniform Rational B-Splines                                     |
| PFM     | Phase Field Method   |
| QPE     | Quarter-Point Element  |
| SBFEM   | Scaled Boundary Finite Element Method                              |
| SED     | Strain Energy Density  |
| SFEM    | Smoothed Finite Element Method                                     |
| SIF     | Stress Intensity Factor  |
| SSY     | Small Scale Yielding   |
| XCQ4    | Extended four-node Consecutive-interpolation Quadrilateral element |
| XFEM    | Extended Finite Element Method                                     |



# Chapter 1

## Introduction

The first chapter of the thesis introduces the motivation behind investigating the phenomenon of coupled thermoelastic fracture. This chapter provides an overview of the current state of the art, highlighting existing knowledge and methodologies to model fracture while identifying research gaps that necessitate further exploration. The chapter concludes by formulating the objectives and outlining the structure of this work.

### 1.1 Motivation

Investigating coupled thermoelastic fracture is crucial in designing various engineering components, including automobiles, aircraft, gas turbines, fuel cells, pressure vessels, and nuclear plants. In many practical applications, ensuring the safety and reliability of materials and structures is of utmost importance. Studying the thermoelastic fracture phenomenon helps identify potential issues related to thermal and mechanical stresses, allowing engineers to design components that bear hostile working conditions. When these stresses exceed the material's strength, defects (cracks) may arise and propagate, ultimately causing the failure. Brittle or quasi-brittle materials like ceramics and concrete are particularly vulnerable to these failure mechanisms.

On the other hand, special purpose materials known as *functionally graded materials* (FGMs) are designed to withstand challenging thermoelastic settings such as higher temperature gradients without losing material strength. These non-homogeneous materials are engineered by a continuous and smooth variation of materials' chemical composition, microstructure, or design attributes. FGMs typically have a ceramic-rich phase suitable for higher temperatures and a metallic-rich phase that provides strength against failure. FGMs can be tailored to suit specific applications such as thermal barrier coatings, wear-resistant coatings, and biomedical materials.

Analytical methods can be employed to study thermoelastic fracture, which provides valuable solutions for the asymptotic stress distribution near the crack. However, such closed-form solutions are generally unavailable for problems with intricate geometries, real-world boundary conditions, complex constitutive models, dynamic evolution of defects, and multi-physics interactions. Numerical methods are preferred over analytical approaches to overcome the challenges present in real-world applications by leveraging the advancements in computational power. Furthermore, analyzing fracture phenomena in FGMs due to their non-homogeneous nature poses additional challenges in engineering applications.

As discussed in the following section, several numerical techniques have been proposed to address the material failure. One such numerical technique is the *scaled boundary finite element method* (SBFEM). The semi-analytical nature of the SBFEM provides an elegant and accurate description of stress singularities in fracture problems. The SBFEM has been successfully applied to model fracture in purely elastic settings. However, modeling fully coupled thermoelastic fracture using the SBFEM is yet to be explored.

## 1.2 State of the Art

The overarching concept of material failure falls under the subject of fracture mechanics. The study of fracture mechanics is classified into *linear elastic fracture mechanics* (LEFM) and *elastic-plastic fracture mechanics* (EPFM). Generally, the assumptions of LEFM apply to brittle materials, and are also referred to as *brittle or quasi-brittle fracture*. Similarly, *ductile fracture* refers to the assumptions of EPFM, which usually occurs in metals. Brittle fracture is characterized by rapid cracking without plastic deformation due to stress exceeding the material's strength. In contrast, ductile fracture is the gradual tearing of material with significant plastic deformation, typically observed in high-ductility materials such as metals. This work considers material failure due to brittle fracture because of its rapid nature; readers are referred to [1] for a comprehensive understanding of ductile fracture.

In 1921, Griffith [2] presented the foundational work on brittle fracture based on the assumptions of LEFM (see Section 2.5.1). After a century of dedicated work, studying brittle fracture remains a very active research topic. Two distinct formulations, i.e., *computational* and *continuum*, are used in LEFM to model fracture using various numerical methods. The detailed formulation of computational models is summarized in [3]; for the details on continuum models, readers are referred to [4].

In continuum formulations, the damage is not represented by an actual (physical) material discontinuity but *regularized* or *smeared* over a certain domain. The smearing of damage is achieved by introducing characteristic length into the discretization. An example of a continuum model is a variational approach proposed in [5] by generalizing Griffith's theory as an energy minimization problem. This variational approach is then regularized in [6], now commonly known as the *phase field method* (PFM). In the PFM, brittle fracture is treated as a coupled problem of displacement and regularized damage, i.e., *phase field* [7–9]. Recently, the PFM has become an attractive approach to model fracture. However, in the PFM, like any other continuum model, the choice of characteristic length dictates the regularization of damage. Thus, smaller characteristic lengths are required to model fracture accurately when the length scales of the domain and the characteristic length are different, leading to significantly higher computational costs.

On the other hand, in the computational models of LEFM, damage is defined as a *discrete* material discontinuity (crack). In discrete fracture modeling, the representation of the crack is more natural and accurate. However, it leads to singular stress behavior near the crack, requiring special attention in modeling fracture. The following discusses numerous numerical methods in the context of discrete fracture.

The thermoelastic fracture is modeled using analytical methods in the early works [10, 11]. These analytical methods are very limited in applications, e.g., simplified geometry and boundary conditions. For complex cases, numerical methods are a necessity. The *finite element method* (FEM) is the most common and versatile numerical method. In the past seven decades, extensive research has taken place to advance the FEM. Now, the FEM has reached a mature development status and become the industry standard for numerical methods. In the early years of the 1970s, the FEM is first used to model the discrete crack behavior in the context of LEFM [12–15]. However, the advent of varieties of other numerical techniques to date indicates that the FEM has certain limitations in modeling fracture problems. The prominent challenges of modeling discrete fractures using the FEM are listed below:

- the requirement of a conforming mesh to represent the material discontinuity (crack) and re-meshing of the problem domain in the case of moving crack,
- the limitation in reproducing the singular stress field, usually by polynomial-based shape or interpolation functions, especially in non-homogeneous materials, such as FGMs,

- the need for additional post-processing methods in evaluating fracture parameters, such as the *stress intensity factors* (SIFs).

In the early works of fracture modeling using the FEM, special purpose *crack tip elements* (CTEs) were used to discretize the vicinity of crack tip [16–19], and the remaining domain was discretized using standard finite elements. Although the shape functions of CTEs can reproduce the stress singularities, they are incompatible with the shape functions of conventional finite elements. Thus, transition elements were required to connect the CTEs with outer elements. Another limitation of CTE shape functions is their inability to represent constant strain modes and rigid body motion [20]. In [21–23], the idea of *quarter-point elements* (QPEs) is proposed. In QPEs, the mid-side node of an element near the crack tip is placed at the quarter-point position. The shift of the node position leads to a nonlinear mapping between the natural and local coordinates. QPEs can reproduce square root singularity throughout the elements. Moreover, using QPEs does not require transition elements as in the case of CTEs, and the whole domain can be discretized using QPEs. In contrast to CTEs, QPEs can model constant strain modes and rigid body motion. However, one of the key limitations of QPEs is that they can only account for the square root singularity. Therefore, QPEs can only reproduce singularities in homogeneous isotropic materials with narrow cracks. In the case of reentrant corners or non-homogeneous materials such as FGMs, QPEs cannot model singular stress behavior.

Following the development of special crack tip elements, a new class of finite element method called the *embedded finite element method* (EFEM) or *strong discontinuity approach* is proposed in [24–26]. The fundamental idea of the EFEM is to capture the jump in the displacement field due to discontinuity in a single element. For this purpose, the approximation of the displacement field is *enriched* by additional parameters, generally called *enrichment*. In the EFEM, the enrichment is inherent to the cracked element only. Thus, the crack growth can be modeled without the need for re-meshing. In the early versions of the EFEM, the correctness of relative rigid body modes was not guaranteed, leading to stress locking [27]. Nevertheless, the modified versions of the EFEM have been applied to a variety of problems, such as piezoelectric ceramics [28], geomaterials [29], electro-mechanical coupled formulations [30], and dynamic fracture [31]. However, some researchers noticed that the EFEM becomes sensitive to the orientation of the discontinuity in relation to the nodes. In unfavorable situations, the element's response is not unique [32].

Based on the EFEM, a very flexible method called *eXtended finite element method* (XFEM) is proposed in [33–35] to model displacement discontinuity. The XFEM introduces the *nodal enrichment* for the elements cut by a crack. The most important characteristic of the XFEM is the use of local partition of unity enrichment [36–38]. The fundamental concept of the XFEM is to decompose the displacement field into continuous and discontinuous parts. The continuous part is the standard finite element approximation. The discontinuous part is the addition to the finite element approximation through the local partition of unity enrichment, generally the asymptotic behavior of singularity. Similar to the EFEM, the crack growth problems are modeled without the requirement of re-meshing. However, contrary to the EFEM, the additional unknowns corresponding to nodal enrichment of the XFEM cannot be condensed on the element level, thus increasing the size of the problem.

Although the XFEM has been developed for elastic fracture modeling, it has also been employed in various other applications, such as two-phase flow [39, 40], biomechanics [41], and fluid-structure interaction [42, 43]. The XFEM has also been successfully used to model coupled thermoelastic fracture [44–51]. Furthermore, the XFEM has also been employed to model fracture in FGMs [52–57]. In recent years, the XFEM has proved to be a versatile numerical technique to model numerous problems; however, the XFEM's drawbacks need to be considered. The XFEM requires a known enrichment function to model the discontinuity accurately. When the analytical description of discontinuity is unknown, the selection of enrichment functions is not straightforward. In such cases, the evaluation of enrichment functions requires cumbersome procedures. Moreover,

the numerical integration in the XFEM requires more attention, especially around the crack tip. Another major concern of the XFEM is the poor convergence rate caused by the *blending elements*, i.e., elements adjacent to the enriched elements [58]. Furthermore, the XFEM can not deal with distorted meshes, which may cause stability issues in problems with high mesh distortion [59]. Along with the aforementioned finite element methods, the *boundary element method* (BEM) has also gained significant attention to model fracture in the past few decades. Similar to the FEM, the BEM was first used to model linear elastic fracture in the early 1970s [60–62]. In the BEM, the weak form is formulated using boundary integral equations, which require the discretization only on the boundary. Consequently, it reduces the complexity of the mesh generation. Moreover, the discretization of spatial dimensions is also reduced by one. In [63–67], the BEM is employed to model thermoelastic fracture. The thermoelastic fracture in FGMs using the BEM is studied in [68, 69]. However, the BEM is only applicable where the fundamental solution (*Green's functions*) can be computed, thus restricting the application range of the BEM to limited problems.

Another class of numerical methods is the *meshless methods* (MMs) that are introduced to circumvent the issues of mesh dependency in approximating the solution and representing the discontinuities. In MMs, the approximation is built from nodes only. Thus, the adaptive  $h$ -refinement can be easily implemented in the MMs. For solid mechanics applications, the MMs based on a global weak form are introduced in [70–72] termed the *element-free Galerkin* (EFG) method. Another popular MM is the *meshless local Petrov-Galerkin* (MLPG) method [73–75] that is based on local weak forms. Although the MMs can model the discontinuities, they also require certain refinement and enrichment schemes around the crack to capture the singularities accurately. Moreover, the nodal interpolation in standard MM does not fulfill the so-called Kronecker-Delta property, which leads to complications in applying essential boundary conditions.

The aforementioned numerical methods for discrete fracture can be combined to exploit their advantages and remedy their limitations. For example, the MM is combined with the FEM by employing strain smoothing techniques resulting in *smoothed finite element methods* (SFEM). In return, the SFEM is combined with the XFEM, leading to *edge-based smoothed extended finite element method* (ES-XFEM). The discussion on the evolution of numerical methods and their combinations is out of the scope of this work. Nevertheless, readers are referred to a few review articles [58, 59, 76–79] for the details.

Although the previously discussed numerical methods can capture discontinuities, they still require additional post-processing techniques to evaluate the SIFs, usually in the form of integrals. One of the most common techniques is conservation integral, i.e.,  $J$ -integral [80, 81], because it has a physical meaning of the energy release rate. However, the  $J$ -integral cannot distinguish between crack opening and shearing modes. Based on  $J$ -integral, an interaction integral ( $I$ -integral) is proposed in [82] using designable auxiliary fields. The early work on  $I$ -integral is dedicated to homogeneous isotropic materials. In [83–85], homogeneous and non-homogeneous auxiliary fields are proposed to develop  $I$ -integral for isotropic and orthotropic FGMs. The evaluation of SIFs for thermoelastic FGMs using  $I$ -integral is established in [86, 87]. The interaction integral method has become the standard technique to obtain the fracture parameters, and its evolution is summarized in [88]. However, the required auxiliary field of  $I$ -integral needs to be determined in advance by the underlying numerical method. Consequently, the accuracy of fracture parameters heavily depends on the accuracy of the numerical method's solution near the crack tip. Moreover, the additional post-processing required to calculate SIFs is burdensome to model fracture.

In the past twenty years, the *scaled boundary finite element method* (SBFEM) emerged as an alternative to the aforementioned numerical methods in modeling fracture. The SBFEM is a semi-analytical method proposed by Wolf and Song [89–91] initially to model unbounded medium-structure interaction. It is first introduced as a *consistent infinitesimal finite-element cell method* [89]. The derivation for elastodynamic problems based on the Galerkin weighted residual technique is first presented in [90], where the term *scaled boundary finite element method* is coined. Over

the last few years, the SBFEM has evolved considerably to address multiple problems using formulations of bounded and unbounded domains. These problems include but are not limited to elastodynamics [92–94], diffusion [95], elastic guided waves [96, 97], electromagnetics [98], sloshing of fluid-filled tanks [99], fluid-structure interaction [100], acoustic-structure interaction [101], poroelasticity [102], shell structures [103], and isogeometric analysis [104, 105]. Additional efforts have also been made to improve the numerical aspects of the SBFEM [106–109]. Moreover, the SBFEM is employed to model regularized fracture using the phase-field and cohesive zone models [110–115].

Like the BEM, in the SBFEM, only the boundary (circumferential direction) of the computational domain is discretized using finite elements, reducing the dimension of spatial discretization by one. The complete geometry is then described by translating the mesh of the boundary along the *scaling direction* (radial direction). In the SBFEM modeling, generally, the equilibrium is strongly applied in the radial direction, while the weak form of equilibrium is only enforced in the circumferential direction. When the behavior of the problem is assumed to be linear, the SBFEM formulation leads to a second-order ordinary differential equation (SBFE equation) in the local radial coordinate. In the case of linear elasticity, the resulting scaled boundary finite element equation can be solved analytically using the eigenvalue method or Schur decomposition. Unlike the BEM, the SBFEM does not require a priori knowledge of a fundamental solution.

One salient feature of the SBFEM is its ability to capture stress singularities conveniently (details are presented in Chapter 6). In the bounded domain, a crack is represented by an *open-element* whose boundary does not form a closed loop. The open boundary is scaled to the point called the *scaling center* that coincides with the crack tip. The stress singularities are evaluated directly using the analytical description of stress in the radial direction dominated by the corresponding order of singularity [116–118]. In [119], the singular stress field is analyzed for thermal loading, where the predefined temperature field is expressed by a power function of the *scaled boundary finite element* (SBFE) radial coordinate. A generalized expression of the stress intensity factor for any given order of stress singularity is derived in [120]. Furthermore, using the semi-analytical solution of SBFEM singular modes, an automatic enrichment of finite elements for stress singularities is proposed in [121].

In the SBFEM, a computational domain is meshed with arbitrary shape elements such as polygons, given that the scaling requirements are satisfied (details are presented in Chapter 3). The choice of scaled boundary polygon elements facilitates the meshing and re-meshing of geometry for discrete crack propagation modeling in elastostatic [122] and elastodynamics [123]. The elastic fracture modeling in FGMs using scaled boundary polygons is addressed in [124–126].

In a linear elastic setting, the uniqueness of the analytical solution of the SBFE equation is guaranteed. However, due to the semi-analytical nature of the SBFEM, analytical solutions of non-linear problems in the radial direction are difficult to derive. Recently, the SBFEM shape functions have been constructed from the analytical solution of linear problems in [124]. These shape functions are then used to model fracture in physically and geometrically non-linear elastomers [127] and for elasto-plastic analysis [128]. An alternative method based on the weak form of equilibrium in both radial and circumferential directions is proposed in [105] to model non-linear problems. In [105], *nonuniform rational B-splines* (NURBS) basis functions are used to approximate the displacements in the radial direction. Considerable effort has been made to extend this approach in modeling physically and geometrically non-linear problems in two- and three-dimensional solids [129–133]. However, due to its fully numerical nature, the built-in SBFEM feature of modeling stress singularities is lost. The direct modeling of stress singularities demands the analytical expression of displacement and, consequently, stress in the radial direction. The work presented in this thesis concerns fracture modeling in linear thermoelasticity. Thus, the weak form of equilibrium is only enforced in the circumferential direction, and the analytical solutions of displacement and temperature fields are obtained in the radial direction.

### 1.3 Objectives and Outline

The scaled boundary finite element method has emerged as a reliable alternative to other numerical methods for modeling various physical problems. The SBFEM is particularly effective in capturing stress singularities accurately and efficiently without requiring additional post-processing. Additionally, using scaled boundary polygon elements enhances the flexibility in meshing and re-meshing of complex geometries, which is necessary for modeling discrete crack propagation. However, the application of the SBFEM in modeling discrete crack propagation within the context of fully coupled thermoelastic problems remains unexplored. Therefore, this work aims to extend the capabilities of SBFEM and assess its effectiveness in modeling thermoelastic fracture in a two-dimensional bounded domain. Furthermore, this work examines fractures caused by thermo-mechanical coupling in specialized engineering materials, specifically functionally graded materials, using the SBFEM.

To this end, first, a uni-directional coupling of temperature and displacement fields is assumed. In uni-directional coupling, the semi-analytical solution of the displacement field is only possible when the known temperature distribution varies as a power function of SBFEM radial coordinates. The SBFEM modeling of fully coupled thermoelasticity can be obtained by introducing the supplementary shape functions. Formulation of supplementary shape functions does not require a priori solution of temperature field. Moreover, the material coefficient matrices of thermoelastic FGMs can also be integrated semi-analytically using the supplementary shape functions. The generalized stress intensity factors can be evaluated directly from the semi-analytical representation of the stress field irrespective of the order of stress singularities. In the case of discrete crack propagation problems, a polygon-based localized re-meshing algorithm that requires minimal changes to the mesh can be employed, and physical variables can be mapped directly using the SBFEM polygon shape functions. The mapping of auxiliary degrees of freedom corresponding to supplementary shape functions can be obtained by constructing and solving a system of linear equations that relates the displacement and auxiliary degrees of freedom.

This thesis comprises nine chapters. Chapter 2 summarizes the fundamentals of kinematics, continuum mechanics, and the governing equations of linear thermoelasticity that are relevant to this work. Furthermore, the basic concepts of linear elastic fracture mechanics (LEFM) are also discussed.

Chapter 3 presents the geometric transformation of a two-dimensional bounded domain into the SBFEM coordinates. Additionally, the SBFEM derivation and solution procedure of heat conduction and linear elasticity equations are briefly discussed. The chapter concludes by illustrating the scaled boundary shape functions of polygon elements for temperature and displacement fields. In Chapter 4, the SBFEM formulation of coupled thermoelasticity is discussed. First, thermal stress is considered as the load vector for the elastostatic problem. A semi-analytical representation of the thermal load vector is obtained for the case where thermal stress is described by the power functions of radial coordinates, i.e., the analytical direction of the SBFEM discretization. However, the modeling of thermal load requires a priori knowledge of the temperature field and thus is limited to the uni-directional coupling. Next, a set of scaled boundary supplementary shape functions is obtained from the particular solution of non-homogeneous term caused by thermal stress. The supplementary shape functions do not require a known temperature field. Finally, the discretization of the governing equation for fully coupled thermoelasticity is obtained using the SBFEM shape functions for displacement enriched by the supplementary shape functions.

Chapter 5 briefly discusses the fundamentals of functionally graded materials. Moreover, the transformation of material grading functions from the Cartesian to scaled boundary coordinates is addressed. In the end, the semi-analytical integration of material coefficient matrices for thermoelastic FGMs is proposed.

Chapter 6 summarizes the built-in ability of the SBFEM to capture stress singularities. Furthermore,

the fracture parameters, such as stress intensity factors, are evaluated directly from their definitions without additional post-processing. For the crack propagation problems, the SIFs are utilized to obtain the path of moving cracks. Next, the generation of polygon elements from the background triangular elements is discussed. The choice of polygon elements facilitates the geometry update by restricting the re-meshing region to a localized patch near a crack. Finally, the mapping of the system after a re-meshing step is considered. A novel approach for mapping auxiliary degrees of freedom associated with the supplementary shape functions is presented.

In Chapter 7, several numerical examples are studied to validate the developed SBFEM in evaluating SIFs and modeling the crack propagation problems in the case of uni-directional coupling.

Chapter 8 also presents several numerical examples that validate the developed SBFEM in fracture modeling for fully coupled thermoelasticity cases.

Chapter 9 provides the concluding remarks on the presented work, discusses the current limitations, and possible further developments.



# Chapter 2

## Theoretical Framework

This chapter outlines the theoretical basis of this work. First, a brief introduction to continuum mechanics is presented to establish the notations and relations of physical quantities. The concept of continuum mechanics includes the kinematics of a body and the balance laws of physical quantities. An essential understanding of fracture behavior is required to address the failure mechanisms in material or structure. Thus, the basic idea of linear fracture mechanics is summarized.

The classical continuum mechanics concepts are taken from the textbooks, such as [134–136]. The fundamentals of linear thermoelasticity are briefly explained using the textbook [137]. The concepts of linear fracture mechanics are taken from the textbooks, e.g. [138, 139]. Readers are referred to the textbooks for a detailed comprehension of these topics.

### 2.1 Kinematics

Continuum mechanics defines the motion of the body from the *reference configuration*  $\mathcal{V}_0$  to the *current or actual configuration*  $\mathcal{V}_c$  (see Fig. 2.1). The non-linear mapping  $\varphi$  of the material point in current configuration  $\mathbf{x}$  is expressed as

$$\mathbf{x} = \varphi(\mathbf{X}, t), \quad (2.1)$$

where  $t$  is time, and  $\mathbf{X}$  is the position of the material point in reference configuration.

A tensor  $\underline{\underline{\mathbf{F}}}$  is introduced to map the line elements from the reference configuration  $d\mathbf{X}$  to the current configuration  $d\mathbf{x}$ , such that

$$d\mathbf{x} = \underline{\underline{\mathbf{F}}} d\mathbf{X}. \quad (2.2)$$

Equation (2.2) indicates that  $\underline{\underline{\mathbf{F}}}$  represents a gradient. Thus,  $\underline{\underline{\mathbf{F}}}$  is called a *deformation gradient*, and in symbolic form it is expressed as

$$\underline{\underline{\mathbf{F}}} = \frac{\partial \varphi(\mathbf{X}, t)}{\partial \mathbf{X}} = \frac{\partial \mathbf{x}}{\partial \mathbf{X}} = \text{Grad}(\mathbf{x}). \quad (2.3)$$

In the following, the differential operators with the first uppercase letter, i.e.,  $\text{Grad}(\cdot)$  and  $\text{Div}(\cdot)$ , characterize quantities with respect to the reference configuration. Operators with the first lowercase letter, i.e.,  $\text{grad}(\cdot)$  and  $\text{div}(\cdot)$ , describe quantities with respect to the current configuration.

In Eq. (2.3), the deformation mapping  $\varphi$  is assumed to be smooth and continuous with respect to  $\mathbf{X}$  and  $t$ . Furthermore, for any fixed time  $t$ , the mapping in Eq. (2.2) has to be one-to-one, which excludes a singularity. Hence, the following condition holds true

$$J = \det \underline{\underline{\mathbf{F}}} > 0. \quad (2.4)$$

Here,  $J$  defines a determinant commonly known as *Jacobian*. Since  $\underline{\underline{\mathbf{F}}}$  cannot be singular, it must be invertible, and Eq. (2.2) can be written as

$$d\mathbf{X} = \underline{\underline{\mathbf{F}}}^{-1} d\mathbf{x}. \quad (2.5)$$

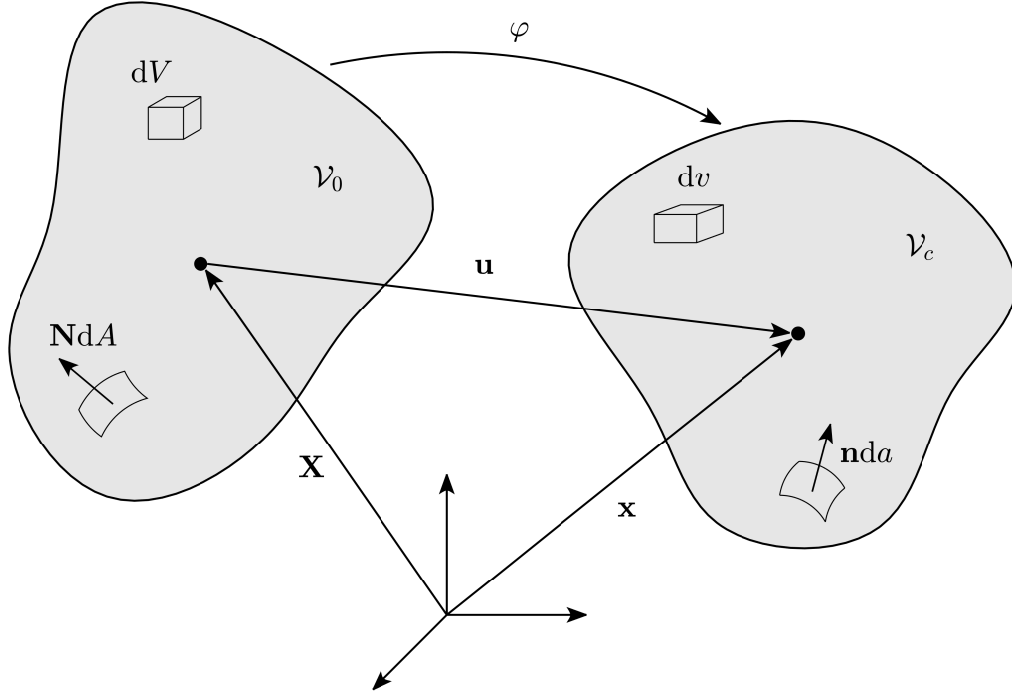


Figure 2.1: Configurations of a body in continuum mechanics.

Next, the transformation of surface area and volume elements is considered. The mapping of the surface elements  $dA$  with the normal vector  $\mathbf{N}$  is given by the formula of *Nanson*

$$\mathbf{n} da = J \underline{\underline{\mathbf{F}}}^{-T} \mathbf{N} dA, \quad (2.6)$$

where  $\mathbf{n}$  is the normal vector of surface elements in the current configuration. The symbol  $\underline{\underline{\mathbf{F}}}$ <sup>-T</sup> denotes the transpose inverse of the deformation gradient. Similarly, the volume elements are transformed by the relation

$$dv = J dV. \quad (2.7)$$

Note that transformation for the covariant gradient of the vector field  $\mathbf{W}(\mathbf{X}) = \mathbf{w}(\mathbf{x}) = \mathbf{w}(\varphi(\mathbf{X}))$  is obtained as [136]

$$\text{Grad}(\mathbf{W}) = \text{grad}(\mathbf{w}) \underline{\underline{\mathbf{F}}} \iff \text{grad}(\mathbf{w}) = \text{Grad}(\mathbf{W}) \underline{\underline{\mathbf{F}}}^{-1} \quad (2.8)$$

Now, by introducing a *displacement vector* as

$$\mathbf{u}(\mathbf{X}, t) = \varphi(\mathbf{X}, t) - \mathbf{X}, \quad (2.9)$$

the deformation gradient  $\underline{\underline{\mathbf{F}}}$  can be expressed as follows

$$\underline{\underline{\mathbf{F}}} = \text{Grad}(\mathbf{X} + \mathbf{u}(\mathbf{X}, t)) = \mathbf{1} + \text{Grad}(\mathbf{u}) = \mathbf{1} + \underline{\underline{\mathbf{H}}}, \quad (2.10)$$

In the above equation, the deformation gradient  $\underline{\underline{\mathbf{F}}}$  is related to the *displacement gradient*  $\underline{\underline{\mathbf{H}}}$  as follows

$$\underline{\underline{\mathbf{H}}} = \text{Grad}(\mathbf{u}) = \frac{\partial \mathbf{u}}{\partial \mathbf{X}} = \frac{\partial \mathbf{x}}{\partial \mathbf{X}} - \frac{\partial \mathbf{X}}{\partial \mathbf{X}} = \underline{\underline{\mathbf{F}}} - \mathbf{1}. \quad (2.11)$$

Next, the dependency of the deformation on time  $t$  is considered. In this work, the over-dot notation  $(\dot{\cdot})$  is used to indicate the time derivative. The velocity of a material point in reference configuration is defined by material time derivative

$$\dot{\mathbf{X}}(\mathbf{X}, t) = \frac{\partial \varphi(\mathbf{X}, t)}{\partial t} = \dot{\varphi}(\mathbf{X}, t). \quad (2.12)$$

Using Eqs. (2.3), (2.8), and (2.12), the time derivative of deformation gradient  $\underline{\underline{F}}$  is written as

$$\dot{\underline{\underline{F}}} = \text{Grad}(\dot{\varphi}(\mathbf{X}, t)) = \text{grad}(\dot{\mathbf{x}}) \underline{\underline{F}}, \quad (2.13)$$

where  $\dot{\mathbf{x}}$  represents the velocity of the material point in the current configuration. Analogously,  $\ddot{\mathbf{x}}$  describes the acceleration of the material point in the current configuration. These velocity and acceleration are defined as

$$\dot{\mathbf{x}} = \frac{d\mathbf{x}}{dt}, \quad \text{and} \quad \ddot{\mathbf{x}} = \frac{d\dot{\mathbf{x}}}{dt}, \quad (2.14)$$

respectively. In Eq. (2.13), the term  $\text{grad}(\dot{\mathbf{x}})$  represents the *spatial velocity gradient*  $\underline{\underline{L}}$ , such that

$$\underline{\underline{L}} = \text{grad}(\dot{\mathbf{x}}) = \frac{\partial \dot{\mathbf{x}}}{\partial \mathbf{x}} = \dot{\underline{\underline{F}}} \underline{\underline{F}}^{-1}. \quad (2.15)$$

Moreover, the spatial velocity gradient can be split into symmetric  $\underline{\underline{d}}$  and skew-symmetric parts as follows

$$\underline{\underline{d}} = \frac{1}{2} (\underline{\underline{L}} + \underline{\underline{L}}^T), \quad (2.16a)$$

$$\underline{\underline{w}} = \frac{1}{2} (\underline{\underline{L}} - \underline{\underline{L}}^T). \quad (2.16b)$$

## 2.2 Strain and Stress Measure

Any invertible second-order tensor that can be decomposed using the *polar decomposition*. Similarly, the deformation gradient  $\underline{\underline{F}}$  in Eq. (2.3) is decomposed into an orthogonal rotation and symmetric positive definite tensors, such that

$$\underline{\underline{F}} = \underline{\underline{R}} \underline{\underline{U}} = \underline{\underline{V}} \underline{\underline{R}}, \quad (2.17)$$

where  $\underline{\underline{R}}$  is the proper orthogonal tensor, i.e.,  $\underline{\underline{R}}^{-1} = \underline{\underline{R}}^T$ , and  $\underline{\underline{U}}, \underline{\underline{V}}$  are the right and left stretch tensors, respectively. Multiplying Eq. (2.17) by  $\underline{\underline{F}}^T$  and using the properties of orthogonal rotation tensor, i.e.,  $\underline{\underline{R}} \underline{\underline{R}}^T = \underline{\underline{R}}^T \underline{\underline{R}} = \mathbf{1}$ , result in

$$\underline{\underline{C}} = \underline{\underline{F}}^T \underline{\underline{F}} = \underline{\underline{U}}^T \underline{\underline{U}} = \underline{\underline{U}}^2, \quad (2.18a)$$

$$\underline{\underline{B}} = \underline{\underline{F}} \underline{\underline{F}}^T = \underline{\underline{V}} \underline{\underline{V}}^T = \underline{\underline{V}}^2, \quad (2.18b)$$

where  $\underline{\underline{C}}$  and  $\underline{\underline{B}}$  are the right and left *Cauchy-Green* tensors, respectively. In a deformable body, strain is induced only by stretching and not by a pure rotation or rigid body displacement. The strain measures describe the stretching of line elements from reference to current configuration, such that

$$d\mathbf{x}^2 - d\mathbf{X}^2 = d\mathbf{x} \cdot d\mathbf{x} - d\mathbf{X} \cdot d\mathbf{X}. \quad (2.19)$$

Using Eqs. (2.2) and (2.18a), Eq. (2.19) is expressed in the reference configuration as

$$d\mathbf{x}^2 - d\mathbf{X}^2 = \underline{\underline{F}} \cdot d\mathbf{X} \cdot \underline{\underline{F}} \cdot d\mathbf{X} - d\mathbf{X} \cdot d\mathbf{X}, \quad (2.20a)$$

$$= d\mathbf{X} \cdot \underline{\underline{C}} \cdot d\mathbf{X} - d\mathbf{X} \cdot d\mathbf{X}, \quad (2.20b)$$

$$= d\mathbf{X} \cdot 2 \underline{\underline{E}} \cdot d\mathbf{X}. \quad (2.20c)$$

Here,  $\underline{\underline{E}}$  describes the *Green-Lagrange* strain tensor and given as

$$\underline{\underline{E}} = \frac{1}{2} (\underline{\underline{F}}^T \underline{\underline{F}} - \mathbf{1}) = \frac{1}{2} (\underline{\underline{C}} - \mathbf{1}). \quad (2.21)$$

Using Eq. (2.10), the Green-Lagrange strain tensor  $\underline{\underline{E}}$  in Eq. (2.21) can be expressed in the form of the displacement gradient as follows

$$\underline{\underline{E}} = \frac{1}{2} \left( \underline{\underline{H}} + \underline{\underline{H}}^T + \underline{\underline{H}}^T \underline{\underline{H}} \right), \quad (2.22a)$$

$$= \frac{1}{2} \left( \text{Grad}(\mathbf{u}) + \text{Grad}(\mathbf{u})^T + \text{Grad}(\mathbf{u})^T \text{Grad}(\mathbf{u}) \right). \quad (2.22b)$$

Analogous to Eq. (2.20), Eq. (2.19) is written in the current configuration using Eqs. (2.5) and (2.18b)

$$d\mathbf{x}^2 - d\mathbf{X}^2 = d\mathbf{x} \cdot 2\underline{\underline{e}} \cdot d\mathbf{x}, \quad (2.23)$$

where  $\underline{\underline{e}}$  is the *Euler-Almansi* strain tensor, such that

$$\underline{\underline{e}} = \frac{1}{2} \left( \mathbf{1} - \underline{\underline{F}}^{-T} \underline{\underline{F}}^{-1} \right) = \frac{1}{2} \left( \mathbf{1} - \underline{\underline{B}}^{-1} \right). \quad (2.24)$$

The relationship between the Green-Lagrange and the Euler-Almansi strain tensors is established using Eqs. (2.21) and (2.24) as follows

$$\underline{\underline{E}} = \underline{\underline{F}}^T \underline{\underline{e}} \underline{\underline{F}}, \quad (2.25)$$

and its material time derivative  $\dot{\underline{\underline{E}}}$  is related to the symmetric part of the spatial velocity gradient Eq. (2.16a)

$$\dot{\underline{\underline{E}}} = \underline{\underline{F}}^T \underline{\underline{d}} \underline{\underline{F}}. \quad (2.26)$$

Next, the stress measures in continuum mechanics are considered. In the current configuration, the stress resultant force  $d\mathbf{f}$  on an infinitesimal surface  $da$  is defined as

$$d\mathbf{f} = \boldsymbol{\tau} da, \quad (2.27)$$

where  $\boldsymbol{\tau}$  is the *surface traction*. The *Cauchy theorem* describes the mapping of the normal vector  $\mathbf{n}$  to the respective surface traction as

$$\boldsymbol{\tau} = \underline{\underline{\sigma}} \mathbf{n}, \quad (2.28)$$

where  $\underline{\underline{\sigma}}$  is the second order symmetric tensor called the *Cauchy stress tensor*. In the reference configuration, stress resultant force  $d\mathbf{f}$  is expressed as

$$d\mathbf{f} = \boldsymbol{\tau}_0 dA, \quad (2.29)$$

where  $\boldsymbol{\tau}_0$  is the *nominal traction*. Similarly to Eq. (2.28), the relation of nominal traction is given as

$$\boldsymbol{\tau}_0 = \underline{\underline{P}} \mathbf{N}, \quad (2.30)$$

where  $\underline{\underline{P}}$  is the *first Piola-Kirchhoff stress tensor* which maps  $\mathbf{N}$  from the reference configuration to corresponding  $\boldsymbol{\tau}_0$  in the current configuration. The relationship between  $\underline{\underline{\sigma}}$  and  $\underline{\underline{P}}$  is given by Nanson's formula in Eq. (2.6), such that

$$\underline{\underline{P}} = J \underline{\underline{F}}^{-T} \underline{\underline{\sigma}} \iff \underline{\underline{\sigma}} = \frac{1}{J} \underline{\underline{F}}^T \underline{\underline{P}}. \quad (2.31)$$

A stress measure in purely reference configuration is obtained by introducing the *second Piola-Kirchhoff stress tensor*  $\underline{\underline{S}}$ , i.e.,

$$\underline{\underline{S}} = \underline{\underline{F}}^{-1} \underline{\underline{P}} = J \underline{\underline{F}}^{-1} \underline{\underline{\sigma}} \underline{\underline{F}}^{-T}. \quad (2.32)$$

## 2.3 Balance Laws

This section presents the balance laws for different physical quantities. These balance laws include the conservation of mass and momentum, first and second laws of thermodynamics, i.e., conservation of energy and entropy inequality, respectively.

Consider a control volume  $\mathcal{V}_t$ , the rate change of any physical quantity  $\varphi$  is balanced by the flux  $\mathbf{q}_\varphi$  of  $\varphi$  into the  $\mathcal{V}_t$  with the production  $h_\varphi$  and supply  $s_\varphi$  of  $\varphi$ , such that

$$\frac{d}{dt} \int_{\mathcal{V}_t} \varphi dv = \int_{\mathcal{V}_t} (h_\varphi + s_\varphi) dv + \int_{\partial\mathcal{V}_t} \mathbf{q}_\varphi \cdot \mathbf{n} da, \quad (2.33)$$

In the control volume  $\mathcal{V}_t$ , the physical quantities are assumed to be smooth and continuous. Therefore, the *Reynold's transport theorem* reads

$$\frac{d}{dt} \int_{\mathcal{V}_t} \varphi dv = \int_{\mathcal{V}_t} \frac{\partial \varphi}{\partial t} dv + \int_{\partial\mathcal{V}_t} \varphi \dot{\mathbf{x}} \cdot \mathbf{n} da, \quad (2.34)$$

and the *Gauss' divergence theorem* follows as

$$\int_{\partial\mathcal{V}_t} \varphi \dot{\mathbf{x}} \cdot \mathbf{n} da = \int_{\mathcal{V}_t} \operatorname{div}(\varphi \dot{\mathbf{x}}) dv. \quad (2.35)$$

Substituting Eqs. (2.34) and (2.35) into Eq. (2.33) yields the balance law of  $\varphi$  in the local form

$$\dot{\varphi} + \varphi \operatorname{div}(\dot{\mathbf{x}}) = \operatorname{div}(\mathbf{q}_\varphi) + h_\varphi + s_\varphi. \quad (2.36)$$

### 2.3.1 Conservation of Mass

In a closed system, the *total mass*  $m$  is conserved, i.e.,  $\mathbf{q}_\rho = \mathbf{0}$  and  $h_\rho = s_\rho = 0$ . For conservation of mass, Eq. (2.33) is written as

$$\frac{d}{dt} \int_{\mathcal{V}_t} \rho dv = 0. \quad (2.37)$$

Using Eq. (2.36), the local form of Eq. (2.37), i.e., continuity equation is expressed as

$$\dot{\rho} + \rho \operatorname{div}(\dot{\mathbf{x}}) = 0. \quad (2.38)$$

### 2.3.2 Conservation of Momentum

In a closed system, the momentum density  $\rho \dot{\mathbf{x}}$  is balanced by the source of momentum inside the body and momentum flux at the surface. The general equation of balance law Eq. (2.36) reads

$$\frac{d}{dt} \int_{\mathcal{V}_t} \rho \dot{\mathbf{x}} dv = \int_{\mathcal{V}_t} \mathbf{p} dv + \int_{\partial\mathcal{V}_t} \boldsymbol{\tau} da, \quad (2.39)$$

where  $\mathbf{p}$  and  $\boldsymbol{\tau}$  are the body forces and surface traction, respectively. Applying the Cauchy theorem Eq. (2.28) and the continuity equation Eq. (2.38) to Eq. (2.39) yields the conservation of linear momentum in the local form

$$\rho \ddot{\mathbf{x}} = \operatorname{div}(\underline{\underline{\sigma}}^T) + \mathbf{p}. \quad (2.40)$$

Analogous to Eq. (2.39), the conservation of angular momentum in the global form reads

$$\frac{d}{dt} \int_{\mathcal{V}_t} \mathbf{x} \times \rho \dot{\mathbf{x}} dv = \int_{\mathcal{V}_t} \mathbf{x} \times \mathbf{p} dv + \int_{\partial\mathcal{V}_t} \mathbf{x} \times \boldsymbol{\tau} da. \quad (2.41)$$

Again, applying the Cauchy theorem Eq. (2.28), the continuity equation Eq. (2.38), and using the conservation of linear momentum Eq. (2.40), the local form of Eq. (2.41) simplifies to

$$\underline{\underline{\sigma}} = \underline{\underline{\sigma}}^T. \quad (2.42)$$

Using Eq. (2.42), the balance law in Eq. (2.40) is expressed in a more convenient form as

$$\rho \ddot{\mathbf{x}} = \operatorname{div}(\underline{\underline{\sigma}}) + \mathbf{p}. \quad (2.43)$$

### 2.3.3 Conservation of Energy

The conservation of energy is given by the first law of thermodynamics. It states that in a control volume  $\mathcal{V}_t$ , the rate of *internal energy*  $\mathcal{U}(\mathcal{V}_t)$  and *kinetic energy*  $\mathcal{K}(\mathcal{V}_t)$  is balanced by the *rate of work of the external forces*  $\mathcal{W}(\mathcal{V}_t)$  and the *heat supply*  $\mathcal{H}(\mathcal{V}_t)$

$$\frac{d}{dt} (\mathcal{U}(\mathcal{V}_t) + \mathcal{K}(\mathcal{V}_t)) = \mathcal{W}(\mathcal{V}_t) + \mathcal{H}(\mathcal{V}_t). \quad (2.44)$$

The rate of internal energy and kinetic energy is defined as follows

$$\frac{d}{dt} (\mathcal{U}(\mathcal{V}_t) + \mathcal{K}(\mathcal{V}_t)) = \frac{d}{dt} \int_{\mathcal{V}_t} \rho \left( \mathcal{U}^* + \frac{|\dot{\mathbf{x}}|^2}{2} \right) dv = \int_{\mathcal{V}_t} \rho (\dot{\mathcal{U}}^* + \dot{\mathbf{x}} \cdot \ddot{\mathbf{x}}) dv, \quad (2.45)$$

where  $\mathcal{U}^*$  is the *specific internal energy* per unit mass. The rate of work of the external forces is given by

$$\mathcal{W}(\mathcal{V}_t) = \int_{\mathcal{V}_t} \mathbf{p} \cdot \dot{\mathbf{x}} dv + \int_{\partial\mathcal{V}_t} \boldsymbol{\tau} \cdot \dot{\mathbf{x}} da, \quad (2.46)$$

and the heat supply is expressed as

$$\mathcal{H}(\mathcal{V}_t) = \int_{\mathcal{V}_t} \rho s^* dv - \int_{\partial\mathcal{V}_t} \mathbf{q} \cdot \mathbf{n} da, \quad (2.47)$$

where  $\mathbf{q}$  is the *heat flux* and  $s^*$  is the *specific heat supply* per unit mass. Substituting Eqs. (2.45), (2.46), and (2.47) into Eq. (2.44) yields

$$\int_{\mathcal{V}_t} \rho (\dot{\mathcal{U}}^* + \dot{\mathbf{x}} \cdot \ddot{\mathbf{x}}) dv = \int_{\mathcal{V}_t} \mathbf{p} \cdot \dot{\mathbf{x}} dv + \int_{\partial\mathcal{V}_t} \boldsymbol{\tau} \cdot \dot{\mathbf{x}} da + \int_{\mathcal{V}_t} \rho s^* dv - \int_{\partial\mathcal{V}_t} \mathbf{q} \cdot \mathbf{n} da. \quad (2.48)$$

Using the balance of linear momentum Eq. (2.43), the Gauss' divergence theorem Eq. (2.35), and employing the symmetric part of spatial velocity gradient  $\underline{\underline{d}}$ , the balance of energy Eq. (2.48) is written in the local form

$$\rho \dot{\mathcal{U}}^* = \rho s^* + \underline{\underline{\sigma}} \cdot \underline{\underline{d}} - \operatorname{div}(\mathbf{q}). \quad (2.49)$$

### 2.3.4 Entropy Inequality

The second law of thermodynamics states that the *entropy*  $\mathcal{S}$  of a system cannot decrease. Considering the general form of balance law Eq. (2.36), the balance law of  $\mathcal{S}$  in the global form reads

$$\frac{d}{dt} \int_{\mathcal{V}_t} \rho \mathcal{S}^* dv = \int_{\mathcal{V}_t} \left( h_{\mathcal{S}} + \frac{\rho s^*}{\bar{\theta}} \right) dv + \int_{\partial\mathcal{V}_t} -\frac{\mathbf{q}}{\bar{\theta}} \cdot \mathbf{n} da, \quad (2.50)$$

where  $\mathcal{S}^*$  is the *entropy density* per unit mass,  $h_{\mathcal{S}}$  is the *production of entropy* in the bulk, and  $\bar{\theta}$  is the absolute temperature. Applying the condition of *entropy inequality* set forth by the second law of thermodynamics, i.e.,  $h_{\mathcal{S}} \geq 0$ , the local form of Eq. (2.50) results in the *Clausius-Duhem inequality*

$$\rho \dot{\mathcal{S}}^* + \operatorname{div} \left( \frac{\mathbf{q}}{\bar{\theta}} \right) - \frac{\rho s^*}{\bar{\theta}} = h_{\mathcal{S}} \geq 0. \quad (2.51)$$

After multiplying Eq. (2.51) with  $\bar{\theta}$ , the global form of Clausius-Duhem inequality reads

$$\int_{\mathcal{V}_t} \rho \bar{\theta} \dot{\mathcal{S}}^* dv - \int_{\mathcal{V}_t} \frac{1}{\bar{\theta}} \operatorname{grad}(\bar{\theta}) \cdot \mathbf{q} dv \geq \int_{\mathcal{V}_t} \rho s^* dv - \int_{\partial\mathcal{V}_t} \mathbf{q} \cdot \mathbf{n} da. \quad (2.52)$$

Using Eqs. (2.47), (2.46), and (2.48), Eq. (2.52) is reformulated as

$$\int_{\mathcal{V}_t} \rho \bar{\theta} \dot{\mathcal{S}}^* dv - \int_{\mathcal{V}_t} \frac{1}{\bar{\theta}} \operatorname{grad}(\bar{\theta}) \cdot \mathbf{q} dv \geq \int_{\mathcal{V}_t} \rho (\dot{\mathcal{U}}^* + \dot{\mathbf{x}} \cdot \ddot{\mathbf{x}}) dv - \mathcal{W}(\mathcal{V}_t). \quad (2.53)$$

Rearranging Eq. (2.53) yields

$$\int_{\mathcal{V}_t} \rho (\dot{\mathcal{U}}^* - \bar{\theta} \dot{\mathcal{S}}^*) dv + \int_{\mathcal{V}_t} \rho \dot{\mathbf{x}} \cdot \ddot{\mathbf{x}} dv \leq \mathcal{W}(\mathcal{V}_t) - \int_{\mathcal{V}_t} \frac{1}{\bar{\theta}} \text{grad}(\bar{\theta}) \cdot \mathbf{q} dv. \quad (2.54)$$

After introducing the *Helmholtz free energy*  $\psi$  and its material time derivative  $\dot{\psi}$ , i.e.,

$$\psi = \mathcal{U}^* - \bar{\theta} \mathcal{S}^*, \quad (2.55a)$$

$$\dot{\psi} = \dot{\mathcal{U}}^* - \bar{\theta} \dot{\mathcal{S}}^* - \dot{\bar{\theta}} \mathcal{S}^*, \quad (2.55b)$$

Eq. (2.54) is expressed in the form of  $\psi$  as follows

$$\mathcal{W}(\mathcal{V}_t) - \int_{\mathcal{V}_t} \rho \dot{\mathbf{x}} \cdot \ddot{\mathbf{x}} dv + \int_{\mathcal{V}_t} \rho (\dot{\psi} + \dot{\bar{\theta}} \mathcal{S}^*) dv - \int_{\mathcal{V}_t} \frac{1}{\bar{\theta}} \text{grad}(\bar{\theta}) \cdot \mathbf{q} dv \geq 0. \quad (2.56)$$

Substituting the balance of linear momentum Eq. (2.43), the Gauss' divergence theorem Eq. (2.35), and using the symmetric part of spatial velocity gradient  $\underline{\underline{\mathbf{d}}}$ , Eq. (2.56) results in the *dissipation inequality*

$$\mathcal{D} = \int_{\mathcal{V}_t} \left[ \underline{\underline{\sigma}} \cdot \underline{\underline{\mathbf{d}}} - \rho (\dot{\psi} + \dot{\bar{\theta}} \mathcal{S}^*) - \frac{1}{\bar{\theta}} \text{grad}(\bar{\theta}) \cdot \mathbf{q} \right] dv \geq 0. \quad (2.57)$$

The above inequality must hold independently for the *conductive dissipation*  $\mathcal{D}_\theta$  and the *intrinsic dissipation*  $\mathcal{D}_{int}$ . Thus, Eq. (2.57) is separated as follows

$$\mathcal{D}_\theta = - \int_{\mathcal{V}_t} \frac{1}{\bar{\theta}} \text{grad}(\bar{\theta}) \cdot \mathbf{q} dv \geq 0, \quad (2.58a)$$

$$\mathcal{D}_{int} = \int_{\mathcal{V}_t} \left[ \underline{\underline{\sigma}} \cdot \underline{\underline{\mathbf{d}}} - \rho (\dot{\psi} + \dot{\bar{\theta}} \mathcal{S}^*) \right] dv \geq 0. \quad (2.58b)$$

In reference configuration, the intrinsic dissipation in Eq. (2.58b) becomes the *Clausius-Planck inequality*.

## 2.4 Linear Thermoelasticity

In the following, the governing equations of linear thermoelasticity are formulated. First, the assumptions of linear elasticity are considered. Next, the constitutive material model for coupled thermoelasticity is presented. In the case of small deformations, a geometrically linear theory is sufficient to describe the kinematics of the body, i.e.,

$$\|\underline{\underline{\mathbf{H}}}\| = \left\| \frac{\partial \mathbf{u}}{\partial \mathbf{X}} \right\| \ll 1. \quad (2.59)$$

Consequently, the distinction between the differentiations with respect to  $\mathbf{x}$  and  $\mathbf{X}$  is unnecessary, thus

$$\frac{\partial(\cdot)}{\partial \mathbf{x}} \approx \frac{\partial(\cdot)}{\partial \mathbf{X}} \Rightarrow \text{grad}(\cdot) \approx \text{Grad}(\cdot), \quad \text{div}(\cdot) \approx \text{Div}(\cdot). \quad (2.60)$$

Considering Eqs. (2.10), (2.11), and (2.59) it can be concluded

$$J = \det \underline{\underline{\mathbf{F}}} \approx 1. \quad (2.61)$$

Furthermore, the higher-order terms of  $\underline{\underline{\mathbf{H}}}$  in Eq. (2.22a) can be neglected in small strain theory. In such a case, the Green-Lagrange  $\underline{\underline{\mathbf{E}}}$  and the Euler-Almansi  $\underline{\underline{\mathbf{e}}}$  strain tensors (see Eqs. (2.61) and (2.25)) become the *infinitesimal strain tensor*  $\underline{\underline{\epsilon}}$ , such that

$$\underline{\underline{\epsilon}} = \frac{1}{2} \left( \text{grad}(\mathbf{u}) + \text{grad}(\mathbf{u})^T \right), \quad (2.62)$$

The following analogous relation for small strain rates holds with the assumptions of a small deformation rate in Eq. (2.26)

$$\dot{\underline{\underline{\epsilon}}} \approx \dot{\underline{\epsilon}} \approx \dot{\underline{d}}. \quad (2.63)$$

The theory of linear thermoelasticity contains all the assumptions of linear elasticity. Additionally, it assumes that the temperature change  $\theta = \bar{\theta} - \theta_0$  is small compared to the reference temperature  $\theta_0$  [137], i.e.,  $|\theta/\theta_0| \ll 1$ .

### 2.4.1 Constitutive Model

This section presents the material models of linear thermoelasticity. The constitutive relations are derived using the dissipation inequality in Eq. (2.58). First, the conductive dissipation in Eq. (2.58a) is satisfied through *Fourier's law*, such that

$$\mathbf{q} = -\underline{\kappa} \operatorname{grad}(\theta), \quad (2.64)$$

where  $\mathbf{q}$  is the heat flux and  $\underline{\kappa}$  is a positive semi-definite *heat conduction tensor*. Next, the intrinsic dissipation inequality in Eq. (2.58b) is considered. The expression for the Helmholtz free energy  $\psi$  is required to satisfy intrinsic or local inequality, i.e., Clausius-Planck inequality. According to [140, 141], the free energy is a function of the deformation gradient and the absolute temperature. For small deformations, the free energy function and its material time derivative are defined as

$$\psi = \psi(\underline{\epsilon}, \bar{\theta}), \quad (2.65a)$$

$$\dot{\psi}(\underline{\epsilon}, \bar{\theta}) = \frac{\partial \psi}{\partial \underline{\epsilon}} \cdot \dot{\underline{\epsilon}} + \frac{\partial \psi}{\partial \bar{\theta}} \dot{\bar{\theta}}. \quad (2.65b)$$

Substituting Eqs. (2.65b) and (2.63) into Eq. (2.58b) and yields the inequality

$$\left( \underline{\sigma} - \rho \frac{\partial \psi}{\partial \underline{\epsilon}} \right) \cdot \dot{\underline{\epsilon}} + \left( -\rho \mathcal{S}^* - \rho \frac{\partial \psi}{\partial \bar{\theta}} \right) \dot{\bar{\theta}} \geq 0. \quad (2.66)$$

Considering the choice of free variables, the inequality in Eq. (2.66) is satisfied by the following relations

$$\underline{\sigma} = \rho \frac{\partial \psi}{\partial \underline{\epsilon}}, \quad (2.67a)$$

$$\mathcal{S}^* = -\frac{\partial \psi}{\partial \bar{\theta}}. \quad (2.67b)$$

The expression for  $\psi$  in Eq. (2.65a) is obtained by expanding  $\underline{\epsilon}$  and  $\bar{\theta}$  in the Taylor series at the reference state, i.e., Maclaurin series [137]

$$\psi(\underline{\epsilon}, \bar{\theta}) = \psi|_0 + \frac{\partial \psi}{\partial \underline{\epsilon}} \Big|_0 \cdot \underline{\epsilon} + \frac{\partial \psi}{\partial \bar{\theta}} \Big|_0 (\bar{\theta} - \theta_0), \quad (2.68)$$

where the notation  $|_0$  denotes the evaluation of a quantity at the reference state. Note that only up to first-order terms are retained in Eq. (2.68). Substituting Eq. (2.68) into Eq. (2.67) results in

$$\underline{\sigma} = \rho \frac{\partial \psi}{\partial \underline{\epsilon}} = \rho \frac{\partial \psi}{\partial \underline{\epsilon}} \Big|_0 + \rho \frac{\partial^2 \psi}{\partial \underline{\epsilon} \partial \underline{\epsilon}} \Big|_0 \cdot \underline{\epsilon} + \rho (\bar{\theta} - \theta_0) \frac{\partial^2 \psi}{\partial \underline{\epsilon} \partial \bar{\theta}} \Big|_0, \quad (2.69a)$$

$$\mathcal{S}^* = -\frac{\partial \psi}{\partial \bar{\theta}} = -\frac{\partial \psi}{\partial \bar{\theta}} \Big|_0 - \frac{\partial^2 \psi}{\partial \underline{\epsilon} \partial \bar{\theta}} \Big|_0 \cdot \underline{\epsilon} - (\bar{\theta} - \theta_0) \frac{\partial^2 \psi}{\partial \bar{\theta}^2} \Big|_0. \quad (2.69b)$$

At the reference state, material is assumed be stress-free, i.e.,  $(\partial\psi/\partial\underline{\epsilon})|_0 = \mathbf{0}$ . Moreover, the reference entropy is also zero at the reference state, such that  $(\partial\psi/\partial\bar{\theta})|_0 = 0$ . Thus, Eq. (2.69) yields the constitutive material model as follows

$$\underline{\sigma} = \underline{\underline{D}} \cdot \underline{\epsilon} - \underline{\underline{M}} \theta, \quad (2.70a)$$

$$\rho \bar{\theta} \dot{S}^* = \bar{\theta} \underline{\underline{M}} \cdot \underline{\dot{\epsilon}} + \rho c \theta, \quad (2.70b)$$

where

$$\underline{\underline{D}} = \rho \frac{\partial^2 \psi}{\partial \underline{\epsilon} \partial \underline{\epsilon}}, \quad (2.71a)$$

$$\underline{\underline{M}} = -\rho \frac{\partial^2 \psi}{\partial \underline{\epsilon} \partial \bar{\theta}}, \quad (2.71b)$$

$$c = -\bar{\theta} \frac{\partial^2 \psi}{\partial \bar{\theta}^2}. \quad (2.71c)$$

In Eq. (2.71),  $\underline{\underline{D}}$ ,  $\underline{\underline{M}}$ , and  $c$  represent the elasticity tensor, the thermo-stress module, and the specific heat at constant strain, respectively. In Eq. (2.71a),  $\underline{\underline{D}}$  is a positive definite tensor. By introducing the tensor of *thermal expansion coefficients*  $\underline{\underline{\beta}}$ , the thermo-stress module can be written as

$$\underline{\underline{M}} = \underline{\underline{D}} \cdot \underline{\underline{\beta}}. \quad (2.72)$$

Substituting Eq. (2.72) into Eq. (2.70a) yields

$$\underline{\sigma} = \underline{\underline{D}} \cdot \left( \underline{\epsilon} - \underline{\underline{\beta}} \theta \right), \quad (2.73)$$

where  $\underline{\underline{\beta}}\theta$  denotes the *thermal strain*.

## 2.4.2 Governing Equations of Linear Thermoelasticity

The governing equations of linear thermoelasticity are derived using the balance laws and the constitutive material model presented in Sections 2.3 and 2.4.1, respectively. The comparison of Eq. (2.55b) and Eq. (2.65b) after multiplying by  $\rho$  results in

$$\rho \left( \dot{U}^* - \bar{\theta} \dot{S}^* - \dot{\bar{\theta}} S^* \right) = \rho \left( \frac{\partial \psi}{\partial \underline{\epsilon}} \cdot \dot{\underline{\epsilon}} + \frac{\partial \psi}{\partial \bar{\theta}} \dot{\bar{\theta}} \right). \quad (2.74)$$

Substituting the equation for the balance of energy Eq. (2.49) into Eq. (2.74) and using Eqs. (2.63) and (2.67) yields

$$\rho \bar{\theta} \dot{S}^* = \rho s^* - \operatorname{div}(\mathbf{q}). \quad (2.75)$$

Applying the assumption of small temperature change by replacing  $\bar{\theta}$  with  $\theta_0$  in Eqs. (2.70b) and (2.75), and substituting the differentiation of Eq. (2.70b) into Eq. (2.75) results in

$$\rho c \dot{\theta} + \theta_0 \underline{\underline{M}} \cdot \dot{\underline{\epsilon}} + \operatorname{div}(\mathbf{q}) = H, \quad (2.76)$$

where  $H = \rho s^*$  indicates the heat supply in bulk.

In fully coupled linear thermoelasticity, Eqs. (2.76) and (2.43) govern the transient heat conduction and the motion of a body, respectively. Equations (2.73) and (2.64) describe the constitutive material model for stress and heat flux. Expressing the governing equations Eqs. (2.76) and

(2.43) and constitutive relations Equations (2.73) and (2.64) in Voigt notation yields the governing equations of linear thermoelasticity

$$\rho c \dot{\theta} + \theta_0 \mathbf{D} \boldsymbol{\beta} \nabla_u \dot{\mathbf{u}} + \nabla \cdot \mathbf{q} = H, \quad (2.77a)$$

$$\rho \ddot{\mathbf{u}} - \nabla_u^T \boldsymbol{\sigma} = \mathbf{p}, \quad (2.77b)$$

$$\boldsymbol{\sigma} = \mathbf{D}(\nabla_u \mathbf{u} - \boldsymbol{\beta} \theta), \quad (2.77c)$$

$$\mathbf{q} = -\kappa \nabla \theta. \quad (2.77d)$$

The governing equation Eq. (2.77) is expressed in the form of displacement  $\mathbf{u}$  and temperature change  $\theta$  as the state variables. In Eq. (2.77c), the constitutive material model can be expressed as engineering constants. Rewriting Eq. (2.77c) in the form of strain yields

$$\nabla_u \mathbf{u} = \boldsymbol{\epsilon} = \mathbf{D}^{-1} \boldsymbol{\sigma} + \boldsymbol{\beta} \theta. \quad (2.78)$$

Standard definitions of plane stress and strain states are applied in a two-dimensional domain. Considering the isotropic material symmetry, Eq. (2.78) is written in Voigt notation as

$$\begin{Bmatrix} \epsilon_{11} \\ \epsilon_{22} \\ \gamma_{12} \end{Bmatrix} = \begin{bmatrix} 1/E & -\nu/E & 0 \\ -\nu/E & 1/E & 0 \\ 0 & 0 & 1/G \end{bmatrix} \begin{Bmatrix} \sigma_{11} \\ \sigma_{22} \\ \sigma_{12} \end{Bmatrix} + \begin{Bmatrix} \alpha \\ \alpha \\ 0 \end{Bmatrix} \theta, \quad (2.79)$$

for plane stress state, and

$$\begin{Bmatrix} \epsilon_{11} \\ \epsilon_{22} \\ \gamma_{12} \end{Bmatrix} = \begin{bmatrix} (1-\nu^2)/E & -\nu(1+\nu)/E & 0 \\ -\nu(1+\nu)/E & (1-\nu^2)/E & 0 \\ 0 & 0 & 1/G \end{bmatrix} \begin{Bmatrix} \sigma_{11} \\ \sigma_{22} \\ \sigma_{12} \end{Bmatrix} + (1+\nu) \begin{Bmatrix} \alpha \\ \alpha \\ 0 \end{Bmatrix} \theta, \quad (2.80)$$

for plane strain state. Here,  $E$ ,  $G$ , and  $\nu$  are Young's modulus, shear modulus, and Poisson's ratio. In the case of orthotropic material symmetry when principal axes 1 and 2 of orthotropy are aligned with  $x$  and  $y$ , the stress and strain relation in Eq. (2.78) is given as

$$\begin{Bmatrix} \epsilon_{11} \\ \epsilon_{22} \\ \gamma_{12} \end{Bmatrix} = \begin{bmatrix} 1/E_1 & -\nu_{12}/E_1 & 0 \\ -\nu_{12}/E_1 & 1/E_2 & 0 \\ 0 & 0 & 1/G_{12} \end{bmatrix} \begin{Bmatrix} \sigma_{11} \\ \sigma_{22} \\ \sigma_{12} \end{Bmatrix} + \begin{Bmatrix} \alpha \\ \alpha \\ 0 \end{Bmatrix} \theta, \quad (2.81)$$

for plane stress state, and

$$\begin{Bmatrix} \epsilon_{11} \\ \epsilon_{22} \\ \gamma_{12} \end{Bmatrix} = \begin{bmatrix} (1-\nu_{31}\nu_{13})/E_1 & -(\nu_{12}+\nu_{13}\nu_{32})/E_1 & 0 \\ -(\nu_{12}+\nu_{13}\nu_{32})/E_1 & (1-\nu_{23}\nu_{32})/E_2 & 0 \\ 0 & 0 & 1/G_{12} \end{bmatrix} \begin{Bmatrix} \sigma_{11} \\ \sigma_{22} \\ \sigma_{12} \end{Bmatrix} + \begin{Bmatrix} \nu_{31}\alpha_3 + \alpha_1 \\ \nu_{32}\alpha_3 + \alpha_2 \\ 0 \end{Bmatrix} \theta, \quad (2.82)$$

for plane strain state. Furthermore, the following relations hold in case of orthotropic material

$$\nu_{21}/E_2 = \nu_{12}/E_1, \quad \nu_{31}/E_3 = \nu_{13}/E_1, \quad \nu_{32}/E_3 = \nu_{23}/E_2. \quad (2.83)$$

## 2.5 Linear Elastic Fracture Mechanics

This section provides a brief overview of linear elastic fracture mechanics (LEFM) to model brittle fracture. The microscopic description of failure, i.e., breaking of atomic bonds, is beyond the scope of this work. However, the fracture is predicted based on the macroscopic quantities, such as stresses, strains, and energy.

On a macroscopic scale, cracks are geometric discontinuities of one dimension lower than the dimension of the structure. For example, in the two-dimensional domain, a crack (discontinuity) is represented by lines forming a narrow wedge. These lines are called *crack faces*, and the endpoint of lines is called a *crack tip*. The following briefly summarises the fracture modeling of brittle materials with the assumption of linear elasticity.

### 2.5.1 Fracture Modelling of Brittle Materials

In the case of material failure, complex processes of atomic bond breaking occur in the so-called *fracture processes zone* in front of the crack tip. Continuum approaches to fracture can not model such events. However, if the fracture processes zone is assumed to be negligibly small compared to the macroscopic dimension of structure, the whole domain, including the crack, can be adequately described by continuum theory. This assumption holds for brittle materials and metals (ductile materials).

In linear elastic fracture mechanics (LEFM), the material is assumed to be elastic in the whole domain right up to fracture. The linear elastic analysis of crack tip fields yields stress and strain singularities at the crack tip. The occurrence of singularities near the crack tip challenges the assumption of linear elastic materials. However, the material will deform inelastically around the crack tip in so-called *yielding zone*. If the yielding zone is assumed to be small, the linear elastic solution approximates stresses and strains well outside the yielding zone. This assumption of the small yielding zone is commonly referred to as *small scale yielding* (SSY), which holds for brittle materials but not metals.

Following the assumptions of LEFM, Griffith [2] provided the framework to model brittle fracture based on the thermodynamic energy balance. Griffith suggested that the relation of *strain energy* ( $\mathcal{E}_e$ ) and *surface energy* ( $\mathcal{E}_s$ ) governs the crack extension in the stressed body. According to Griffith's theory, the rate of change of *potential energy* ( $\mathcal{P}$ ) with crack length  $a$  is zero, i.e.,

$$\frac{\partial \mathcal{P}}{\partial a} = \frac{\partial(\mathcal{E}_e - \mathcal{E}_s)}{\partial a} = 0. \quad (2.84)$$

The identity in Eq. (2.84) indicates that the strain energy release rate equals the rate of increase of surface energy. Thus, the crack propagates when the strain energy release rate exceeds the energy absorbed in creating new surfaces. Griffith's theory is based on the global energy balance and does not consider the stress fields near the crack tip. However, in the case of complex loading conditions, the analytical expression of the energy release rate cannot be formulated.

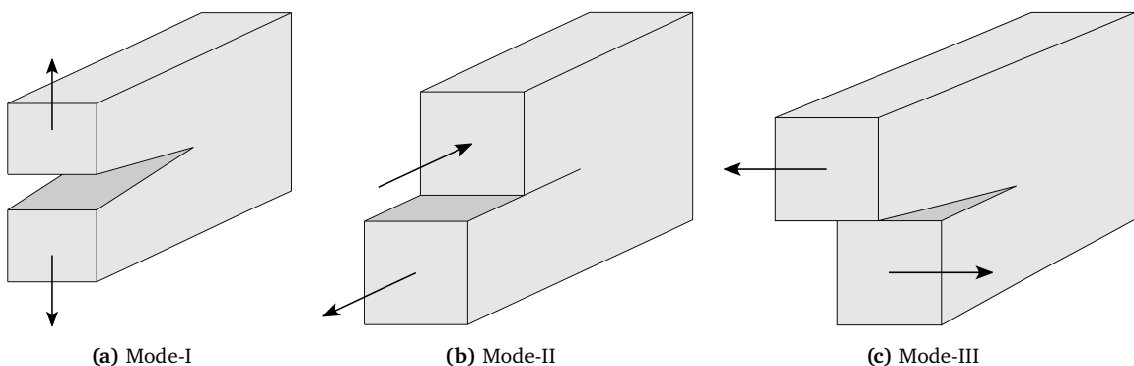


Figure 2.2: Crack opening modes.

The relation of fracture corresponding to the stress-strain fields near the crack tip was first introduced by Irwin [142]. Irwin modified Griffith's theory and identified three basic modes of crack extension as shown in Fig. 2.2. The most important case for practical applications is *Mode-I*, characterized by the opening of crack perpendicular to crack faces. In *Mode-II*, the crack faces slide relative to each other, resulting in shear stress. *Mode-III* characterized by the tearing of the crack faces in the plane of the crack. Irwin also found that each mode of crack extension has the same nature of stress field but different magnitudes irrespective of the loading and geometry. The effects of loading and geometry can be distinguished through a single parameter termed as *stress intensity factor* (SIF). Moreover, this modification formulated by Irwin can handle the assumptions of the SSY. In this work, a discrete representation of a crack is considered. Thus, a

fracture is determined using Irwin's modification, i.e., SIFs.

### 2.5.2 Stress Intensity Factors

In 1939 [143], Westergaard proposed a solution for the stress field surrounding a crack in an infinite plate. Westergaard's solution was expressed in rectangular coordinates represented by complex numbers. In 1957 [142], Irwin defined the stress intensity factor as the near-crack-tip approximation to Westergaard's solution in polar coordinates (see Figure 2.3). Irwin suggested in a two-dimensional domain with a crack, the crack opening modes (see Fig. 2.2) relate to stress intensity factors (SIFs).

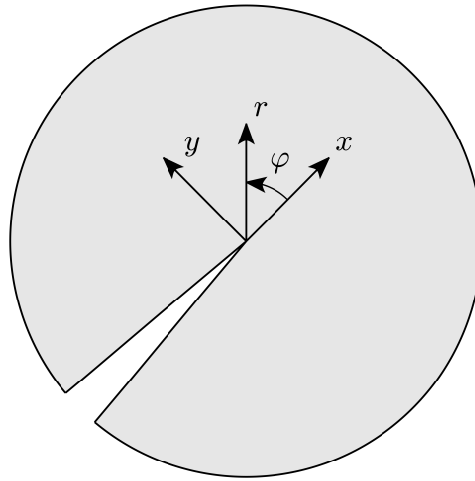


Figure 2.3: A domain with a crack in polar and Cartesian coordinates.

In a certain area around the crack tip significantly larger than process and yielding zones, the stress field is dominated by the singular stress  $\sigma^{(s)}$ . For a narrow crack in a homogeneous isotropic material, the expression for  $\sigma^{(s)}$  at the vicinity of the crack tip corresponding to three crack opening modes is given in [138] as

$$\begin{Bmatrix} \sigma_x^{(s)} \\ \sigma_y^{(s)} \\ \sigma_{xy}^{(s)} \end{Bmatrix} = \frac{K_I}{\sqrt{2\pi r}} \cos(\varphi/2) \begin{Bmatrix} 1 - \sin(\varphi/2) \sin(3\varphi/2) \\ 1 + \sin(\varphi/2) \sin(3\varphi/2) \\ \sin(\varphi/2) \cos(3\varphi/2) \end{Bmatrix}, \quad (2.85a)$$

$$\begin{Bmatrix} \sigma_x^{(s)} \\ \sigma_y^{(s)} \\ \sigma_{xy}^{(s)} \end{Bmatrix} = \frac{K_{II}}{\sqrt{2\pi r}} \begin{Bmatrix} -\sin(\varphi/2) [2 + \cos(\varphi/2) \cos(3\varphi/2)] \\ \sin(\varphi/2) \cos(\varphi/2) \cos(3\varphi/2) \\ \cos(\varphi/2) [1 - \sin(\varphi/2) \sin(3\varphi/2)] \end{Bmatrix}, \quad (2.85b)$$

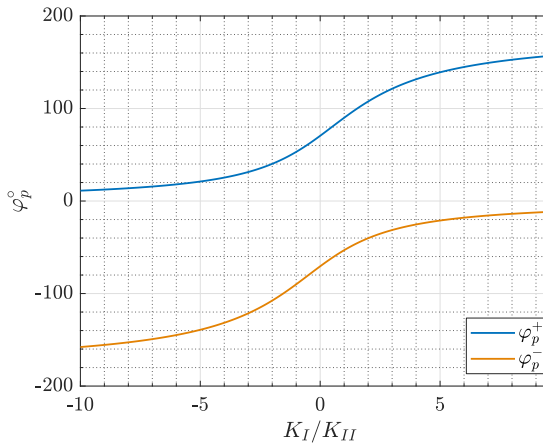
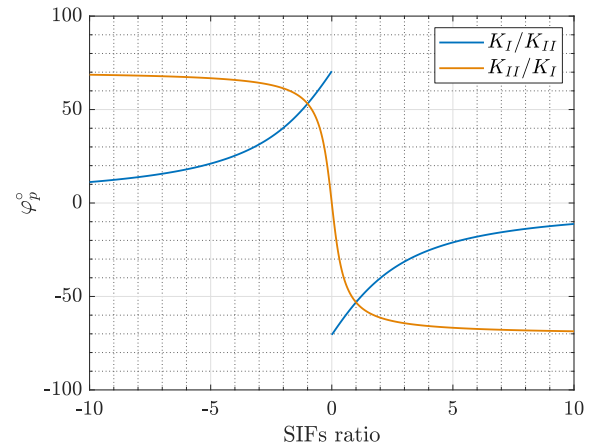
$$\begin{Bmatrix} \sigma_{xz}^{(s)} \\ \sigma_{yz}^{(s)} \end{Bmatrix} = \frac{K_{III}}{\sqrt{2\pi r}} \begin{Bmatrix} -\sin(\varphi/2) \\ \cos(\varphi/2) \end{Bmatrix}. \quad (2.85c)$$

Here, the symbols  $K_I$ ,  $K_{II}$ , and  $K_{III}$  denote the stress intensity factors corresponding to crack opening modes I, II, and III, respectively. In Eq. (2.85), the loading conditions and geometry do not affect the distribution of the singular stress field. The SIFs determine the intensity and magnitude of singular stress regarding loading, geometry, and crack length. The SIFs play a vital role in the mechanics of brittle fracture. They can be used to predict the path of moving crack problems.

### 2.5.3 Prediction of Crack Path Based on SIFs

In brittle fracture, the crack propagates immediately upon extension. In discrete crack propagation, the sudden crack extension is governed by the state of stress-field near the crack tip. The state of stress in the vicinity of crack tip is characterized by the stress intensity factors. Predicting the crack paths is essential to model the propagating cracks. Several well-known criteria are available in the literature to predict the crack propagation angle based on SIFs. For example, the maximum circumferential/tangential stress criterion (MTS) [144], the minimum strain energy density criterion (SED) [145], and the maximum energy release rate criterion (MERR) [146]. The MTS criterion dictates that the crack propagates when the maximum circumferential stress in a finite radius from a crack tip exceeds a critical value. According to the SED, the crack extends when the minimum strain energy density reaches the critical value. The minimum value is evaluated at a finite radius from a crack tip. Similarly, the MERR suggests the crack extension occurs in the direction corresponding to the maximum potential/strain energy when it reaches a critical value. In all criteria, the critical value is given by a material parameter relating to fracture toughness  $K_C$ .

Furthermore, MTS and MERR are two-dimensional criteria, while SED is three-dimensional. However, in certain cases of edge cracks, shear type of loading, and angled cracks, the SED failed to predict the crack paths [138]. In the MERR, a variation of strain energy is required to predict the crack path. In certain cases, the analytical description of strain energy is not available, thus, limiting the application of the MERR criterion. Nevertheless, after the initial crack kink, all of these criteria predict the crack trajectory to attain the principle of local symmetry [147], such that  $K_{II} = 0$ .

(a)  $\varphi_p$  obtained at different SIF ratios using Eq. (2.86)(b)  $\varphi_p$  obtained at different SIF ratios using Eq. (2.87)

**Figure 2.4:** Variation of crack propagation angle with respect to SIF ratio. (a) The values of  $\varphi_p^+$  and  $\varphi_p^-$  corresponding to  $K_I/K_{II}$  using Eq. (2.86). (b)  $\varphi_p$  obtained at different SIF ratios using Eq. (2.87).

The MTS criterion can be utilized directly by exploiting the expression of singular stress and, by extension, the SIFs in polar coordinates (see Eq. (2.85)). According to the MTS, the crack propagation angle  $\varphi_p$  in local crack coordinates is given as

$$\varphi_p = 2(\tan)^{-1} \left[ \frac{1}{4} \left( \frac{K_I}{K_{II}} \pm \sqrt{\left( \frac{K_I}{K_{II}} \right)^2 + 8} \right) \right]. \quad (2.86)$$

In the above equation, the crack propagation angle is governed by the ratio of SIFs, i.e.,  $K_I/K_{II}$ . It is evident from Eq. (2.86) that  $\varphi_p = 0$  if  $K_{II} = 0$ . Additionally, when  $K_{II} < 0$ , then  $\varphi_p > 0$ , and vice versa. Figure 2.4(a) presents both values of  $\varphi_p$  obtained using Eq. (2.86) at different ratios

of  $K_I/K_{II}$ . Here,  $\varphi_p^+$  and  $\varphi_p^-$  indicate the considered sign of the term in Eq. (2.86). For certain cases, one of two values of  $|\varphi_p|$  reaches  $180^\circ$  while the other remains in the acceptable range of a crack propagation angle. Selecting one  $\varphi_p$  out of two possible values requires unification during the crack propagation simulations.

A computationally more robust expression for  $\varphi_p$  is considered in [147] as follows

$$\varphi_p = 2 \left( \tan \right)^{-1} \left[ \frac{-2K_{II}/K_I}{1 + \sqrt{1 + 8(K_{II}/K_I)^2}} \right], \quad (2.87)$$

where the ratio  $K_{II}/K_I$  dictates the swerving of the crack paths. Figure 2.4(b) shows the obtained values of  $\varphi_p$  for different  $K_I/K_{II}$  and  $K_{II}/K_I$  ratios. As illustrated in Figure 2.4(b), any given ratio of  $K_{II}/K_I$  yields an acceptable value of  $\varphi_p$ . This work employs the modified MTS criterionEq. (2.87) to obtain the crack propagation angle.

# Chapter 3

## Scaled Boundary Finite Element Method

This chapter summarizes the fundamentals of the scaled boundary finite element method in modeling a two-dimensional bounded domain. For the comprehensive analysis of the SBFEM, readers are referred to the textbooks on the topic authored by J. P. Wolf [148] and C. Song [149]. The SBFEM is a semi-analytical approach that requires discretization only on the boundary of the computational domain, thus reducing the dimension of spatial description by one. In the bounded domain, the discretized boundary is *scaled* in the radial direction towards the interior to describe the complete domain. Generally, this representation of the computational domain leads to the semi-analytical equations for the system's state variable. Additionally, the SBFEM can model stress singularities without requiring any post-processing (details will be discussed in Chapter 6). In the following, Section 3.1 describes and transforms a geometry in SBFEM coordinates. Section 3.2 presents the SBFEM derivation and solution of the Laplace equation of heat conduction. Section 3.3 describes the derivation and solution procedure of the SBFEM for linear elasticity. Section 3.4 illustrates the scaled boundary polygon shape functions for temperature and displacement fields.

### 3.1 Description of Geometry in SBFEM

This section presents the geometric transformation of a domain  $\Omega$  with a boundary  $\Gamma$  into a scaled boundary finite element  $S$ -domain. The main focus of this work is modeling two-dimensional bounded domains; hence, only the transformation of bounded domains is discussed. For the modeling details of unbounded domains, readers are referred to [148].

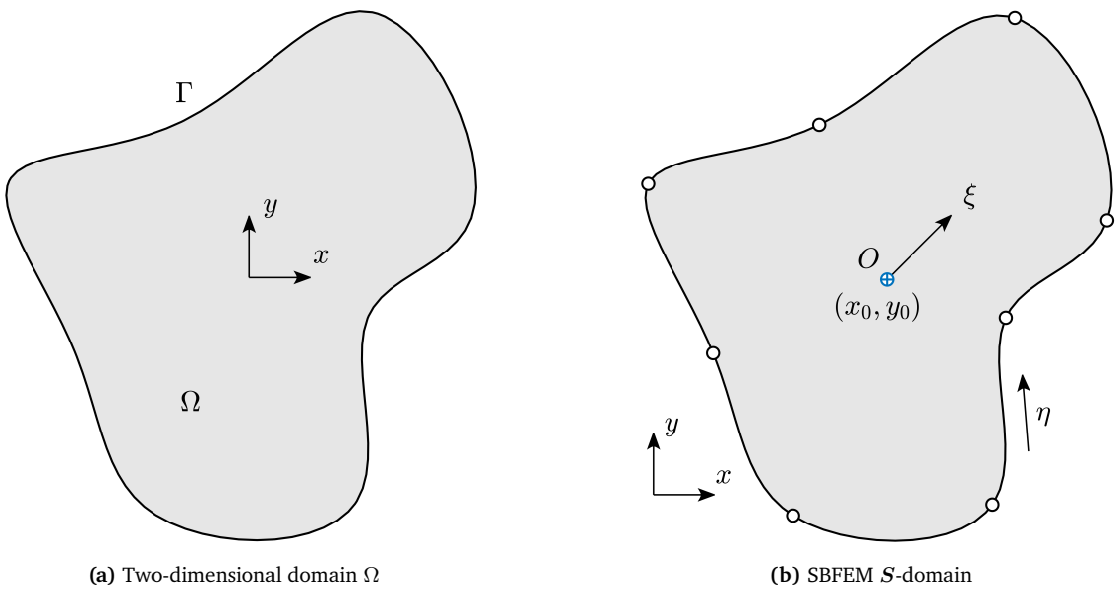


**Figure 3.1:** Geometric transformation of a domain  $\Omega$  with a boundary  $\Gamma$  into scaled boundary finite element  $S$ -domain.

The scaled boundary finite element method utilizes the *Duffy transformation* [150] to transform the Cartesian coordinates  $(x, y)$  to scaled boundary coordinates  $(\xi, \eta)$  for any given bounded domain  $\Omega$ . First, the domain boundary is discretized in the circumferential direction. The discretization of a scaled boundary is defined by SBFEM natural coordinate  $\eta$  (see Fig. 3.1). The discretized domain's boundary is then scaled onto a point called *scaling center*  $O$  described by a natural scaled boundary coordinate  $\xi$ . Using the SBFEM coordinates, a computational domain can be represented by any arbitrary-sided straight or curved element as long as the condition for scaling is satisfied. Moreover, a geometric discontinuity, such as a crack, can be modeled using an *open-element*. The following presents the modeling of bounded domains using polygon elements. The requirements for the scaling of a boundary and the modeling of open-element are discussed. The coordinate transformation from Cartesian to scaled boundary coordinates is described in Section 3.1.2.

### 3.1.1 Modeling of Bounded Domains

In a bounded domain, the scaled boundary coordinate  $\xi$  holds the values  $0 \leq \xi \leq 1$ , such that  $\xi = 0$  at the scaling center  $O$ , and  $\xi = 1$  at the boundary  $\Gamma$ . When the geometry of domain  $\Omega$  is *star-convex*, the scaled boundary transformation is guaranteed. Any given shape is a star-convex if *there exists a region from which every point on the boundary  $\Gamma$  is visible* [149]. Conversely, there is a point inside a polygon when connected to every point on the boundary; the lines connecting these points must remain inside the domain (see Fig. 3.2(a)). Furthermore, if the angle of visibility from the scaling center to the boundary is very small or close to  $180^\circ$ , the accuracy of the solution will be affected. This can be mitigated by subdividing the domain  $\Omega$  into smaller  $S$ -domains as shown in Fig. 3.2(b).

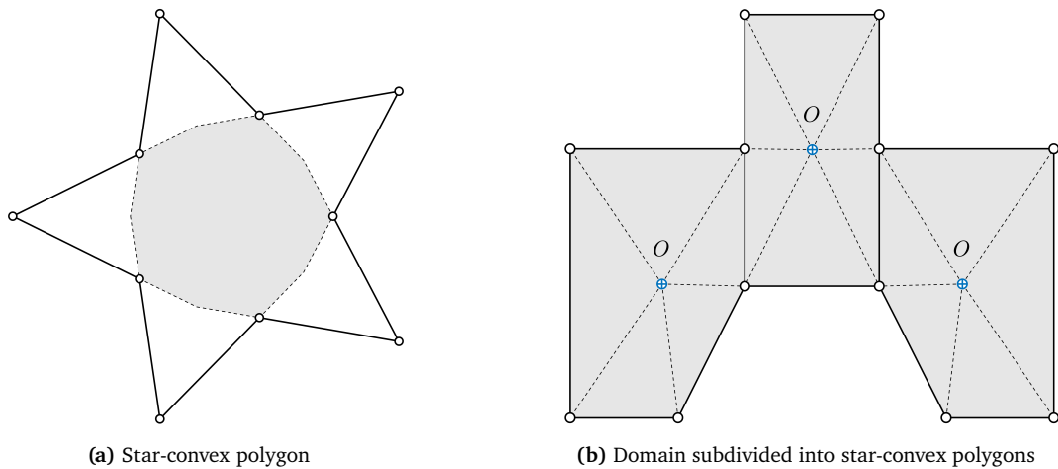


**Figure 3.2:** Two examples of star-convex polygons. (a) A polygon with shaded kernel from which every point of the boundary is visible. (b) Domain  $\Omega$  subdivided into smaller star-convex domains.

Once the scaling requirement of the domain is satisfied, any given shape of the domain's boundary  $\Gamma$  is divided into edges, in a piecewise manner. Figure 3.3(a) shows a three-node line element in physical space  $(x, y)$ . Figure 3.3(b) shows a parent element in scaled boundary natural coordinate  $\eta$ , where  $-1 \leq \eta \leq 1$ . Any point on the boundary is interpolated using one-dimensional FEM shape functions as depicted in Figs. 3.3(c–e). In scaling process, each discretized line element forms a subdomain  $S^e$  along with the radial lines originated from the scaling center (see Fig. 3.4(a)). The radial lines corresponding to the vertex of line elements are termed as *side-faces*  $\Gamma^s$ . Note that, only the boundary of the  $S^e$  subdomain is discretized. The scaled boundary finite element is assembled using piece-wise combination of several  $S^e$  subdomains as shown in Fig. 3.4(b).

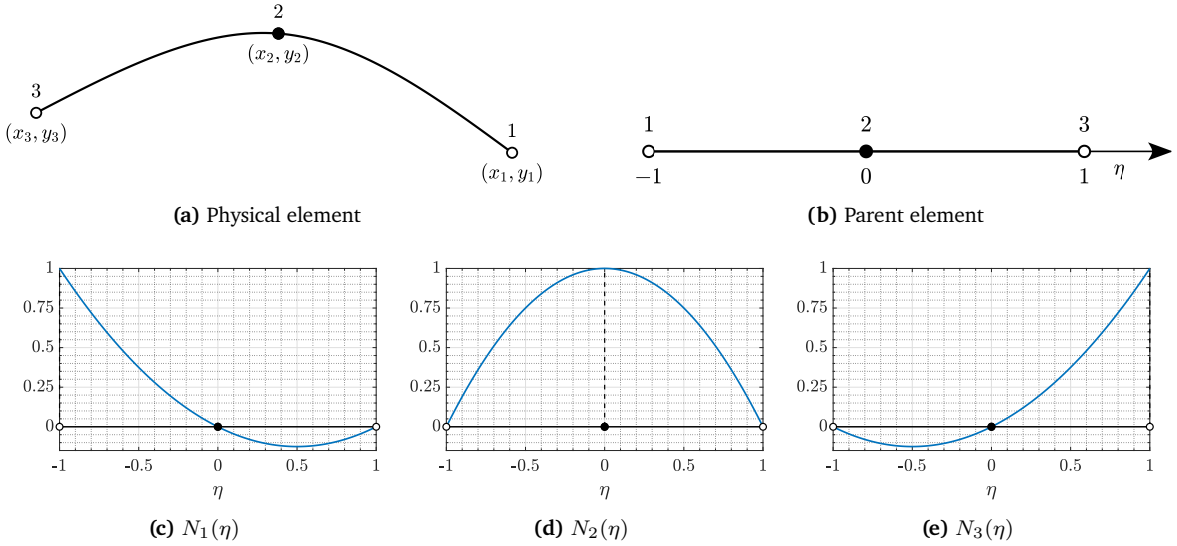


**Figure 3.3:** A three-node line element with vertices  $\circ$  and mid-side node  $\bullet$ . (a) A three-node physical element, (b) a corresponding parent element to in a natural SBFEM coordinate  $\eta$ , and (c–e) Shape functions in  $\eta$ .

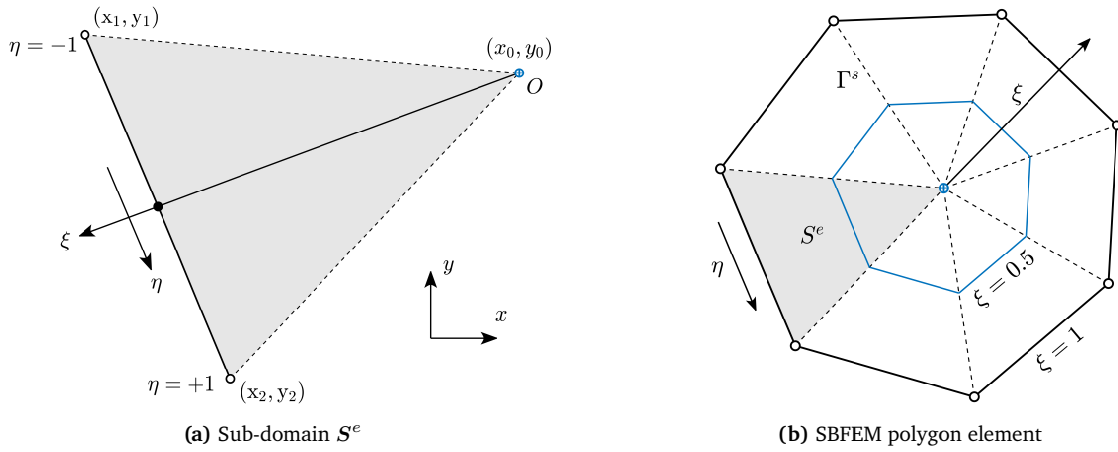


**Figure 3.4:** Scaled boundary finite element discretization. (a)  $S^e$  subdomain covered by a line element and radial lines passing through  $O$ . (b) Scaled boundary finite element assembled using several  $S^e$  subdomains.

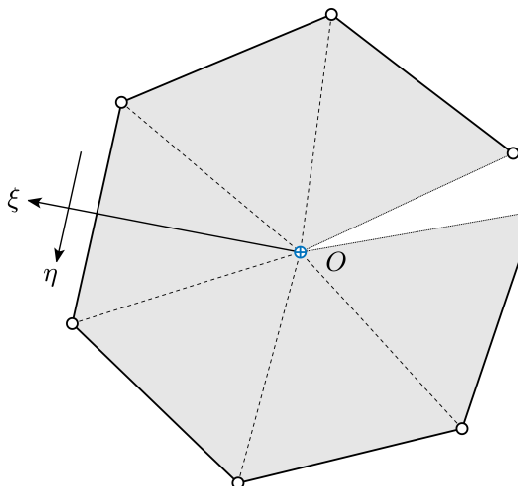


**Figure 3.5:** An open scaled boundary finite element with discrete crack faces.

One of the key features of SBFEM is modeling of a discrete crack using so-called open-element (see Fig. 3.5). In an open-element, the scaling center is put at the crack tip. The crack faces passing through the scaling center are not discretized. The rest of the boundary remains open and does not form a closed loop. Generally, the narrow cracks exhibit the square root singularity in the vicinity of the crack tip for homogeneous and isotropic materials. One of the main advantages of employing open-element is the capturing the singularity semi-analytically. Moreover, In the SBFEM, polygons with any arbitrary number of sides can discretize the domain. The general procedure of generating polygon shapes and the modeling details of an open-element are discussed in Chapter 6.

### 3.1.2 Transformation of Coordinates

In this section, the transformation from Cartesian coordinates  $(x, y)$  to SBFEM coordinates  $(\xi, \eta)$  in bounded domains is presented. The mathematical function to transform Cartesian coordinates to local coordinates is given as follows

$$x(\xi, \eta) = x_0 + \xi \bar{\mathbf{N}}(\eta) \mathbf{x}_b, \quad (3.1a)$$

$$y(\xi, \eta) = y_0 + \xi \bar{\mathbf{N}}(\eta) \mathbf{y}_b, \quad (3.1b)$$

where  $(x_0, y_0)$  are the Cartesian coordinates of a scaling center. The SBFEM coordinate  $\xi$  is nothing but the scaling parameter of the boundary. The vectors  $\mathbf{x}_b$  and  $\mathbf{y}_b$  denote the nodal coordinates of a line element at the boundary measured from the scaling center  $(x_0, y_0)$ .  $\bar{\mathbf{N}}(\eta)$  is a vector of One-dimensional polynomial interpolation functions of coordinate  $\eta$  that satisfies the *partition of unity condition* (see Figs. 3.3(c–e)). For example,  $\bar{\mathbf{N}}(\eta)$  for a three-node line element is given as follows

$$\bar{\mathbf{N}}(\eta) = \left[ -\frac{1}{2}\eta(1-\eta) \quad 1-\eta^2 \quad \frac{1}{2}\eta(1+\eta) \right]. \quad (3.2)$$

Next, the transformation of partial derivatives from Cartesian coordinates  $(x, y)$  to scaled boundary coordinates  $(\xi, \eta)$  is discussed. They are formulated by applying the following chain rule

$$\frac{\partial}{\partial \xi} = \frac{\partial}{\partial x} \frac{\partial x}{\partial \xi} + \frac{\partial}{\partial y} \frac{\partial y}{\partial \xi}, \quad (3.3a)$$

$$\frac{\partial}{\partial \eta} = \frac{\partial}{\partial x} \frac{\partial x}{\partial \eta} + \frac{\partial}{\partial y} \frac{\partial y}{\partial \eta}. \quad (3.3b)$$

They can be written in matrix form as

$$\begin{Bmatrix} \frac{\partial}{\partial \xi} \\ \frac{\partial}{\partial \eta} \end{Bmatrix} = \mathbf{J}(\xi, \eta) \begin{Bmatrix} \frac{\partial}{\partial x} \\ \frac{\partial}{\partial y} \end{Bmatrix}, \quad (3.4)$$

where  $\mathbf{J}(\xi, \eta)$  is a Jacobian matrix expressed as

$$\mathbf{J}(\xi, \eta) = \begin{bmatrix} x_{,\xi} & y_{,\xi} \\ x_{,\eta} & y_{,\eta} \end{bmatrix}. \quad (3.5)$$

The convention  $(*)_{,\xi}$  and  $(*)_{,\eta}$  is used to denote the partial derivatives with respect to  $\xi$  and  $\eta$ , respectively. The derivatives of Cartesian coordinates with respect to scaled boundary coordinates

are derived using Eq. (3.1)

$$x_{,\xi} = \mathbf{x}_b(\eta) = \bar{\mathbf{N}}(\eta)\mathbf{x}_b, \quad (3.6a)$$

$$y_{,\xi} = \mathbf{y}_b(\eta) = \bar{\mathbf{N}}(\eta)\mathbf{y}_b, \quad (3.6b)$$

$$x_{,\eta} = \xi \mathbf{x}_b(\eta)_{,\eta} = \xi \bar{\mathbf{N}}(\eta)_{,\eta} \mathbf{x}_b, \quad (3.6c)$$

$$y_{,\eta} = \xi \mathbf{y}_b(\eta)_{,\eta} = \xi \bar{\mathbf{N}}(\eta)_{,\eta} \mathbf{y}_b. \quad (3.6d)$$

Substituting Eq. (3.6) into Eq. (3.5) and separating the coordinates  $\xi$  and  $\eta$  result in

$$\begin{Bmatrix} \frac{\partial}{\partial \xi} \\ \frac{\partial}{\partial \eta} \end{Bmatrix} = \begin{bmatrix} 1 & 0 \\ 0 & \xi \end{bmatrix} \mathbf{J}(\eta) \begin{Bmatrix} \frac{\partial}{\partial x} \\ \frac{\partial}{\partial y} \end{Bmatrix}, \quad (3.7)$$

where  $\mathbf{J}(\eta)$  is the Jacobian matrix at the boundary ( $\xi = 1$ ).  $\mathbf{J}(\eta)$  is a function of  $\eta$  that only depends on the geometry of line elements. Inverting Eq. (3.7) results in the transformation of partial derivatives from Cartesian coordinates to scaled boundary coordinates

$$\begin{Bmatrix} \frac{\partial}{\partial x} \\ \frac{\partial}{\partial y} \end{Bmatrix} = \mathbf{J}(\eta)^{-1} \begin{Bmatrix} \frac{\partial}{\partial \xi} \\ \frac{1}{\xi} \frac{\partial}{\partial \eta} \end{Bmatrix}, \quad (3.8)$$

where the inverse of Jacobian matrix at the boundary is constructed as follows

$$\mathbf{J}(\eta)^{-1} = \frac{1}{|\mathbf{J}(\eta)|} \begin{bmatrix} y_b(\eta),\eta & -y_b(\eta) \\ -x_b(\eta),\eta & x_b(\eta) \end{bmatrix}, \quad (3.9)$$

and the determinant of  $\mathbf{J}(\eta)$  is given as

$$|\mathbf{J}(\eta)| = y_b(\eta),\eta x_b(\eta) - y_b(\eta)x_b(\eta),\eta. \quad (3.10)$$

Substituting Eq. (3.9) into Eq. (3.4) and separating partial derivatives of  $\xi$  and  $\eta$  into different terms result in the transformation of the partial derivatives as follows

$$\begin{Bmatrix} \frac{\partial}{\partial x} \\ \frac{\partial}{\partial y} \end{Bmatrix} = \frac{1}{|\mathbf{J}(\eta)|} \begin{Bmatrix} y_b(\eta),\eta \\ -x_b(\eta),\eta \end{Bmatrix} \frac{\partial}{\partial \xi} + \frac{1}{|\mathbf{J}(\eta)|} \frac{1}{\xi} \begin{Bmatrix} -y_b(\eta) \\ x_b(\eta) \end{Bmatrix} \frac{\partial}{\partial \eta}. \quad (3.11)$$

The next step is to formulate the infinitesimal area  $d\Omega$  and length  $d\Gamma$  of a domain in local scaled boundary coordinates  $\xi$  and  $\eta$ . Figure 3.6(a) shows a scaled boundary subdomain with several coordinate curves at constant  $\xi$  and  $\eta$ .  $\Gamma^\xi$  denotes the curves with a constant value of  $\xi$ , while  $\Gamma^\eta$  describes the curves with a constant  $\eta$ .

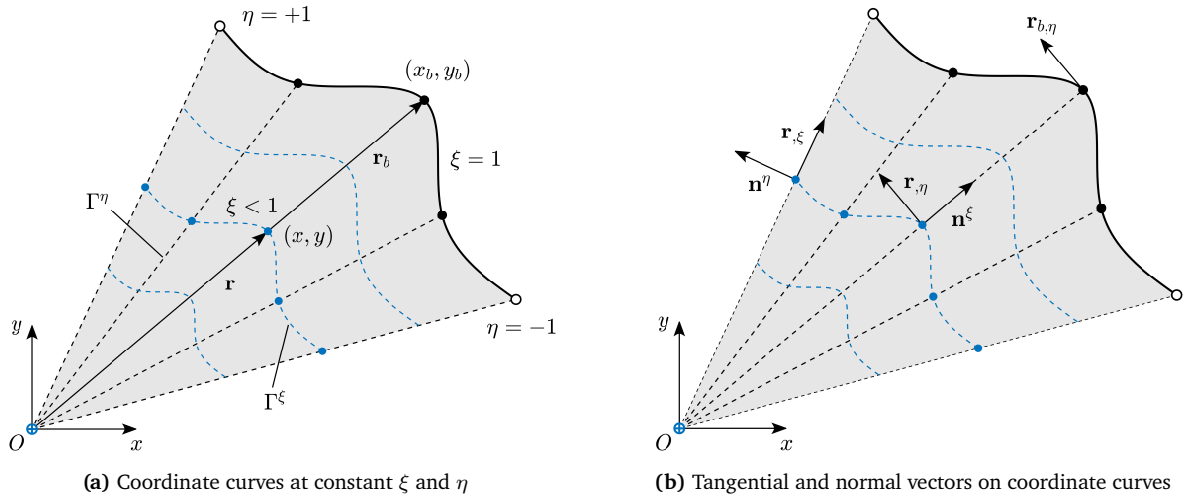


**Figure 3.6:** Scaled boundary subdomain  $S^e$ . (a) Coordinate curves  $\Gamma^\xi$  and  $\Gamma^\eta$  with constant  $\xi$  and  $\eta$ , respectively. (b) Tangential and normal vectors on coordinate curves

Consider an arbitrary point  $(x, y)$  inside the domain with a position vector  $\mathbf{r}$  as follows

$$\mathbf{r} = x\mathbf{i} + y\mathbf{j} = \xi\mathbf{r}_b, \quad (3.12)$$

where  $\mathbf{i}$  and  $\mathbf{j}$  are the unit vectors and  $\mathbf{r}_b$  is the position vector of the point  $(x_b, y_b)$  on the boundary i.e.  $\xi = 1$

$$\mathbf{r}_b = x_b(\eta)\mathbf{i} + y_b(\eta)\mathbf{j}, \quad (3.13)$$

and its length as

$$|\mathbf{r}_b| = l^\eta(\eta) = \sqrt{(x_b(\eta))^2 + (y_b(\eta))^2}. \quad (3.14)$$

In Fig. 3.6(b), the tangential vector  $\mathbf{r}_{,\eta}$  on curve  $\Gamma^\xi$  at point  $(x, y)$  is expressed as follows

$$\mathbf{r}_{,\eta} = \xi\mathbf{r}_{b,\eta}, \quad (3.15a)$$

$$= \xi(x_{b,\eta}\mathbf{i} + y_{b,\eta}\mathbf{j}), \quad (3.15b)$$

and the magnitudes of  $\mathbf{r}_{,\eta}$  and  $\mathbf{r}_{b,\eta}$  are given as

$$|\mathbf{r}_{,\eta}| = \xi|\mathbf{r}_{b,\eta}|, \quad (3.16a)$$

$$|\mathbf{r}_{b,\eta}| = l^\xi(\eta) = \sqrt{(x_{b,\eta})^2 + (y_{b,\eta})^2}. \quad (3.16b)$$

The infinitesimal length along the curve  $\Gamma^\xi$  is expressed as

$$d\Gamma = |\mathbf{r}_{,\eta}| d\eta = \xi|\mathbf{r}_{b,\eta}| d\eta. \quad (3.17)$$

Substituting Eq. (3.16) into Eq. (3.17) results in the infinitesimal length

$$d\Gamma = \xi l^\xi(\eta) d\eta. \quad (3.18)$$

The normal vector  $\mathbf{n}^\xi$  on the curve  $\Gamma^\xi$  is independent of  $\xi$ . It can be formulated by rotating the tangential vector  $\mathbf{r}_{,\eta}$  as follows

$$\mathbf{n}^\xi = \frac{y_{b,\eta}}{|\mathbf{r}_{b,\eta}|}\mathbf{i} - \frac{x_{b,\eta}}{|\mathbf{r}_{b,\eta}|}\mathbf{j}, \quad (3.19a)$$

$$\mathbf{n}^\xi = \frac{1}{l^\xi(\eta)} \begin{Bmatrix} y_{b,\eta} \\ -x_{b,\eta} \end{Bmatrix}. \quad (3.19b)$$

Furthermore, it can be shown that the determinant of the Jacobian matrix at the boundary  $|\mathbf{J}(\eta)|$  is equal to the area of the parallelogram created by the vectors  $\mathbf{r}_b$  and  $\mathbf{r}_{b,\eta}$

$$|\mathbf{r}_b \times \mathbf{r}_{b,\eta}| = \begin{vmatrix} 1 & 1 & k \\ x_b(\eta) & y_b(\eta) & 0 \\ x_{b,\eta} & y_{b,\eta} & 0 \end{vmatrix}, \quad (3.20a)$$

$$= x_b(\eta)y_{b,\eta} - y_b(\eta)x_{b,\eta}, \quad (3.20b)$$

$$= |\mathbf{J}(\eta)|, \quad (3.20c)$$

where  $\mathbf{k}$  is the unit vector along the direction perpendicular to  $x - y$  plane. To formulate the infinitesimal area  $d\Omega$ , the infinitesimal changes in scaled boundary coordinates  $d\xi$  and  $d\eta$  are considered. Figure 3.6(b) shows the coordinate curve  $\Gamma^\eta$  with a constant value of  $\eta$  and its tangential  $\mathbf{r}_{,\xi}$  and normal  $\mathbf{n}^\eta$  vectors. The vector  $\mathbf{r}_{,\xi}$  is given as follows

$$\mathbf{r}_{,\xi} = (\xi \mathbf{r}_b)_{,\xi}, \quad (3.21a)$$

$$= x_b(\eta)\mathbf{i} + y_b(\eta)\mathbf{j}, \quad (3.21b)$$

and the vector  $\mathbf{n}^\eta$  as

$$\mathbf{n}^\eta = -\frac{y_b(\eta)}{|\mathbf{r}_b|}\mathbf{i} + \frac{x_b(\eta)}{|\mathbf{r}_b|}\mathbf{j}, \quad (3.22a)$$

$$\mathbf{n}^\eta = \frac{1}{l^\eta(\eta)} \begin{Bmatrix} -y_b(\eta) \\ x_b(\eta) \end{Bmatrix}. \quad (3.22b)$$

The infinitesimal area is expressed by the cross product of the tangential vectors of constant coordinate curves and infinitesimal changes in scaled boundary coordinate as

$$d\Omega = |(\mathbf{r}_{,\xi} d\xi) \times (\mathbf{r}_{,\eta} d\eta)| \quad (3.23a)$$

$$= \begin{vmatrix} 1 & 1 & k \\ x_b(\eta) & y_b(\eta) & 0 \\ \xi x_{b,\eta} & \xi y_{b,\eta} & 0 \end{vmatrix} d\xi d\eta \quad (3.23b)$$

$$= \xi (x_b(\eta)y_{b,\eta} - y_b(\eta)x_{b,\eta}) d\xi d\eta. \quad (3.23c)$$

Substituting Eq. (3.10) into Eq. (3.23c) results in the infinitesimal area as

$$d\Omega = \xi |\mathbf{J}(\eta)| d\xi d\eta. \quad (3.24)$$

The SBFEM transformation of Cartesian coordinates in scaled boundary local coordinates  $(\xi, \eta)$  is given by Eq. (3.1). The transformation of the partial derivatives are expressed by Eq. (3.11). Furthermore, the infinitesimal area  $d\Omega$  and infinitesimal length  $d\Gamma$  are described by Eqs. (3.24) and (3.18), respectively.

## 3.2 SBFEM for Laplace Equation

This section presents the derivation of the SBFE equation and its solution for steady-state heat conduction process. The derivation procedure is similar to diffusion explained in [151]. Here, the derivation is presented for completeness. The temperature change governs by the conservation of

energy given in Eq. (2.77a). For a steady-state heat conduction process in the absence of internal heat generation and prescribed nodal flux, Eq. (2.77a) is reduced to

$$\nabla^T \mathbf{q} = 0. \quad (3.25)$$

The constitutive relation of temperature and flux governs by the Fourier's law of heat conduction in Eq. (2.77d). For isotropic materials  $\kappa$  is a scalar property. Substituting Eq. (2.77d) into Eq. (3.25) results in the Laplace equation that governs the steady-state heat conduction

$$\nabla^2 \theta = 0. \quad (3.26)$$

The partial differential equation in Eq. (3.25) is completed by introducing the boundary conditions as follows

$$\theta = \theta_b \quad \text{on} \quad \Gamma'_1, \quad (3.27a)$$

$$q_n = \bar{q} \quad \text{on} \quad \Gamma'_2, \quad (3.27b)$$

where  $\theta_b$  is the prescribed temperature change on  $\Gamma'_1$ ,  $q_n$  is the amplitude of the normal flux on boundary and,  $\bar{q}$  is the prescribed normal flux on  $\Gamma'_2$ . The equilibrium on the boundary results in

$$q_n = \mathbf{n}^T \mathbf{q}, \quad (3.28)$$

where  $\mathbf{n}$  describes the outward unit normal vector  $\mathbf{n} = [n_x \ n_y]^T$  on surface  $\Gamma'_2$ . It is assumed that the two surfaces  $\Gamma'_1$  and  $\Gamma'_2$  can not overlap.

### 3.2.1 Derivation of SBFE Equation in Temperature Change

In the above, the balance equation of heat flux Eq. (3.25) is in Cartesian coordinates. The Cartesian coordinates of the bounded domain is transformed into scaled boundary coordinates as described in Section 3.1.2. The procedure of geometric transformation only affects the spatial coordinates of the domain similar to the FEM mapping of a parent element. The gradients in Eq. (3.25) are transformed in scaled boundary coordinates by using the relation of partial derivatives given in Eq. (3.11)

$$\nabla = \bar{\mathbf{b}}_1(\eta) \frac{\partial}{\partial \xi} + \frac{1}{\xi} \bar{\mathbf{b}}_2(\eta) \frac{\partial}{\partial \eta}, \quad (3.29)$$

where

$$\bar{\mathbf{b}}_1(\eta) = \frac{1}{|\mathbf{J}(\eta)|} \begin{Bmatrix} y_b(\eta), \eta \\ -x_b(\eta), \eta \end{Bmatrix}, \quad (3.30a)$$

$$\bar{\mathbf{b}}_2(\eta) = \frac{1}{|\mathbf{J}(\eta)|} \begin{Bmatrix} -y_b(\eta) \\ x_b(\eta) \end{Bmatrix}. \quad (3.30b)$$

Note that the symbol  $(\bar{\cdot})$  indicates the property  $(\cdot)$  belongs to a thermal system. Using the above equations, it can be shown that the following identity holds

$$(\bar{\mathbf{b}}_2(\eta) |\mathbf{J}(\eta)|)_{,\eta} = -\bar{\mathbf{b}}_1(\eta) |\mathbf{J}(\eta)|. \quad (3.31)$$

Next, the transformation of the normal flux from Cartesian to scaled boundary coordinate is discussed. Substituting the definitions of the normal vectors Eqs. (3.19b) and (3.22b) into Eq. (3.28) and using Eq. (3.30) results in

$$q_n^\xi = \frac{|\mathbf{J}(\eta)|}{l^\xi(\eta)} \bar{\mathbf{b}}_1^T(\eta) \mathbf{q}, \quad (3.32a)$$

$$q_n^\eta = \frac{|\mathbf{J}(\eta)|}{l^\eta(\eta)} \bar{\mathbf{b}}_2^T(\eta) \mathbf{q}, \quad (3.32b)$$

where,  $q_n^\xi$  and  $q_n^\eta$  denote the flux normal to the  $\Gamma^\xi$  and  $\Gamma^\eta$ , respectively.

To derive the scaled boundary finite element equation in temperature, the contribution of one subdomain  $S^e$  is considered (see Fig. 3.6). The global system is constructed by assembling the contributions of each  $S^e$  within the element. In SBFEM, temperature field is represented numerically in circumferential direction and analytically in radial direction. The temperature at the boundary  $\xi = 1$  is interpolated by using the same isoparametric shape functions that are used to interpolate the geometry as given in Eq. (3.2). Introducing the unknown functions  $\theta(\xi)$  along the radial direction passing through the nodes and the scaling center, temperature at given local coordinates is interpolated as

$$\theta(\xi, \eta) = \bar{\mathbf{N}}(\eta)\theta(\xi). \quad (3.33)$$

Substituting Eqs. (3.33) and (3.29) into Eq. (2.77d) results in

$$\mathbf{q}(\xi, \eta) = -\kappa \left( \bar{\mathbf{B}}_1(\eta)\theta(\xi),_\xi + \frac{1}{\xi}\bar{\mathbf{B}}_2(\eta)\theta(\xi) \right), \quad (3.34)$$

for isotropic materials, where

$$\bar{\mathbf{B}}_1(\eta) = \bar{\mathbf{b}}_1(\eta)\bar{\mathbf{N}}(\eta), \quad (3.35a)$$

$$\bar{\mathbf{B}}_2(\eta) = \bar{\mathbf{b}}_2(\eta)\bar{\mathbf{N}}(\eta),_\eta. \quad (3.35b)$$

The method of weighted residuals is considered to derive the finite element approximation of governing equation. Analogous to the unknown function of temperature distribution in Eq. (3.33), the weighting function is discretized as follows

$$\delta\theta(\xi, \eta) = \bar{\mathbf{N}}(\eta)\delta\theta(\xi). \quad (3.36)$$

To formulate internal nodal flux  $\bar{\mathbf{Q}}(\xi)$  corresponding to internal temperature  $\theta(\xi)$ , a virtual work principle is applied on a curve with constant value of  $\xi$  i.e.  $\Gamma^\xi$

$$\delta\theta^T(\xi)\bar{\mathbf{Q}}(\xi) = - \int_{\Gamma^\xi} \delta\theta^T \mathbf{n}^\xi \mathbf{q} d\Gamma. \quad (3.37)$$

Note that the dependency of  $\eta$  is dropped for convenience. Also, the argument  $(\xi, \eta)$  is omitted if the function depends on both  $\xi$  and  $\eta$ . Substituting weighting functions Eq. (3.36), expression of normal vector Eq. (3.19) and the integral transformation Eq. (3.18) into Eq. (3.37) and comparing with Eq. (3.30a) results in

$$\delta\theta^T(\xi)\bar{\mathbf{Q}}(\xi) = -\delta\theta^T(\xi) \int_{-1}^{+1} \bar{\mathbf{N}}^T \frac{|\mathbf{J}|}{l^\xi(\eta)} \bar{\mathbf{b}}_1^T \mathbf{q} \xi l^\xi(\eta) d\eta. \quad (3.38)$$

Rearranging Eq. (3.38) by using Eqs. (3.35a) and (3.34) yields equation for the internal nodal flux

$$\bar{\mathbf{Q}}(\xi) = -\xi \int_{-1}^{+1} \bar{\mathbf{B}}_1^T \mathbf{q} |\mathbf{J}| d\eta, \quad (3.39a)$$

$$\bar{\mathbf{Q}}(\xi) = \xi \int_{-1}^{+1} \bar{\mathbf{B}}_1^T \kappa \left( \bar{\mathbf{B}}_1 \theta(\xi),_\xi + \frac{1}{\xi} \bar{\mathbf{B}}_2 \theta(\xi) \right) |\mathbf{J}| d\eta. \quad (3.39b)$$

Now, the method of weighted residuals is applied in the circumferential direction. For that purpose, Eq. (3.25) is first multiplied by the test function  $\delta\theta = \delta\theta(\xi, \eta)$  and then integrated over the domain as follows

$$\int_{\Omega} \delta\theta \nabla^T \mathbf{q} d\Omega - \int_{\Omega} \delta\theta H d\Omega = 0. \quad (3.40)$$

Substituting Eq. (3.29) into Eq. (3.40) results in

$$\int_{\Omega} \delta\theta \bar{\mathbf{b}}_1^T \mathbf{q}_{,\xi} d\Omega + \int_{\Omega} \delta\theta \frac{1}{\xi} \bar{\mathbf{b}}_2^T \mathbf{q}_{,\eta} d\Omega - \int_{\Omega} \delta\theta H d\Omega = \mathbf{0}. \quad (3.41)$$

The domain integrals in the above equation are transformed into scaled boundary coordinates by using Eq. (3.24) as follows

$$\begin{aligned} \int_0^1 \xi \left( \int_{\Gamma^\xi} \delta\theta \bar{\mathbf{b}}_1^T \mathbf{q}_{,\xi} |\mathbf{J}| d\eta \right) d\xi + \int_0^1 \left( \int_{\Gamma^\xi} \delta\theta \bar{\mathbf{b}}_2^T \mathbf{q}_{,\eta} |\mathbf{J}| d\eta \right) d\xi \\ - \int_0^1 \xi \left( \int_{\Gamma^\xi} \delta\theta H |\mathbf{J}| d\eta \right) d\xi = \mathbf{0}. \end{aligned} \quad (3.42)$$

In the above identity, the first integral shows the limits of the bounded domain and the second integral  $\Gamma^\xi$  denotes the curve with constant value  $\xi$  (see Fig. 3.6). For one  $S^e$ , the limits of integral  $\Gamma^\xi$  is  $\eta = [-1, +1]$ . The second term in Eq. (3.42) is expressed as  $\mathbf{L}$  and considered for the sub-derivation

$$\mathbf{L} = \int_0^1 \left( \int_{-1}^{+1} \delta\theta \bar{\mathbf{b}}_2^T \mathbf{q}_{,\eta} |\mathbf{J}| d\eta \right) d\xi. \quad (3.43)$$

Applying integration by parts i.e., Green's theorem results in

$$\mathbf{L} = \int_0^1 \left( \delta\theta \bar{\mathbf{b}}_2^T |\mathbf{J}| \mathbf{q} \Big|_{\eta=-1}^{\eta=+1} - \int_{-1}^{+1} \left( \delta\theta \bar{\mathbf{b}}_2^T |\mathbf{J}| \right)_{,\eta} \mathbf{q} d\eta \right) d\xi. \quad (3.44)$$

The first term in Eq. (3.44) is traction-like flux along the radial lines of  $S^e$  subdomain passing through the scaling center. During the assembly process of a complete domain, the contributions of traction-like flux cancel out from the neighboring  $S^e$  except for prescribed flux [152]. Applying the chain rule for the derivative with respect to  $\eta$  in the second term of Eq. (3.44) yields

$$\begin{aligned} \mathbf{L} = \int_0^1 \left[ \delta\theta \bar{\mathbf{b}}_2^T |\mathbf{J}| \mathbf{q} \Big|_{\eta=-1}^{\eta=+1} - \left( \int_{-1}^{+1} \delta\theta_{,\eta} \bar{\mathbf{b}}_2^T |\mathbf{J}| \mathbf{q} d\eta \right. \right. \\ \left. \left. + \int_{-1}^{+1} \delta\theta \left( \bar{\mathbf{b}}_2^T |\mathbf{J}| \right)_{,\eta} \mathbf{q} d\eta \right) \right] d\xi. \end{aligned} \quad (3.45)$$

Using the identities in Eqs. (3.31) and (3.32b), Eq. (3.45) is reformulated as

$$\mathbf{L} = \int_0^1 \left( \delta\theta l^n q_n^n \Big|_{\eta=-1}^{\eta=+1} - \int_{-1}^{+1} \delta\theta_{,\eta} \bar{\mathbf{b}}_2^T \mathbf{q} |\mathbf{J}| d\eta + \int_{-1}^{+1} \delta\theta \bar{\mathbf{b}}_1^T \mathbf{q} |\mathbf{J}| d\eta \right) d\xi, \quad (3.46)$$

Substituting the sub-derivation of term  $\mathbf{L}$  Eq. (3.46) into Eq. (3.42) results in

$$\begin{aligned} \int_0^1 \left( \xi \int_{-1}^{+1} \delta\theta \bar{\mathbf{b}}_1^T \mathbf{q}_{,\xi} |\mathbf{J}| d\eta + \delta\theta l^n q_n^n \Big|_{\eta=-1}^{\eta=+1} - \int_{-1}^{+1} \delta\theta_{,\eta} \bar{\mathbf{b}}_2^T \mathbf{q} |\mathbf{J}| d\eta \right. \\ \left. + \int_{-1}^{+1} \delta\theta \bar{\mathbf{b}}_1^T \mathbf{q} |\mathbf{J}| d\eta - \xi \int_{-1}^{+1} \delta\theta H |\mathbf{J}| d\eta \right) d\xi = \mathbf{0}. \end{aligned} \quad (3.47)$$

Enforcing the balance condition in Eq. (3.25) by setting the integrand over the domain to zero in  $\xi$  direction

$$\begin{aligned} \xi \int_{-1}^{+1} \delta\theta \bar{\mathbf{b}}_1^T \mathbf{q}_{,\xi} |\mathbf{J}| d\eta + \delta\theta l^n q_n^n \Big|_{\eta=-1}^{\eta=+1} - \int_{-1}^{+1} \delta\theta_{,\eta} \bar{\mathbf{b}}_2^T \mathbf{q} |\mathbf{J}| d\eta \\ + \int_{-1}^{+1} \delta\theta \bar{\mathbf{b}}_1^T \mathbf{q} |\mathbf{J}| d\eta - \xi \int_{-1}^{+1} \delta\theta H |\mathbf{J}| d\eta = \mathbf{0}. \end{aligned} \quad (3.48)$$

Substituting Eqs. (3.36) and (3.35) into Eq. (3.48) results in the following equation for arbitrary  $\delta\theta(\xi)$

$$\xi \int_{-1}^{+1} \bar{\mathbf{B}}_1^T \mathbf{q}_{,\xi} |\mathbf{J}| d\eta + \int_{-1}^{+1} \bar{\mathbf{B}}_1^T \mathbf{q} |\mathbf{J}| d\eta - \int_{-1}^{+1} \bar{\mathbf{B}}_2^T \mathbf{q} |\mathbf{J}| d\eta = \mathbf{f}_q(\xi) + \xi \mathbf{f}_h(\xi), \quad (3.49)$$

with

$$\mathbf{f}_q(\xi) = -\bar{\mathbf{N}}^T l^\eta q_n^\eta \Big|_{\eta=-1}^{\eta=+1}, \quad (3.50a)$$

$$\mathbf{f}_h(\xi) = \int_{-1}^{+1} \bar{\mathbf{N}}^T H |\mathbf{J}| d\eta. \quad (3.50b)$$

Here,  $\mathbf{f}_q$  and  $\mathbf{f}_h$  represent the nodal flux resulting from the normal flux on the side-faces  $\Gamma^s$  and internal heat source, respectively. During the assembly process, the contribution of  $\mathbf{f}_q$  will cancel out with the contribution of neighboring  $S^e$  except for those of prescribed flux on  $\Gamma^s$ . Using Eq. (3.34), Eq. (3.49) is reformulated as

$$\begin{aligned} & \int_{-1}^{+1} \bar{\mathbf{B}}_1^T \kappa \left( \bar{\mathbf{B}}_1 \theta(\xi),_\xi + \frac{1}{\xi} \bar{\mathbf{B}}_2 \theta(\xi) \right)_{,\xi} |\mathbf{J}| d\eta + \int_{-1}^{+1} \bar{\mathbf{B}}_1^T \kappa \left( \bar{\mathbf{B}}_1 \theta(\xi),_\xi + \frac{1}{\xi} \bar{\mathbf{B}}_2 \theta(\xi) \right) |\mathbf{J}| d\eta \\ & - \int_{-1}^{+1} \bar{\mathbf{B}}_2^T \kappa \left( \bar{\mathbf{B}}_1 \theta(\xi),_\xi + \frac{1}{\xi} \bar{\mathbf{B}}_2 \theta(\xi) \right) |\mathbf{J}| d\eta = \xi \mathbf{f}_h(\xi) + \mathbf{f}_q(\xi). \end{aligned} \quad (3.51)$$

Introducing the coefficient matrices  $\bar{\mathbf{E}}_0$ ,  $\bar{\mathbf{E}}_1$ , and  $\bar{\mathbf{E}}_2$  as

$$\bar{\mathbf{E}}_0 = \int_{-1}^{+1} \bar{\mathbf{B}}_1^T \kappa \bar{\mathbf{B}}_1 |\mathbf{J}| d\eta, \quad (3.52a)$$

$$\bar{\mathbf{E}}_1 = \int_{-1}^{+1} \bar{\mathbf{B}}_2^T \kappa \bar{\mathbf{B}}_1 |\mathbf{J}| d\eta, \quad (3.52b)$$

$$\bar{\mathbf{E}}_2 = \int_{-1}^{+1} \bar{\mathbf{B}}_2^T \kappa \bar{\mathbf{B}}_2 |\mathbf{J}| d\eta, \quad (3.52c)$$

Eq. (3.48) results in the second-order ordinary scaled boundary finite element equation in temperature change

$$\xi^2 \bar{\mathbf{E}}_0 \theta(\xi),_{\xi\xi} + \xi \left( \bar{\mathbf{E}}_0 - \bar{\mathbf{E}}_1 + \bar{\mathbf{E}}_1^T \right) \theta(\xi),_\xi - \bar{\mathbf{E}}_2 \theta(\xi) = \bar{\mathbf{F}}(\xi), \quad (3.53)$$

where

$$\bar{\mathbf{F}}(\xi) = \xi \mathbf{f}_h(\xi) + \mathbf{f}_q(\xi), \quad (3.54)$$

with  $\mathbf{f}_h(\xi)$  and  $\mathbf{f}_q(\xi)$  correspond to the internal heat generation and nodal flux, respectively. Note that the coefficient matrices in Eq. (3.52) depend only on  $\eta$  and material property. The coefficient matrices are first calculated for one subdomain  $S^e$  and then assembled for the whole element. Also, the matrices  $\bar{\mathbf{E}}_0$  and  $\bar{\mathbf{E}}_2$  are symmetric. The internal nodal flux  $\bar{\mathbf{Q}}$  is also rewritten in form of coefficient matrices  $\bar{\mathbf{E}}_0$  and  $\bar{\mathbf{E}}_1$  by substituting Eqs. (3.52a) and (3.52b) into Eq. (3.39)

$$\bar{\mathbf{Q}}(\xi) = \xi \bar{\mathbf{E}}_0 \theta(\xi),_\xi + \bar{\mathbf{E}}_1^T \theta(\xi). \quad (3.55)$$

For a vanishing internal heat source and prescribed flux, the non-homogeneous term in Eq. (3.53) reduced to zero

$$\xi^2 \bar{\mathbf{E}}_0 \theta(\xi),_{\xi\xi} + \xi \left( \bar{\mathbf{E}}_0 - \bar{\mathbf{E}}_1 + \bar{\mathbf{E}}_1^T \right) \theta(\xi),_\xi - \bar{\mathbf{E}}_2 \theta(\xi) = \mathbf{0}. \quad (3.56)$$

The scaled boundary finite element equation for temperature change Eq. (3.56) is a system of  $\bar{N}$  homogeneous ordinary differential equations of a second-order. Here,  $\bar{N}$  is the number of degrees of freedom of a scaled boundary element at the boundary. In the following, the solution procedure of SBFE equation in temperature change is discussed.

### 3.2.2 Solution of SBFE Equation by Eigenvalue Decomposition

To solve the SBFE equation, the second-order system of equations in Eq. (3.56) is first transformed into the system of first-order equations of size  $2\bar{N}$  [149]. In the first step of transformation, Eq. (3.55) is rearranged as follows

$$\xi \boldsymbol{\theta}(\xi),_{\xi} = \bar{\mathbf{E}}_0^{-1} \bar{\mathbf{Q}}(\xi) - (\bar{\mathbf{E}}_0^{-1} \bar{\mathbf{E}}_1^T) \boldsymbol{\theta}(\xi). \quad (3.57)$$

Next, the first derivatives of nodal flux functions in Eq. (3.55) are evaluated

$$\xi \bar{\mathbf{Q}}(\xi),_{\xi} = \xi^2 \bar{\mathbf{E}}_0 \boldsymbol{\theta}(\xi),_{\xi\xi} + \xi \bar{\mathbf{E}}_0 \boldsymbol{\theta}(\xi),_{\xi\xi} + \xi \bar{\mathbf{E}}_1^T \boldsymbol{\theta}(\xi),_{\xi}. \quad (3.58)$$

Comparing Eqs. (3.58) and (3.56) result in the new expression for the derivative of nodal flux as

$$\xi \bar{\mathbf{Q}}(\xi),_{\xi} = \xi \bar{\mathbf{E}}_1 \boldsymbol{\theta}(\xi),_{\xi} + \bar{\mathbf{E}}_2 \boldsymbol{\theta}(\xi). \quad (3.59)$$

Substituting Eq. (3.57) into Eq. (3.59) and rearranging the resulting equation leads to

$$\begin{aligned} \xi \bar{\mathbf{Q}}(\xi),_{\xi} &= (\bar{\mathbf{E}}_0^{-1} \bar{\mathbf{Q}}(\xi) - \bar{\mathbf{E}}_0^{-1} \bar{\mathbf{E}}_1^T \boldsymbol{\theta}(\xi)) \bar{\mathbf{E}}_1 + \bar{\mathbf{E}}_2 \boldsymbol{\theta}(\xi), \\ &= (\bar{\mathbf{E}}_1 \bar{\mathbf{E}}_0^{-1}) \bar{\mathbf{Q}}(\xi) - (\bar{\mathbf{E}}_1 \bar{\mathbf{E}}_0^{-1} \bar{\mathbf{E}}_1^T) \boldsymbol{\theta}(\xi) + \bar{\mathbf{E}}_2 \boldsymbol{\theta}(\xi). \end{aligned} \quad (3.60)$$

Combining Eqs. (3.57) and (3.60) and writing in a matrix form yields

$$\xi \begin{Bmatrix} \boldsymbol{\theta}(\xi),_{\xi} \\ \bar{\mathbf{Q}}(\xi),_{\xi} \end{Bmatrix} = - \begin{bmatrix} \bar{\mathbf{E}}_0^{-1} \bar{\mathbf{E}}_1^T & -\bar{\mathbf{E}}_0^{-1} \\ \bar{\mathbf{E}}_1 \bar{\mathbf{E}}_0^{-1} \bar{\mathbf{E}}_1^T - \bar{\mathbf{E}}_2 & -\bar{\mathbf{E}}_1 \bar{\mathbf{E}}_0^{-1} \end{bmatrix} \begin{Bmatrix} \boldsymbol{\theta}(\xi) \\ \bar{\mathbf{Q}}(\xi) \end{Bmatrix}. \quad (3.61)$$

By introducing the variable  $\bar{\mathbf{X}}(\xi)$  of size  $2\bar{N}$  with  $\bar{N}$  numbers of nodal temperature functions and  $\bar{N}$  numbers of internal nodal flux functions as

$$\bar{\mathbf{X}}(\xi) = \begin{Bmatrix} \boldsymbol{\theta}(\xi) \\ \bar{\mathbf{Q}}(\xi) \end{Bmatrix}, \quad (3.62)$$

Eq. (3.61) is written in the form of  $\bar{\mathbf{X}}(\xi)$  as the first-order ordinary differential equation

$$\xi \bar{\mathbf{X}}(\xi),_{\xi} = -\bar{\mathbf{Z}} \bar{\mathbf{X}}(\xi). \quad (3.63)$$

Here, the coefficient matrix  $\bar{\mathbf{Z}}$  is described as

$$\bar{\mathbf{Z}} = \begin{bmatrix} \bar{\mathbf{E}}_0^{-1} \bar{\mathbf{E}}_1^T & -\bar{\mathbf{E}}_0^{-1} \\ \bar{\mathbf{E}}_1 \bar{\mathbf{E}}_0^{-1} \bar{\mathbf{E}}_1^T - \bar{\mathbf{E}}_2 & -\bar{\mathbf{E}}_1 \bar{\mathbf{E}}_0^{-1} \end{bmatrix}, \quad (3.64)$$

where the matrix  $\bar{\mathbf{Z}}$  is a Hamiltonian matrix that satisfies the  $\mathbf{J}_{2\bar{N}}$ -orthogonality, i.e.

$$(\mathbf{J}_{2\bar{N}} \bar{\mathbf{Z}})^T = \mathbf{J}_{2\bar{N}} \bar{\mathbf{Z}}, \quad (3.65)$$

with

$$\mathbf{J}_{2\bar{N}} = \begin{bmatrix} \mathbf{0} & \mathbf{I} \\ -\mathbf{I} & \mathbf{0} \end{bmatrix}. \quad (3.66)$$

A well-known solution of the differential equation in Eq. (3.63) is proposed in the form of power function [149]

$$\bar{\mathbf{X}}(\xi) = \xi^{-\lambda} \Phi. \quad (3.67)$$

Substituting the postulated formal solution in Eq. (3.67) into Eq. (3.63) entails

$$\bar{\mathbf{Z}}\Phi = \Phi\lambda. \quad (3.68)$$

Equation (3.68) is simply the eigenvalue problem of coefficient matrix  $\bar{\mathbf{Z}}$ . The general solution of  $\bar{\mathbf{X}}(\xi)$  is a linear combination of eigenvectors of  $\bar{\mathbf{Z}}$  multiplied by power functions of  $\xi$  with the corresponding eigenvalues as exponents. That is,

$$\bar{\mathbf{X}}(\xi) = \Phi\xi^{-\lambda}\bar{\mathbf{c}} = \sum_{i=1}^{2N} \Phi_i \xi^{-\lambda_i} \bar{c}_i, \quad (3.69)$$

where  $\Phi, \lambda$  are the eigenvectors and eigenvalues of  $\bar{\mathbf{Z}}$  and  $\bar{\mathbf{c}}$  are the integration constants of size  $2N$ .

One of the key features of the Hamiltonian matrix is that its eigenvalues occur in negative and positive pairs. In the case of complex eigenvalues, a pair of complex conjugates exists. In Eq. (3.69), the matrix  $\xi^{-\lambda}$  is partitioned into negative and positive blocks and sorted concerning the real parts of the eigenvalues  $\lambda$ . Furthermore, the eigenvectors  $\Phi$  are also separated corresponding to nodal temperature and flux functions. Now, Eq. (3.69) is reformulated as

$$\begin{Bmatrix} \theta(\xi) \\ \bar{\mathbf{Q}}(\xi) \end{Bmatrix} = \begin{bmatrix} \Phi_n^\theta & \Phi_p^\theta \\ \Phi_n^q & \Phi_p^q \end{bmatrix} \begin{bmatrix} \lfloor \xi^{-\lambda_n} \rfloor & \mathbf{0} \\ \mathbf{0} & \lfloor \xi^{-\lambda_p} \rfloor \end{bmatrix} \begin{Bmatrix} \bar{\mathbf{c}}_n \\ \bar{\mathbf{c}}_p \end{Bmatrix}. \quad (3.70)$$

Here,  $\lambda_n$  and  $\lambda_p$  indicate the negative and positive blocks of eigenvalues, such that  $\text{Re}(\lambda_n) = -\text{Re}(\lambda_p)$ .  $\lfloor \cdot \rfloor$  denotes a block of diagonal matrix. Rewriting the matrix equation Eq. (3.70) in form of system of equations leads to

$$\theta(\xi) = \Phi_n^\theta \xi^{-\lambda_n} \bar{\mathbf{c}}_n + \Phi_p^\theta \xi^{-\lambda_p} \bar{\mathbf{c}}_p, \quad (3.71a)$$

$$\bar{\mathbf{Q}}(\xi) = \Phi_n^q \xi^{-\lambda_n} \bar{\mathbf{c}}_n + \Phi_p^q \xi^{-\lambda_p} \bar{\mathbf{c}}_p. \quad (3.71b)$$

The second terms in Eqs. (3.71a) and (3.71b) correspond to a block with positive eigenvalues. In a bounded domain i.e.  $0 \leq \xi \leq 1$ , the integration constants  $\bar{\mathbf{c}}_p$  in Eq. (3.71) must be zero for the finiteness of the solution as  $\xi \rightarrow 0$ . Eq. (3.71) is reduced to

$$\theta(\xi) = \Phi_n^\theta \xi^{-\lambda_n} \bar{\mathbf{c}}_n, \quad (3.72a)$$

$$\bar{\mathbf{Q}}(\xi) = \Phi_n^q \xi^{-\lambda_n} \bar{\mathbf{c}}_n. \quad (3.72b)$$

Eliminating the integration constants in Eq. (3.72) yields

$$\bar{\mathbf{Q}}(\xi) = \Phi_n^q \left( \Phi_n^\theta \right)^{-1} \theta(\xi) \quad (3.73)$$

Eq. (3.73) describes the temperature-flux relation in a scaled boundary finite element. The static stiffness-like matrix is obtained from the above relation at the boundary at  $\xi = 1$

$$\bar{\mathbf{Q}}(\xi = 1) = \bar{\mathbf{K}}\theta(\xi = 1) \quad (3.74)$$

where  $\bar{\mathbf{K}}$  is expressed as

$$\bar{\mathbf{K}} = \Phi_n^q \left( \Phi_n^\theta \right)^{-1}. \quad (3.75)$$

The integration constants in Eq. (3.72a) are obtained from the temperature solution at the boundary ( $\xi = 1$ ) as

$$\bar{\mathbf{c}} = \left( \Phi_n^\theta \right)^{-1} \theta_b. \quad (3.76)$$

Here,  $\theta_b = \theta(\xi = 1)$  and  $\bar{c}$  are the integration constants corresponding to the negative block  $\bar{c} = \bar{c}_n$ . Substituting Eq. (3.76) into Eq. (3.72a) and using Eq. (3.33) yields the expression for the temperature distribution in a subdomain  $S^e$

$$\theta(\xi, \eta) = \bar{\chi}(\xi, \eta)\theta_b(\eta), \quad (3.77)$$

where  $\bar{\chi}(\xi, \eta)$  describes a matrix of shape function as

$$\bar{\chi}(\xi, \eta) = \bar{\mathbf{N}}(\eta) \left( \Phi_n^\theta \right)^{(e)} \xi^{-\lambda_n} \left( \Phi_n^\theta \right)^{-1}. \quad (3.78)$$

Note that the superscript  $(e)$  indicates the degrees of freedom corresponding to individual subdomain  $S^e$ .

### 3.3 SBFEM for Elastostatics

This section focuses on the derivation and solution of the SBFE equation in displacement for the elastostatics problem. The detailed derivation is presented in [152]. The principal idea follows the steady-state heat conduction process in Section 3.2. However, a robust solution procedure of Schur decomposition is utilized instead of eigenvalue decomposition. The argumentation in favor of Schur decomposition is discussed in the following.

For elastostatics, the governing equation of balance of momentum Eq. (2.77b) is reduced to the static equilibrium as follows

$$\nabla_u^T \sigma + p = 0, \quad (3.79)$$

where  $\sigma$  denotes the stress vector,  $p$  is a vector of the body forces, and  $\nabla_u$  is the differential operator for linear elasticity. In a two-dimensional domain  $\Omega$  with surface  $\Gamma$ , stress components in Voigt notation is given as  $\sigma = [\sigma_x \ \sigma_y \ \sigma_{xy}]^T$  and  $\nabla_u$  is expressed as follows

$$\nabla_u = \begin{bmatrix} \frac{\partial}{\partial x} & 0 \\ 0 & \frac{\partial}{\partial y} \\ \frac{\partial}{\partial y} & \frac{\partial}{\partial x} \end{bmatrix}. \quad (3.80)$$

Hooke's law gives the material constitutive relation

$$\sigma = D\epsilon. \quad (3.81)$$

For in-plane motion, a strain-displacement relationship is given as

$$\epsilon = \nabla_u \mathbf{u} = \begin{bmatrix} \frac{\partial}{\partial x} & 0 \\ 0 & \frac{\partial}{\partial y} \\ \frac{\partial}{\partial y} & \frac{\partial}{\partial x} \end{bmatrix} \begin{Bmatrix} u_x \\ u_y \end{Bmatrix}. \quad (3.82)$$

Introducing the boundary conditions of displacements and surface traction as follows

$$\mathbf{u} = \mathbf{u}_b \quad \text{on} \quad \Gamma_1, \quad (3.83a)$$

$$\boldsymbol{\tau} = \bar{\boldsymbol{\tau}} \quad \text{on} \quad \Gamma_2, \quad (3.83b)$$

where  $\mathbf{u}_b$  and  $\bar{\tau}$  are the prescribed displacements and surface traction at the boundary  $\Gamma_1$  and  $\Gamma_2$ , respectively. It is assumed that the surfaces  $\Gamma_1$  and  $\Gamma_2$  do not intersect. In Eq. (3.83b), the surface traction  $\boldsymbol{\tau} = [\tau_x \ \tau_y]^T$  at the boundary are related to stress vector. The equilibrium on the boundary leads to

$$\boldsymbol{\tau} = \mathbf{n}_u^T \boldsymbol{\sigma}, \quad (3.84)$$

where  $\mathbf{n}_u$  depends on the components of the outward unit normal vector  $\mathbf{n} = [n_x \ n_y]^T$ , such that

$$\mathbf{n}_u = \begin{bmatrix} n_x & 0 \\ 0 & n_y \\ n_y & n_x \end{bmatrix}. \quad (3.85)$$

### 3.3.1 Derivation of SBFE Equation in Displacement

In the first derivation step of the SBFE equation in displacement, the linear differential operator of the displacement field in Eq. (3.79) is transformed to scaled boundary coordinates using Eq. (3.11) as follows

$$\nabla_u = \mathbf{b}_1(\eta) \frac{\partial}{\partial \xi} + \frac{1}{\xi} \mathbf{b}_2(\eta) \frac{\partial}{\partial \eta}, \quad (3.86)$$

where

$$\mathbf{b}_1(\eta) = \frac{1}{|\mathbf{J}(\eta)|} \begin{bmatrix} y_b(\eta),\eta & 0 \\ 0 & -x_b(\eta),\eta \\ -x_b(\eta),\eta & y_b(\eta),\eta \end{bmatrix}, \quad (3.87a)$$

$$\mathbf{b}_2(\eta) = \frac{1}{|\mathbf{J}(\eta)|} \begin{bmatrix} -y_b(\eta) & 0 \\ 0 & x_b(\eta) \\ x_b(\eta) & -y_b(\eta) \end{bmatrix}. \quad (3.87b)$$

Similar to a temperature field, displacements are also represented numerically in the circumferential direction and analytically in the radial direction. Introducing the sought-after displacements functions  $\mathbf{u}(\xi)$  in the radial direction, the interpolation of displacements at given  $\xi$  and  $\eta$  are expressed as

$$\mathbf{u}(\xi, \eta) = \mathbf{N}(\eta) \mathbf{u}(\xi), \quad (3.88)$$

where  $\mathbf{N}(\eta)$  is a matrix of shape functions

$$\mathbf{N}(\eta) = \begin{bmatrix} N_1 \mathbf{I} & N_2 \mathbf{I} & \dots \end{bmatrix}. \quad (3.89)$$

Here,  $\mathbf{I}$  is an identity matrix of size  $2 \times 2$  and  $[N_1 \ N_2 \ \dots]$  are the values of shape function at given  $\eta$  (see Fig. 3.3).

Substituting Eqs. (3.86) and (3.88) into Eq. (3.82) and using Eq. (3.81) result in the definitions of stress and strain in local coordinates  $\xi$  and  $\eta$

$$\boldsymbol{\epsilon}(\xi, \eta) = \mathbf{B}_1(\eta) \mathbf{u}(\xi),_{\xi} + \frac{1}{\xi} \mathbf{B}_2(\eta) \mathbf{u}(\xi), \quad (3.90a)$$

$$\boldsymbol{\sigma}(\xi, \eta) = \mathbf{D} \left( \mathbf{B}_1(\eta) \mathbf{u}(\xi),_{\xi} + \frac{1}{\xi} \mathbf{B}_2(\eta) \mathbf{u}(\xi) \right), \quad (3.90b)$$

where

$$\mathbf{B}_1(\eta) = \mathbf{b}_1(\eta) \mathbf{N}(\eta), \quad (3.91a)$$

$$\mathbf{B}_2(\eta) = \mathbf{b}_2(\eta) \mathbf{N}(\eta),_{\eta}. \quad (3.91b)$$

Next, the traction in Eq. (3.84) are written in scaled boundary coordinates using Eq. (3.85) as  $\boldsymbol{\tau}(\xi, \eta) = [\tau_x(\xi, \eta) \ \tau_y(\xi, \eta)]^T$

$$\boldsymbol{\tau}(\xi, \eta) = \begin{bmatrix} n_x & 0 & n_y \\ 0 & n_y & n_x \end{bmatrix} \boldsymbol{\sigma}(\xi, \eta). \quad (3.92)$$

Substituting the definitions of the normal vectors Eqs. (3.19b) and (3.22b) into Eq. (3.92) and using Eq. (3.87) result in

$$\boldsymbol{\tau}^\xi(\xi, \eta) = \frac{|\mathbf{J}(\eta)|}{l^\xi(\eta)} \mathbf{b}_1^T(\eta) \boldsymbol{\sigma}(\xi, \eta), \quad (3.93a)$$

$$\boldsymbol{\tau}^\eta(\xi, \eta) = \frac{|\mathbf{J}(\eta)|}{l^\eta(\eta)} \mathbf{b}_2^T(\eta) \boldsymbol{\sigma}(\xi, \eta), \quad (3.93b)$$

where  $\boldsymbol{\tau}^\xi$  and  $\boldsymbol{\tau}^\eta$  indicate the surface traction on the curves  $\Gamma^\xi$  and  $\Gamma^\eta$ , respectively. For the discretization of the governing equation, the weight functions are postulated similar to the unknown displacement functions in Eq. (3.88)

$$\delta \mathbf{u}(\xi, \eta) = \mathbf{N}(\eta) \delta \mathbf{u}(\xi). \quad (3.94)$$

The internal nodal forces  $\mathbf{Q}(\xi)$  corresponding to unknown displacement functions  $\mathbf{u}(\xi)$  are derived by applying a principle of virtual work on a curve with a constant value of  $\xi$ . Considering the surface traction in Eq. (3.93a), a principle of virtual work is written as follows

$$\delta \mathbf{u}^T(\xi) \mathbf{Q}(\xi) = \int_{\Gamma^\xi} \delta \mathbf{u}^T(\xi, \eta) \boldsymbol{\tau}^\xi(\xi, \eta) d\Gamma. \quad (3.95)$$

Substituting weighting functions of displacement field Eq. (3.94), the integral transformation Eq. (3.18), and the expression of  $\boldsymbol{\tau}^\xi(\xi, \eta)$  Eq. (3.93a) into Eq. (3.95) yields

$$\mathbf{Q}(\xi) = \xi \int_{-1}^{+1} \mathbf{N}^T \mathbf{b}_1^T \boldsymbol{\sigma} |\mathbf{J}| d\eta. \quad (3.96)$$

Note that the function arguments  $(\xi, \eta)$  and  $(\eta)$  are dropped for simplicity. Substituting Eqs. (3.91a) and (3.91b) into Eq. (3.96) results in the expression for the internal nodal forces

$$\mathbf{Q}(\xi) = \xi \int_{-1}^{+1} \mathbf{B}_1^T \boldsymbol{\sigma} |\mathbf{J}| d\eta, \quad (3.97a)$$

$$\mathbf{Q}(\xi) = \xi \int_{-1}^{+1} \mathbf{B}_1^T \mathbf{D} \left( \mathbf{B}_1 \mathbf{u}(\xi),_\xi + \frac{1}{\xi} \mathbf{B}_2 \mathbf{u}(\xi) \right) |\mathbf{J}| d\eta. \quad (3.97b)$$

The SBFE equation in displacement is obtained analogously to the SBFE equation in temperature Eq. (3.56). Applying the method of weighted residuals to Eq. (3.79) in the absence of body forces and side-face traction yields the SBFE homogeneous second-order differential equations in displacement

$$\xi^2 \mathbf{E}_0 \mathbf{u}(\xi),_{\xi\xi} + \xi \left( \mathbf{E}_0 - \mathbf{E}_1 + \mathbf{E}_1^T \right) \mathbf{u}(\xi),_\xi - \mathbf{E}_2 \mathbf{u}(\xi) = \mathbf{0}, \quad (3.98)$$

where

$$\mathbf{E}_0 = \int_{-1}^{+1} \mathbf{B}_1^T \mathbf{D} \mathbf{B}_1 |\mathbf{J}| d\eta, \quad (3.99a)$$

$$\mathbf{E}_1 = \int_{-1}^{+1} \mathbf{B}_2^T \mathbf{D} \mathbf{B}_1 |\mathbf{J}| d\eta, \quad (3.99b)$$

$$\mathbf{E}_2 = \int_{-1}^{+1} \mathbf{B}_2^T \mathbf{D} \mathbf{B}_2 |\mathbf{J}| d\eta. \quad (3.99c)$$

Note the coefficient matrices  $\mathbf{E}_0$ ,  $\mathbf{E}_1$ , and  $\mathbf{E}_2$  are independent of  $\xi$ . They are first integrated for one subdomain  $S^e$  and then assembled for the whole element. The expression of internal nodal forces  $\mathbf{Q}(\xi)$  is also written in the form of coefficient matrices by substituting Eqs. (3.99a) and (3.99b) into Eq. (3.97b)

$$\mathbf{Q}(\xi) = \xi \mathbf{E}_0 \mathbf{u}(\xi),_{\xi} + \mathbf{E}_1^T \mathbf{u}(\xi). \quad (3.100)$$

The SBFE equation in displacement Eq. (3.98) is a system of  $N$  number of equations where  $N$  is the number of degrees of freedom.

### 3.3.2 Solution of SBFE Equation by Schur Decomposition

Similar to the SBFE equation in temperature, the SBFE equation in displacement is transformed to  $2N$  equations as

$$\xi \begin{bmatrix} \mathbf{u}(\xi),_{\xi} \\ \mathbf{Q}(\xi),_{\xi} \end{bmatrix} = - \begin{bmatrix} \mathbf{E}_0^{-1} \mathbf{E}_1^T & -\mathbf{E}_0^{-1} \\ \mathbf{E}_1 \mathbf{E}_0^{-1} \mathbf{E}_1^T - \mathbf{E}_2 & -\mathbf{E}_1 \mathbf{E}_0^{-1} \end{bmatrix} \begin{Bmatrix} \mathbf{u}(\xi) \\ \mathbf{Q}(\xi) \end{Bmatrix}. \quad (3.101)$$

By introducing the variable  $\mathbf{X}(\xi)$ , Eq. (3.101) is rewritten as follows

$$\xi \mathbf{X}(\xi),_{\xi} = -\mathbf{Z} \mathbf{X}(\xi), \quad (3.102)$$

where  $\mathbf{Z}$  is Hamiltonian matrix of size  $2N$

$$\mathbf{Z} = \begin{bmatrix} \mathbf{E}_0^{-1} \mathbf{E}_1^T & -\mathbf{E}_0^{-1} \\ \mathbf{E}_1 \mathbf{E}_0^{-1} \mathbf{E}_1^T - \mathbf{E}_2 & -\mathbf{E}_1 \mathbf{E}_0^{-1} \end{bmatrix}. \quad (3.103)$$

The transformed SBFE equation in displacement and internal nodal forces Eq. (3.102) can also be solved using the method of eigenvalue decomposition as described in Section 3.2.2. However, the eigenvalue method may lead to solution loss and numerical difficulties if the resulting eigenvectors are almost parallel. This issue is circumvented by employing the method of real Schur decomposition with a matrix power functions introduced in [107]. Here, only the summary of Schur decomposition is presented.

The coefficient matrix  $\mathbf{Z}$  in Eq. (3.103) is transformed into the real Schur form matrix by applying the orthogonal transformation

$$\mathbf{V}^T \mathbf{Z} \mathbf{V} = \mathbf{S} = \begin{bmatrix} \mathbf{S}_n & * \\ \mathbf{0} & \mathbf{S}_p \end{bmatrix}, \quad (3.104)$$

where  $\mathbf{V}$  are the Schur vectors and  $\mathbf{S}$  is the quasi-upper triangular matrix of Schur form. The matrix  $\mathbf{S}$  contains  $2 \times 2$  blocks on diagonal corresponding to complex conjugate eigenvalues and  $1 \times 1$  blocks corresponding to real eigenvalues. The diagonal blocks are sorted in ascending order of eigenvalues where  $\mathbf{S}_n$  and  $\mathbf{S}_p$  correspond to negative and positive eigenvalues, respectively. Note that only the real part of the eigenvalues is considered in sorting. Furthermore, the matrix  $\mathbf{S}$  in Eq. (3.104) is block diagonalized such that

$$\mathbf{Z} \Psi = \Psi \mathbf{S}, \quad (3.105)$$

where

$$\mathbf{S} = \begin{bmatrix} \mathbf{S}_n & \mathbf{0} \\ \mathbf{0} & \mathbf{S}_p \end{bmatrix} = \text{diag}(\mathbf{S}_1, \dots, \mathbf{S}_{N-1}, \begin{bmatrix} \mathbf{S}_N & \mathbf{I} \\ \mathbf{0} & \mathbf{S}_{N+1} \end{bmatrix}, \mathbf{S}_{N+2}, \dots, \mathbf{S}_{2N}), \quad (3.106)$$

and  $\Psi$  are the accumulated transformation matrix resulting from the block diagonalization

$$\begin{aligned}\Psi &= \begin{bmatrix} \Psi^u \\ \Psi^f \end{bmatrix} = \begin{bmatrix} \Psi_n^u & \Psi_p^u \\ \Psi_n^f & \Psi_p^f \end{bmatrix}, \\ &= \begin{bmatrix} \Psi_1^u & \dots & \Psi_{N-1}^u & \Psi_N^u & \Psi_{N+1}^u & \Psi_{N+2}^u & \dots & \Psi_{2N}^u \\ \Psi_1^f & \dots & \Psi_{N-1}^f & \Psi_N^f & \Psi_{N+1}^f & \Psi_{N+2}^f & \dots & \Psi_{2N}^f \end{bmatrix}.\end{aligned}\quad (3.107)$$

In Eq. (3.106), the blocks  $\mathbf{S}_N$  and  $\mathbf{S}_{N+1}$  indicate the zero eigenvalues that can not be decoupled further. Additionally, Eq. (3.107) shows the accumulated transformation vectors partitioned as  $\Psi^u$  and  $\Psi^f$  corresponding to internal displacements  $\mathbf{u}(\xi)$  and internal forces  $\mathbf{Q}(\xi)$ , respectively. For the detailed derivation of Schur decomposition and block diagonalization, readers are referred to [107]. Following the property of the Hamiltonian matrix, the accumulated transformation matrix is  $\mathbf{J}_{2N}$ -orthogonal, i.e.,

$$\Psi_i^T \mathbf{J}_{2N} \Psi_j = \left( -\Psi_{\bar{i}}^T \mathbf{J}_{2N} \Psi_i \right)^T = \begin{cases} \mathbf{H}_i & \text{when } j = \bar{i}, \\ 0 & \text{when } j \neq \bar{i}, \end{cases} \quad (3.108)$$

where  $\bar{i} = 2N + 1 - i$ , and

$$\mathbf{J}_{2N} = \begin{bmatrix} \mathbf{0} & \mathbf{I} \\ -\mathbf{I} & \mathbf{0} \end{bmatrix}. \quad (3.109)$$

Pre-multiplying Eq. (3.105) with  $-\Psi_{\bar{i}}^T \mathbf{J}_{2N}$  and using Eq. (3.108) yield

$$-\Psi_{\bar{i}}^T \mathbf{J}_{2N} \mathbf{Z} \Psi_j = \begin{cases} \mathbf{H}_i^T \mathbf{S}_i & \text{when } j = i, \\ 0 & \text{when } j \neq i. \end{cases} \quad (3.110)$$

Now, the solution of variable  $\mathbf{X}(\xi)$  in Eq. (3.102) is postulated in the form of matrix power functions of  $\xi$  as follows

$$\mathbf{X}(\xi) = \Psi \xi^{-\mathbf{S}} \mathbf{c}, \quad (3.111)$$

where  $\mathbf{c}$  are the integration constants. Expanding  $\mathbf{S}$  and  $\Psi$  in Eq. (3.111) using Eqs. (3.106) and (3.107), respectively, yields the expression for  $\mathbf{u}(\xi)$  and  $\mathbf{Q}(\xi)$  as

$$\mathbf{u}(\xi) = \Psi_n^u \xi^{-\mathbf{S}_n} \mathbf{c}_n + \Psi_p^u \xi^{-\mathbf{S}_p} \mathbf{c}_p, \quad (3.112a)$$

$$\mathbf{Q}(\xi) = \Psi_n^f \xi^{-\mathbf{S}_n} \mathbf{c}_n + \Psi_p^f \xi^{-\mathbf{S}_p} \mathbf{c}_p. \quad (3.112b)$$

In a bounded domain, i.e.,  $0 \leq \xi \leq 1$ , the solution of Eq. (3.112) must remain finite at  $\xi = 0$ . Enforcing the condition for finiteness of solution, Eq. (3.112) is reduced to

$$\mathbf{u}(\xi) = \Psi_n^u \xi^{-\mathbf{S}_n} \mathbf{c}_n, \quad (3.113a)$$

$$\mathbf{Q}(\xi) = \Psi_n^f \xi^{-\mathbf{S}_n} \mathbf{c}_n. \quad (3.113b)$$

The integration constants  $\mathbf{c}_n$  are obtained from the displacement solution at the boundary  $\xi = 1$  by substituting  $\mathbf{u}_b = \mathbf{u}(\xi = 1)$  in Eq. (3.113a)

$$\mathbf{c}_n = (\Psi_n^u)^{-1} \mathbf{u}_b. \quad (3.114)$$

Finally, the stiffness matrix is obtained at the boundary by eliminating the integration constants from Eq. (3.113)

$$\mathbf{Q}(\xi = 1) = \hat{\mathbf{K}} \mathbf{u}(\xi = 1), \quad (3.115)$$

where the stiffness matrix  $\hat{\mathbf{K}}$  is given as

$$\hat{\mathbf{K}} = \Psi_n^f (\Psi_n^u)^{-1}. \quad (3.116)$$

The displacements at any given local coordinates  $\xi$  and  $\eta$  are interpolated using the solution at the boundary  $\mathbf{u}_b$ . Substituting Eq. (3.114) into Eq. (3.113a) and using Eq. (3.88) result in

$$\mathbf{u}(\xi, \eta) = \chi(\xi, \eta) \mathbf{u}_b(\eta), \quad (3.117)$$

where  $\chi(\xi, \eta)$  are the scaled boundary shape functions for the displacement field

$$\chi(\xi, \eta) = \mathbf{N}(\eta) (\Psi_n^u)^{(e)} \xi^{-\mathbf{S}_n} (\Psi_n^u)^{-1}. \quad (3.118)$$

The superscript  $(e)$  indicates the degrees of freedom corresponding to individual  $S^e$ .

Next, the evaluation of stress and strain is considered. Once the solution of displacement at the boundary is obtained, the integration constants  $\mathbf{c}_n$  can be calculated using Eq. (3.114). The derivative of Eq. (3.113a) with respect to radial coordinate  $\xi$  is expressed as

$$\mathbf{u}(\xi)_{,\xi} = -\mathbf{S}_n \Psi_n^u \xi^{-\mathbf{S}_n - \mathbf{I}} \mathbf{c}_n. \quad (3.119)$$

Substituting Eqs. (3.113a) and (3.119) in Eq. (3.90) yields the formulation of strains and stresses at local coordinates  $\xi$  and  $\eta$  within one subdomain  $S^e$  as follows

$$\boldsymbol{\epsilon}(\xi, \eta) = \sum_{i=1}^N \Psi_{ei}(\eta) \xi^{-\mathbf{S}_i - \mathbf{I}} \mathbf{c}_i, \quad (3.120a)$$

$$\boldsymbol{\sigma}(\xi, \eta) = \sum_{i=1}^N \Psi_{\sigma i}(\eta) \xi^{-\mathbf{S}_i - \mathbf{I}} \mathbf{c}_i, \quad (3.120b)$$

where  $\Psi_{ei}(\eta)$  and  $\Psi_{\sigma i}$  are the strain and stress modes, respectively. Their definitions are expressed as

$$\Psi_{ei}(\eta) = -\mathbf{B}_1(\eta) (\Psi_i^u)^{(e)} \mathbf{S}_i + \mathbf{B}_2(\eta) (\Psi_i^u)^{(e)}, \quad (3.121a)$$

$$\Psi_{\sigma i}(\eta) = \mathbf{D} \left( -\mathbf{B}_1(\eta) (\Psi_i^u)^{(e)} \mathbf{S}_i + \mathbf{B}_2(\eta) (\Psi_i^u)^{(e)} \right). \quad (3.121b)$$

Note that strain and stress are calculated for each mode individually. A simple superposition rule is applied to evaluate the overall contribution of each mode.

## 3.4 Shape Functions of Polygon Elements

This section presents a few illustrations of the scaled boundary polygon shape functions. The temperature and displacement fields are interpolated using the shape functions given in Eqs. (3.78) and (3.118), respectively. These shape functions are written separately as functions of  $\eta$  and  $\xi$

$$\bar{\chi}(\xi, \eta) = \bar{\mathbf{N}}(\eta) (\bar{\chi}_\xi(\xi))^{(e)}, \quad (3.122a)$$

$$\chi(\xi, \eta) = \mathbf{N}(\eta) (\chi_\xi(\xi))^{(e)}. \quad (3.122b)$$

where

$$\bar{\chi}_\xi(\xi) = \Phi_n^\theta \xi^{-\lambda_n} \left( \Phi_n^\theta \right)^{-1}, \quad (3.123a)$$

$$\chi_\xi(\xi) = \Psi_n^u \xi^{-\mathbf{S}_n} (\Psi_n^u)^{-1}. \quad (3.123b)$$

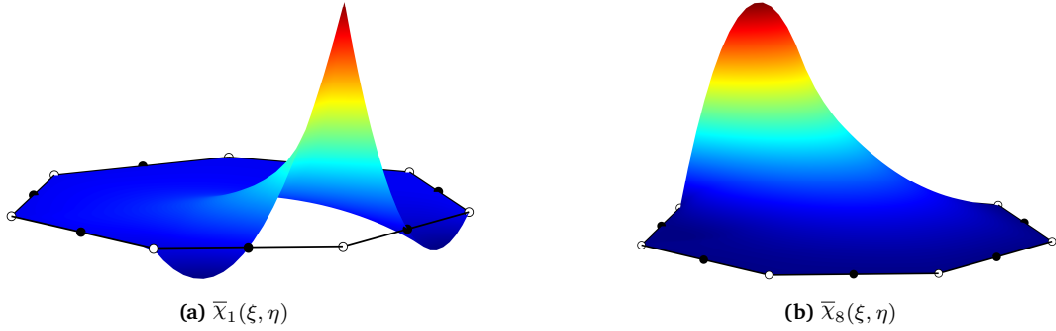


**Figure 3.7:** Scaled boundary shape functions  $\bar{X}(\xi, \eta)$  of a close heptagon discretized by a three-node line elements on the boundary. (a)  $\bar{X}_1(\xi, \eta)$  corresponding to node one and (b)  $\bar{X}_8(\xi, \eta)$  corresponding to node eight.

Here,  $\bar{X}_\xi(\xi)$  and  $X_\xi(\xi)$  describe temperature and displacement fields in  $\xi$  direction, respectively. These matrices do not depend on the interpolation in  $\eta$  direction. Hence, they hold the contribution for the whole scaled boundary element irrespective of individual subdomain  $S^e$ . The interpolation in  $\eta$  direction depends on the degrees of freedom corresponding to each  $S^e$  and discretization on the boundary, i.e.,  $\bar{\mathbf{N}}(\eta)$  and  $\mathbf{N}(\eta)$ . Note that in Eq. (3.122), the superscript  $(e)$  indicates the rows of the matrices  $\bar{X}_\xi(\xi)$  and  $X_\xi(\xi)$  corresponding to the degrees of freedom of a given  $S^e$ .

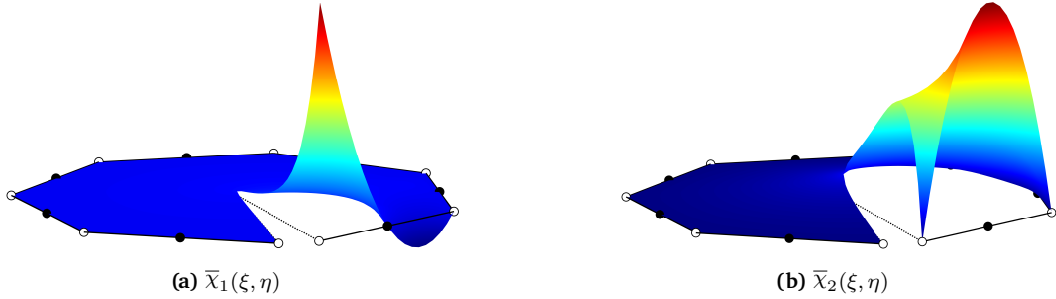


**Figure 3.8:** Scaled boundary shape functions  $\bar{X}(\xi, \eta)$  of an open-element discretized by three-node line elements on the boundary. (a)  $\bar{X}_1(\xi, \eta)$  corresponding to node number one and, (b)  $\bar{X}_2(\xi, \eta)$  corresponding to node number two.

Figure 3.7 shows a plot of selected scaled boundary shape functions in Eq. (3.123a) for a closed heptagon meshed with a three-node line elements. Figures 3.7(a) and 3.7(b) depict the plot of  $\bar{X}(\xi, \eta)$  corresponding to node one and node eight, respectively. Similarly, Figs. 3.8(a) and 3.8(b) show the plot of an open-element meshed with a three-node line elements. It is apparent from Fig. 3.8 that the scaled boundary open-element incorporates discontinuity seamlessly. Only the shape functions of the temperature field are shown in Figs. 3.7 and 3.8. Similar shape functions of the displacement field are obtained for each degree of freedom in  $u_x$  and  $u_y$ .

# Chapter 4

## SBFEM for Thermoelasticity

This chapter presents the formulation of coupled thermoelasticity using the scaled boundary finite element. Section 4.1 discusses thermal stress modeling as a load vector for elastostatic problems. The thermal stress caused by a temperature change results in the non-homogeneous SBFM equation in displacement. Furthermore, the evaluation of a particular solution for a non-homogeneous SBFM equation in displacement is presented. For the case of a temperature change as a power function of coordinates, the thermal load vector is integrated semi-analytically, as discussed in Section 4.2. For a detailed explanation, readers are referred to [119].

To evaluate the thermal load vector, the solution of the temperature field must be known a prior. Consequently, applying thermal stress as load vector results in uni-directional coupling of temperature and displacement fields. The scaled boundary supplementary shape functions are formulated in [153] to overcome a known temperature field requirement. The scaled boundary shape functions for the displacement field are enriched by the supplementary shape functions, as presented in Section 4.3.

Section 4.4 presents the discretization of governing equations for fully coupled thermoelasticity Eq. (2.77). The scaled boundary polygon shape functions for displacement enriched by supplementary shape functions are employed for that purpose.

### 4.1 Thermal Stress Analogous to Load

This section considers the effects of initial thermal stress as a non-homogeneous term for the SBFM equation in displacement. The fundamental derivation steps are similar to the homogeneous case presented in Section 3.3. Here, the discussion is focused on evaluating the effects of non-homogeneous terms. The formulation is derived for a static case with pre-existing initial stress that leads to a weak (uni-directional) coupling of temperature and displacements. In the case of thermo-elastic equilibrium, the governing equation of balance of momentum Eq. (2.77b) with constitutive relations Eq. (2.77c) reads

$$\nabla_u^T \boldsymbol{\sigma} + \mathbf{p} = \mathbf{0}, \quad (4.1a)$$

$$\boldsymbol{\sigma} = \mathbf{D} \nabla_u \mathbf{u} + \boldsymbol{\sigma}_0, \quad (4.1b)$$

where the initial thermal stress  $\boldsymbol{\sigma}_0$  is expressed as

$$\boldsymbol{\sigma}_0 = -\mathbf{D} \boldsymbol{\epsilon}_0, \quad (4.2)$$

and the initial thermal strain  $\boldsymbol{\epsilon}_0$  caused by the temperature change is defined as

$$\boldsymbol{\epsilon}_0 = \beta \theta. \quad (4.3)$$

Similar to Eq. (3.90b), the stress in Eq. (4.1b) is written in scaled boundary coordinates as follows

$$\boldsymbol{\sigma}(\xi, \eta) = \mathbf{D} \left( \mathbf{B}_1(\eta) \mathbf{u}(\xi), \xi + \frac{1}{\xi} \mathbf{B}_2(\eta) \mathbf{u}(\xi) \right) + \boldsymbol{\sigma}_0(\xi, \eta). \quad (4.4)$$

The internal nodal forces are expressed using Eq. (3.97a) as

$$\hat{\mathbf{Q}}(\xi) = \xi \int_{-1}^{+1} \mathbf{B}_1(\eta)^T \boldsymbol{\sigma}(\xi, \eta) |\mathbf{J}(\eta)| d\eta, \quad (4.5)$$

where  $\hat{\mathbf{Q}}(\xi)$  holds the contribution of both mechanical and thermal stresses. Substituting Eq. (4.4) into Eq. (4.5) results in

$$\hat{\mathbf{Q}}(\xi) = \xi \int_{-1}^{+1} \mathbf{B}_1^T \left( \mathbf{D} \mathbf{B}_1 \mathbf{u}(\xi, \eta) + \frac{1}{\xi} \mathbf{D} \mathbf{B}_2 \mathbf{u}(\xi) + \boldsymbol{\sigma}_0 \right) |\mathbf{J}| d\eta. \quad (4.6)$$

Note that the function arguments  $(\xi, \eta)$  and  $(\eta)$  are omitted for convenience. Comparing Eqs. (3.97a) and (3.100) with Eq. (4.6) reveals

$$\hat{\mathbf{Q}}(\xi) = \xi \int_{-1}^{+1} \mathbf{B}_1^T \mathbf{D} \left( \mathbf{B}_1 \mathbf{u}(\xi, \eta) + \frac{1}{\xi} \mathbf{B}_2 \mathbf{u}(\xi) \right) |\mathbf{J}| d\eta + \hat{\mathbf{Q}}_0(\xi), \quad (4.7a)$$

$$= \xi \mathbf{E}_0 \mathbf{u}(\xi, \eta) + \mathbf{E}_1^T \mathbf{u}(\xi) + \hat{\mathbf{Q}}_0(\xi), \quad (4.7b)$$

$$= \mathbf{Q}(\xi) + \hat{\mathbf{Q}}_0(\xi), \quad (4.7c)$$

where

$$\hat{\mathbf{Q}}_0(\xi) = \xi \int_{-1}^{+1} \mathbf{B}_1^T \boldsymbol{\sigma}_0 |\mathbf{J}| d\eta. \quad (4.8)$$

Analogous to the homogeneous SBFE equation in displacement, the non-homogeneous equation is derived by applying the Galerkin method of weighted residuals to Eq. (4.1a) in the circumferential direction. The discretization of the governing equation yields

$$\int_{-1}^{+1} \mathbf{B}_1^T (\xi(\boldsymbol{\sigma} - \boldsymbol{\sigma}_0))_{,\xi} |\mathbf{J}| d\eta - \int_{-1}^{+1} \mathbf{B}_2^T (\boldsymbol{\sigma} - \boldsymbol{\sigma}_0) |\mathbf{J}| d\eta + \frac{1}{\xi} \mathbf{F}(\xi) = \mathbf{0}, \quad (4.9)$$

where  $\mathbf{F}(\xi)$  is the non-homogeneous term that is given as

$$\mathbf{F}(\xi) = \xi \mathbf{f}_t(\xi) + \xi^2 \mathbf{f}_g(\xi) + \xi \mathbf{f}_p(\xi). \quad (4.10)$$

Here,  $\mathbf{f}_t$  are the nodal forces resulting from surface traction acting on side-faces  $\Gamma^s$ ,  $\mathbf{f}_g$  are the nodal forces due to body forces, and  $\mathbf{f}_p$  represents the contribution of the thermal stress. Their definitions are

$$\mathbf{f}_t(\xi) = \mathbf{N}^T l^\eta \boldsymbol{\tau}^\eta \Big|_{\eta=-1}^{\eta=+1}, \quad (4.11a)$$

$$\mathbf{f}_g(\xi) = \int_{-1}^{+1} \mathbf{N}^T \mathbf{p} |\mathbf{J}| d\eta, \quad (4.11b)$$

$$\mathbf{f}_p(\xi) = \int_{-1}^{+1} \left( \mathbf{B}_1^T (\xi \boldsymbol{\sigma}_0)_{,\xi} - \mathbf{B}_2^T \boldsymbol{\sigma}_0 \right) |\mathbf{J}| d\eta, \quad (4.11c)$$

respectively. Substituting Eqs. (4.6) and (4.8) into Eq. (4.9) and using Eq. (4.4) results in

$$\left( \hat{\mathbf{Q}}(\xi) - \hat{\mathbf{Q}}_0(\xi) \right)_{,\xi} - \int_{-1}^{+1} \mathbf{B}_2^T \mathbf{D} \left( \mathbf{B}_1 \mathbf{u}(\xi, \eta) + \frac{1}{\xi} \mathbf{B}_2 \mathbf{u}(\xi) \right) |\mathbf{J}| d\eta + \frac{1}{\xi} \mathbf{F}(\xi) = \mathbf{0}. \quad (4.12)$$

Multiplying Eq. (4.12) with  $\xi$  and using the expression of the coefficient matrices in Eq. (3.99) yield

$$\xi \left( \hat{\mathbf{Q}}(\xi) - \hat{\mathbf{Q}}_0(\xi) \right)_{,\xi} - \xi \mathbf{E}_1 \mathbf{u}(\xi, \eta) - \mathbf{E}_2 \mathbf{u}(\xi) + \mathbf{F}(\xi) = \mathbf{0}. \quad (4.13)$$

Solving for  $(\hat{\mathbf{Q}}(\xi) - \hat{\mathbf{Q}}_0(\xi))$  from Eq. (4.7b) and substituting it in Eq. (4.13) results in the SBFE second-order non-homogeneous differential equations in displacement

$$\xi^2 \mathbf{E}_0 \mathbf{u}(\xi)_{,\xi\xi} + \xi \left( \mathbf{E}_0 - \mathbf{E}_1 + \mathbf{E}_1^T \right) \mathbf{u}(\xi)_{,\xi} - \mathbf{E}_2 \mathbf{u}(\xi) + \mathbf{F}(\xi) = \mathbf{0}. \quad (4.14)$$

Similar to the solution procedure of homogeneous SBFE equation in Eq. (3.56), Eq. (4.14) is first transformed to the first-order system with  $2N$  number of equations. To this end, the derivative of displacement functions are obtained from Eq. (4.7b) as follows

$$\xi \mathbf{u}(\xi)_{,\xi} = \mathbf{E}_0^{-1} \left( \hat{\mathbf{Q}}(\xi) - \hat{\mathbf{Q}}_0(\xi) \right) - \mathbf{E}_0^{-1} \mathbf{E}_1^T \mathbf{u}(\xi). \quad (4.15)$$

Eliminating  $\mathbf{u}(\xi)_{,\xi}$  in Eq. (4.13) using Eq. (4.15) yields the SBFE equation in the form of internal nodal forces and displacement functions as

$$\xi \left( \hat{\mathbf{Q}}(\xi) - \hat{\mathbf{Q}}_0(\xi) \right)_{,\xi} - \mathbf{E}_1 \mathbf{E}_0^{-1} \left( \hat{\mathbf{Q}}(\xi) - \hat{\mathbf{Q}}_0(\xi) \right) + \left( \mathbf{E}_1 \mathbf{E}_0^{-1} \mathbf{E}_1^T - \mathbf{E}_2 \right) \mathbf{u}(\xi) + \mathbf{F}(\xi) = \mathbf{0}. \quad (4.16)$$

By introducing the variable  $\hat{\mathbf{X}}(\xi)$  of size  $2N$  as

$$\hat{\mathbf{X}}(\xi) = \begin{Bmatrix} \mathbf{u}(\xi) \\ \hat{\mathbf{Q}}(\xi) - \hat{\mathbf{Q}}_0(\xi) \end{Bmatrix}, \quad (4.17)$$

Eqs. (4.14) and (4.16) are rearranged as follows

$$\xi \hat{\mathbf{X}}(\xi)_{,\xi} = -\mathbf{Z} \hat{\mathbf{X}}(\xi) - \begin{Bmatrix} \mathbf{0} \\ \mathbf{F}(\xi) \end{Bmatrix}, \quad (4.18)$$

where the matrix  $\mathbf{Z}$  is given in Eq. (3.103).

To solve the non-homogeneous SBFE equation in Eq. (4.18), the coefficient matrix  $\mathbf{Z}$  is first transformed using the real Schur decomposition as explained in Section 3.3.2. Then, the solution is written in the form of accumulated transformation vectors Eq. (3.107) as base functions [119]

$$\hat{\mathbf{X}}(\xi) = \Psi \mathbf{g}(\xi) = \sum_{i=1}^{2N} \Psi_i \mathbf{g}_i(\xi), \quad (4.19)$$

where  $\mathbf{g}_i(\xi)$  are the generalized coordinate functions. The expression for displacement functions  $\mathbf{u}(\xi)$  and internal nodal forces  $\hat{\mathbf{Q}}(\xi)$  are obtained by substituting Eq. (4.19) into Eq. (4.17)

$$\mathbf{u}(\xi) = \Psi^u \mathbf{g}(\xi) = \sum_{i=1}^{2N} \Psi_i^u \mathbf{g}_i(\xi), \quad (4.20a)$$

$$\hat{\mathbf{Q}}(\xi) = \Psi^f \mathbf{g}(\xi) + \hat{\mathbf{Q}}_0(\xi) = \sum_{i=1}^{2N} \Psi_i^f \mathbf{g}_i(\xi) + \hat{\mathbf{Q}}_0(\xi). \quad (4.20b)$$

Now, Eq. (4.18) is written in the form of base functions and generalized coordinate functions by substituting Eq. (4.19) into Eq. (4.18) as follows

$$\xi \Psi \mathbf{g}(\xi)_{,\xi} = -\mathbf{Z} \Psi \mathbf{g}(\xi) - \begin{Bmatrix} \mathbf{0} \\ \mathbf{F}(\xi) \end{Bmatrix}. \quad (4.21)$$

Equation (4.21) is a coupled equation system requiring decoupling. For this purpose, Eq. (4.21) is first pre-multiplied by  $-\Psi_i^T \mathbf{J}_{2N}$ , then using Eqs. (3.108) and (3.110) result in

$$\xi \mathbf{H}_i^T \mathbf{g}(\xi)_{,\xi} = -\mathbf{H}_i^T \mathbf{S}_i \mathbf{g}_i(\xi) + \Psi_i^T \mathbf{J}_{2N} \begin{Bmatrix} \mathbf{0} \\ \mathbf{F}(\xi) \end{Bmatrix}. \quad (4.22)$$

Now, pre-multiplying Eq. (4.22) with  $\mathbf{H}_i^{-T}$  yields the decoupled system of equations as

$$\xi \mathbf{g}_i(\xi)_{,\xi} = -\mathbf{S}_i \mathbf{g}_i(\xi) - \mathbf{f}_i^{(g)}(\xi), \quad (4.23)$$

where the transformed non-homogeneous term  $\mathbf{f}_i^{(g)}(\xi)$  is given as

$$\mathbf{f}_i^{(g)}(\xi) = -\mathbf{H}_i^{-T} \Psi_i^T \mathbf{J}_{2N} \begin{Bmatrix} \mathbf{0} \\ \mathbf{F}(\xi) \end{Bmatrix} = -\mathbf{H}_i^{-T} (\Psi_i^u)^T \mathbf{F}(\xi). \quad (4.24)$$

The generalized coordinate functions hold the contribution of both homogeneous and particular solutions; they can be separated as follows

$$\mathbf{g}_i(\xi) = \mathbf{g}_i^{(h)}(\xi) + \mathbf{g}_i^{(p)}(\xi), \quad (4.25)$$

where  $\mathbf{g}_i^{(h)}(\xi)$  and  $\mathbf{g}_i^{(p)}(\xi)$  represent the homogeneous and particular solutions, respectively. The formal solution of homogeneous part  $\mathbf{g}_i^{(h)}(\xi)$  is postulated in the form of power functions of radial coordinate  $\xi$  as follows

$$\mathbf{g}_i^{(h)}(\xi) = \xi^{-\mathbf{S}_i} \hat{\mathbf{c}}_i, \quad (4.26)$$

where  $\hat{\mathbf{c}}_i$  is a vector of arbitrary integration constants. Similar to homogeneous solution, the particular solution  $\mathbf{g}_i^{(p)}(\xi)$  is obtained by replacing the integration constants with unknown functions  $\hat{\mathbf{c}}_i(\xi)$ , such that

$$\mathbf{g}_i^{(p)}(\xi) = \xi^{-\mathbf{S}_i} \hat{\mathbf{c}}_i(\xi). \quad (4.27)$$

Substituting the particular solution of generalized coordinate functions Eq. (4.27) into the system of non-homogeneous equations Eq. (4.23) results in

$$\hat{\mathbf{c}}_i(\xi)_{,\xi} = -\xi^{\mathbf{S}_i - \mathbf{I}} \mathbf{f}_i^{(g)}(\xi). \quad (4.28)$$

The complete solution of generalized coordinate functions in Eq. (4.25) is obtained by substituting the integration of Eq. (4.28) into Eq. (4.27) and using Eq. (4.26)

$$\mathbf{g}_i(\xi) = \xi^{-\mathbf{S}_i} \left( \hat{\mathbf{c}}_i - \int_1^\xi \zeta^{\mathbf{S}_i - \mathbf{I}} \mathbf{f}_i^{(g)}(\zeta) d\zeta \right). \quad (4.29)$$

Equation (4.29) satisfies Eq. (4.23) for any lower limit of the integral. Therefore, it is chosen as one for simplicity. For the block with real positive eigenvalues, i.e.  $\text{Re}(\mathbf{S}_i) > 0$ , it is apparent that  $\xi^{-\mathbf{S}_i}$  is not admissible as it tends to infinity in Eq. (4.29). The integration constants  $\hat{\mathbf{c}}_i$  are obtained from the boundary condition at  $\xi = 0$

$$\hat{\mathbf{c}}_i = \int_1^0 \zeta^{\mathbf{S}_i - \mathbf{I}} \mathbf{f}_i^{(g)}(\zeta) d\zeta \quad \text{when } \text{Re}(\mathbf{S}_i) > 0. \quad (4.30)$$

For the block with real negative eigenvalues, i.e.  $\text{Re}(\mathbf{S}_i) < 0$ , the boundary condition is satisfied for any integration constants  $\hat{\mathbf{c}}_i$  in Eq. (4.29). Therefore, the solution of generalized coordinates functions is written as

$$\mathbf{g}_i(\xi) = \begin{cases} \xi^{-\mathbf{S}_i} \hat{\mathbf{c}}_i + \mathbf{g}_i^{(p)}(\xi) & \text{when } \text{Re}(\mathbf{S}_i) < 0, \\ \mathbf{g}_i^{(p)}(\xi) & \text{when } \text{Re}(\mathbf{S}_i) > 0, \end{cases} \quad (4.31)$$

where the particular solution  $\mathbf{g}_i^{(p)}(\xi)$  is given as

$$\mathbf{g}_i^{(p)}(\xi) = \begin{cases} -\xi^{-\mathbf{S}_i} \int_1^\xi \zeta^{\mathbf{S}_i - \mathbf{I}} \mathbf{f}_i^{(g)}(\zeta) d\zeta & \text{when } \operatorname{Re}(\mathbf{S}_i) < \mathbf{0}, \\ -\xi^{-\mathbf{S}_i} \int_0^\xi \zeta^{\mathbf{S}_i - \mathbf{I}} \mathbf{f}_i^{(g)}(\zeta) d\zeta & \text{when } \operatorname{Re}(\mathbf{S}_i) > \mathbf{0}. \end{cases} \quad (4.32)$$

In the case of zero eigenvalues, there exist two coupled diagonal blocks  $\mathbf{S}_N = \mathbf{0}$  and  $\mathbf{S}_{N+1} = \mathbf{0}$  in Eq. (3.106). Consequently, the solution of generalized coordinate functions corresponding to these blocks, i.e.  $\mathbf{g}_N(\xi)$  and  $\mathbf{g}_{N+1}(\xi)$ , are also coupled. Hence, they have to be solved simultaneously. For  $i = [N \ N+1]$ , Eq. (4.23) is written as

$$\xi \begin{Bmatrix} \mathbf{g}_N(\xi) \\ \mathbf{g}_{N+1}(\xi) \end{Bmatrix}_{,\xi} = \begin{bmatrix} \mathbf{0} & \mathbf{I} \\ \mathbf{0} & \mathbf{0} \end{bmatrix} \begin{Bmatrix} \mathbf{g}_N(\xi) \\ \mathbf{g}_{N+1}(\xi) \end{Bmatrix} + \begin{Bmatrix} \mathbf{f}_N^{(g)}(\xi) \\ \mathbf{f}_{N+1}^{(g)}(\xi) \end{Bmatrix}. \quad (4.33)$$

Here,  $\mathbf{f}_N^{(g)}(\xi)$  and  $\mathbf{f}_{N+1}^{(g)}(\xi)$  are obtained from Eq. (4.24). Following the same procedure as for the case where  $\operatorname{Re}(\mathbf{S}_i) \neq \mathbf{0}$ , the solution of  $\mathbf{g}_N(\xi)$  and  $\mathbf{g}_{N+1}(\xi)$  is formulated as

$$\mathbf{g}_N(\xi) = \hat{\mathbf{c}}_N + \mathbf{g}_N^{(p)}(\xi) \quad \text{when } \mathbf{S}_N = \mathbf{S}_{N+1} = \mathbf{0}, \quad (4.34a)$$

$$\mathbf{g}_{N+1}(\xi) = \mathbf{g}_{N+1}^{(p)}(\xi) \quad \text{when } \mathbf{S}_N = \mathbf{S}_{N+1} = \mathbf{0}, \quad (4.34b)$$

with the particular solution  $\mathbf{g}_N^{(p)}(\xi)$  and  $\mathbf{g}_{N+1}^{(p)}(\xi)$  given as

$$\mathbf{g}_N^{(p)}(\xi) = - \int_1^\xi \frac{1}{\zeta} \left( \mathbf{f}_N^{(g)}(\zeta) + \int_0^\zeta \frac{1}{\hat{\zeta}} \mathbf{f}_{N+1}^{(g)}(\hat{\zeta}) d\hat{\zeta} \right) d\zeta, \quad (4.35a)$$

$$\mathbf{g}_{N+1}^{(p)}(\xi) = - \int_0^\xi \frac{1}{\zeta} \mathbf{f}_{N+1}^{(g)}(\zeta) d\zeta. \quad (4.35b)$$

The particular solution  $\mathbf{g}_i^{(p)}(\xi)$  in Eq. (4.31) depends on integrating the transformed non-homogeneous term  $\mathbf{f}_i^{(g)}(\xi)$  in the radial direction.

## 4.2 Thermal Load as Power Functions of Coordinates

Analytically integrating a particular solution in Eq. (4.31) is possible for some instances. One such case is the temperature distribution as the power function of the coordinates [119]. The SBFEM solution of temperature field in Eq. (3.77) is a series of power functions in radial coordinates  $\xi$ . Consequently, the resulting thermal stress  $\sigma_0$  can also be expressed as a series of power functions in  $\xi$ . Thus, integrating a particular solution in Eq. (4.31) can be solved analytically. Here, the solution of one term in the series is discussed. A simple superposition rule is applied to assemble the contributions of all terms in the series. The temperature distribution in Eq. (3.77) corresponding to  $j^{th}$  term of the series is expressed as

$$\theta(\xi, \eta) = \bar{\mathbf{N}}(\eta) \Phi_j^\theta \xi^{-\lambda_j} \bar{c}_j. \quad (4.36)$$

The thermal stress  $\sigma_0$  caused by the given temperature change is obtained by substituting Eq. (4.36) into Eqs. (4.3) and (4.2) as follows

$$\sigma_0(\xi, \eta) = -\mathbf{D}\beta \bar{\mathbf{N}}(\eta) \Phi_j^\theta \xi^{-\lambda_j} \bar{c}_j. \quad (4.37)$$

Substituting Eq. (4.37) in Eq. (4.11c) results in

$$\mathbf{f}_p(\xi) = \bar{\mathbf{p}}_0 \xi^{-\lambda_j}, \quad (4.38)$$

where

$$\bar{\mathbf{p}}_0 = - \int_{-1}^{+1} \left( \mathbf{B}_1^T(\eta) \mathbf{D} \boldsymbol{\beta}(-\lambda_j + 1) - \mathbf{B}_2^T(\eta) \mathbf{D} \boldsymbol{\beta} \right) \theta_j(\eta) |\mathbf{J}(\eta)| d\eta, \quad (4.39)$$

with

$$\theta_j(\eta) = \bar{\mathbf{N}}(\eta) \boldsymbol{\Phi}_j^\theta \bar{c}_j. \quad (4.40)$$

The non-homogeneous term  $\mathbf{F}(\xi)$  for vanishing body forces and side-face traction is formulated by substituting Eq. (4.38) into Eq. (4.10) as

$$\mathbf{F}(\xi) = \bar{\mathbf{p}}_0 \xi^h, \quad (4.41)$$

where

$$h = -\lambda_j + 1. \quad (4.42)$$

For the finiteness of integrals in particular solution Eq. (4.32), it is required that  $h > 0$ . Inspecting Eqs. (3.77) and (3.78) reveals that  $-\lambda_j > -1$ , i.e.  $h > 0$ , always hold. Substituting Eq. (4.41) in Eq. (4.24) yields the transformed non-homogeneous term corresponding to temperature change as

$$\mathbf{f}_i^{(g)}(\xi) = \bar{\mathbf{f}}_i^{(g)} \xi^h = -\mathbf{H}_i^{-T} [\boldsymbol{\Psi}_i^u]^T \bar{\mathbf{p}}_0 \xi^h. \quad (4.43)$$

Now, the particular solution  $\mathbf{g}_i^{(p)}(\xi)$  is evaluated by substituting Eq. (4.43) into Eq. (4.32) and performing the integration analytically results in

$$\mathbf{g}_i^{(p)}(\xi) = -(\mathbf{S}_i + h\mathbf{I})^{-1} \bar{\mathbf{f}}_i^{(g)} \xi^h \quad \text{when } \operatorname{Re}(\mathbf{S}_i) \neq \mathbf{0}. \quad (4.44)$$

Similarly, the block with zero eigenvalues is written as

$$\mathbf{g}_N^{(p)}(\xi) = \frac{1}{h} \left( \frac{1}{h} \bar{\mathbf{f}}_{N+1}^{(g)} - \bar{\mathbf{f}}_N^{(g)} \right) \xi^h \quad \text{when } \mathbf{S}_N = \mathbf{S}_{N+1} = \mathbf{0}, \quad (4.45a)$$

$$\mathbf{g}_{N+1}^{(p)}(\xi) = -\frac{1}{h} \bar{\mathbf{f}}_{N+1}^{(g)} \xi^h \quad \text{when } \mathbf{S}_N = \mathbf{S}_{N+1} = \mathbf{0}. \quad (4.45b)$$

When  $h$  is close to the eigenvalues  $\operatorname{Re}(\mathbf{S}_i)$ , the term  $(\mathbf{S}_i + h\mathbf{I})^{-1}$  may become singular. Although the analytical integration of a particular solution is still possible, it is better to perform numerical integration. For the details, readers are referred to [119].

Once the particular solution is obtained, the expressions for the displacement functions  $\mathbf{u}(\xi)$  and the internal nodal forces  $\hat{\mathbf{Q}}(\xi)$  are determined by substituting Eqs. (4.31) and (4.34) into Eq. (4.20) as follows

$$\mathbf{u}(\xi) = \sum_{i=1}^N \boldsymbol{\Psi}_i^u \xi^{-\mathbf{S}_i} \hat{\mathbf{c}}_i + \sum_{i=1}^{2N} \boldsymbol{\Psi}_i^u \mathbf{g}_i^{(p)}(\xi), \quad (4.46a)$$

$$\hat{\mathbf{Q}}(\xi) = \sum_{i=1}^N \boldsymbol{\Psi}_i^f \xi^{-\mathbf{S}_i} \hat{\mathbf{c}}_i + \sum_{i=1}^{2N} \boldsymbol{\Psi}_i^f \mathbf{g}_i^{(p)}(\xi) + \hat{\mathbf{Q}}_0(\xi). \quad (4.46b)$$

The stiffness matrix is formulated by relating the displacement functions  $\mathbf{u}(\xi)$  and the internal nodal forces  $\hat{\mathbf{Q}}(\xi)$  at the boundary. Substituting  $\xi = 1$  into Eq. (4.46) yields

$$\mathbf{u}(\xi = 1) = \sum_{i=1}^N \boldsymbol{\Psi}_i^u \left( \hat{\mathbf{c}}_i + \mathbf{g}_i^{(p)}(\xi = 1) \right) + \sum_{i=N+1}^{2N} \boldsymbol{\Psi}_i^u \mathbf{g}_i^{(p)}(\xi = 1), \quad (4.47a)$$

$$\hat{\mathbf{Q}}(\xi = 1) = \sum_{i=1}^N \boldsymbol{\Psi}_i^f \left( \hat{\mathbf{c}}_i + \mathbf{g}_i^{(p)}(\xi = 1) \right) + \sum_{i=N+1}^{2N} \boldsymbol{\Psi}_i^f \mathbf{g}_i^{(p)}(\xi = 1) + \hat{\mathbf{Q}}_0(\xi = 1). \quad (4.47b)$$

Eliminating the integration constants  $\hat{\mathbf{c}}_i$  from above equations results in

$$\hat{\mathbf{Q}}(\xi = 1) = \hat{\mathbf{K}}\mathbf{u}(\xi = 1) - \mathbf{R}^F, \quad (4.48)$$

where the stiffness matrix  $\hat{\mathbf{K}}$  is given as

$$\hat{\mathbf{K}} = \Psi_n^f (\Psi_n^u)^{-1}, \quad (4.49)$$

and the nodal load vector  $\mathbf{R}^F$  is written as

$$\mathbf{R}^F = -\hat{\mathbf{Q}}_0(\xi = 1) - (\Psi_p^f - \hat{\mathbf{K}}\Psi_p^u) \mathbf{g}_p^{(p)}(\xi = 1). \quad (4.50)$$

Here,  $\mathbf{g}_p^{(p)}(\xi = 1)$  denotes the particular solution of generalized coordinate functions corresponding to the blocks of positive real eigenvalues.

Next, the formulation of the stress field is considered. After calculating the solution of the displacement at the boundary, the integration constants  $\hat{\mathbf{c}}_i$  are obtained using Eq. (4.47a). The derivative of displacement field with respect to radial coordinate  $\xi$  is formulated analytically using Eqs. (4.46a) and (4.23) as follows

$$\mathbf{u}(\xi),_{\xi} = - \sum_{i=1}^N \Psi_i^u \mathbf{S}_i \xi^{-\mathbf{S}_i - \mathbf{I}} \hat{\mathbf{c}}_i + \sum_{i=1}^{2N} \Psi_i^u \xi^{-1} \left( -\mathbf{S}_i \mathbf{g}_i^{(p)}(\xi) - \mathbf{f}_i^{(g)}(\xi) \right). \quad (4.51)$$

Note that the contribution of only a particular solution in Eq. (4.23) is considered. Substituting Eqs. (4.51) and (4.46a) into Eq. (4.4) yields the expression of stress at any local coordinate  $\xi$  and  $\eta$  within one subdomain  $S^e$

$$\boldsymbol{\sigma}(\xi, \eta) = \sum_{i=1}^N \Psi_{\sigma i}(\eta) \xi^{-\mathbf{S}_i - \mathbf{I}} \hat{\mathbf{c}}_i + \sum_{i=1}^{2N} \xi^{-1} \left( \Psi_{\sigma i}(\eta) \mathbf{g}_i^{(p)}(\xi) - \mathbf{D}\mathbf{B}_1(\eta) \Psi_i^u \mathbf{f}_i^{(g)}(\xi) \right) + \boldsymbol{\sigma}_0(\xi, \eta), \quad (4.52)$$

where  $\Psi_{\sigma i}(\eta)$  are the stress modes. Their definition is given in Eq. (3.121b).

The uni-directional coupling of temperature and displacement fields is evaluated by a *sequential* scheme [154]. First, the SBFEM solution of the temperature field is obtained using Eq. (3.77), and then the thermal load vector corresponding to temperature change is constructed using Eq. (4.50). After formulating the stiffness matrix and the nodal load vector, the displacement solution is calculated similarly to the finite element method.

## 4.3 Supplementary Shape Functions

The previous section discusses the formulation of a thermal load vector resulting from the known temperature distribution. Such formulation is sufficient to model the uni-directional coupling of temperature and displacement fields. However, it cannot solve for both temperature and displacement fields simultaneously which is necessary to obtain full coupling. This section presents the brief formulation of the scaled boundary supplementary shape functions to enrich the interpolation functions of displacement derived in Section 3.3.2. These shape functions are derived from the particular solution of generalized coordinate functions in Eq. (4.29). Furthermore, a prior temperature solution is not required to construct the supplementary shape functions. The detailed derivation of the supplementary shape function is given in [153].

In the first step, the thermal stress caused by a temperature change is evaluated by substituting Eq. (3.78) into Eqs. (4.3) and (4.2) as

$$\boldsymbol{\sigma}_0(\xi, \eta) = \mathbf{D}\beta \bar{\mathbf{N}}(\eta) \left( \Phi_n^{\theta} \right)^{(e)} \xi^{-\lambda_n} \bar{\mathbf{c}}. \quad (4.53)$$

Substituting the expression of thermal stress in Eq. (4.53) into Eq. (4.11c) yields

$$\mathbf{f}_p(\xi) = \hat{\mathbf{p}}_0 \xi^{-\lambda_n} \bar{\mathbf{c}}, \quad (4.54)$$

where

$$\hat{\mathbf{p}}_0 = \int_{-1}^{+1} \left( -\mathbf{B}_1^T(\eta) \mathbf{D} \beta \bar{\mathbf{N}}(\eta) \left( \Phi_n^\theta \right)^{(e)} (-\lambda_n + \mathbf{I}) + \mathbf{B}_2^T(\eta) \mathbf{D} \beta \bar{\mathbf{N}}(\eta) \left( \Phi_n^\theta \right)^{(e)} \right) |\mathbf{J}(\eta)| d\eta. \quad (4.55)$$

For vanishing body forces and side-face traction, the non-homogeneous term  $\mathbf{F}(\xi)$  in Eq. (4.10) becomes

$$\mathbf{F}(\xi) = \xi \mathbf{f}_p(\xi). \quad (4.56)$$

Applying the transformation given in Eq. (4.24) to Eq. (4.56) results in

$$\mathbf{f}_i^{(g)}(\xi) = \mathbf{G}_i \xi^{-\lambda_n + \mathbf{I}} \bar{\mathbf{c}}, \quad (4.57)$$

where  $\mathbf{G}_i$  is expressed as

$$\mathbf{G}_i = -\mathbf{H}_i^{-T} (\Psi_i^u)^T \hat{\mathbf{p}}_0. \quad (4.58)$$

The contribution of the particular solution for the blocks of eigenvalues  $\text{Re}(\mathbf{S}_i) \neq \mathbf{0}$  is evaluated by substituting Eq. (4.57) into Eq. (4.32) and integrating the resulting equation analytically

$$\mathbf{g}_i^{(p)}(\xi) = - \sum_{j=1}^{\bar{N}} \left( \frac{1}{\mathbf{S}_i + (-\lambda_j + 1) \mathbf{I}} \right) \mathbf{G}_i^j \xi^{-\lambda_j + 1} \bar{c}_j \quad \text{when } \text{Re}(\mathbf{S}_i) \neq \mathbf{0}. \quad (4.59)$$

Note that the  $j$  index of quantity  $\mathbf{G}_i$  is written in superscript for clarity. Analogous to the block of eigenvalues  $\text{Re}(\mathbf{S}_i) \neq \mathbf{0}$ , the particular solution for the block of zero eigenvalues, i.e.  $\mathbf{S}_N = \mathbf{S}_{N+1} = \mathbf{0}$  is obtained by substituting Eq. (4.57) into Eq. (4.35) as follows

$$\mathbf{g}_N^{(p)}(\xi) = \sum_{j=1}^{\bar{N}} \left( - \left( \frac{1}{-\lambda_j + 1} \right) \mathbf{G}_N^j + \left( \frac{1}{-\lambda_j + 1} \right)^2 \mathbf{G}_{N+1}^j \right) \xi^{-\lambda_j + 1} \bar{c}_j, \quad (4.60a)$$

$$\mathbf{g}_{N+1}^{(p)}(\xi) = \sum_{j=1}^{\bar{N}} -\mathbf{G}_{N+1}^j \left( \frac{1}{-\lambda_j + 1} \right) \xi^{-\lambda_j + 1} \bar{c}_j. \quad (4.60b)$$

Considering Eqs. (4.59) and (4.60), it is observed that the contribution of each block  $\mathbf{S}_i$  can be written in a matrix form irrespective of their eigenvalues. To assimilate the particular solution in matrix form, introducing  $\bar{\boldsymbol{\lambda}}$  as

$$\bar{\boldsymbol{\lambda}} = \text{diag}(-\lambda_1 + 1, -\lambda_2 + 1, \dots, -\lambda_{\bar{N}} + 1) \quad \text{for } j = 1, 2 \dots \bar{N}, \quad (4.61)$$

and  $\mathbf{A}$  as

$$\mathbf{A} = [\mathbf{A}_1 \ \mathbf{A}_2 \ \dots \ \mathbf{A}_{\bar{N}}] \quad \text{for } j = 1, 2 \dots \bar{N}, \quad (4.62)$$

where

$$\mathbf{A}_j = - \left( \frac{1}{\mathbf{S}_i + (-\lambda_j + 1) \mathbf{I}} \right) \mathbf{G}_i^j. \quad (4.63)$$

Now, the particular solution in Eqs. (4.59) and (4.60) is written in form of  $\bar{\boldsymbol{\lambda}}$  and  $\mathbf{A}$  as

$$\mathbf{g}^{(p)}(\xi) = \mathbf{A} \xi^{\bar{\boldsymbol{\lambda}}} \bar{\mathbf{c}}. \quad (4.64)$$

Analyzing the structure of the complete solution of the generalized coordinate functions in Eq. (4.29) reveals

$$\mathbf{g}(\xi) = \xi^{-\mathbf{S}_n} \hat{\mathbf{c}}_n + \mathbf{A} \xi^{\bar{\boldsymbol{\lambda}}} \bar{\mathbf{c}}. \quad (4.65)$$

Substituting Eq. (4.65) into Eq. (4.20a) yields the expression for the displacement functions as follows

$$\mathbf{u}(\xi) = \Psi_n^u \xi^{-\mathbf{S}_n} \hat{\mathbf{c}}_n + \Psi^u \mathbf{A} \xi^{\bar{\lambda}} \bar{\mathbf{c}}, \quad (4.66)$$

where the integration constants  $\hat{\mathbf{c}}_n$  correspond to the block of  $\mathbf{S}_i$  with negative real part of eigenvalues as well as  $\mathbf{S}_N$  block. The integration constants are determined from the solution at the boundary at  $\xi = 1$  as

$$\hat{\mathbf{c}}_n = (\Psi_n^u)^{-1} (\mathbf{u}_b - \Psi^u \mathbf{A} \bar{\mathbf{c}}), \quad (4.67)$$

where  $\mathbf{u}_b = \mathbf{u}(\xi = 1)$ . Substituting the definition of integration constants Eq. (4.67) into the expression of displacement functions Eq. (4.66) results in

$$\mathbf{u}(\xi) = \Upsilon \xi^\Lambda \Pi \hat{\mathbf{u}}_b, \quad (4.68)$$

where

$$\Upsilon = [\Psi_n^u \quad \Psi^u \mathbf{A}], \quad (4.69a)$$

$$\Lambda = \begin{bmatrix} -\mathbf{S}_n & \\ & \bar{\lambda} \end{bmatrix}, \quad (4.69b)$$

$$\Pi = \begin{bmatrix} (\Psi_n^u)^{-1} & -(\Psi_n^u)^{-1} \Psi^u \mathbf{A} \\ & \mathbf{I} \end{bmatrix}, \quad (4.69c)$$

$$\hat{\mathbf{u}}_b = [\mathbf{u}_b \quad \bar{\mathbf{c}}]^T. \quad (4.69d)$$

Note that the  $\hat{\mathbf{u}}_b$  in Eq. (4.69d) consists of the displacement solution at boundary  $\mathbf{u}_b$  as well as the thermal integration constants. The size of  $\hat{\mathbf{u}}_b$  is  $N + \bar{N}$ , where  $N$  are the degrees of freedom of nodal displacements, and  $\bar{N}$  is the number of nodes in scaled boundary finite element.

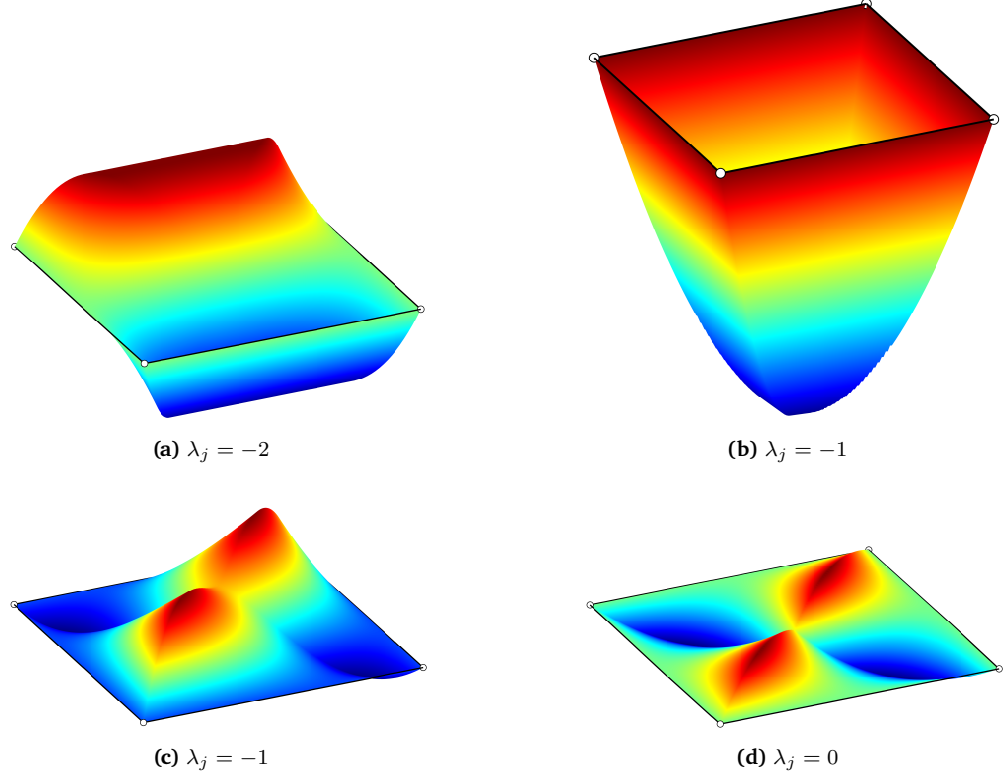


**Figure 4.1:** Supplementary shape functions  $\hat{\chi}^{(p)}(\xi, \eta)$  of quadrilateral element corresponding to (a)  $\lambda_j = -2$ , (b)  $\lambda_j = -1$ , (c)  $\lambda_j = -1$ , and (d)  $\lambda_j = 0$ .

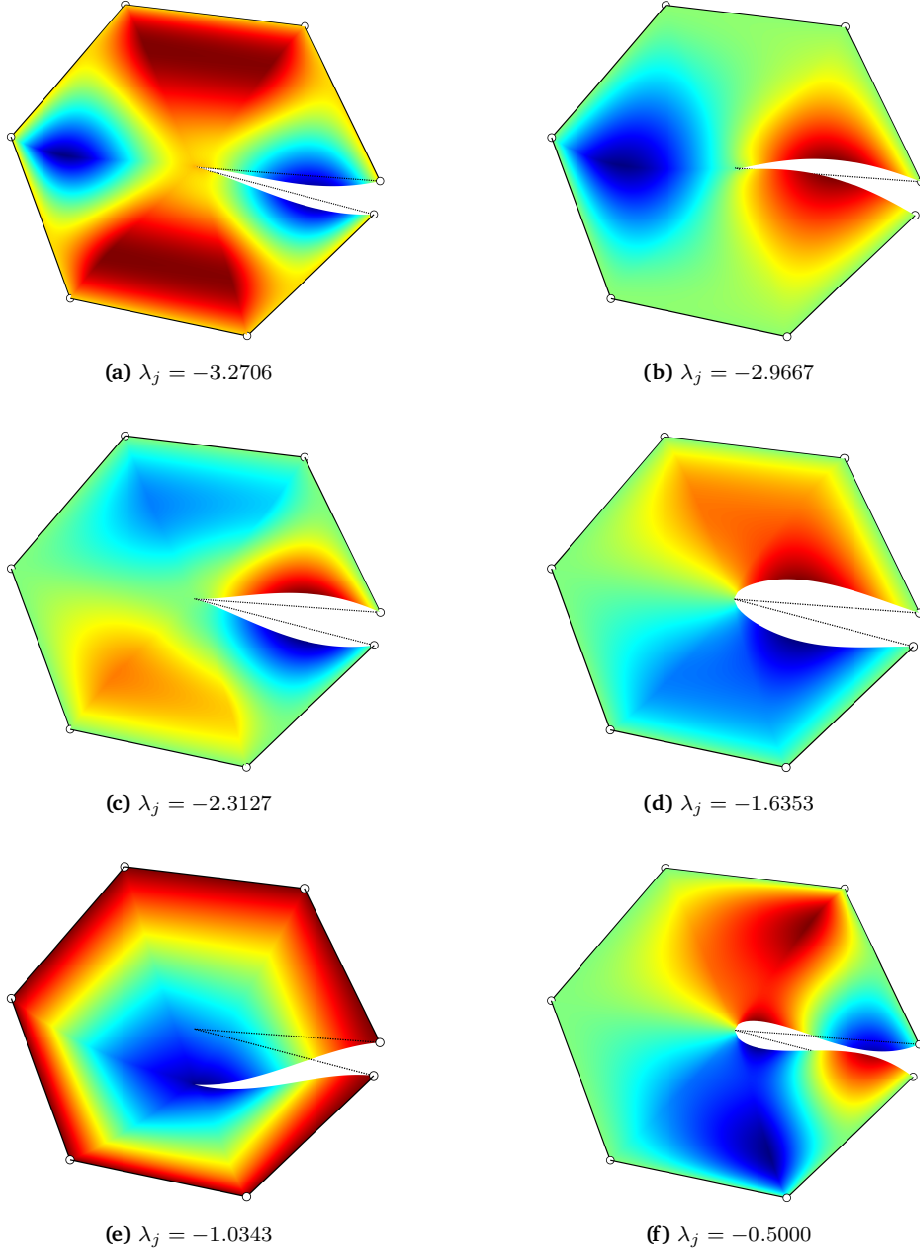


**Figure 4.2:** Supplementary shape functions  $\hat{\chi}^{(p)}(\xi, \eta)$  of seven-node open-element corresponding to (a)  $\lambda_j = -3.2706$ , (b)  $\lambda_j = -2.9667$ , (c)  $\lambda_j = -2.3127$ , (d)  $\lambda_j = -1.6353$ , (e)  $\lambda_j = -1.0343$ , and (f)  $\lambda_j = -0.5000$ .

Now, the expression for the displacement interpolation at local coordinates  $\xi$  and  $\eta$  is obtained by substituting Eq. (4.68) into Eq. (3.88)

$$\mathbf{u}(\xi, \eta) = \hat{\chi}(\xi, \eta) \hat{\mathbf{u}}_b, \quad (4.70)$$

where  $\hat{\chi}$  is

$$\hat{\chi}(\xi, \eta) = \mathbf{N}(\eta) (\boldsymbol{\Upsilon})^{(e)} \xi^{\boldsymbol{\Lambda}} \boldsymbol{\Pi}. \quad (4.71)$$

The shape functions in Eq. (4.71) consists of the homogeneous and supplementary shape functions, such that

$$\hat{\chi}(\xi, \eta) = \begin{bmatrix} \hat{\chi}^{(h)}(\xi, \eta) & \hat{\chi}^{(p)}(\xi, \eta) \end{bmatrix}. \quad (4.72)$$

Here,  $\hat{\chi}^{(h)}(\xi, \eta)$  is related to the homogeneous solution of SBFE equation in displacement, and  $\hat{\chi}^{(p)}(\xi, \eta)$  are the supplementary shape functions derived from the particular solution. They are

given as

$$\hat{\chi}^{(h)}(\xi, \eta) = \chi(\xi, \eta) = \mathbf{N}(\eta) (\Psi_n^u)^{(e)} \xi^{-\mathbf{S}_n} (\Psi_n^u)^{-1}, \quad (4.73a)$$

$$\hat{\chi}^{(p)}(\xi, \eta) = \mathbf{N}(\eta) \left( (\Psi^u)^{(e)} \mathbf{A} \xi^{\bar{\lambda}} - (\Psi_n^u)^{(e)} \xi^{-\mathbf{S}_n} (\Psi_n^u)^{-1} (\Psi^u)^{(e)} \mathbf{A} \right). \quad (4.73b)$$

In Eq. (4.73b), the supplementary shape functions  $\hat{\chi}^{(p)}(\xi, \eta)$  mainly depend on the eigenvalues  $\lambda_n$  of the thermal system (see Eq. (4.61)). The variation of state variables is of form  $\xi^{\lambda_j+1}$ . The number of supplementary shape functions is the same as the number of nodes in a scaled boundary element. Figure 4.1 shows plots of the supplementary shape functions of a closed quadrilateral meshed with linear (two-node) line elements corresponding to the different values of  $\lambda_j$ . A symmetric closed quadrilateral element has two same eigenvalues,  $\lambda_j = -1$ , with different mode shapes. Consequently, the supplementary shape functions corresponding to these eigenvalues are also different, as shown in Figs. 4.1(b) and 4.1(c). Similarly, Fig. 4.2 depicts the supplementary shape functions of an open polygon element for selective values of  $\lambda_j$ .

## 4.4 Discretization of Coupled Thermoelastic Equations

This section covers the discretization of governing equations for fully coupled thermoelasticity using scaled boundary shape functions. The governing equations of coupled thermoelasticity Eqs. (2.77a) and (2.77b) are completed by introducing boundary conditions analogous to Sections 3.2 and 3.3. In a two-dimensional domain  $\Omega$  with surface  $\Gamma$ , the weak form of the governing equations Eqs. (2.77a) and (2.77b) is formulated as [153]

$$\begin{aligned} & \int_{\Omega} \delta\theta \frac{\rho c}{\theta_0} \dot{\theta} d\Omega + \int_{\Omega} \nabla^T \delta\theta \frac{\kappa}{\theta_0} \nabla\theta d\Omega + \int_{\Omega} \delta\theta \mathbf{D}\beta \nabla_u \dot{\mathbf{u}} d\Omega \\ &= \int_{\Omega} \delta\theta \frac{H}{\theta_0} d\Omega + \int_{\Gamma'_2} \delta\theta \frac{\bar{q}}{\theta_0} d\Gamma, \end{aligned} \quad (4.74a)$$

$$\begin{aligned} & \int_{\Omega} \delta\mathbf{u}^T \rho \ddot{\mathbf{u}} d\Omega + \int_{\Omega} (\nabla_u \delta\mathbf{u})^T \mathbf{D} \nabla_u \mathbf{u} d\Omega - \int_{\Omega} (\nabla_u \delta\mathbf{u})^T \mathbf{D} \beta \theta d\Omega \\ &= \int_{\Omega} \delta\mathbf{u}^T \mathbf{p} d\Omega + \int_{\Gamma_2} \delta\mathbf{u}^T \bar{\tau} d\Gamma, \end{aligned} \quad (4.74b)$$

where  $\delta\theta$  and  $\delta\mathbf{u}$  are the weighting functions of temperature and displacement fields, respectively. The scaled boundary shape functions given in Eq. (3.77) interpolate the temperature field. The displacement field's interpolation is obtained using homogeneous and supplementary functions given in Eq. (4.70). The weighting functions  $\delta\theta$  and  $\delta\mathbf{u}$  in Eqs. (4.74a) and (4.74b) are also interpolated analogous to  $\theta(\xi, \eta)$  and  $\mathbf{u}(\xi, \eta)$  as

$$\delta\theta(\xi, \eta) = \bar{\chi}(\xi, \eta) \delta\theta_b, \quad (4.75a)$$

$$\delta\mathbf{u}(\xi, \eta) = \hat{\chi}(\xi, \eta) \delta\hat{\mathbf{u}}_b. \quad (4.75b)$$

Using the expressions of  $\nabla$  and  $\nabla_u$  given in Eqs. (3.11) and (3.86), the derivatives of temperature and displacement fields and their corresponding weighting functions are expressed in the form of their nodal values as

$$\nabla\theta = \bar{\mathbf{B}}(\xi, \eta) \theta_b, \quad (4.76a)$$

$$\nabla\delta\theta = \bar{\mathbf{B}}(\xi, \eta) \delta\theta_b, \quad (4.76b)$$

$$\nabla_u \mathbf{u} = \mathbf{B}(\xi, \eta) \hat{\mathbf{u}}_b, \quad (4.76c)$$

$$\nabla_u \delta\mathbf{u} = \mathbf{B}(\xi, \eta) \delta\hat{\mathbf{u}}_b, \quad (4.76d)$$

where

$$\bar{\mathbf{B}}(\xi, \eta) = \Phi_q(\eta) \xi^{-\lambda_n - \mathbf{I}} \left( \Phi_n^\theta \right)^{-1}, \quad (4.77a)$$

$$\mathbf{B}(\xi, \eta) = \Upsilon_\epsilon(\eta) \xi^{\Lambda - \mathbf{I}} \Pi. \quad (4.77b)$$

Here,  $\Phi_q(\eta)$  and  $\Upsilon_\epsilon(\eta)$  are the flux and stain modes. They are expressed as

$$\Phi_q(\eta) = -\bar{\mathbf{B}}_1(\eta) \left( \Phi_n^\theta \right)^{(e)} \boldsymbol{\lambda}_n + \bar{\mathbf{B}}_2(\eta) \left( \Phi_n^\theta \right)^{(e)}, \quad (4.78a)$$

$$\Upsilon_\epsilon(\eta) = \mathbf{B}_1(\eta) (\Upsilon)^{(e)} \boldsymbol{\Lambda} + \mathbf{B}_2(\eta) (\Upsilon)^{(e)}. \quad (4.78b)$$

Substituting Eq. (4.76) into Eq. (4.74) and using Eq. (4.77) result in

$$\begin{aligned} \delta \boldsymbol{\theta}_b^T & \left( \int_{\Omega} \bar{\mathbf{x}}^T \frac{\rho c}{\theta_0} \bar{\mathbf{x}} d\Omega \dot{\boldsymbol{\theta}}_b + \int_{\Omega} \bar{\mathbf{B}}^T \frac{\kappa}{\theta_0} \mathbf{B} d\Omega \boldsymbol{\theta}_b + \int_{\Omega} \bar{\mathbf{x}}^T \mathbf{D} \boldsymbol{\beta} \mathbf{B} d\Omega \dot{\mathbf{u}}_b \right) \\ &= \delta \boldsymbol{\theta}_b^T \left( \int_{\Omega} \bar{\mathbf{x}}^T \frac{H}{\theta_0} d\Omega + \int_{\Gamma'_2} \bar{\mathbf{x}}^T \frac{\bar{q}}{\theta_0} d\Gamma \right), \end{aligned} \quad (4.79a)$$

$$\begin{aligned} \delta \dot{\mathbf{u}}_b^T & \left( \int_{\Omega} \hat{\mathbf{x}}^T \rho \hat{\mathbf{x}} d\Omega \ddot{\mathbf{u}}_b + \int_{\Omega} \mathbf{B}^T \mathbf{D} \mathbf{B} d\Omega \dot{\mathbf{u}}_b - \int_{\Omega} \mathbf{B}^T \mathbf{D} \boldsymbol{\beta} \bar{\mathbf{x}} d\Omega \boldsymbol{\theta}_b \right) \\ &= \delta \dot{\mathbf{u}}_b^T \left( \int_{\Omega} \hat{\mathbf{x}}^T \mathbf{p} d\Omega + \int_{\Gamma_2} \hat{\mathbf{x}}^T \bar{\boldsymbol{\tau}} d\Gamma \right). \end{aligned} \quad (4.79b)$$

The function arguments  $\xi$  and  $\eta$  are omitted. For an arbitrary  $\delta \boldsymbol{\theta}_b$  and  $\delta \dot{\mathbf{u}}_b$ , Eq. (4.79) is reduced to

$$\begin{aligned} \int_{\Omega} \bar{\mathbf{x}}^T \frac{\rho c}{\theta_0} \bar{\mathbf{x}} d\Omega \dot{\boldsymbol{\theta}}_b + \int_{\Omega} \bar{\mathbf{B}}^T \frac{\kappa}{\theta_0} \mathbf{B} d\Omega \boldsymbol{\theta}_b + \int_{\Omega} \bar{\mathbf{x}}^T \mathbf{D} \boldsymbol{\beta} \mathbf{B} d\Omega \dot{\mathbf{u}}_b \\ = \int_{\Omega} \bar{\mathbf{x}}^T \frac{H}{\theta_0} d\Omega + \int_{\Gamma'_2} \bar{\mathbf{x}}^T \frac{\bar{q}}{\theta_0} d\Gamma, \end{aligned} \quad (4.80a)$$

$$\begin{aligned} \int_{\Omega} \hat{\mathbf{x}}^T \rho \hat{\mathbf{x}} d\Omega \ddot{\mathbf{u}}_b + \int_{\Omega} \mathbf{B}^T \mathbf{D} \mathbf{B} d\Omega \dot{\mathbf{u}}_b - \int_{\Omega} \mathbf{B}^T \mathbf{D} \boldsymbol{\beta} \bar{\mathbf{x}} d\Omega \boldsymbol{\theta}_b \\ = \int_{\Omega} \hat{\mathbf{x}}^T \mathbf{p} d\Omega + \int_{\Gamma_2} \hat{\mathbf{x}}^T \bar{\boldsymbol{\tau}} d\Gamma. \end{aligned} \quad (4.80b)$$

Similar to the mass, damping, and stiffness matrices of FEM, Eq. (4.80) is arranged in a matrix form as

$$\begin{bmatrix} \mathbf{M}_u & \mathbf{0} \\ \mathbf{0} & \mathbf{0} \end{bmatrix} \begin{Bmatrix} \ddot{\mathbf{u}}_b \\ \ddot{\boldsymbol{\theta}}_b \end{Bmatrix} + \begin{bmatrix} \mathbf{0} & \mathbf{0} \\ \mathbf{K}_c^T & \mathbf{C}_\theta \end{bmatrix} \begin{Bmatrix} \dot{\mathbf{u}}_b \\ \dot{\boldsymbol{\theta}}_b \end{Bmatrix} + \begin{bmatrix} \mathbf{K}_u & -\mathbf{K}_c \\ \mathbf{0} & \mathbf{K}_\theta \end{bmatrix} \begin{Bmatrix} \mathbf{u}_b \\ \boldsymbol{\theta}_b \end{Bmatrix} = \begin{Bmatrix} \mathbf{F}_u \\ \mathbf{F}_\theta \end{Bmatrix}, \quad (4.81)$$

where the definitions of coefficient matrices are given as

$$\mathbf{M}_u = \int_{\Omega} \hat{\mathbf{x}}^T \rho \hat{\mathbf{x}} d\Omega, \quad (4.82a)$$

$$\mathbf{C}_\theta = \int_{\Omega} \bar{\mathbf{x}}^T \frac{\rho c}{\theta_0} \bar{\mathbf{x}} d\Omega, \quad (4.82b)$$

$$\mathbf{K}_u = \int_{\Omega} \mathbf{B}^T \mathbf{D} \mathbf{B} d\Omega, \quad (4.82c)$$

$$\mathbf{K}_\theta = \int_{\Omega} \bar{\mathbf{B}}^T \frac{\kappa}{\theta_0} \bar{\mathbf{B}} d\Omega, \quad (4.82d)$$

$$\mathbf{K}_c = \int_{\Omega} \mathbf{B}^T \mathbf{D} \beta \bar{\boldsymbol{\chi}} d\Omega, \quad (4.82e)$$

$$\mathbf{F}_u = \int_{\Omega} \hat{\boldsymbol{\chi}}^T \mathbf{p} d\Omega + \int_{\Gamma} \hat{\boldsymbol{\chi}}^T \bar{\boldsymbol{\tau}} d\Gamma, \quad (4.82f)$$

$$\mathbf{F}_{\theta} = \int_{\Omega} \bar{\boldsymbol{\chi}}^T \frac{H}{\theta_0} d\Omega + \int_{\Gamma} \bar{\boldsymbol{\chi}}^T \frac{\bar{q}}{\theta_0} d\Gamma. \quad (4.82g)$$

The coefficient matrices  $\mathbf{M}_u$ ,  $\mathbf{C}_{\theta}$ ,  $\mathbf{K}_u$ ,  $\mathbf{K}_{\theta}$ , and  $\mathbf{K}_c$  are the mass, thermal mass, stiffness, thermal stiffness, and coupling matrices, respectively.  $\mathbf{F}_u$  is the external force of the elastic system that holds the contribution of external body forces  $\mathbf{p}$  and the prescribed traction  $\bar{\boldsymbol{\tau}}$ . Similarly,  $\mathbf{F}_{\theta}$  is the external force of the thermal system that depends on the internal heat generation  $H$  and prescribed flux  $\bar{q}$ . In Eq. (4.82), all the coefficient matrices are functions of scaled boundary coordinates. First, the domain integral in Eq. (4.82) is transformed to scaled boundary coordinates using Eq. (3.24). Then using the definitions of scaled boundary shape functions and their derivatives in Eqs. (3.78), (4.71), and (4.76), the coefficient matrices are written as

$$\mathbf{M}_u = \boldsymbol{\Pi}^T \mathbf{X}_{mu} \boldsymbol{\Pi}, \quad (4.83a)$$

$$\mathbf{C}_{\theta} = \left( \boldsymbol{\Phi}_n^{\theta} \right)^{-T} \mathbf{X}_{c\theta} \left( \boldsymbol{\Phi}_n^{\theta} \right)^{-1}, \quad (4.83b)$$

$$\mathbf{K}_u = \boldsymbol{\Pi}^T \mathbf{X}_{ku} \boldsymbol{\Pi}, \quad (4.83c)$$

$$\mathbf{K}_{\theta} = \left( \boldsymbol{\Phi}_n^{\theta} \right)^{-T} \mathbf{X}_{k\theta} \left( \boldsymbol{\Phi}_n^{\theta} \right)^{-1}, \quad (4.83d)$$

$$\mathbf{K}_c = \boldsymbol{\Pi}^T \mathbf{X}_{kc} \left( \boldsymbol{\Phi}_n^{\theta} \right)^{-1}, \quad (4.83e)$$

where the matrices  $\mathbf{X}_{mu}$ ,  $\mathbf{X}_{c\theta}$ ,  $\mathbf{X}_{ku}$ ,  $\mathbf{X}_{k\theta}$ , and  $\mathbf{X}_{kc}$  are given as

$$\mathbf{X}_{mu} = \int_{\xi} \xi^{\boldsymbol{\Lambda}^T + \mathbf{I}} \mathbf{Y}_{mu} \xi^{\boldsymbol{\Lambda}} d\xi, \quad (4.84a)$$

$$\mathbf{X}_{c\theta} = \int_{\xi} \xi^{-\lambda_n^T + \mathbf{I}} \mathbf{Y}_{c\theta} \xi^{-\lambda_n} d\xi, \quad (4.84b)$$

$$\mathbf{X}_{ku} = \int_{\xi} \xi^{\boldsymbol{\Lambda}^T - \mathbf{I}} \mathbf{Y}_{ku} \xi^{\boldsymbol{\Lambda}} d\xi, \quad (4.84c)$$

$$\mathbf{X}_{k\theta} = \int_{\xi} \xi^{-\lambda_n^T - \mathbf{I}} \mathbf{Y}_{k\theta} \xi^{-\lambda_n} d\xi, \quad (4.84d)$$

$$\mathbf{X}_{kc} = \int_{\xi} \xi^{\boldsymbol{\Lambda}^T} \mathbf{Y}_{kc} \xi^{-\lambda_n} d\xi. \quad (4.84e)$$

Here, the matrices  $\mathbf{Y}_{mu}$ ,  $\mathbf{Y}_{c\theta}$ ,  $\mathbf{Y}_{ku}$ ,  $\mathbf{Y}_{k\theta}$ , and  $\mathbf{Y}_{kc}$  are expressed as

$$\mathbf{Y}_{mu} = \int_{\eta} \left( (\boldsymbol{\Upsilon})^{(e)} \right)^T \mathbf{N}^T \rho \mathbf{N} (\boldsymbol{\Upsilon})^{(e)} |\mathbf{J}| d\eta, \quad (4.85a)$$

$$\mathbf{Y}_{c\theta} = \int_{\eta} \left( \left( \boldsymbol{\Phi}_n^{\theta} \right)^{(e)} \right)^T \bar{\mathbf{N}}^T \frac{\rho c}{\theta_0} \bar{\mathbf{N}} \left( \boldsymbol{\Phi}_n^{\theta} \right)^{(e)} |\mathbf{J}| d\eta, \quad (4.85b)$$

$$\mathbf{Y}_{ku} = \int_{\eta} \boldsymbol{\Upsilon}_{\epsilon}^T \mathbf{D} \boldsymbol{\Upsilon}_{\epsilon} |\mathbf{J}| d\eta, \quad (4.85c)$$

$$\mathbf{Y}_{k\theta} = \int_{\eta} \boldsymbol{\Phi}_q^T \frac{\boldsymbol{\kappa}}{\theta_0} \boldsymbol{\Phi}_q |\mathbf{J}| d\eta, \quad (4.85d)$$

$$\mathbf{Y}_{kc} = \int_{\eta} \mathbf{\Upsilon}_\epsilon^T \mathbf{D} \beta \bar{\mathbf{N}} \left( \Phi_n^\theta \right)^{(e)} |\mathbf{J}| d\eta. \quad (4.85e)$$

The matrices  $\mathbf{Y}_{ij}$  depend only on the discretization in the circumferential direction. They are integrated for each line element separately and assembled for the whole scaled boundary finite element. Using the properties of matrix exponents and integration by parts, the integration of matrices  $\mathbf{X}_{ij}$  with respect to  $\xi$  are formulated as [153]

$$\mathbf{X}_{mu} (\Lambda + \mathbf{I}) + (\Lambda + \mathbf{I})^T \mathbf{X}_{mu} = \mathbf{Y}_{mu}, \quad (4.86a)$$

$$\mathbf{X}_{c\theta} (-\lambda_n + \mathbf{I}) + (-\lambda_n + \mathbf{I})^T \mathbf{X}_{c\theta} = \mathbf{Y}_{c\theta}, \quad (4.86b)$$

$$\mathbf{X}_{ku} (\Lambda) + (\Lambda)^T \mathbf{X}_{ku} = \mathbf{Y}_{ku}, \quad (4.86c)$$

$$\mathbf{X}_{k\theta} (-\lambda_n) + (-\lambda_n)^T \mathbf{X}_{k\theta} = \mathbf{Y}_{k\theta}, \quad (4.86d)$$

$$\mathbf{X}_{kc} (-\lambda_n) + (\Lambda + \mathbf{I})^T \mathbf{X}_{kc} = \mathbf{Y}_{kc}, \quad (4.86e)$$

where, Eqs. (4.86a)–(4.86d) are Lyapunov equations and Eq. (4.86e) is a Sylvester equation. Their solutions facilitate the computation of all the coefficient matrices in Eq. (4.84). After obtaining the solution of all  $\mathbf{X}_{ij}$  matrices, the coefficient matrices in Eq. (4.83) are obtained semi-analytically. Next, the integration of load vectors  $\mathbf{F}_u$  and  $\mathbf{F}_\theta$  is considered. For constant values of  $\mathbf{p}$ ,  $\bar{\tau}$ ,  $H$ , and  $\bar{q}$ , the integration of Eqs. (4.82f) and (4.82g) are performed numerically in circumferential direction  $\eta$  and analytically in radial direction  $\xi$ . This results in

$$\mathbf{F}_u = \mathbf{\Pi}^T \left( \Lambda^T + 2\mathbf{I} \right)^{-1} \int_{\eta} \mathbf{\Upsilon}^T \mathbf{N}^T \mathbf{p} |\mathbf{J}| d\eta + \int_{\eta} \mathbf{N}^T \bar{\tau} l^\xi d\eta, \quad (4.87a)$$

$$\mathbf{F}_\theta = \left( \Phi_n^\theta \right)^{-T} \left( -\lambda_n^T + 2\mathbf{I} \right)^{-1} \left( \Phi_n^\theta \right)^T \int_{\eta} \bar{\mathbf{N}}^T \frac{H}{\theta_0} |\mathbf{J}| d\eta + \int_{\eta} \bar{\mathbf{N}}^T \frac{\bar{q}}{\theta_0} l^\xi d\eta. \quad (4.87b)$$

For varying  $\mathbf{p}$ ,  $\bar{\tau}$ ,  $H$ , and  $\bar{q}$ , they are first expressed in scaled boundary coordinates  $\xi$  and  $\eta$  before the semi-analytical integration.

Now, the evaluation of stress using homogeneous and supplementary shape functions is addressed. After calculating the solution at the boundary, the derivative of the displacement field is obtained from the Eqs. (4.70) and (4.71) as follows

$$\mathbf{u}(\xi, \eta),_\xi = \mathbf{N}(\eta) (\mathbf{\Upsilon})^{(e)} \Lambda \xi^{\Lambda - \mathbf{I}} \mathbf{\Pi} \hat{\mathbf{u}}_b. \quad (4.88)$$

Substituting Eqs. (4.88), (4.70), and (4.71) into Eq. (4.4) results in the interpolation of stress field at a given local coordinates  $\xi$  and  $\eta$  as

$$\boldsymbol{\sigma}(\xi, \eta) = \mathbf{D} (\mathbf{\Upsilon}_\epsilon(\eta))^{(e)} \xi^{\Lambda - \mathbf{I}} \mathbf{\Pi} \hat{\mathbf{u}}_b + \boldsymbol{\sigma}_0(\xi, \eta), \quad (4.89)$$

where  $(\mathbf{\Upsilon}_\epsilon(\eta))^{(e)}$  are the strain modes expressed in Eq. (4.78b). The initial thermal stress  $\boldsymbol{\sigma}_0(\xi, \eta)$  is evaluated by substituting the scaled boundary solution of temperature field Eqs. (3.77) and (3.78) into Eqs. (4.3) and (4.2)

$$\boldsymbol{\sigma}(\xi, \eta) = (\mathbf{\Upsilon}_\sigma(\eta))^{(e)} \xi^{\Lambda - \mathbf{I}} \mathbf{\Pi} \hat{\mathbf{u}}_b - \mathbf{D} \beta \bar{\mathbf{N}}(\eta) \left( \Phi_n^\theta \right)^{(e)} \xi^{-\lambda_n} \left( \Phi_n^\theta \right)^{-1} \theta_b, \quad (4.90)$$

where  $(\mathbf{\Upsilon}_\sigma)^{(e)}$  are the stress modes, i.e.,  $(\mathbf{\Upsilon}_\sigma)^{(e)} = \mathbf{D} (\mathbf{\Upsilon}_\epsilon)^{(e)}$ . Note that the superscript  $(e)$  indicates the degrees of freedom corresponding to one subdomain  $S^e$ .

# Chapter 5

## Modeling of Functionally Graded Materials in SBFEM

This chapter deals with the modeling of functionally graded materials (FGMs) in the scaled boundary finite element method. First, a brief overview of FGMs is discussed in Section 5.1. Section 5.2 reiterates the transformation of spatially varying material properties from Cartesian coordinates to scaled boundary coordinates presented in [124]. The semi-analytical integration of coefficient matrices in Eq. (4.83) is already published in [155]. Here, it is repeated for completeness.

### 5.1 Fundamentals of FGMs

In this section, a general overview of functionally graded materials is presented. FGMs provide structural integrity and heat-resistant behavior by reducing thermal stress in extreme temperatures. They are state-of-the-art composite materials of two or more constituents, usually ceramics and metals. The ceramics constituent provides heat resistance, while the metals provide ductility and strength. Although the FGMs are non-homogeneous, their constituents have spatially varying volume fraction that changes physical properties continuously. Any function of Cartesian coordinates, such as the hyperbolic tangent function, exponential function, or power-law function, can define the spatially varying volume fractions. For example,

$$P(x, y) = P^m e^{(x/W)}, \quad (5.1a)$$

$$P(x, y) = P^c + (P^m - P^c) \left( \frac{y}{L} \right)^\gamma. \quad (5.1b)$$

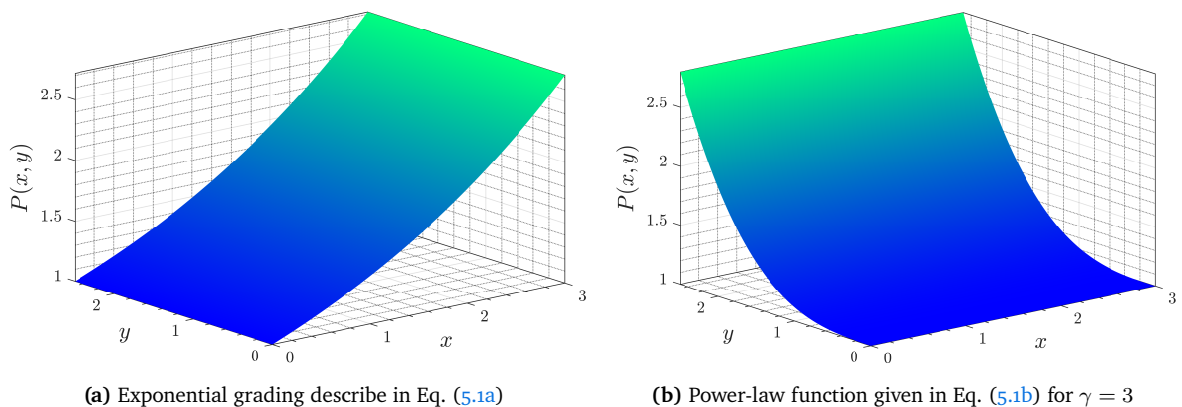


**Figure 5.1:** A few examples of FGMs in Cartesian coordinates. (a) Variation of material property given by an exponential function in Eq. (5.1a). (b) Material constituents of ceramic and metal describe by a power-law function in Eq. (5.1b) with a gradient index  $\gamma = 3$ .

Equations (5.1a) and (5.1b) are the volume fractions defined by an exponential function and power-law, respectively. Here,  $P(x, y)$  is any given material property of the system.  $P^m$  and  $P^c$

indicate the material property of fully metal and fully ceramic volume fractions. In Eq. (5.1b), the symbol  $\gamma$  describes the gradient index of the power-law function.  $W$  and  $L$  are the width and length of the FGM plate.

Figures 5.1(a) and 5.1(b) show variation of a material property  $P(x, y)$  given in Eqs. (5.1a) and (5.1b), respectively. Note that the spatial variation of FGMs can also depend on both  $x$  and  $y$  simultaneously.

## 5.2 Representation of FGMs in Local Coordinates

This section transforms material variation in FGMs from Cartesian coordinates to scaled boundary coordinates by employing the procedure introduced in [124]. For that purpose, any given material variation is represented as a polynomial surface in Cartesian coordinates within each scaled boundary polygon element are as follows

$$P(\hat{x}, \hat{y}) = P_0 + P_1\hat{x} + P_2\hat{y} + P_3\hat{x}^2 + P_4\hat{x}\hat{y} + P_5\hat{y}^2 + \dots, \quad (5.2)$$

where  $(\hat{x}, \hat{y})$  are the Cartesian coordinates measured from the scaling center of the polygon element. The coefficients  $P_k$  in Eq. (5.2) are evaluated using the least-squares fit method over each scaled boundary polygon element. The integration points of a line element within a polygon element are selected to achieve the surface fitting. As suggested in [124], the selection of fitting points on the boundary is adequate to model the material variation in scaled boundary coordinates. Using Eq. (3.1), the Cartesian coordinates  $(\hat{x}, \hat{y})$  are written in the form of the scaled boundary coordinates

$$\hat{x} = \xi x_\eta(\eta), \quad (5.3a)$$

$$\hat{y} = \xi y_\eta(\eta), \quad (5.3b)$$

where,  $x_\eta(\eta) = \bar{\mathbf{N}}(\eta)\mathbf{x}_b$  and  $y_\eta(\eta) = \bar{\mathbf{N}}(\eta)\mathbf{y}_b$ . Substituting Eq. (5.3) into Eq. (5.2) yields

$$\begin{aligned} P(\xi, \eta) &= P_0\xi^0 + (P_1x_\eta(\eta) + P_2y_\eta(\eta))\xi^1 + (P_3x_\eta^2(\eta) + P_4x_\eta(\eta)y_\eta(\eta) + P_5y_\eta^2(\eta))\xi^2 + \dots \\ &= P^{(0)}(\eta)\xi^0 + P^{(1)}(\eta)\xi^1 + P^{(2)}(\eta)\xi^2 + \dots + P^{(n)}(\eta)\xi^n \\ &= \sum_{k=0}^n P^{(k)}(\eta)\xi^k. \end{aligned} \quad (5.4)$$

The symbol  $P^{(k)}$  indicates the fitted polynomial coefficients in scaled boundary coordinates. They are functions of  $\eta$  coordinate only. To accurately perform the fitting of material variation, the size of the scaled boundary polygon element must be small enough to model the grading function. Additionally, the order of polynomial fit, i.e.,  $n$ , should be high enough to capture the steep gradients within the polygon element. In most cases, the order polynomial fit  $n = 2$  is sufficient to represent the material variation in scaled boundary coordinates [124].

The spatial variation of material properties is written in scaled boundary coordinates by using Eq. (5.4) as follows

$$\boldsymbol{\kappa}(\xi, \eta) = \boldsymbol{\kappa}^{(0)}(\eta)\xi^0 + \boldsymbol{\kappa}^{(1)}(\eta)\xi^1 + \boldsymbol{\kappa}^{(2)}(\eta)\xi^2 + \dots, \quad (5.5a)$$

$$\mathbf{D}(\xi, \eta) = \mathbf{D}^{(0)}(\eta)\xi^0 + \mathbf{D}^{(1)}(\eta)\xi^1 + \mathbf{D}^{(2)}(\eta)\xi^2 + \dots, \quad (5.5b)$$

$$\hat{\mathbf{D}}(\xi, \eta) = \hat{\mathbf{D}}^{(0)}(\eta)\xi^0 + \hat{\mathbf{D}}^{(1)}(\eta)\xi^1 + \hat{\mathbf{D}}^{(2)}(\eta)\xi^2 + \dots, \quad (5.5c)$$

$$\rho(\xi, \eta) = \rho^{(0)}(\eta)\xi^0 + \rho^{(1)}(\eta)\xi^1 + \rho^{(2)}(\eta)\xi^2 + \dots, \quad (5.5d)$$

$$\hat{m}(\xi, \eta) = \hat{m}^{(0)}(\eta)\xi^0 + \hat{m}^{(1)}(\eta)\xi^1 + \hat{m}^{(2)}(\eta)\xi^2 + \dots. \quad (5.5e)$$

Here,  $\hat{\mathbf{D}}$  is a matrix product of the elasticity matrix and thermo-stress module, i.e.,  $\hat{\mathbf{D}} = \mathbf{D}\beta$ . The symbol  $\hat{m}$  denotes a scalar product of density and specific heat such that  $\hat{m} = \rho c$ . Each matrix component is fitted separately for the material properties with matrix representation.

Now, two meshes with different numbers of polygon elements are considered to illustrate the accuracy of polynomial fitting in scaled boundary coordinates. Figures 5.2(a) and 5.2(b) show meshes with 20 and 52 polygon elements, respectively. Moreover, a set of two fitting orders, i.e.,  $n = [1\ 2]$ , are also studied along with different meshes. Figure 5.3 demonstrates the fitting of material variation at the selective nodal coordinates of polygon meshes for different values of  $n$ . Figure 5.3(a) indicates the fitting of the exponential grading function defined in Eq. (5.1a). Figure 5.3(b) depicts the variation of the power-law function given in Eq. (5.1b) for  $\gamma = 3$ .

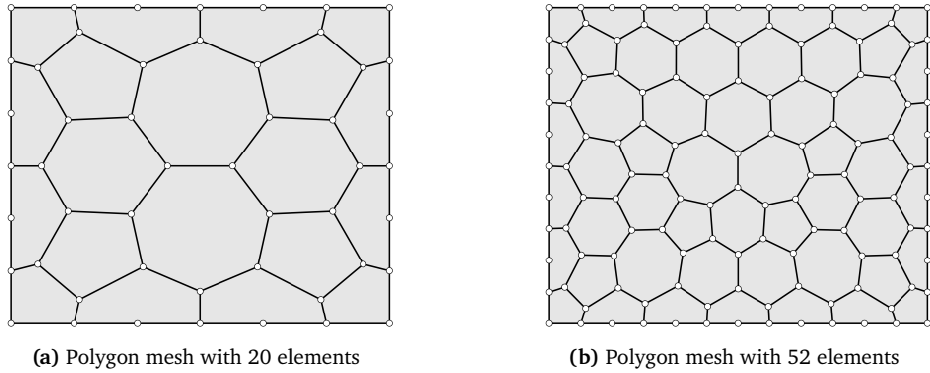


**Figure 5.2:** Polygon meshes considered for the fitting of a material variation in FGMs. (a) Mesh with 20 polygon elements. (b) Mesh with 52 polygon elements.

For the quantitative analysis, error percentages in material fitting are calculated at all the nodal coordinates of meshes shown in Fig. 5.2. Tables 5.1 and 5.2 present the maximum error percentage observed in exponential grading Eq. (5.1a) and power-law function Eq. (5.1b) with  $\gamma = 3$  for varying  $n$  and different meshes. It is observed that the accuracy of polynomial fitting increases with increasing fitting order. Additionally, the fitting of material variation is also influenced by the size of the polygon element, as indicated by Tables 5.1 and 5.2. In most cases, the polynomial fitting order  $n = 2$  is sufficient to accurately model the variation as long as the size of polygon elements is small enough.

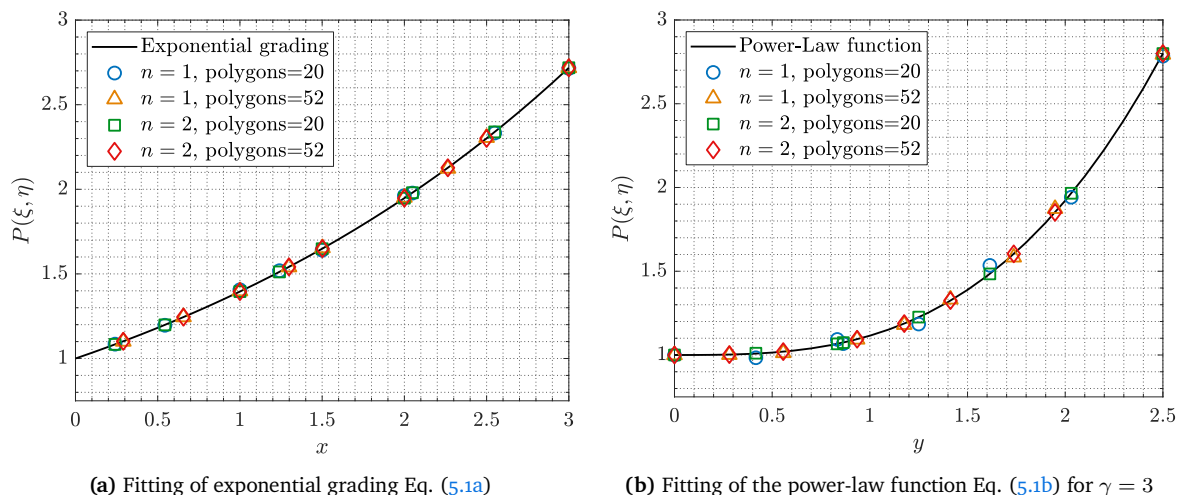


**Figure 5.3:** Fitting of material property  $P(\xi, \eta)$  at selective nodal coordinates for various polynomial orders and meshes. (a) Fitting of exponential material grading defined in Eq. (5.1a). (b) Fitting of material grading described by the power-law function given in Eq. (5.1b) for  $\gamma = 3$ .

| Fitting order $n$ | Polygons | Maximum error in % |
|-------------------|----------|--------------------|
| 1                 | 20       | 0.7417             |
|                   | 52       | 0.2268             |
| 2                 | 20       | 0.0252             |
|                   | 52       | 0.0041             |

**Table 5.1:** Maximum error percentage in the fitting of exponential material variation in Eq. (5.1a).

| Fitting order $n$ | Polygons | Maximum error in % |
|-------------------|----------|--------------------|
| 1                 | 20       | 3.3979             |
|                   | 52       | 1.6934             |
| 2                 | 20       | 0.2315             |
|                   | 52       | 0.0765             |

**Table 5.2:** Maximum error percentage in the fitting of material variation defined by a power-law function in Eq. (5.1b) with  $\gamma = 3$ .

Finally, Fig. 5.4 illustrates the qualitative fitting of spatially varying material property for  $n = 2$  at all the nodal coordinates of mesh shown in Fig. 5.2(b). The surface plots represent the material variation in Cartesian coordinates. The nodes of polygonal mesh indicate the fitted values of material property. Figure 5.4(a) represents the material grading expressed by an exponential function in Eq. (5.1a). Similarly, Fig. 5.4(b) shows the material variation defined by the power-law function given in Eq. (5.1b) for  $\gamma = 3$ .

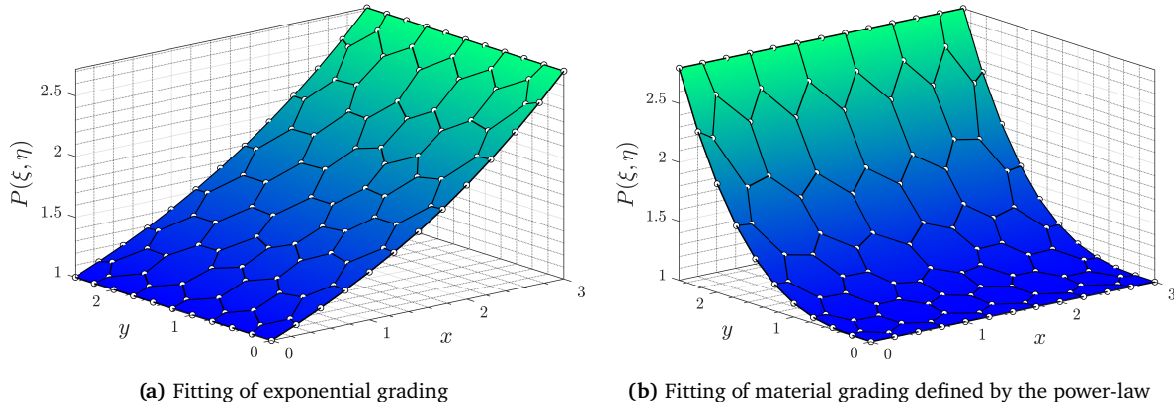


**Figure 5.4:** Fitting of spatially varying material property in scaled boundary coordinates for  $n = 2$  and a mesh with 52 polygons. (a) Fitting of exponential material grading defined in Eq. (5.1a). (b) Fitting of material grading described by the power-law function given in Eq. (5.1b) for  $\gamma = 3$ .

The following section discusses the integration of coefficient matrices of thermoelastic system Eq. (4.81) in scaled boundary coordinates for functionally graded materials.

### 5.3 Integration of Coefficient Matrices

In functionally graded materials, the coefficient matrices  $\mathbf{M}_u$ ,  $\mathbf{C}_\theta$ ,  $\mathbf{K}_u$ ,  $\mathbf{K}_\theta$ , and  $\mathbf{K}_c$  of fully coupled thermoelastic systems in Eq. (4.81) are still integrated semi-analytically. However, the coefficient

matrices  $\bar{\mathbf{E}}_i$  and  $\mathbf{E}_i$  in Eqs. (3.56) and (3.98) are obtained using the constant material parameters, typically at the scaling center. Consequently, the scaled boundary polygon and supplementary shape functions in Eqs. (3.78) and (4.72) are also derived for constant material parameters. The coefficient matrices  $\bar{\mathbf{E}}_i$  and  $\mathbf{E}_i$  mainly depend on the shape of the polygon element. The material properties of thermal conductivity and Young's modulus only scale the values of  $\bar{\mathbf{E}}_i$  and  $\mathbf{E}_i$  in Eqs. (3.52) and (3.99). Thus, the shape functions derived from the constant material parameters are independent of thermal conductivity and Young's modulus. However, they are dependent on Poisson's ratio. Hence, a sufficiently small size of the scaled boundary polygon element is required to model FGMs.

Now, utilizing the expressions of material variation in scaled boundary coordinates in Eq. (5.5), the matrices in Eq. (4.83) are rewritten as

$$\mathbf{M}_u = \mathbf{\Pi}^T \left[ \sum_{k=0}^n \mathbf{X}_{mu}^{(k)}(\xi, \eta) \right] \mathbf{\Pi}, \quad (5.6a)$$

$$\mathbf{C}_\theta = \left( \mathbf{\Phi}_n^\theta \right)^{-T} \left[ \sum_{k=0}^n \mathbf{X}_{c\theta}^{(k)}(\xi, \eta) \right] \left( \mathbf{\Phi}_n^\theta \right)^{-1}, \quad (5.6b)$$

$$\mathbf{K}_u = \mathbf{\Pi}^T \left[ \sum_{k=0}^n \mathbf{X}_{ku}^{(k)}(\xi, \eta) \right] \mathbf{\Pi}, \quad (5.6c)$$

$$\mathbf{K}_\theta = \left( \mathbf{\Phi}_n^\theta \right)^{-T} \left[ \sum_{k=0}^n \mathbf{X}_{k\theta}^{(k)}(\xi, \eta) \right] \left( \mathbf{\Phi}_n^\theta \right)^{-1}, \quad (5.6d)$$

$$\mathbf{K}_c = \mathbf{\Pi}^T \left[ \sum_{k=0}^n \mathbf{X}_{kc}^{(k)}(\xi, \eta) \right] \left( \mathbf{\Phi}_n^\theta \right)^{-1}, \quad (5.6e)$$

where  $\mathbf{M}_u$ ,  $\mathbf{C}_\theta$ ,  $\mathbf{K}_u$ ,  $\mathbf{K}_\theta$ , and  $\mathbf{K}_c$  depend on the spatial variation of  $\rho$ ,  $\hat{m}$ ,  $\mathbf{D}$ ,  $\boldsymbol{\kappa}$ , and  $\hat{\mathbf{D}}$ , respectively. In Eq. (5.6), the matrices  $\mathbf{X}_{ij}^{(k)}$  correspond to each term of fitting represented by  $k$ . They are integrated for each  $k$  individually. The contributions of all terms of  $k$  are summed up using a super-position rule. Similar to Eq. (4.84), the definitions of  $\mathbf{X}_{ij}^{(k)}$  are given as follows

$$\mathbf{X}_{mu}^{(k)}(\xi, \eta) = \int_\xi \xi^{\mathbf{\Lambda}^T + (k+1)\mathbf{I}} \mathbf{Y}_{mu}^{(k)}(\eta) \xi^{\mathbf{\Lambda}} d\xi, \quad (5.7a)$$

$$\mathbf{X}_{c\theta}^{(k)}(\xi, \eta) = \int_\xi \xi^{-\lambda_n^T + (k+1)\mathbf{I}} \mathbf{Y}_{c\theta}^{(k)}(\eta) \xi^{-\lambda_n} d\xi, \quad (5.7b)$$

$$\mathbf{X}_{ku}^{(k)}(\xi, \eta) = \int_\xi \xi^{\mathbf{\Lambda}^T + (k-1)\mathbf{I}} \mathbf{Y}_{ku}^{(k)}(\eta) \xi^{\mathbf{\Lambda}} d\xi, \quad (5.7c)$$

$$\mathbf{X}_{k\theta}^{(k)}(\xi, \eta) = \int_\xi \xi^{-\lambda_n^T + (k-1)\mathbf{I}} \mathbf{Y}_{k\theta}^{(k)}(\eta) \xi^{-\lambda_n} d\xi, \quad (5.7d)$$

$$\mathbf{X}_{kc}^{(k)}(\xi, \eta) = \int_\xi \xi^{\mathbf{\Lambda}^T + k\mathbf{I}} \mathbf{Y}_{kc}^{(k)}(\eta) \xi^{-\lambda_n} d\xi. \quad (5.7e)$$

Here, the matrices  $\mathbf{Y}_{ij}^{(k)}$  are the functions of  $\eta$  coordinate. Consequently, they only depend on the material variation in the circumferential direction. Similar to  $\mathbf{X}_{ij}^{(k)}$ , the matrices  $\mathbf{Y}_{ij}^{(k)}$  are also integrated for each fitted term  $k$  separately. Analogous to Eq. (4.85), the matrices  $\mathbf{Y}_{ij}^{(k)}$  are expressed as

$$\mathbf{Y}_{mu}^{(k)} = \int_{\eta} \left( (\boldsymbol{\Upsilon})^{(e)} \right)^T \mathbf{N}^T \rho^{(k)} \mathbf{N} (\boldsymbol{\Upsilon})^{(e)} |\mathbf{J}| d\eta, \quad (5.8a)$$

$$\mathbf{Y}_{c\theta}^{(k)} = \int_{\eta} \left( (\boldsymbol{\Phi}_n^{\theta})^{(e)} \right)^T \bar{\mathbf{N}}^T \frac{\hat{m}^{(k)}}{\theta_0} \bar{\mathbf{N}} (\boldsymbol{\Phi}_n^{\theta})^{(e)} |\mathbf{J}| d\eta, \quad (5.8b)$$

$$\mathbf{Y}_{ku}^{(k)} = \int_{\eta} \boldsymbol{\Upsilon}_{\epsilon}^T \mathbf{D}^{(k)} \boldsymbol{\Upsilon}_{\epsilon} |\mathbf{J}| d\eta, \quad (5.8c)$$

$$\mathbf{Y}_{k\theta}^{(k)} = \int_{\eta} \boldsymbol{\Phi}_q^T \frac{\boldsymbol{\kappa}^{(k)}}{\theta_0} \boldsymbol{\Phi}_q |\mathbf{J}| d\eta, \quad (5.8d)$$

$$\mathbf{Y}_{kc}^{(k)} = \int_{\eta} \boldsymbol{\Upsilon}_{\epsilon}^T \hat{\mathbf{D}}^{(k)} \bar{\mathbf{N}} (\boldsymbol{\Phi}_n^{\theta})^{(e)} |\mathbf{J}| d\eta. \quad (5.8e)$$

The function argument  $\eta$  is dropped for convenience. Once the matrices  $\mathbf{Y}_{ij}^{(k)}$  are integrated numerically for each term in  $k$ , the matrices  $\mathbf{X}_{ij}^{(k)}$  are integrated analytically using the properties of matrix exponents and integration by parts as

$$\mathbf{X}_{mu}^{(k)} (\Lambda + 0.5k\mathbf{I}) + (\Lambda + 0.5k\mathbf{I})^T \mathbf{X}_{mu}^{(k)} = \mathbf{Y}_{mu}^{(k)}, \quad (5.9a)$$

$$\mathbf{X}_{c\theta}^{(k)} (-\boldsymbol{\lambda}_n + 0.5k\mathbf{I}) + (-\boldsymbol{\lambda}_n + 0.5k\mathbf{I})^T \mathbf{X}_{c\theta}^{(k)} = \mathbf{Y}_{c\theta}^{(k)}, \quad (5.9b)$$

$$\mathbf{X}_{ku}^{(k)} (\Lambda + 0.5k\mathbf{I}) + (\Lambda + 0.5k\mathbf{I})^T \mathbf{X}_{ku}^{(k)} = \mathbf{Y}_{ku}^{(k)}, \quad (5.9c)$$

$$\mathbf{X}_{k\theta}^{(k)} (-\boldsymbol{\lambda}_n + 0.5k\mathbf{I}) + (-\boldsymbol{\lambda}_n + 0.5k\mathbf{I})^T \mathbf{X}_{k\theta}^{(k)} = \mathbf{Y}_{k\theta}^{(k)}, \quad (5.9d)$$

$$\mathbf{X}_{kc}^{(k)} (-\boldsymbol{\lambda}_n) + (\Lambda + k\mathbf{I})^T \mathbf{X}_{kc}^{(k)} = \mathbf{Y}_{kc}^{(k)}. \quad (5.9e)$$

Here, Eqs. (5.9a)–(5.9d) are Lyapunov equations, and Eq. (5.9e) is the Sylvester equation. After evaluating the solution of  $\mathbf{X}_{ij}^{(k)}$  corresponding to each term in  $k$  and summing up all the contributions, the coefficient matrices in Eq. (5.6) are integrated semi-analytically.

# Chapter 6

## Fracture Modeling Using SBFEM

This chapter deals with modeling linear elastic fracture using the scaled boundary finite element method. First, the evaluation fracture parameters, such as stress intensity factors (SIFs), is addressed. A series of power functions of the radial coordinate represents the SBFEM solution space. In the case of stress singularity, one term of the series dominates the stress field. Thus, the SBFEM can capture the stress singularity accurately, alleviating the need for post-processing. The first section presents the capturing of singular stress and related fracture parameters. Next, the formulation of generalized stress intensity factors is presented that are evaluated directly from their definitions in Section 2.5.2. The SIFs are then utilized to predict the crack path when modeling crack propagation problems, as discussed in Section 2.5.3. The second section briefly outlines the procedure for generating the polygon meshes. Next, the localized re-meshing technique for the update of the geometry is presented in Section 6.2.2. The requirement of mesh mapping after the re-meshing step is considered in Section 6.2.3.

### 6.1 Evaluation of Fracture Parameters

This section employs the scaled boundary finite element method to evaluate well-known fracture parameters, i.e., stress intensity factors (SIFs). One of the key advantages of the SBFEM is its ability to capture the stress singularities without the need for additional post-processing, for example, domain integrals.

The SBFEM is feasible in evaluating various stress singularities, such as power-logarithmic or singularities at multi-material corners [116, 118–120, 149]. In the SBFEM, the expression of stress is nothing but the superposition of several mode shapes, i.e., eigenforms. In an open SBFE (see Fig. 3.5), one of these eigenforms has the eigenvalues with real parts  $-I < \text{Re}(S_i) < 0$  in Eq. (3.120b) that dominates the stress field.

The following presents the SBFEM definition and evaluation of singular stress in the vicinity of the crack tip. After capturing the singular stress, the SIFs are calculated directly from their definitions.

#### 6.1.1 Capturing of Singular Stress

This section presents the SBFEM expression of singular stress for the cases of a wedge or a narrow crack. Three physical problems are considered, i.e., purely mechanical, uni-directional coupling, and fully coupled thermoelasticity. Figure 6.1(a) shows a polygon mesh of a domain with a crack. Figure 6.1(b) depicts an open SBFE with overlapping crack tip and scaling center. The crack faces are not discretized and assumed to be traction free.

The definition of stress in the SBFEM for purely mechanical cases is given in Eq. (3.120b). In case of open SBFE, two eigenvalues with real parts  $-I < \text{Re}(S_i) < 0$  dominate the singular stress field as  $\xi \rightarrow 0$ . Denoting these eigenvalues as  $S^{(s)}$  in Eq. (3.120b), the expression for the singular stress in scaled boundary coordinates is written as

$$\sigma^{(s)}(\xi, \eta) = \Psi_{\sigma}^{(s)}(\eta) \xi^{-S^{(s)} - I} c^{(s)}, \quad (6.1)$$

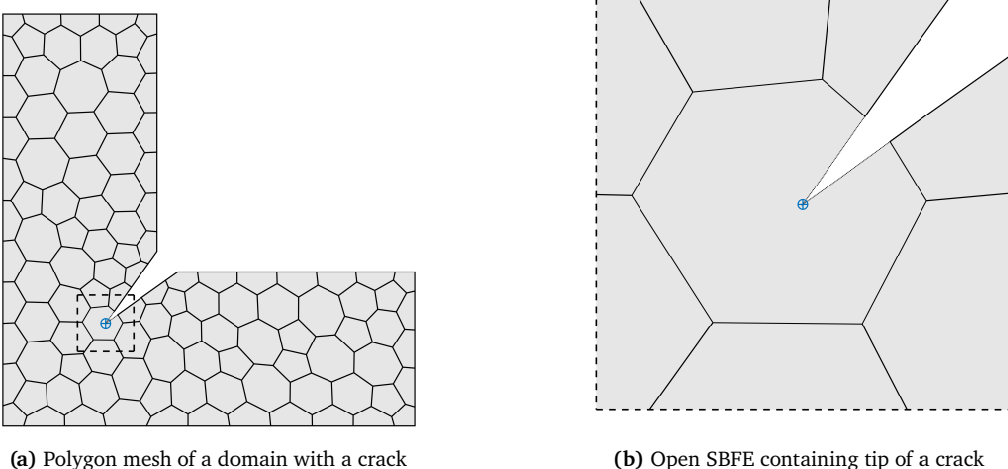


**Figure 6.1:** Polygon mesh of a domain with an open SBFE at a crack tip. (a) Global polygon mesh of a domain with a wedge. (b) Open SBFE containing the tip of a crack with un-discretized crack faces.

where  $\Psi_{\sigma}^{(s)}$  and  $c^{(s)}$  are the stress modes and integration constants corresponding to the singular mode  $S^{(s)}$ .

Next, the SBFEM evalutaion of singular stress in the uni-directional and full coupling is considered. Equations (4.52) and (4.90) present the stress fields in the uni-directional (sequential) and fully coupled schemes, respectively. For completeness, the formulation of stress in the uni-directional case is rewritten

$$\sigma(\xi, \eta) = \sum_{i=1}^N \Psi_{\sigma i}(\eta) \xi^{-S_i - I} \hat{c}_i + \sum_{i=1}^{2N} \xi^{-1} \left( \Psi_{\sigma i}(\eta) g_i^{(p)}(\xi) - D B_1(\eta) \Psi_i^u f_i^{(g)}(\xi) \right) + \sigma_0(\xi, \eta). \quad (6.2)$$

Analysis of Eq. (6.2) reveals that the particular solution  $g_i^{(p)}(\xi)$ , thermal load vector  $f_i^{(g)}(\xi)$ , and the initial thermal stress  $\sigma_0(\xi, \eta)$  do not contribute to the stress singularity. The particular solutions  $g_i^{(p)}(\xi)$  in Eqs. (4.44) and (4.45) are proportional to  $\xi^h$ . Similarly, Eq. (4.43) shows that  $f_i^{(g)}(\xi)$  is also proportional to  $\xi^h$ . It is evident from Eq. (4.42) that  $h \geq 1$  always holds. The initial stress  $\sigma_0(\xi, \eta)$  is a function of temperature distribution, and the condition  $-\lambda_j \geq 0$  is unconditionally true in Eq. (4.36). Thus, only the first term in Eq. (6.2) becomes singular for  $-I < \text{Re}(S_i) < 0$  when  $\xi \rightarrow 0$ , such that

$$\sigma^{(s)}(\xi, \eta) = \Psi_{\sigma}^{(s)}(\eta) \xi^{-S^{(s)} - I} \hat{c}^{(s)}, \quad (6.3)$$

where  $\hat{c}^{(s)}$  are the integration constants of uni-directionally coupled system corresponding to the singular modes  $S^{(s)}$ .

Now, the stress field in the fully coupled case Eq. (4.90) is reconsidered

$$\sigma(\xi, \eta) = \Upsilon_{\sigma}(\eta) \xi^{\Lambda - I} \Pi \hat{u}_b - D \beta \bar{N}(\eta) \Phi_n^{\theta} \xi^{-\lambda_n} \left( \Phi_n^{\theta} \right)^{-1} \theta_b. \quad (6.4)$$

The superscript  $(*)^{(e)}$  indicating the contribution of an individual subdomain is dropped for convenience. The second term of Eq. (6.4) expresses the distribution of initial thermal stress  $\sigma_0(\xi, \eta)$ . Analogous to the uni-directional coupling,  $\sigma_0(\xi, \eta)$  is regular in full coupling because  $-\lambda_n \geq 0$  is always satisfied in Eq. (4.53). The first term of Eq. (6.4) represents the contributions of homogeneous and supplementary shape functions for stress. The contribution of supplementary shape functions does not lead to stress singularity [153]. Such can be verified by inspecting the structure of matrix  $\Lambda$  in Eq. (4.69b). The block of eigenvalues with real parts  $-I < \text{Re}(S_i) < 0$ , i.e.,  $S^{(s)}$ , dictates the stress field compared to any other block in  $\Lambda$ . In Eq. (4.69b), the diagonal block  $\bar{\Lambda}$  indicates the contribution of supplementary shape functions. Equation (4.61) shows that

each entry of  $\bar{\lambda} \geq \mathbf{I}$ . Separating the contributions of  $\mathbf{S}^{(s)}$  in Eq. (6.4) using Eqs. (4.69), (3.121b), and (4.67) yields the expression of singular stress in fully coupled thermoelasticity

$$\boldsymbol{\sigma}^{(s)}(\xi, \eta) = \Psi_{\sigma}^{(s)}(\eta) \xi^{-\mathbf{S}^{(s)} - \mathbf{I}} \hat{\mathbf{c}}^{(s)}. \quad (6.5)$$

Here, the definitions of  $\Psi_{\sigma}^{(s)}$ ,  $\mathbf{S}^{(s)}$ , and  $\hat{\mathbf{c}}^{(s)}$  are the same as in Eq. (6.3). Note that the definition of singular stress for coupled cases in Eqs. (6.3) and (6.5) is similar to a purely mechanical case in Eq. (6.1), except for integration constants. Furthermore, the SBFEM expression of singular stress in Eq. (6.5) is generalized for any stress singularity and can be used to calculate generalized SIFs [149].

### 6.1.2 Convergence of Singular Modes

This section presents the convergence of singular modes in the SBFEM solution in the case of crack tip singularity. A plate with a homogeneous isotropic material and a crack exhibits a well-known square root singularity. Similarly, for an open SBFE element with the scaling center placed at the crack tip (see Fig. 6.2(a)), the eigenvalue/Schur decomposition of the  $\mathbf{Z}$  matrix in Eq. (3.103) contains a pair of eigenvalues with  $\mathbf{S}^{(s)} = -0.5\mathbf{I}$ . Note that the crack opening shown in Fig. 6.2(a) is exaggerated for visualization purposes.

In SBFEM, the numerically obtained eigenvalues of the singular mode depend on the shape and the refinement of the polygon element. Consequently, evaluating singular stress in Eqs. (6.1), (6.3), and (6.5) also depends on the shape and refinement of the polygon element. If the opening angle of a discontinuity is not sufficiently small, it leans more towards the wedge/reentrant corner rather than a crack. Moreover, the open SBFE must be sufficiently refined to capture the  $\mathbf{S}^{(s)}$  accurately. The refinement of SBFE is obtained by increasing the number of line elements through the subdivision of polygon edges. Another way to achieve the refinement is to increase the order of shape functions of a line element, commonly known as  $p$ -refinement.

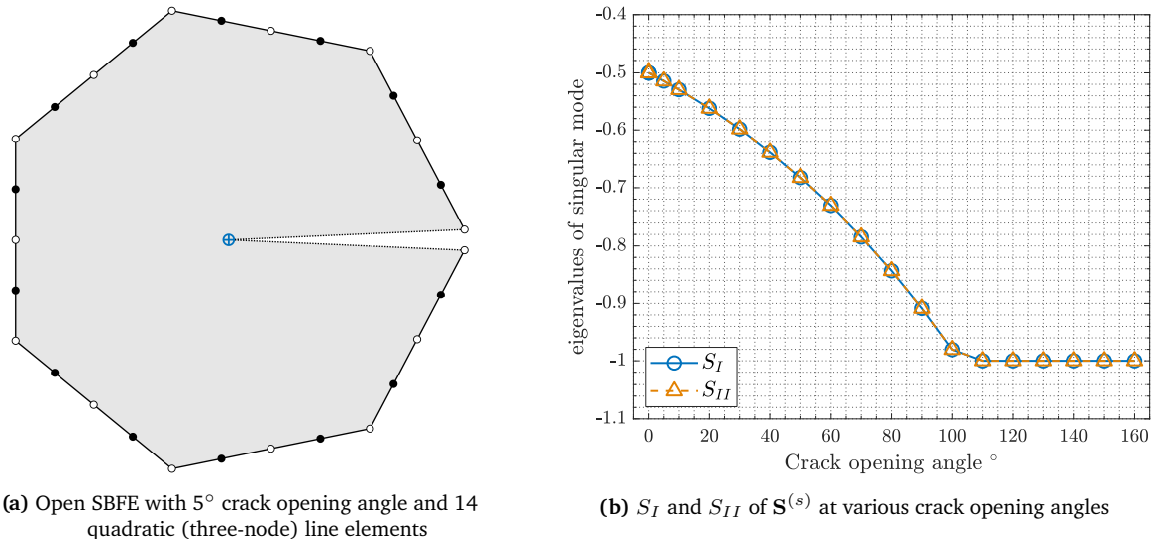


**Figure 6.2:** An open SBFE with  $5^\circ$  crack opening angle and the effects of crack opening angle on  $\mathbf{S}^{(s)}$ . (a) SBFE with  $5^\circ$  crack opening angle and 14 quadratic (three-node) line elements. (b) The effects of crack opening angles on  $\mathbf{S}^{(s)}$  in a polygon with 28 quadratic line elements.

To study the convergence behavior of the singular mode  $\mathbf{S}^{(s)}$ , a regular scaled boundary polygon element is considered as depicted in Fig. 6.2(a). First, the effects of the crack opening angle are analyzed. Fig. 6.2(b) presents both the eigenvalues of  $S_I$  and  $S_{II}$  of the singular mode  $\mathbf{S}^{(s)}$  at different crack opening angles. The results of  $S_I$  and  $S_{II}$  in Fig. 6.2(b) are obtained with 28

quadratic line elements. As expected, with increasing crack opening angle, the singularity moves away from the square root type towards the reentrant corner. It is observed that an opening angle less than or equal to  $10^{-4}$  is sufficient to represent a crack numerically.

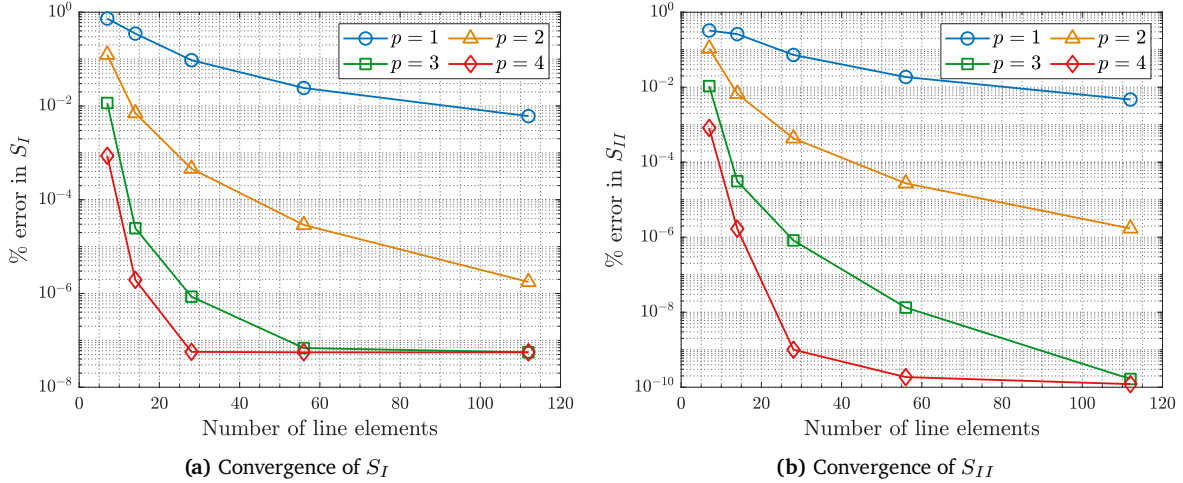


**Figure 6.3:** Convergence of singular modes  $S^{(s)}$  with respect to number and order of line elements. (a) Percentage error in  $S_I$ . (b) Percentage error in  $S_{II}$ .

Next, the effect of the number and order of line elements on  $\mathbf{S}^{(s)}$  is considered. For this purpose, the crack opening angle of  $10^{-7}$  is selected in Fig. 6.2(a). Figures 6.3(a) and 6.3(b) present the percentage error of  $S_I$  and  $S_{II}$ , respectively. The error percentage is calculated by comparing the eigenvalues obtained at different numbers and orders of line elements with the known analytical value of  $-0.5$ , such that

$$\% \text{ error in } S_I = \left| \frac{-0.5 - S_I}{-0.5} \right| \times 100 \quad \text{and} \quad \% \text{ error in } S_{II} = \left| \frac{-0.5 - S_{II}}{-0.5} \right| \times 100. \quad (6.6)$$

A convergent behavior in the  $\mathbf{S}^{(s)}$  values is observed with the increasing number and order of line elements. It is noted that  $S_{II}$  converge to a higher precision than  $S_I$ . The difference in the values of  $S_I$  and  $S_{II}$  results from the numerical inaccuracy of eigenvalue/Schur decomposition. However, the error percentage is significantly small to affect the evaluation of singular stress. An open SBFE with more than 20 line elements of order greater than or equal to two yields the error percentage of less than  $10^{-3}$  in the values of  $S_I$  and  $S_{II}$ . Note that the accuracy of  $\mathbf{S}^{(s)}$  only depends on refining a polygon element containing un-discretized crack faces and not on the global polygonal mesh (see Fig. 6.1).

Once the singular stress is recovered using the SBFEM expression in Eqs. (6.1), (6.3), and (6.5), the SIFs are calculated directly from their definition.

### 6.1.3 Calculation of Generalized SIFs

Consider a homogeneous isotropic domain where the crack is located on the negative  $\tilde{x}$ -axis, and the origin of the polar coordinates  $(\tilde{r}, \varphi)$  placed at the crack tip, as shown in Fig. 6.4. The analytical solution of stress is an asymptotic field near the crack tip that is expressed as a series of power functions with real exponent [118, 156]

$$\sigma_{\tilde{x}}(\tilde{r}, \varphi) = \sum_{n=1}^{\infty} \frac{n}{2} \tilde{r}^{\frac{n}{2}-1} \left\{ a_n^1 \left[ \left( 2 + \frac{n}{2} + (-1)^n \right) \cos \left( \frac{n}{2} - 1 \right) \varphi - \left( \frac{n}{2} - 1 \right) \cos \left( \frac{n}{2} - 3 \right) \varphi \right] \right.$$

$$-a_n^2 \left[ \left( 2 + \frac{n}{2} - (-1)^n \right) \sin \left( \frac{n}{2} - 1 \right) \varphi - \left( \frac{n}{2} - 1 \right) \sin \left( \frac{n}{2} - 3 \right) \varphi \right] \}, \quad (6.7a)$$

$$\begin{aligned} \sigma_{\tilde{y}}(\tilde{r}, \varphi) = & \sum_{n=1}^{\infty} \frac{n}{2} \tilde{r}^{\frac{n}{2}-1} \left\{ a_n^1 \left[ \left( 2 - \frac{n}{2} - (-1)^n \right) \cos \left( \frac{n}{2} - 1 \right) \varphi + \left( \frac{n}{2} - 1 \right) \cos \left( \frac{n}{2} - 3 \right) \varphi \right] \right. \\ & \left. - a_n^2 \left[ \left( 2 - \frac{n}{2} + (-1)^n \right) \sin \left( \frac{n}{2} - 1 \right) \varphi + \left( \frac{n}{2} - 1 \right) \sin \left( \frac{n}{2} - 3 \right) \varphi \right] \right\}, \end{aligned} \quad (6.7b)$$

$$\begin{aligned} \sigma_{\tilde{x}\tilde{y}}(\tilde{r}, \varphi) = & \sum_{n=1}^{\infty} \frac{n}{2} \tilde{r}^{\frac{n}{2}-1} \left\{ a_n^1 \left[ \left( \frac{n}{2} - 1 \right) \sin \left( \frac{n}{2} - 3 \right) \varphi - \left( \frac{n}{2} + (-1)^n \right) \sin \left( \frac{n}{2} - 1 \right) \varphi \right] \right. \\ & \left. + a_n^2 \left[ \left( \frac{n}{2} - 1 \right) \cos \left( \frac{n}{2} - 3 \right) \varphi - \left( \frac{n}{2} - (-1)^n \right) \cos \left( \frac{n}{2} - 1 \right) \varphi \right] \right\}. \end{aligned} \quad (6.7c)$$

In the above equation, the stress field is independent of material properties. Moreover, the coefficients  $a_n^1$  and  $a_n^2$  are real numbers that depend on the applied boundary conditions. For  $n = 1$ , the asymptotic stress field in Eq. (6.7) tends to be singular when  $\tilde{r} \rightarrow 0$ . In a two-dimensional setting, the crack tearing mode, i.e., mode-III, does not exist for in-plane problems. Evaluating the summation for  $n = 1$  in Eq. (6.7), the singular components of stress  $\sigma_{\tilde{y}}^{(s)}$  and  $\sigma_{\tilde{x}\tilde{y}}^{(s)}$  relate to the SIFs in Eq. (2.85) at  $\varphi = 0^\circ$ , such that [118]

$$K_I = \sqrt{2\pi\tilde{r}} \sigma_{\tilde{y}}^{(s)}(\tilde{r}, \varphi = 0) = \sqrt{2\pi} a_1^1, \quad (6.8a)$$

$$K_{II} = \sqrt{2\pi\tilde{r}} \sigma_{\tilde{x}\tilde{y}}^{(s)}(\tilde{r}, \varphi = 0) = \sqrt{2\pi} a_1^2, \quad (6.8b)$$

where  $\sigma_{ij}^{(s)}$  are the components of singular stress in polar coordinates, the coefficients  $a_1^1$  and  $a_1^2$  relate to the SIFs. Furthermore, the radial distribution of singular stress in Eq. (6.8) is the same as in Eq. (6.1), and the coefficients  $a_1^1$  and  $a_1^2$  in Eq. (6.8) also correspond to the singular modes  $S^{(s)}$  [118].

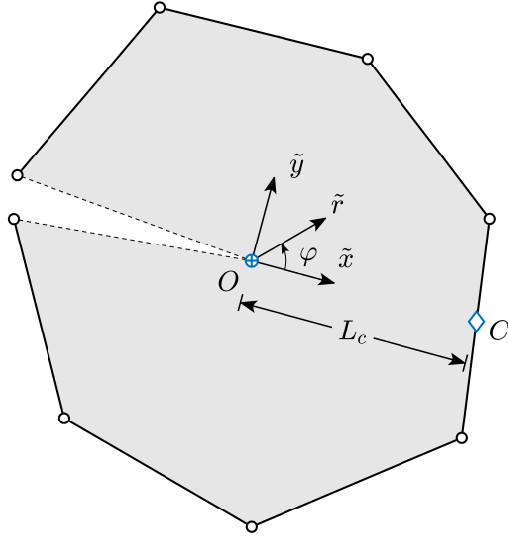


**Figure 6.4:** A homogeneous isotropic domain with a crack, the same as an open scaled boundary finite polygon element in polar coordinates with the origin and scaling center at the crack tip.

As discussed, the SBFEM formulation of singular stress fields in purely mechanical and coupled cases is the same except for integration constants. Here, SIFs are evaluated based on singular stress for a fully coupled case in Eq. (6.5). The calculation of SIFs remains the same for the mechanical and uni-directionally coupled cases.

To obtain the SBFEM expression of generalized SIFs, first, the scaled boundary radial coordinate  $\xi$  is transformed to polar coordinates by introducing the characteristic length  $L_c$  (see Fig. 6.4)

$$\xi = \frac{\tilde{r}}{\tilde{r}_b(\varphi)} = \frac{L_c}{\tilde{r}_b(\varphi)} \times \frac{\tilde{r}}{L_c}, \quad (6.9)$$

where  $\tilde{r}_b(\varphi)$  is the distance from the scaling center to the boundary at angle  $\varphi$ . The matrix power function of  $\xi$  in Eq. (6.5) is rewritten in polar coordinates using Eq. (6.9)

$$\xi^{-\mathbf{S}^{(s)} - \mathbf{I}} = \left( \frac{L_c}{\tilde{r}_b(\varphi)} \right)^{-\mathbf{S}^{(s)} - \mathbf{I}} \left( \frac{\tilde{r}}{L_c} \right)^{-\mathbf{S}^{(s)} - \mathbf{I}}. \quad (6.10)$$

Substituting Eq. (6.10) into Eq. (6.5) results in the SBFEM expression of singular stress in polar coordinates

$$\boldsymbol{\sigma}^{(s)}(\tilde{r}, \varphi) = \boldsymbol{\Psi}_{\sigma L_c}^{(s)}(\varphi) \left( \frac{\tilde{r}}{L_c} \right)^{-\mathbf{S}^{(s)} - \mathbf{I}} \hat{\mathbf{c}}^{(s)}, \quad (6.11)$$

where  $\boldsymbol{\Psi}_{\sigma L_c}^{(s)}(\varphi)$  is the singular stress mode at characteristic length  $L_c$

$$\boldsymbol{\Psi}_{\sigma L_c}^{(s)}(\varphi) = \boldsymbol{\Psi}_{\sigma}^{(s)}(\eta(\varphi)) \left( \frac{L_c}{\tilde{r}_b(\varphi)} \right)^{-\mathbf{S}^{(s)} - \mathbf{I}}. \quad (6.12)$$

Following the classical definition, two stress intensity factors,  $K_I$  and  $K_{II}$ , are defined using the two stress components in polar coordinates, i.e.,  $\sigma_{\varphi}^{(s)}(\tilde{r}, \varphi)$  and  $\sigma_{\tilde{r}\varphi}^{(s)}(\tilde{r}, \varphi)$ , respectively. In such case, the singular stress in Eq. (6.11) has two components

$$\boldsymbol{\sigma}^{(s)}(\tilde{r}, \varphi) = \begin{Bmatrix} \sigma_{\varphi}^{(s)}(\tilde{r}, \varphi) \\ \sigma_{\tilde{r}\varphi}^{(s)}(\tilde{r}, \varphi) \end{Bmatrix}, \quad (6.13)$$

and  $\boldsymbol{\Psi}_{\sigma L_c}^{(s)}(\varphi)$  in Eq. (6.12) becomes a  $2 \times 2$  matrix corresponding to Eq. (6.13). The definition of generalized SIFs based on the order of stress singularity is defined in [120]

$$\boldsymbol{\sigma}^{(s)}(\tilde{r}, \varphi) = \frac{1}{\sqrt{2\pi L_c}} \left( \frac{\tilde{r}}{L_c} \right)^{-\tilde{\mathbf{S}}^{(s)}} \mathbf{K}(\varphi), \quad (6.14)$$

where  $\tilde{\mathbf{S}}^{(s)}$  is the order of the singularity, such that

$$\tilde{\mathbf{S}}^{(s)} = \boldsymbol{\Psi}_{\sigma L_c}^{(s)}(\varphi) (\mathbf{S}^{(s)} + \mathbf{I}) (\boldsymbol{\Psi}_{\sigma L_c}^{(s)}(\varphi))^{-1}. \quad (6.15)$$

Comparing Eq. (6.14) to Eq. (6.11), the generalized stress intensity factors at angle  $\varphi$  are evaluated directly using the singular stress modes

$$\mathbf{K}(\varphi) = \sqrt{2\pi L_c} \boldsymbol{\Psi}_{\sigma L_c}^{(s)}(\varphi) \hat{\mathbf{c}}^{(s)}, \quad (6.16)$$

where  $\mathbf{K}(\varphi) = [K_I(\varphi) \ K_{II}(\varphi)]^T$ . Using Eq. (6.16), the generalized SIFs  $\mathbf{K}(\varphi)$  can easily be calculated at any given angle  $\varphi$ . The singular stress modes at characteristic length  $\boldsymbol{\Psi}_{\sigma L_c}^{(s)}(\varphi)$  are first evaluated at discrete Gauss points located on the boundary and then interpolated at  $\eta(\varphi)$ . In Eq. (6.16), the dimension of the generalized SIFs is (Stress  $\times \sqrt{\text{Length}}$ ) which is independent of the orders of singularity.

In a homogeneous isotropic medium, the order of singularity in Eq. (6.15) is of square root type, i.e.,  $\tilde{\mathbf{S}}^{(s)} = 0.5\mathbf{I}$ . It can be shown that substituting  $\tilde{\mathbf{S}}^{(s)} = 0.5\mathbf{I}$  in Eq. (6.14) at  $\varphi = 0$  yields the same definition of SIFs as the classical case in Eq. (6.8). Similarly, other types of stress singularity

that occur in an interfacial crack between two isotropic or anisotropic materials, V-notch at a bi-material interface, and power-logarithmic singularities can be captured using the SBFEM expression of generalized SIFs in Eq. (6.16). For the details, readers are referred to [118, 120, 149].

In the SBFEM, singular stress is calculated semi-analytically at the boundary. Moreover, only the contribution of singular modes is sufficient to evaluate the singular stress. In this work, the generalized SIFs are evaluated in front of the crack tip, i.e.,  $\varphi = 0$ . In the case of fully coupled thermoelasticity, the history of transient SIFs is evaluated at each time step using Eq. (6.16). For FGMs, the material properties are taken at the scaling center to calculate the stress modes  $\Psi_{\sigma}^{(s)}$  in Eq. (6.12).

## 6.2 Meshing and Re-meshing of Polygon Elements

In discrete crack propagation analysis, the geometry of the domain needs to be updated and re-meshed according to the crack extension to maintain the actual representation of an evolving crack. Each analysis step requires the crack propagation angle  $\varphi_p$  and the crack incremental length  $\Delta a$  to obtain the path of moving cracks. For a single quasi-static step, the crack incremental length is a user-defined parameter that has to be chosen according to the problem. If the crack does not travel in a straight line, a small crack increment is necessary to model the propagating cracks accurately.

In the dynamic analysis, the crack extension length  $\Delta a_e$  can be determined using the given crack velocity at each time step. The resulting  $\Delta a_e$  is usually very small and yields accurate crack paths. However, invoking a re-meshing algorithm at each time step is computationally expensive and, for certain cases, even unnecessary. A crack extension length at each time step  $\Delta a_e$  can be accumulated until the threshold length is reached. The threshold or crack accumulation length is also a user input denoted as  $\Delta a$ . The choice of crack propagation length for each re-meshing step is based on the trade-off between accuracy of crack paths and computational cost.

In this work, the scaled boundary polygon elements are employed to discretize the geometry. The polygon elements are generated using the *background triangular* elements as discussed in [111]. During the crack propagation step, the geometry is updated by invoking the localized re-meshing algorithm developed in [123]. This section briefly explains the generation of polygon elements and the localized re-meshing of a patch near the crack tip.

### 6.2.1 Generation of Polygon Mesh

In the scaled boundary finite element method, the geometry can be discretized with any arbitrary-sided polygon elements as long as the scaling requirement is satisfied. The polygon elements facilitate the meshing of complex geometries. They can also provide a flexible and robust technique to remesh the geometry locally as the crack propagates. Here, the polygon elements are generated using the background triangular elements.

First, a triangular representation of the given domain  $\Omega$  is obtained by a well known procedure of *Delaunay triangulation* [157]. A triangular mesh is generated by using an open source software called *Gmsh* is employed [158]. The domain boundary  $\Gamma$  is represented by a finite number of points and passed to Gmsh, yielding the triangulation. Moreover, the density of the triangular mesh can be altered by simply defining the mesh characteristic length  $h$  at each discrete point on the boundary. Figures 6.5(a) and 6.5(b) show the triangular meshes of a sample domain obtained using different  $h$ . In Figs. 6.5(a) and 6.5(b), the symbols  $\bullet$  and  $\circ$  indicate the vertices and the centroids of triangles, respectively. The marker  $\bullet$  denotes the input points of the boundary that are used to generate the triangular mesh.

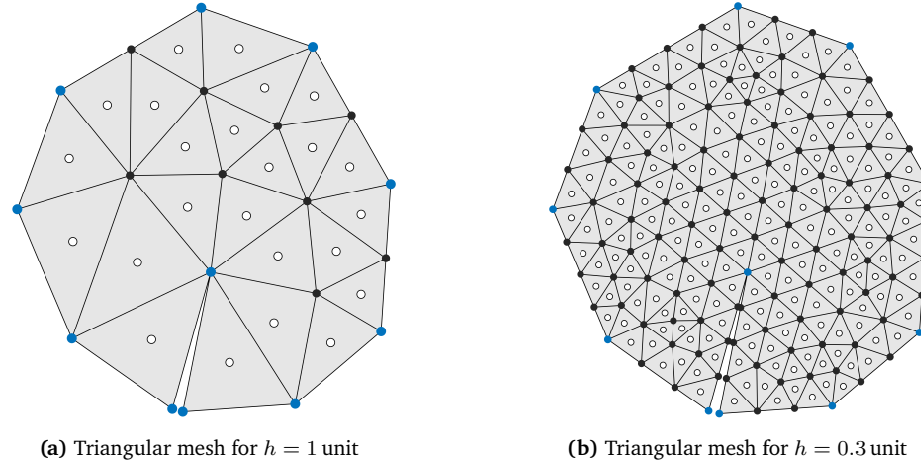


**Figure 6.5:** Delaunay triangulation of a domain  $\Omega$  with boundary  $\Gamma$  at different mesh characteristic length  $h$ . The markers  $\bullet$ ,  $\circ$ , and  $\bullet$  symbolize the vertices, centroids, and input points on the boundary  $\Gamma$ , respectively. (a) Triangular mesh for  $h = 1$  unit. (b) Triangular mesh for  $h = 0.3$  unit.

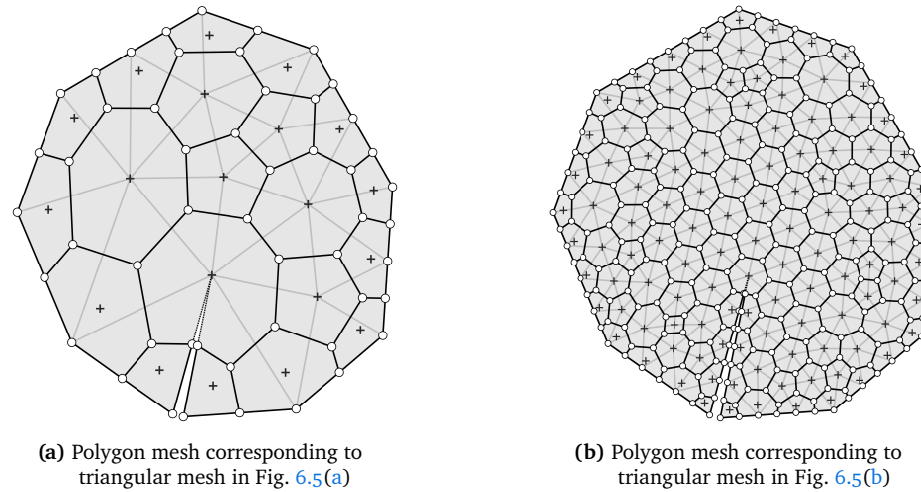


**Figure 6.6:** Polygon meshes obtained from the triangular meshes following the transformation with  $\circ$  and  $+$  as the vertices and the scaling centers, respectively. (a) Polygon mesh corresponding to Fig. 6.5(a) for  $h = 1$  unit. (b) Polygon mesh corresponding to Fig. 6.5(b) for  $h = 0.3$  unit.

Next, creating polygon mesh based on the existing triangular mesh is considered. A simple procedure to obtain a polygon mesh from a triangular mesh is outlined in [111] as summarized below

- The polygon edges are created by connecting the centroids of the triangles.
- The vertices of triangles are now the centroids of polygon elements and act as the scaling centers. In the case of an open polygon, the crack tip is the scaling center.
- On the boundary  $\Gamma$ , the vertices of triangles become the vertices of polygons. Moreover, the midpoint of the triangles' edges at the boundary is also converted to the vertices of polygons. The scaling centers of the polygons at the boundary are located at the geometric center.

Applying the aforementioned transformation onto the triangular meshes in Figs. 6.5(a) and 6.5(b) results in the polygon meshes as illustrated in Figs. 6.6(a) and 6.6(b). In Fig. 6.6,  $\circ$  and  $+$  denote the vertices and the scaling centers of the polygon elements, respectively. One of the key advantages of triangular elements is their ability to mesh complex geometries. As a

result, the polygon meshes generated from the background triangular elements instill the same capability of modeling complex geometries. In addition, the scaled boundary polygon elements are not restricted to a certain number of edges. Thus, using open elements, they can seamlessly incorporate any discontinuities, such as cracks. As an example, Figs. 6.7(a) and 6.7(b) show polygon meshes of complex geometries. Figure 6.7(a) depicts the mesh of a circular domain with a curved interface. Figure 6.7(b) illustrates a quarter of a circular disk with multiple cracks emanating from perforation.

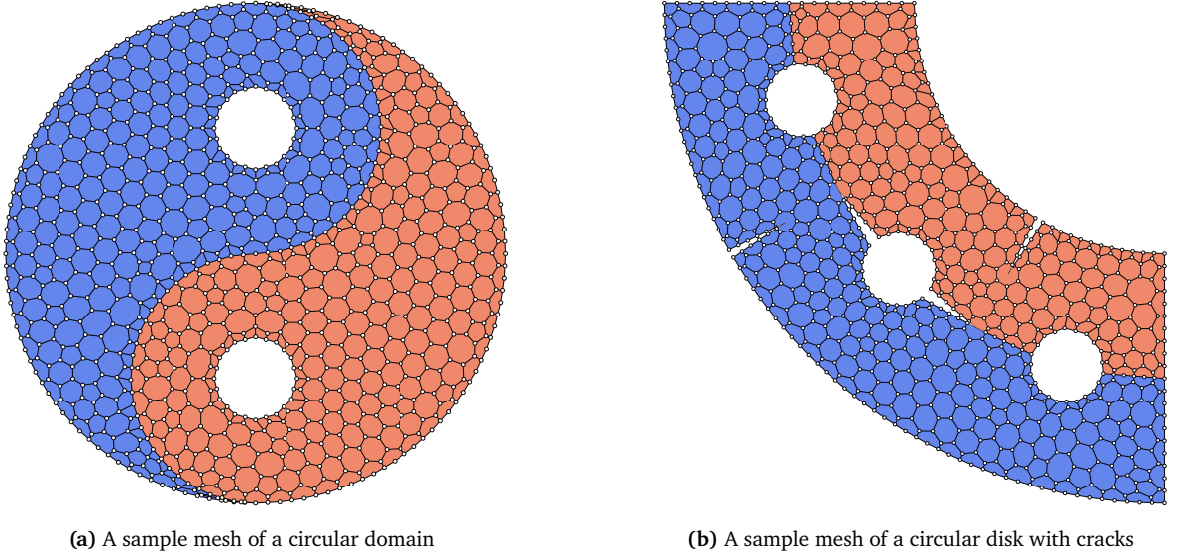


**Figure 6.7:** Sample polygon meshes of complex geometries.

### 6.2.2 Localized Re-meshing Technique

This section presents the re-meshing of the polygon elements required for discrete crack propagation simulations. A localized re-meshing technique based on background triangular elements is reported in [123]. This work generates the polygon elements using the triangular mesh, as discussed in the previous section. Therefore, it is natural to perform the re-meshing using the existing triangular mesh. To this end, only a small patch near the propagating crack is re-meshed, alleviating the need to update the complete polygon mesh.

In crack propagation modeling, the new location of the crack tip is determined using the crack propagation angle  $\varphi_p$  and crack incremental length  $\Delta a$ . Consider a propagating crack in a domain discretized with a polygon mesh using background triangular elements as illustrated in Fig. 6.8(a). The current and new locations of the crack tips are indicated by (●) and (●), respectively. The line in green (—) describes the extension of the discrete crack.

The following steps are taken to perform the localized re-meshing of the polygon elements:

- In the first step, the background triangular elements are identified that are intersected by the crack extension. Figure 6.8(b) shows the intersected triangles in orange.
- The re-meshing patch is selected by adding the layer of triangles neighboring to the intersected triangles. The boundary of the re-meshing patch is illustrated by blue color in Fig. 6.8(b).
- Next, the patch is updated to include the crack extension. For this purpose, the tip of the current crack is inflated to allow for discontinuity. The inflated points are then connected to the new crack tip. Figure 6.8(c) presents the updated patch. Moreover, the triangles inside the re-meshing patch are removed from the triangular mesh.

- A new triangular mesh of the patch is generated using the Delaunay triangulation as shown in Fig. 6.8(d).
- Figure 6.8(e) depicts the updated triangular mesh with the crack extension. The updated mesh is obtained by stitching the new mesh of the patch back to the existing triangular mesh. Note that special care is taken to ensure that the boundaries of a patch and existing triangular meshes conform.
- The updated polygon mesh is generated by transforming the triangular mesh into polygons as described in Section 6.2.1. Figure 6.8(f) shows the polygon mesh resulting from the localized re-meshing near the crack extension.

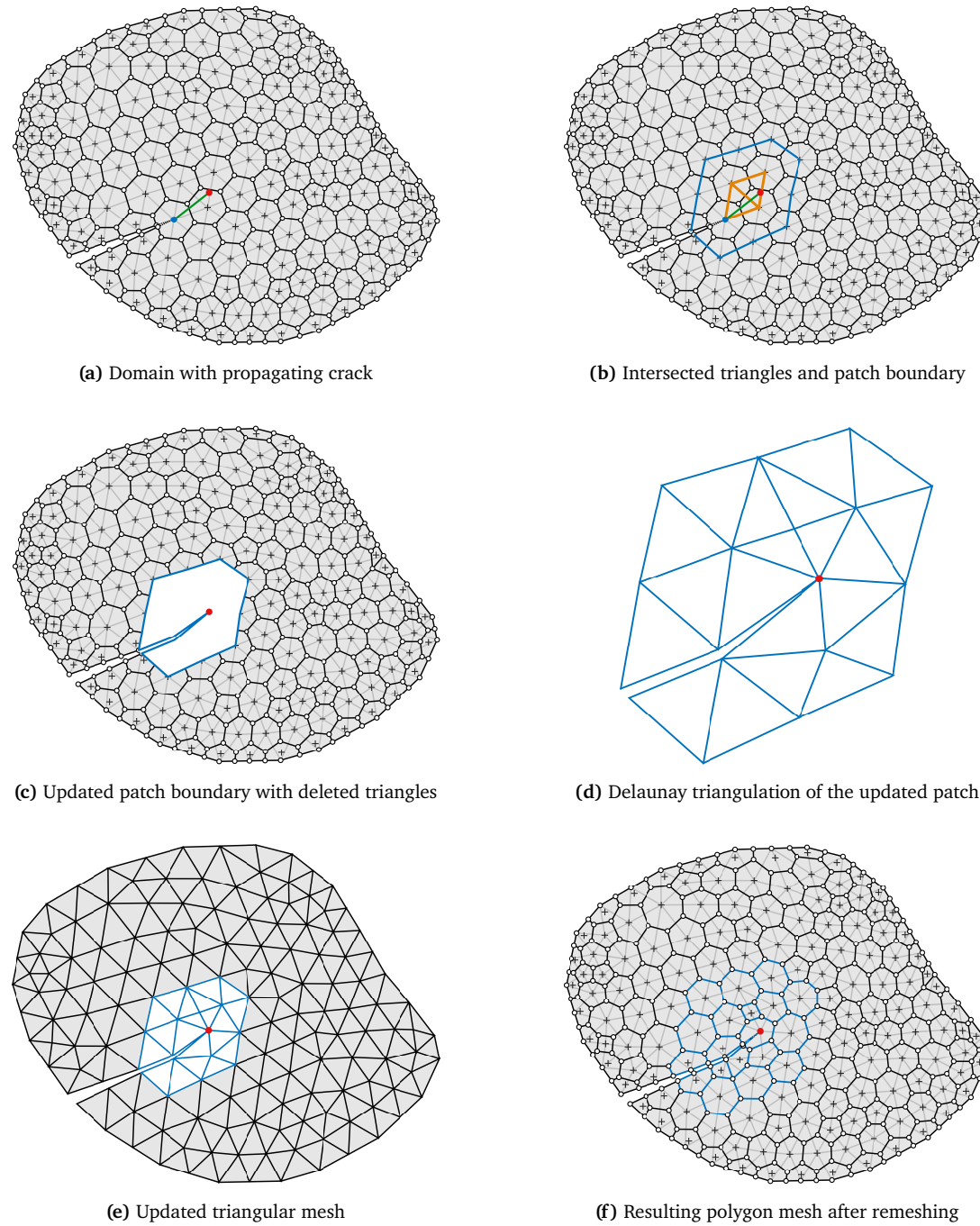


**Figure 6.8:** A localized re-meshing technique of polygon elements based on background triangular elements.

The updated polygon mesh is created from the triangular mesh of the complete domain to avoid the non-conformity of polygon edges at the patch boundary. Nevertheless, the re-meshing of polygon elements only occurs in the small region near the crack extension, as indicated by the blue color in Fig. 6.8(f). The re-meshing procedure can be applied to multiple cracks propagating without intersection. The following explains the mapping of the global system and the state variables after re-meshing.

### 6.2.3 Mapping of Re-meshed System

After the crack extension, the mesh is updated using the localized re-meshing technique. Albeit the change in the mesh is restricted to a small patch, the global system of coefficient matrices and state variables needs to be updated accordingly.

Figure 6.9 illustrates a re-meshed patch corresponding to Fig. 6.8(f). Within Fig. 6.9, the polygonal elements existing prior to the re-meshing process are denoted as *old elements*. Following the re-meshing, newly generated polygons resulting from crack extension are identified as *new elements*. Notably, the nodes along the patch's boundary remain unchanged throughout the re-meshing process. Therefore, *boundary nodes* serve as anchor points for the seamless stitching of the re-meshed patch into the entire mesh (see Figs. 6.9 and 6.8). In Fig. 6.9, nodes categorized as *deleted* and *new* pertain to the nodes of old and new elements, excluding those along the boundary.

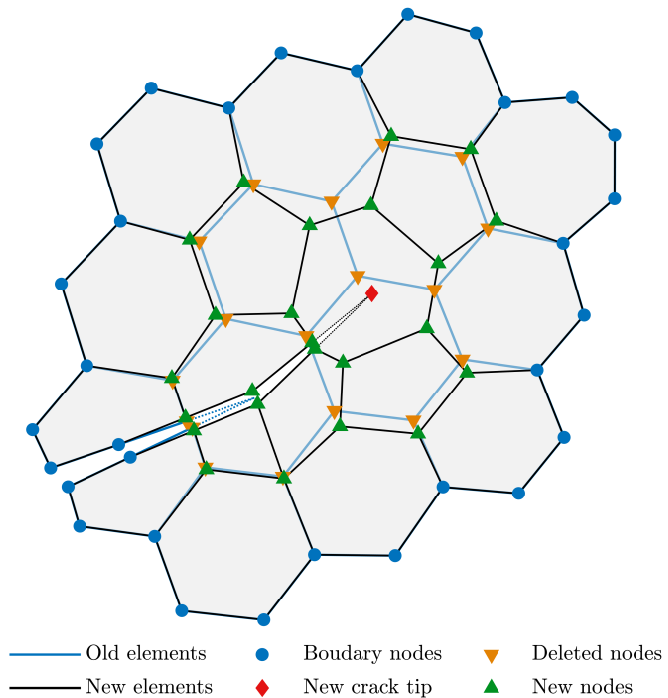


Figure 6.9: Mapping of the global system after localized re-meshing a patch.

The updated global system of coefficient matrices is derived through modifying contributions from degrees of freedom (DOFs). That is, removing and adding the contributions of DOFs corresponding to deleted and new nodes, respectively. It is important to note that the contribution of DOFs associated with boundary nodes remains unchanged. Similarly, the solution vectors of state variables are updated by removing the solution of deleted DOFs and incorporating the solution of new DOFs. However, the solution to new DOFs needs to be determined and necessitates solution mapping. If the nodal coordinates of new nodes are known, then the solution of state variables of new DOFs can be obtained through interpolation using the SBFEM shape functions.

To this end, all system properties within the re-meshed patch are characterized in two distinct sets,

denoted by subscripts  $(*)_i$  and  $(*)_j$ , representing the system's state before and after re-meshing. First, the local coordinates  $(\xi)_i$  and  $(\eta)_i$  of new nodes are identified within the old elements by inverse mapping using Eq. (3.1). Then, the solution of temperature and displacement DOFs of new nodes is interpolated using the SBFEM shape functions in Eqs. (3.77) and (4.70), such that

$$(\theta_b(\xi, \eta))_j = (\bar{\chi}(\xi, \eta))_i (\theta_b(\eta))_i, \quad (6.17a)$$

$$(\mathbf{u}_b(\xi, \eta))_j = (\hat{\chi}(\xi, \eta))_i (\hat{\mathbf{u}}_b)_i, \quad (6.17b)$$

where  $(\theta_b)_j$  and  $(\mathbf{u}_b)_j$  indicate the solution of temperature and displacements of new nodes, respectively. Note that in the re-meshed system, the new nodes are located on the boundary of the new elements, i.e.,  $(\xi)_j = 1$ .

Furthermore, the solution of first- and second-order time derivatives of state variables are also interpolated using the same SBFEM shape functions. Analogous to Eq. (6.17), the first-order time derivatives of temperature  $(\dot{\theta}_b)_j$  and displacement  $(\dot{\mathbf{u}}_b)_j$  of new nodes are evaluated as

$$(\dot{\theta}_b(\xi, \eta))_j = (\bar{\chi}(\xi, \eta))_i (\dot{\theta}_b(\eta))_i, \quad (6.18a)$$

$$(\dot{\mathbf{u}}_b(\xi, \eta))_j = (\hat{\chi}(\xi, \eta))_i (\dot{\hat{\mathbf{u}}}_b)_i, \quad (6.18b)$$

and the second-order time derivatives  $(\ddot{\theta}_b)_j$ ,  $(\ddot{\mathbf{u}}_b)_j$  are interpolated as

$$(\ddot{\theta}_b(\xi, \eta))_j = (\bar{\chi}(\xi, \eta))_i (\ddot{\theta}_b(\eta))_i, \quad (6.19a)$$

$$(\ddot{\mathbf{u}}_b(\xi, \eta))_j = (\hat{\chi}(\xi, \eta))_i (\ddot{\hat{\mathbf{u}}}_b)_i. \quad (6.19b)$$

In the case of fully coupled thermoelasticity, the SBFEM discretization of the global system described in Eq. (4.81) consists of both the solution of state variables and the solution of additional DOFs associated with supplementary shape functions (supplementary DOFs), namely,

$$\hat{\mathbf{u}}_b = [\mathbf{u}_b \quad \mathbf{u}_s]^T, \quad \dot{\hat{\mathbf{u}}}_b = [\dot{\mathbf{u}}_b \quad \dot{\mathbf{u}}_s]^T, \quad \ddot{\hat{\mathbf{u}}}_b = [\ddot{\mathbf{u}}_b \quad \ddot{\mathbf{u}}_s]^T. \quad (6.20)$$

Here, the vector  $\mathbf{u}_s$  denotes the solution of supplementary DOFs, with its first- and second-order time derivatives as  $\dot{\mathbf{u}}_s$  and  $\ddot{\mathbf{u}}_s$ , respectively. The number of supplementary DOFs is the same as the number of nodes in an element. However, they relate not to specific nodes but to the whole element. Thus, the solution mapping of the supplementary DOFs is not as trivial as the interpolation of the state variables expressed in Eqs. (6.17), (6.18), and (6.19).

To obtain the solution of supplementary DOFs, additional mapping points are introduced within each new element as illustrated in Fig. 6.10. For each new element, a system of linear algebraic equations is constructed using Eq. (6.17b) as

$$(\hat{\mathbf{u}}_b)_j = ([\hat{\chi}])_j^{-1} (\mathbf{u}_b)_i. \quad (6.21)$$

In Eq. (6.21),  $([\hat{\chi}])_j$  describes the matrix of shape functions for all mapping points within each new element. The vector  $(\mathbf{u}_b)_i$  indicates the solution of displacement DOFs at mapping points. The required number of additional mapping points relates to the number of nodes in the new element. The number of mapping points must be greater or equal to 1.5 times the number of nodes. For example, an element with eight nodes requires a minimum of twelve mapping points to obtain the solution of eight supplementary DOFs. Therefore, in Eq. (6.21), the size of matrix  $([\hat{\chi}])_j$  is  $24 \times 24$ , and the length of vectors  $(\mathbf{u}_b)_i$  and  $(\hat{\mathbf{u}}_b)_j$  is also 24. Now, consider the darker shaded element with eight nodes in Fig. 6.10. Here, 14 mapping points are used to obtain a uniform distribution of mapping points within each subdomain. In this case, the matrix  $([\hat{\chi}])_j$  is

of size  $28 \times 24$ , and the lengths of vectors  $(\mathbf{u}_b)_i$  and  $(\hat{\mathbf{u}}_b)_j$  are 28 and 24, respectively. When the number of mapping points is greater than the required, the system of linear equations in Eq. (6.21) is overdetermined, and  $([\hat{\chi}])_j$  is a non-square matrix. Therefore, the well-known Moore-Penrose inverse matrix generalization [159, 160] is used to evaluate the pseudo-inverse of matrix  $([\hat{\chi}])_j$ . Nevertheless, the increase in the number of mapping points does not affect the length of  $(\hat{\mathbf{u}}_b)_j$  but only the size of  $([\hat{\chi}])_j$  and  $(\mathbf{u}_b)_i$ .

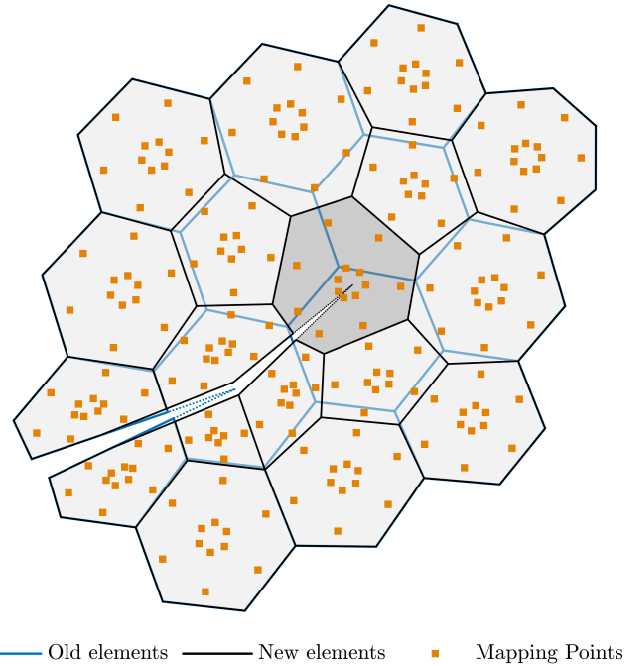


**Figure 6.10:** Additional mapping points within each new elements to obtain the solution of supplementary DOFs.

The location of individual mapping point is determined with respect to  $(\eta)_j$  and  $(\xi)_j$  coordinates in each subdomain. The integration points of the Gauss quadrature rule are chosen as  $(\eta)_j$  coordinates. The number of integration points is selected equal to the order of line element order  $p$ . Similarly, the  $(\xi)_j$  coordinates are also the two integration points of the Gauss quadrature rule, which are then transformed linearly (see Eq. (6.22)). As an example, the  $(\eta)_j$  and  $(\xi)_j$  coordinates within a subdomain for  $p = 2$  are given as

$$(\eta)_j = \pm \frac{1}{\sqrt{3}}, \quad \text{and} \quad (\xi)_j = \frac{1}{2} \left( 1 \pm \frac{1}{\sqrt{3}} \right). \quad (6.22)$$

Note that the number and location of  $(\xi)_j$  remain the same irrespective of  $p$  to satisfy the condition of minimum required mapping points. The location of  $2p$  mapping points in each subdomain is obtained by inverse mapping using Eq. (3.1), and the combinations of each  $(\eta)_j$  and  $(\xi)_j$ . The solution of displacement DOFs at mapping points  $(\mathbf{u}_b)_i$  in Eq. (6.21) is calculated analogous to the solution of new nodes described earlier. The matrix of shape functions  $([\hat{\chi}])_j$  in Eq. (6.21) is formulated using Eq. (4.70). The systems of equations for the solution of first- and second-order time derivatives are constructed according to Eq. (6.21), such that

$$(\dot{\hat{\mathbf{u}}}_b)_j = ([\hat{\chi}])_j^{-1} (\dot{\mathbf{u}}_b)_i, \quad (6.23a)$$

$$(\ddot{\hat{\mathbf{u}}}_b)_j = ([\hat{\chi}])_j^{-1} (\ddot{\mathbf{u}}_b)_i. \quad (6.23b)$$

After solving the system of equations in Eqs. (6.21), (6.23a), and (6.23b), the solution of supplementary DOFs are separated from state variables using Eq. (6.20).



# Chapter 7

## Numerical Examples Part-I: Uni-directional Coupling

This chapter presents the numerical examples of fracture modeling caused by thermal stress. Here, the uni-directional coupling of temperature and displacement fields is considered. One of the ways of achieving the uni-directional coupling is to employ the *Sequential* approach, as described in Section 4.2. In this approach, a prior solution of the temperature field is required to obtain the effects of thermal stress on the displacement field as a load vector. Another way of modeling uni-directional coupling is to reduce the discretized equation of fully coupled thermoelasticity in Eq. (4.81) by ignoring the time derivatives of state variables, such that

$$\begin{bmatrix} \mathbf{K}_u & -\mathbf{K}_c \\ \mathbf{0} & \mathbf{K}_\theta \end{bmatrix} \begin{Bmatrix} \hat{\mathbf{u}}_b \\ \theta_b \end{Bmatrix} = \begin{Bmatrix} \mathbf{F}_u \\ \mathbf{F}_\theta \end{Bmatrix}. \quad (7.1)$$

Like fully coupled thermoelasticity, the discretization in Eq. (7.1) also utilized the scaled boundary polygon and supplementary shape functions. The distinction between the modeling approaches, i.e., thermal stress as a load vector and employment of supplementary shape functions, are termed as *Sequential* and *Coupled*, respectively.

The first section illustrates the efficacy of the SBFEM in capturing stress intensity factors, as discussed in Section 6.1. In this section, both modeling approaches are considered. In the second section, the modeling of fracture in functionally graded materials is presented. The third section validates the SBFEM for quasi-static crack propagation problems under thermo-mechanical loads. The required re-meshing of the domain involving propagating cracks is performed by localized re-meshing, as discussed in Section 6.2. The presented results in Sections 7.2 and 7.3 are obtained using only the *Coupled* approach for convenience.

Unless mentioned otherwise, all the numerical examples utilized the scaled boundary polygon elements with quadratic (three-node) line elements, i.e.,  $p = 2$ . Furthermore, each edge of a polygon element containing a crack is subdivided into four edges to increase the efficiency in calculating the stress intensity factors. The crack faces are assumed to be insulated in all the examples.

### 7.1 Validation of Stress Intensity Factors

In this section, three numerical examples are presented to demonstrate the accuracy of the SBFEM in calculating the stress intensity factors. The first example considers a plate with an edge crack under constant flux. The application of constant flux parallel to crack faces results in mode-I fracture. A plate with a center crack under constant flux perpendicular to crack faces is analyzed. This results in the mode-II fracture. Finally, a mixed-mode fracture problem is considered by analyzing a plate with an inclined center crack. The examples considered in this section are already published in [154]. Here, they are presented for completeness.

### 7.1.1 Mode-I Fracture – Plate with Edge Crack

This example analyzes a plate with an edge crack under constant flux, as shown in Fig. 7.1(a). This example has been studied in several other papers using different numerical methods. For example, by using the extended finite element method (XFEM) in [44], the singular edge-based smoothed finite element method (ES-FEM) in [161], and the extended four-node consecutive-interpolation quadrilateral element (XCQ4) in [162].

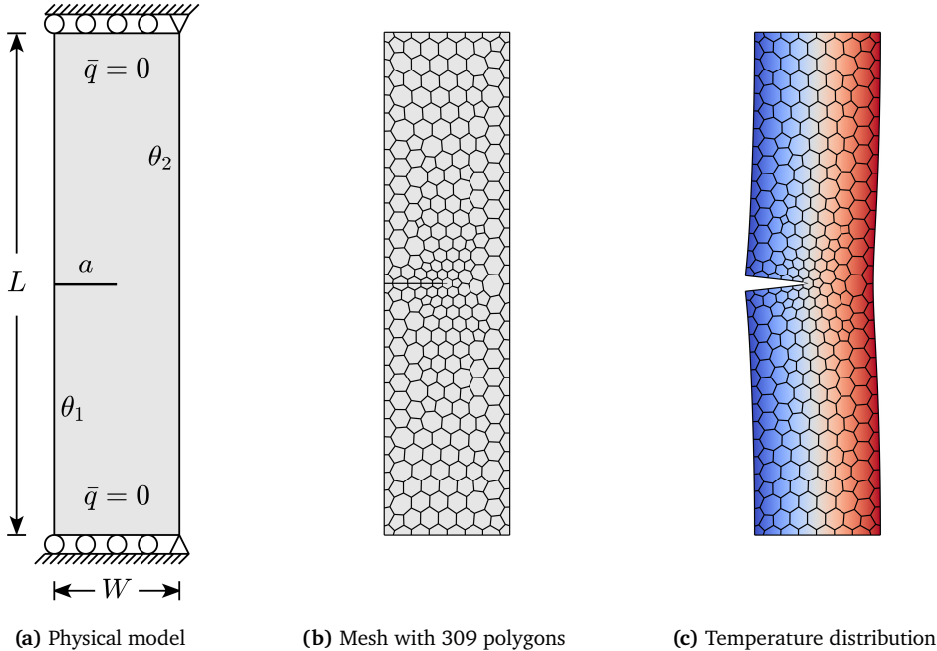


**Figure 7.1:** A physical and numerical model of a plate with an edge crack under constant flux parallel to a crack. (a) Geometry and boundary conditions. (b) A sample mesh with 309 polygon elements. (c) The temperature distribution with scaled deformations.

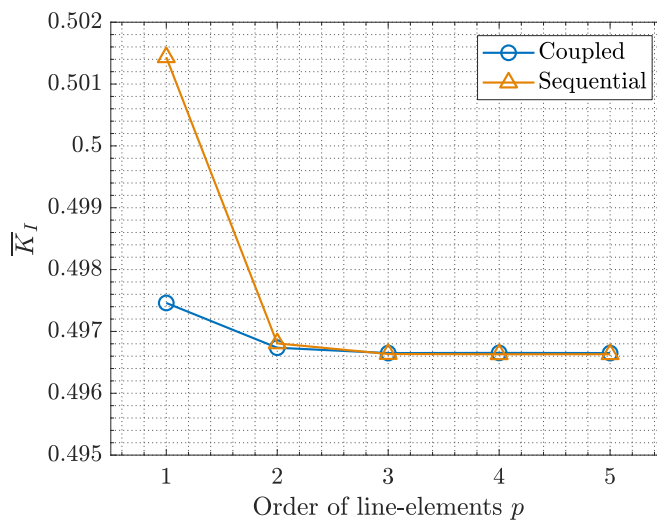


**Figure 7.2:** Convergence of mode-I stress intensity factors for increasing order of line elements.

The geometry of the plate is defined by width and lengths as  $W = 0.5$  m and  $L = 2$  m. The plate also contains discontinuity as an edge crack of length  $a = 0.25$  m. The arbitrary material properties of the plate are  $E = 1$  GPa,  $\nu = 0$ ,  $\kappa = 1 \text{ W}(\text{m}^\circ\text{C})^{-1}$ , and  $\alpha = 0.01 (\text{ }^\circ\text{C})^{-1}$ . Initially, the plate is at a reference temperature of  $\theta_0 = 0^\circ\text{C}$ . Then it is subjected to a temperature change

of  $\theta_1 = -50^\circ\text{C}$  and  $\theta_2 = 50^\circ\text{C}$  at the left and right sides, respectively. All the other sides are assumed to be insulated. Furthermore, the plate's top and bottom sides are restricted vertically. Both top and bottom corners on the right side are also constrained horizontally. Additionally, a plane strain state is assumed. The subjugation of temperature change results in a mode-I fracture. Figures 7.1(b) and 7.1(c) illustrate a sample mesh with 309 polygon elements and the resulting temperature distribution, respectively. In Fig. 7.1(c), the distorted mesh represents the scaled deformation for visualization purposes. The stress intensity factors are normalized such that  $\bar{K}_I = K_I(1 - \nu)/E\alpha\theta_2\sqrt{\pi a}$ .

| Coupled | Sequential | XFEM [44] | ES-FEM [161] | XCQ4 [162] |
|---------|------------|-----------|--------------|------------|
| 0.4966  | 0.4965     | 0.4955    | 0.496        | 0.496      |

**Table 7.1:** Results of normalized mode-I stress intensity factors for  $p = 2$  and 309 polygon elements.

First, a convergence study is conducted for the order of line elements  $p$  considering a high-density mesh with 2316 polygon elements. Figure 7.2 shows the convergence of normalized mode-I stress intensity factors for both coupled and sequential procedures. It is observed that the coupled approach has a higher convergence rate as compared to the sequential approach. The sequential approach relies on the accuracy of a prior solution of the temperature field. In certain cases, a linear (two-node) line element, i.e.,  $p = 1$ , cannot accurately capture the solution of the temperature field.

Nevertheless, both modeling approaches yield the same results for a line element with more than two nodes. Moreover, Table 7.1 lists the results of  $\bar{K}_I$  for a mesh with 309 polygon elements and  $p = 2$  compared with the reference solutions. The results of both coupled and sequential approaches are in excellent agreement with the reference solutions.

### 7.1.2 Mode-II Fracture – Plate with Center Crack

In this example, a plate with a center crack is analyzed. The plate is subjected to heat flux perpendicular to the crack resulting in mode-II stress intensity factors. Figure 7.3(a) presents the physical model of the plate. The geometry is defined as  $W = L = 1\text{ m}$ .

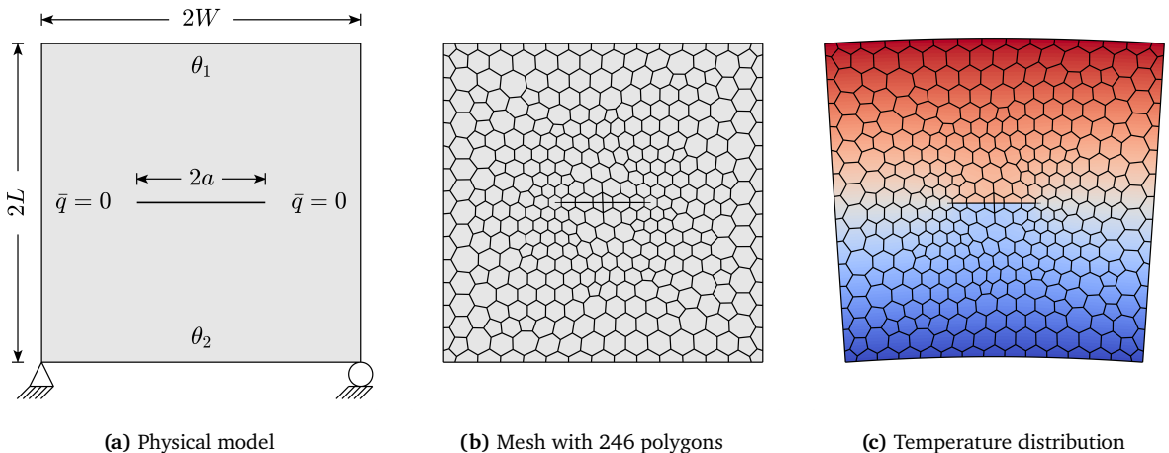


**Figure 7.3:** A physical and numerical model of a plate with a center crack under constant flux perpendicular to crack  
 (a) Geometry and boundary conditions. (b) A sample mesh of 246 polygon elements and  $a/W = 0.3$ . (c) The temperature distribution with scaled deformations at  $a/W = 0.3$ .

Different numbers of crack lengths  $a$  are taken into consideration. The plate is subjected to the

temperature changes of  $\theta_1 = 10^\circ\text{C}$  and  $\theta_2 = -10^\circ\text{C}$  at the top and bottom sides. Initially, the plate is at a reference temperature of  $\theta_0 = 0^\circ\text{C}$ . Furthermore, the bottom corner point of the left side is constrained in the horizontal and vertical directions. The bottom corner point of the right side is constrained in the vertical direction. The material properties of the plate are  $E = 1 \text{ GPa}$ ,  $\nu = 0.3$ ,  $\kappa = 1 \text{ W}(\text{m}^\circ\text{C})^{-1}$ , and  $\alpha = 1 (\text{ }^\circ\text{C})^{-1}$ . A plane strain state is assumed. Figures 7.3(b) and 7.3(c) show a sample mesh of 246 polygon elements and temperature distribution with scaled deformations. The mode-II stress intensity factor is normalized as  $\bar{K}_{II} = K_{II}/E\alpha\theta_1\sqrt{\pi W}$ . Figure 7.4(a) describes the convergence of  $\bar{K}_{II}$  for the quadratic order of line elements, i.e.,  $p = 2$ . Similar to the previous example, it is noted that the results of the coupled approach have a higher convergence rate for increasing mesh density than the sequential approach. However, for both approaches, the difference in the values of  $\bar{K}_{II}$  is of order  $10^{-4}$ .

| $a/W$    | 0.1  | 0.2  | 0.3  | 0.4  | 0.5  | 0.6  |
|----------|------|------|------|------|------|------|
| Polygons | 208  | 228  | 246  | 202  | 226  | 222  |
| Nodes    | 1198 | 1306 | 1404 | 1184 | 1312 | 1300 |

Table 7.2: Number of polygon and nodes used at different  $a/W$ .

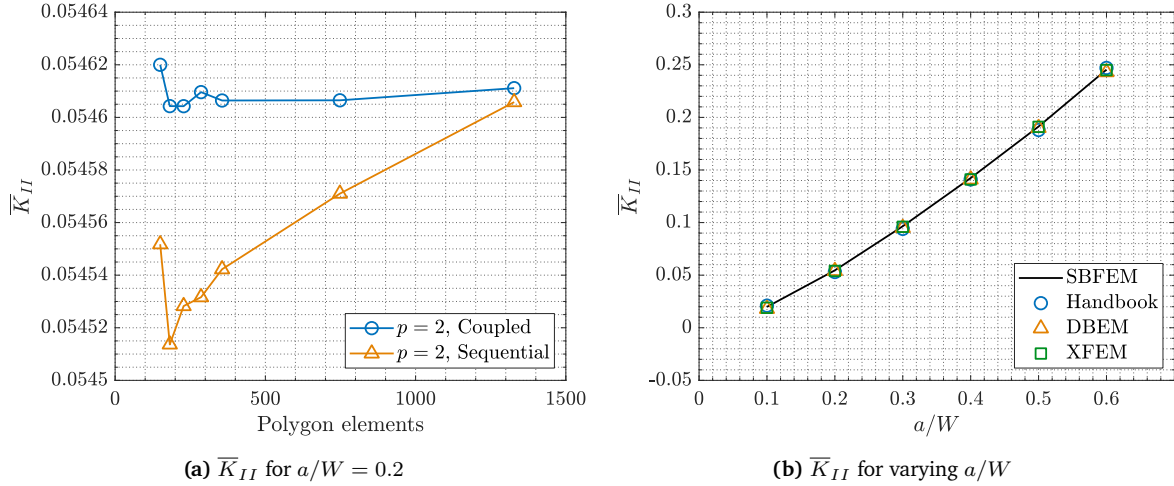


Figure 7.4: Convergence and results of  $\bar{K}_{II}$  of a plate with center crack. (a) Convergence of  $\bar{K}_{II}$  over the mesh density for  $a/W = 0.2$  and  $p = 2$ . (b)  $\bar{K}_{II}$  of coupled approach for varying  $a/W$ ,  $p = 2$ , and the maximum number of 246 polygon elements. The results are compared with the reference solutions of XFEM [44], DBEM [66], and Handbook [163].

| $a/W$ | Coupled | Sequential | XFEM [44] | DBEM [66] | Handbook [163] |
|-------|---------|------------|-----------|-----------|----------------|
| 0.1   | 0.0198  | 0.0198     | 0.019     | 0.018     | 0.021          |
| 0.2   | 0.0546  | 0.0545     | 0.054     | 0.054     | 0.053          |
| 0.3   | 0.0965  | 0.0964     | 0.096     | 0.095     | 0.094          |
| 0.4   | 0.1424  | 0.1423     | 0.141     | 0.141     | 0.141          |
| 0.5   | 0.1913  | 0.1912     | 0.191     | 0.19      | 0.188          |
| 0.6   | 0.2454  | 0.2451     | 0.245     | 0.243     | 0.247          |

Table 7.3: Results of  $\bar{K}_{II}$  for a plate with a center crack for different  $a/W$  compared to the reference solutions.

Next, Fig. 7.4(b) shows the results of  $\bar{K}_{II}$  of coupled approach for  $p = 2$  and varying  $a/W$ .

Table 7.2 lists the number of polygon elements used to obtain the values of  $\bar{K}_{II}$  at various  $a/W$  ratios. Furthermore, the results are compared with the reference solutions of XFEM [44], DBEM [66], and Handbook [163]. Table 7.3 lists the numeric values of  $\bar{K}_{II}$  for different  $a/W$ . It is observed that the values  $\bar{K}_{II}$  increase monotonically with increasing  $a/W$ . The results are in excellent agreement with the reference solutions.

### 7.1.3 Mixed-mode Fracture – Plate with Inclined Center Crack

This example analyzes a plate with an inclined center crack, as shown in Fig. 7.5(a). The plate with an inclined crack is subjected to the temperature change in the vertical direction resulting in a mixed-mode fracture.

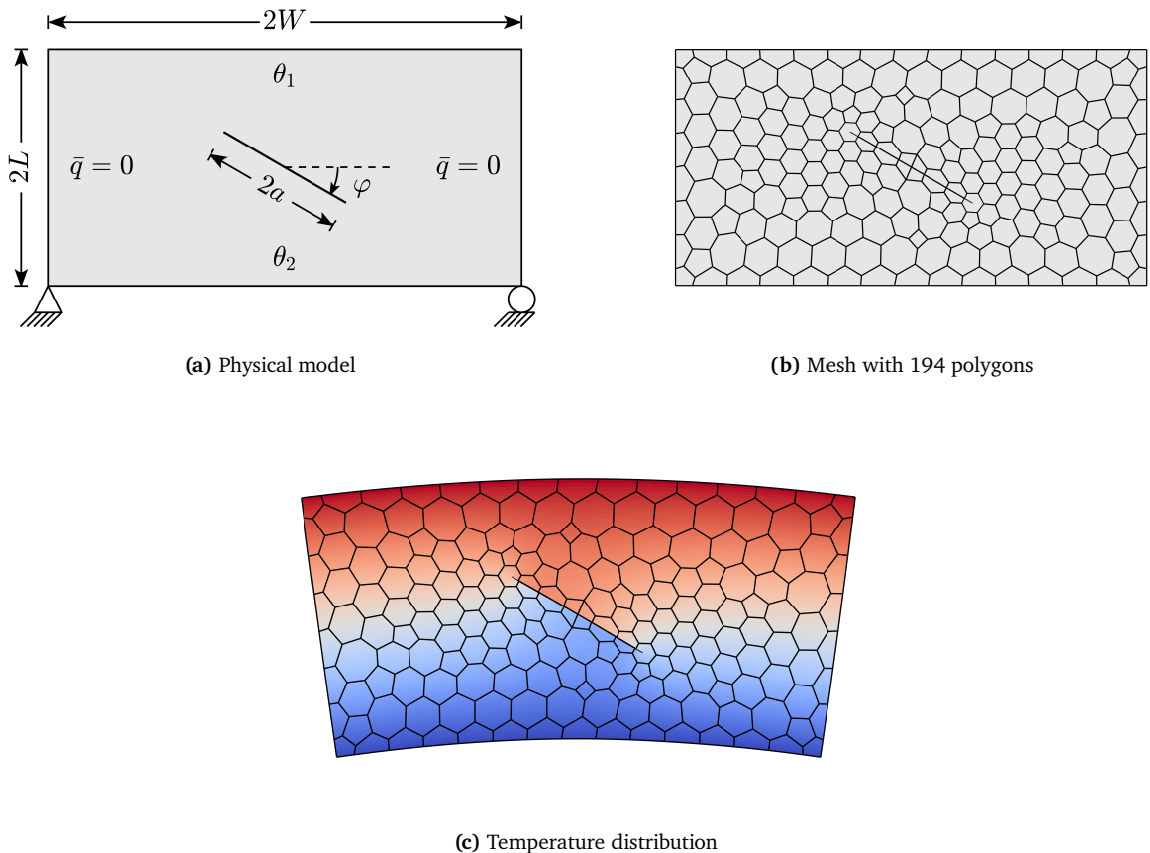


**Figure 7.5:** A plate with an inclined center crack. (a) Geometry and boundary conditions. (b) A sample mesh of 194 polygon elements for  $a/W = 0.3$  and  $\varphi = 30^\circ$ . (c) The temperature distribution with scaled deformations for  $a/W = 0.3$  and  $\varphi = 30^\circ$ .

The geometry of the plate is defined as  $W = 1$  m and  $L = 0.5$  m. The inclined crack is at an angle of  $\varphi$  from the horizontal axis in a clockwise direction. The effects of different crack configurations, i.e.,  $a$  and  $\varphi$ , on fracture, are considered. The plate is subjected to the temperature changes of  $\theta_1 = 10^\circ\text{C}$  and  $\theta_2 = -10^\circ\text{C}$  at the top and bottom sides. The reference temperature of the plate is  $\theta_0 = 0^\circ\text{C}$ . The bottom corner point of the left side is constrained in the horizontal and vertical directions. The bottom corner point of the right side is constrained in the vertical direction. The material properties of the plate are  $E = 1$  GPa,  $\nu = 0.3$ ,  $\kappa = 1 \text{ W} (\text{m}^\circ\text{C})^{-1}$ , and  $\alpha = 1 (\text{ }^\circ\text{C})^{-1}$ . A plane strain state is assumed.

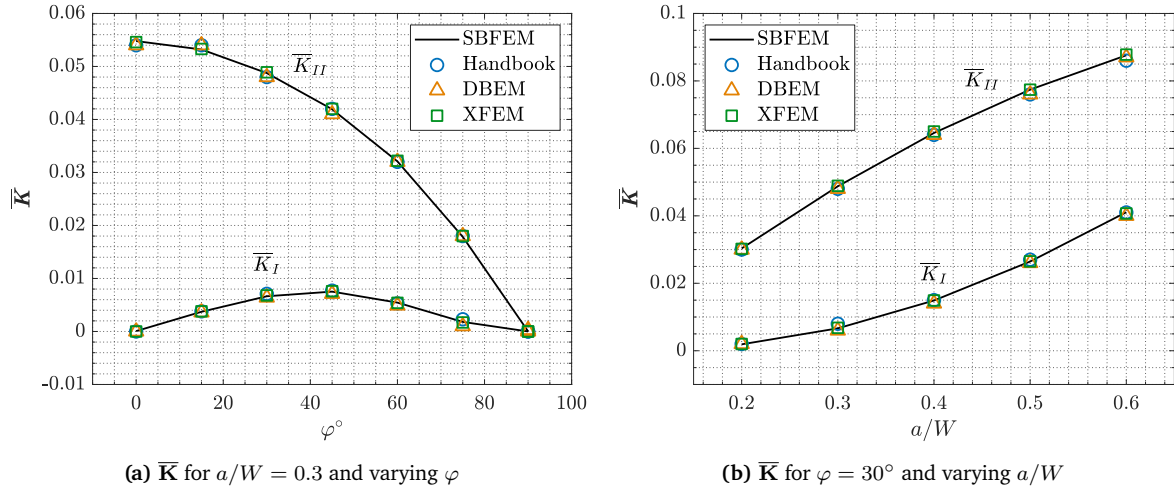


Figure 7.6:  $\bar{K}$  in a plate with an inclined center crack. (a) Variation of  $\bar{K}$  for varying  $\varphi$  at  $a/W = 0.3$ . (b) Variation of  $\bar{K}$  for varying  $a/W$  for  $\varphi = 30^\circ$ .

Figures 7.5(b) and 7.5(c) describe the mesh of 194 polygon elements and temperature distribution with scaled deformations for  $\varphi = 30^\circ$  and  $a/W = 0.3$ . The results of stress intensity factors are compared with the reference solutions of XFEM [44], DBEM [66], and Handbook [163] for different configurations of crack. The stress intensity factors are normalized as  $\bar{K} = K/K_0$  with  $K_0 = E\alpha\theta_1(W/L)\sqrt{2W}$ .

Figures 7.6(a) and 7.6(b) present the results of normalized stress intensity factors compared to the reference solutions. Figure 7.6(a) illustrates the variation of  $\bar{K}$  as a function of the crack inclination angle for constant  $a/W = 0.3$ . Higher values of  $\bar{K}_{II}$  are observed compared to  $\bar{K}_I$ . Furthermore,  $\bar{K}_{II}$  decreases with increasing crack inclination. Figure 7.6(b) describes the effects of  $a/W$  on  $\bar{K}$  for constant  $\varphi = 30^\circ$ . Higher values of  $\bar{K}_{II}$  are also observed in the case of varying crack lengths. Both  $\bar{K}_I$  and  $\bar{K}_{II}$  increase monotonically with the increase of  $a/W$ . The results are in good agreement with the reference solutions.

## 7.2 Stress Intensity Factors in FGMs

This section presents three numerical examples to illustrate fracture modeling in functionally graded materials using the SBFEM. In all examples, an edge crack in the plate causes stress singularities that lead to a fracture. The first example considers a plate with linearly varying isotropic material properties. The second numerical example deals with a steep material gradient defined by a hyperbolic tangent function. Lastly, the orthotropic material variation governed by a power-law function is considered.

### 7.2.1 Plate with Linearly Varying Material Properties

This example presents a validation of thermo-elastic fracture modeling in functionally graded materials using SBFEM. For this purpose, a plate with an edge crack and linearly varying isotropic material properties are considered. The solution to this problem using the SBFEM is already published in [155]. Here, the example is presented again for completeness. Figure 7.7(a) shows a physical model of an isotropic plate with a linear material gradient in  $x$ -direction. The width and length of the plate are  $W = 1$  m and  $L = 4$  m. The preexisting crack is assumed to be of varying length. Furthermore, the plate is at a reference temperature of  $\theta_0 = 0^\circ\text{C}$ . The right side of the plate is subjected to a temperature change of  $\theta_2 = 1^\circ\text{C}$ , while the left side is kept at the reference temperature, i.e.,  $\theta_1 = \theta_0$ . All the other sides are insulated.

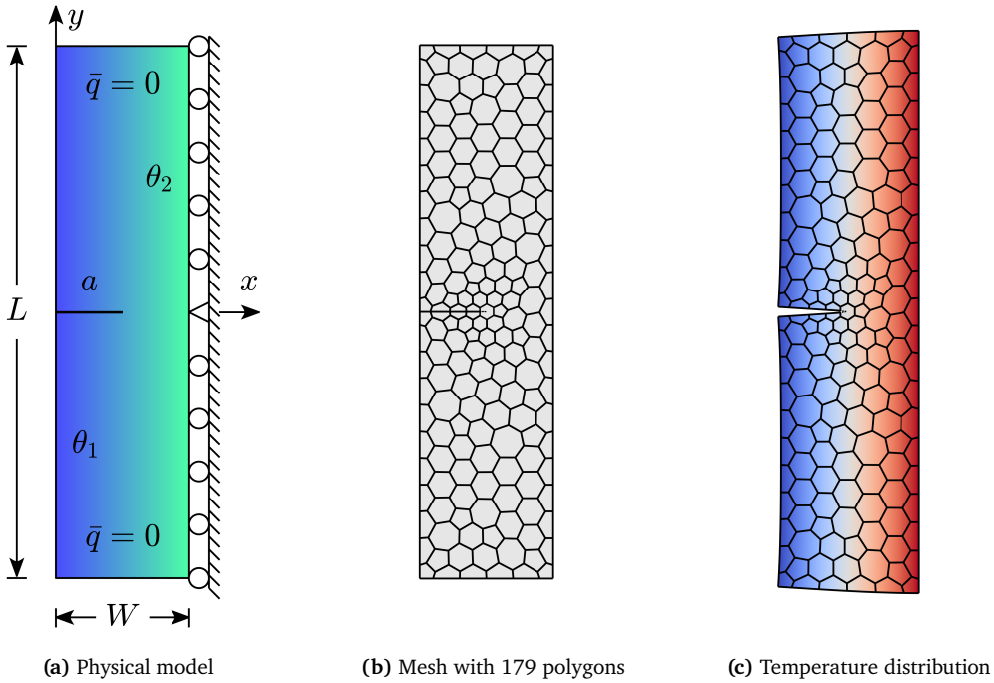


**Figure 7.7:** A plate with an edge crack and linearly varying material properties. (a) A physical model of a plate. (b) A sample mesh with 179 polygon elements for  $a/W = 0.5$ . (c) Temperature distribution and scaled deformations at  $a/W = 0.5$ .

Additionally, the right side of the plate is constrained in  $x$ -direction, with the midpoint of the right side also constrained in  $y$ -direction. The plate is assumed to be in a plane strain state. A constant value of thermal conductivity, i.e.,  $\kappa(x) = 1 \text{ W (m}^\circ\text{C)}^{-1}$ , is considered. The functional grading of other material properties is defined as follows

$$E(x) = E^0 + (E^1 - E^0)x, \quad (7.2a)$$

$$\nu(x) = \nu^0 + (\nu^1 - \nu^0)x, \quad (7.2b)$$

$$\alpha(x) = \alpha^0 + (\alpha^1 - \alpha^0)x, \quad (7.2c)$$

where Table 7.4 presents the values of material properties at  $x = 0$  and  $x = W$ .

| $x$ | $E \text{ MPa}$         | $\nu$          | $\alpha (\text{ }^\circ\text{C})^{-1}$ |
|-----|-------------------------|----------------|--|
| 0   | $E^0 = 1 \times 10^5$   | $\nu^0 = 0.3$  | $\alpha^0 = 1.67 \times 10^{-5}$       |
| $W$ | $E^1 = 0.5 \times 10^5$ | $\nu^1 = 0.35$ | $\alpha^1 = 1 \times 10^{-5}$          |

**Table 7.4:** Material properties at the left and right sides of a FG plate.

The given material variation is a linear function of the  $x$  coordinate. Hence, the polynomial fitting order of  $n = 1$  is chosen in Eq. (5.4). Figures 7.7(b) and 7.7(c) show a sample mesh of 179 polygon elements and the temperature distribution with scaled deformations for  $a/W = 0.5$ , respectively. The convergence study over the number of polygons is performed, and the results of  $K_I$  are compared with the reference solution of interaction integrals [86]. The number of polygon elements used in obtaining the results at different  $a/W$  are listed in Table 7.5. Figure 7.8(a) presents the resulting mode-I stress intensity factors using different polygon elements for  $a/W = 0.5$ . A convergent behavior of  $K_I$  is observed with increasing mesh density. A difference of 0.245% is observed compared to the reference solution for the mesh with  $\approx 600$  polygon elements.

| $a/W$    | 0.1  | 0.2  | 0.3  | 0.4  | 0.5  | 0.6  | 0.7  | 0.8  |
|----------|------|------|------|------|------|------|------|------|
| Polygons | 604  | 599  | 612  | 618  | 616  | 614  | 613  | 620  |
| Nodes    | 3262 | 3241 | 3314 | 3348 | 3342 | 3334 | 3339 | 3382 |

**Table 7.5:** Number of nodes and polygon elements used to discretize the FG plate with linearly varying material properties at different  $a/W$ .

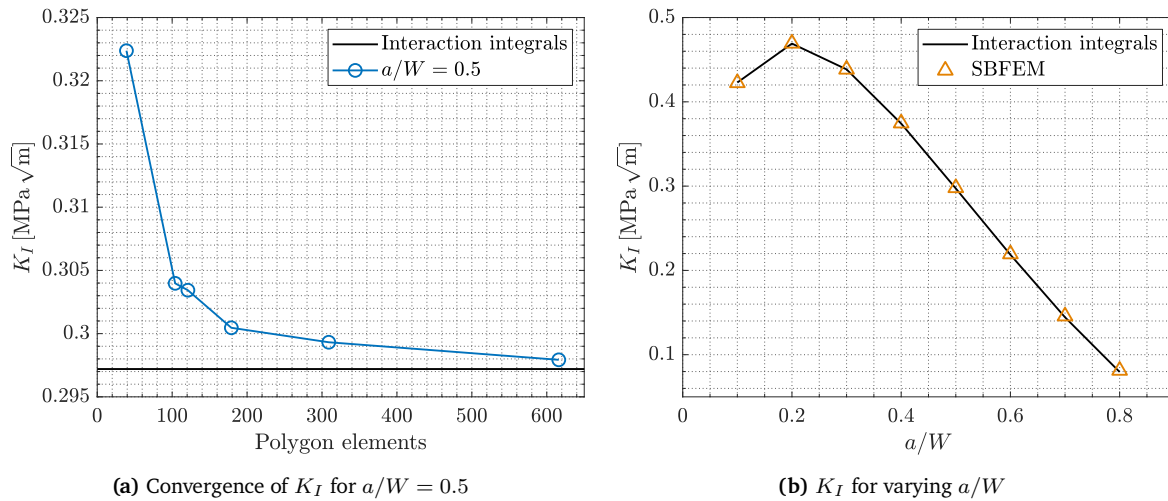


**Figure 7.8:** Results of  $K_I$  in FG plate with linearly varying material properties. (a) Converge of  $K_I$  with increasing number of polygon elements for  $a/W = 0.5$  and  $p = 2$ . (b)  $K_I$  at different  $a/W$  with a maximum number of 620 polygon elements and  $p = 2$ . The results are compared with the reference solution of interaction integrals in [86].

Figure 7.8(b) and Table 7.6 present the results of  $K_I$  for varying  $a/W$  compared to the reference solution in [86]. It is observed that the values of  $K_I$  increase until  $a/W = 0.2$ . Afterward, they started to decline as  $a/W$  increased. Compared to the reference solution, the maximum difference of 2.2% is noted for  $a/W = 0.8$ . In [86], the reported number of elements and nodes used in the discretization of FG plate are 568 and 1163, respectively. Note that the method of interaction integrals requires additional post-processing, i.e.,  $J$ -integral to obtain the stress intensity factors.

| $a/W$ | 0.1    | 0.2    | 0.3    | 0.4    | 0.5    | 0.6    | 0.7    | 0.8    |
|-------|--------|--------|--------|--------|--------|--------|--------|--------|
| SBFEM | 0.4225 | 0.4693 | 0.4385 | 0.3747 | 0.2979 | 0.2194 | 0.1457 | 0.0813 |
| [86]  | 0.4229 | 0.4691 | 0.4385 | 0.3742 | 0.2972 | 0.2186 | 0.1444 | 0.0795 |

**Table 7.6:** Comparison of  $K_I$  with the method of interaction integrals [86] for varying  $a/W$  in FG plate with linear material gradient.

## 7.2.2 Plate with Hyperbolic Tangent Material Gradient

This example considers a plate with an edge crack and a steep material gradient defined by a hyperbolic tangent function. Figure 7.9(a) depicts the physical model of an FG plate with isotropic material properties varying in the  $x$ -direction. The geometry of the plate is defined by  $W = 2$  m and  $L = 4$  m. Varying length of an edge crack  $a$  is considered. The reference temperature of the plate is  $\theta_0 = 0$  °C. The applied temperature change of the left side is  $\theta_1 = -10$  °C while the temperature of the right side is kept constant at the reference temperature, such that  $\theta_2 = \theta_0$ . All the other sides are insulated. The bottom side of the plate is constrained in the  $y$ -direction. Also,

the left corner point of the bottom side is constrained in the  $x$ -direction. Both plane strain and stress states are considered.

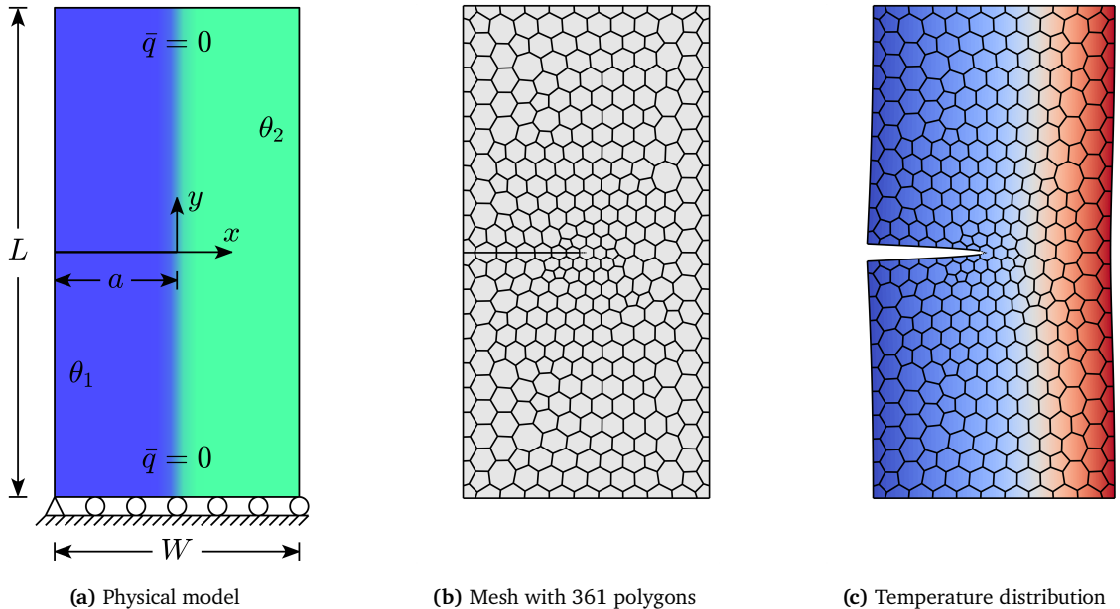


**Figure 7.9:** A plate with an edge crack and hyperbolic tangent material gradient. (a) A physical model of a plate. (b) A sample mesh with 361 polygon elements for  $a/W = 0.5$ . (c) Temperature distribution and scaled deformations at  $a/W = 0.5$ .

The material properties of an isotropic plate are the function of the  $x$ -coordinate and are expressed as follows

$$E(x) = \frac{E^+ + E^-}{2} + \frac{E^+ - E^-}{2} \tanh(\gamma x), \quad (7.3a)$$

$$\nu(x) = \frac{\nu^+ + \nu^-}{2} + \frac{\nu^+ - \nu^-}{2} \tanh(\omega x), \quad (7.3b)$$

$$\alpha(x) = \frac{\alpha^+ + \alpha^-}{2} + \frac{\alpha^+ - \alpha^-}{2} \tanh(\omega x), \quad (7.3c)$$

$$\kappa(x) = \frac{\kappa^+ + \kappa^-}{2} + \frac{\kappa^+ - \kappa^-}{2} \tanh(\omega x), \quad (7.3d)$$

where the gradient indices  $\gamma = 15 \text{ (m)}^{-1}$  and  $\omega = 5 \text{ (m)}^{-1}$ . The additional coefficients  $(*)^-$  and  $(*)^+$  are given in Table 7.7. A sample mesh with 361 polygon elements and temperature distribution with scaled deformations for  $a/W = 0.5$  are shown in Figures 7.9(b) and 7.9(c), respectively.

| $x$    | $E \text{ MPa}$ | $\nu$         | $\alpha \text{ (K)}^{-1}$ | $\kappa \text{ W (mK)}^{-1}$ |
|--------|-----------------|---------------|---------------------------|------------------------------|
| $-W/2$ | $E^- = 3$       | $\nu^- = 0.1$ | $\alpha^- = 0.03$         | $\kappa^- = 3$               |
| $W/2$  | $E^+ = 1$       | $\nu^+ = 0.3$ | $\alpha^+ = 0.01$         | $\kappa^+ = 1$               |

**Table 7.7:** Additional material coefficients of hyperbolic tangent gradation.

A steep material gradient is present between  $a/W = 0.4$  and  $a/W = 0.6$  in the given Eq. (7.3). Thus, a convergence study is performed over the increasing number of polygon elements and polynomial fitting order  $n$  in Eq. (5.4). Figure 7.10(a) shows the values of  $K_I$  for the different

numbers of polygon elements and fitting order. As expected,  $n = 1$  is insufficient to fit the material variation.

| $a/W$    | 0.1  | 0.2  | 0.3  | 0.4  | 0.5  | 0.6  | 0.7  | 0.8  |
|----------|------|------|------|------|------|------|------|------|
| Polygons | 572  | 609  | 621  | 645  | 679  | 654  | 643  | 619  |
| Nodes    | 3068 | 3261 | 3329 | 3457 | 3635 | 3518 | 3467 | 3355 |

**Table 7.8:** Number of nodes and polygon elements used to discretize the FG plate with hyperbolic tangent material variation at different  $a/W$ .

Nevertheless, a convergent behavior is observed for increasing number of polygon elements and fitting order. As suggested in Section 5.2,  $n = 2$  is adequate to fit any given material variation as long as the size of polygon elements is sufficiently small. Figure 7.10(b) shows the values of  $K_I$  for  $n = 2$  at different  $a/W$  compared to the reference solution of interaction integrals in [86]. For varying  $a/W$ , the number of polygon elements used to obtain the results of  $K_I$  are listed in Table 7.8.

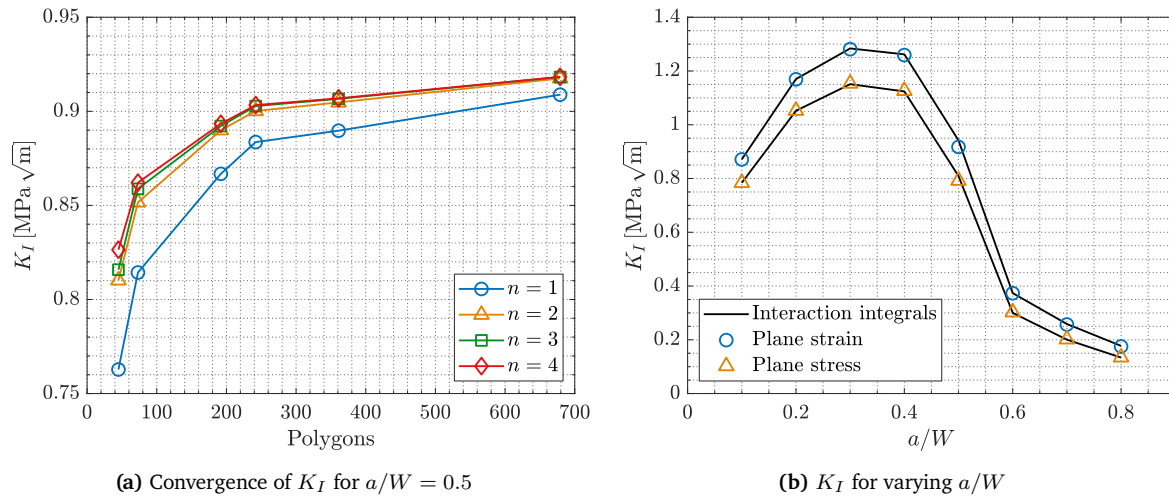


**Figure 7.10:** Results of  $K_I$  in FG plate with material variation defined by hyperbolic tangent function. (a) Convergence of  $K_I$  with increasing number of polygon elements and fitting order  $n$  for  $a/W = 0.5$ . (b)  $K_I$  at different  $a/W$  with the maximum number of 679 polygon elements and  $n = 2$ . The results are compared with the reference solution of interaction integrals in [86] for plane strain and plane stress states.

| $a/W$ | Plane Strain |        | Plane Stress |        |
|-------|--------------|--------|--------------|--------|
|       | SBFEM        | [86]   | SBFEM        | [86]   |
| 0.1   | 0.8709       | 0.8713 | 0.784        | 0.7841 |
| 0.2   | 1.1691       | 1.17   | 1.0527       | 1.052  |
| 0.3   | 1.2812       | 1.284  | 1.1534       | 1.151  |
| 0.4   | 1.2592       | 1.262  | 1.1264       | 1.124  |
| 0.5   | 0.9175       | 0.9417 | 0.7922       | 0.8092 |
| 0.6   | 0.3732       | 0.3737 | 0.3025       | 0.3002 |
| 0.7   | 0.2568       | 0.2588 | 0.2019       | 0.2006 |
| 0.8   | 0.1753       | 0.1774 | 0.1348       | 0.1338 |

**Table 7.9:** Comparison of  $K_I$  with the method of interaction integrals [86] for varying  $a/W$  and  $n = 2$  in FG plate with hyperbolic tangent material gradient.

Additionally, Table 7.9 presents the same numeric values of  $K_I$  for both plane strain and plane stress states, as shown in Fig. 7.10(b). The higher values of  $K_I$  are observed in the plane strain state compared to the plane stress state. The maximum difference of 2.57% is noted compared to the reference solution at  $a/W = 0.5$ , where the steep material gradient is present. The results presented in Table 7.9 are obtained with  $n = 2$ .

### 7.2.3 Orthotropic Plate with Power-law Material Gradient

In the last example of this section, an orthotropic functionally graded plate with a center crack is studied. The results of this numerical example have already been published in [155]. Figure 7.11(a) shows the physical model of the plate. The material variation is a function of the  $y$  coordinate. The bottom side of the plate ( $y = 0$ ) is 100% metal, i.e., nickel (Ni), and the top side of the plate ( $y = L$ ) is 100% orthotropic ceramic, i.e., alumina ( $\text{Al}_2\text{O}_3$ ). The 1st, 2nd, and out of plane principal axes of orthotropy are aligned with  $x$ ,  $y$ , and  $z$  axes, respectively. The geometry of the plate is defined by  $W = 1$  m,  $L/W = 0.4$ , and  $a/W = 0.1$ . Different vertical positions of the crack, i.e.,  $b/W$ , are considered in the modeling.

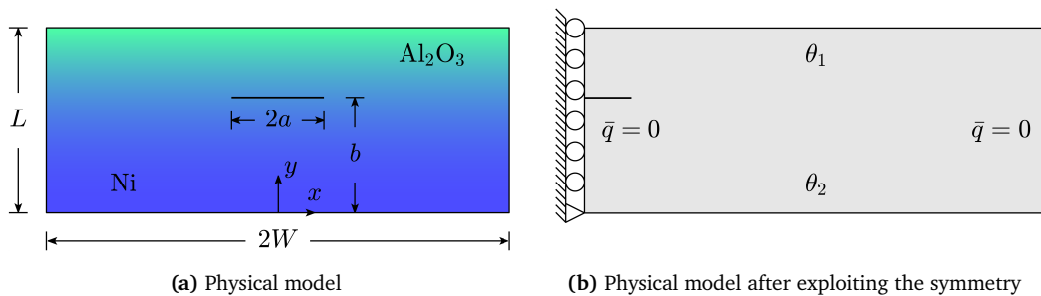


**Figure 7.11:** Model of an orthotropic FG plate with a center crack. (a) A complete model of the plate. (b) Model of the plate after exploiting symmetry.

Initially, the plate is at a reference temperature of  $\theta_0 = 1100$  K. Afterward, the temperature change of  $\theta_1 = \theta_0$  is applied on the top side of the plate. The bottom side is kept at the reference temperature by setting the temperature change of  $\theta_2 = 0$  K. All the other sides are insulated. Owing to the symmetry of the problem along the  $y$ -axis, only half of the plate is modeled, as shown in Fig. 7.11(b). Additionally, the left side of the plate is constrained in  $x$ -direction, and the lower corner point of the left side is also constrained in  $y$ -direction. A state of plane strain is assumed.

The material variation in the  $y$ -direction is defined by a power-law function as follows

$$P(y) = P^m + (P^c - P^m) \left( \frac{y}{L} \right)^r, \quad (7.4)$$

where  $P^m$  and  $P^c$  denote metal and ceramic material properties, respectively. Table 7.10 lists the thermal and mechanical material properties of metal (Ni) and ceramic ( $\text{Al}_2\text{O}_3$ ). In Eq. (7.4),  $P(y)$  represents the variation of  $E_1$ ,  $E_2$ ,  $G_{12}$ ,  $\nu_{12}$ ,  $\nu_{13}$ ,  $\nu_{31}$ ,  $\nu_{32}$ ,  $\alpha_1$ ,  $\alpha_2$ ,  $\alpha_3$ ,  $\kappa_1$ , and  $\kappa_2$ . Furthermore, the superscript  $r$  defines the gradient index of the mentioned properties respectively, i.e.,  $\gamma_1$ ,  $\gamma_2$ ,  $\gamma_{12}$ ,  $\beta_{12}$ ,  $\beta_{13}$ ,  $\beta_{31}$ ,  $\beta_{32}$ ,  $\delta_1$ ,  $\delta_2$ ,  $\delta_3$ ,  $\omega_1$ , and  $\omega_2$ . For all the properties, the gradient index  $r$  is a positive constant.  $r < 1$  signifies the metal-rich profile, while  $r > 1$  symbolizes the ceramic-rich profile.

| Properties                       | Nickel (Ni)       | Alumina ( $\text{Al}_2\text{O}_3$ ) |                      |                    |
|----------------------------------|-------------------|-------------------------------------|----------------------|--------------------|
| modulus GPa                      | $E^m = 204$       | $E_1^c = 90.43$                     | $E_2^c = 116.36$     | $G_{12}^c = 38.21$ |
| $\alpha 10^{-6} (\text{K})^{-1}$ | $\alpha^m = 13.3$ | $\alpha_1^c = 8$                    | $\alpha_2^c = 7.5$   | $\alpha_3^c = 9$   |
| $\kappa \text{ W (mK)}^{-1}$     | $\kappa^m = 70$   | $\kappa_1^c = 21.25$                | $\kappa_2^c = 29.82$ |                    |
| $\nu$                            | $\nu^m = 0.31$    | $\nu_{12}^c = 0.22$                 | $\nu_{13}^c = 0.14$  |                    |
|                                  |                   | $\nu_{31}^c = 0.14$                 | $\nu_{32}^c = 0.21$  |                    |

**Table 7.10:** Thermal and mechanical material properties of nickel (Ni) and alumina ( $\text{Al}_2\text{O}_3$ ).

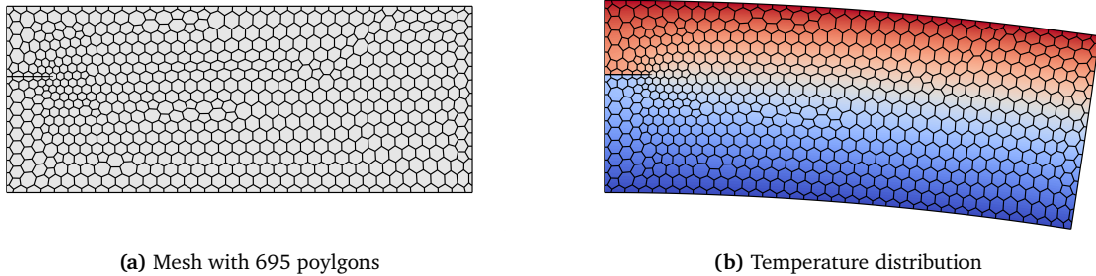


**Figure 7.12:** Mesh and temperature distribution of the FG plate with orthotropic material gradient defined by power-law function. (a) Mesh with 695 polygon elements for  $b/W = 0.25$ . (b) Temperature distribution and scaled deformation for  $b/W = 0.25$  and  $\omega_2=1$ .

The effects of any individual material property on thermo-elastic fracture can be studied independently. Here, the effect of thermal conductivity in the  $y$ -direction  $\kappa_2$  is considered for validation purposes. The gradient indices of other properties are chosen as  $\gamma_1 = \gamma_2 = \gamma_{12} = 2$ ,  $\beta_{12} = \beta_{13} = \beta_{31} = \beta_{32} = 1.5$ ,  $\delta_1 = \delta_2 = \delta_3 = 3$ , and  $\omega_1 = 4$ . Figures 7.12(a) and 7.12(b) show a mesh with 695 polygon elements and temperature distribution with scaled deformation, respectively, for  $b/W = 0.25$  and  $\omega_2 = 1$ . The stress intensity factors are normalized as  $\bar{\mathbf{K}} = \mathbf{K}/\alpha_1^c E_1^c \theta_0 \sqrt{\pi a}$ . The results of normalized stress intensity factors  $\bar{\mathbf{K}}$  are compared to the reference solution of  $J_k$ -integral in [164]. Figures 7.13(a) and 7.13(b) present the values of  $\bar{K}_I$  and  $\bar{K}_{II}$  at different  $b/W$  for varying gradient index  $\omega_2$ .

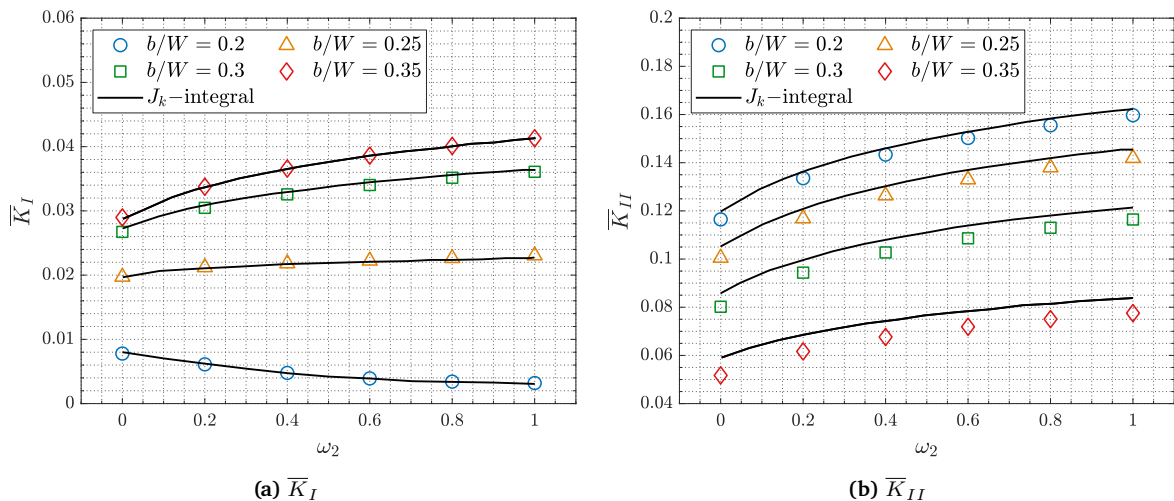


**Figure 7.13:** Normalized stress intensity factors of an orthotropic FG plate for varying  $b/W$  and  $\omega_2$  compared to the reference solution of  $J_k$ -integral in [164]. (a) Normalized mode-I stress intensity factors  $\bar{K}_I$ . (b) Normalized mode-II stress intensity factors  $\bar{K}_{II}$ .

For constant values of gradient index  $\omega_2$ ,  $\bar{K}_I$  increases with increasing  $b/W$ . Contrary to  $\bar{K}_I$ ,  $\bar{K}_{II}$  decreases with increasing  $b/W$  for constant  $\omega_2$ . Compared to  $\bar{K}_I$ , higher values of  $\bar{K}_{II}$  are noted for all  $b/W$ . The results of normalized stress intensity factors are in good agreement with the reference solution reported in [164].

## 7.3 Quasi-Static Crack Propagation

This section presents three problems of propagating cracks under thermo-mechanical loading in uni-directional coupling. The first example considers a cruciform-shaped panel with a corner crack. This problem of quasi-static crack propagation holds the benchmark status in uni-directional coupling. Using the SBFEM sequential procedure, the results of crack paths under different thermo-mechanical loading are presented in [154]. Here, they are presented for coupled approach. The second example considers a perforated plate with an edge crack. Similar to the first example, the results of this perforated plate are published in [154] using a sequential approach. Finally, a plate with multiple perforations and cracks emanating from one of these perforations is considered. In all problems, the re-meshing of domains is achieved using the localized re-meshing technique based on background-triangular elements, as discussed in Section 6.2.2.

### 7.3.1 Corner Crack in Cruciform Panel

This example deals with a cruciform-shaped panel with a corner crack under different thermo-mechanical boundary conditions. This example is first studied in [65] using the dual boundary element method (DBEM). Afterward, it is reproduced in several other works of literature using varieties of other numerical methods, e.g., [44, 161, 162, 165–169]. Figure 7.14(a) shows a model of the cruciform-shaped panel with a corner crack.

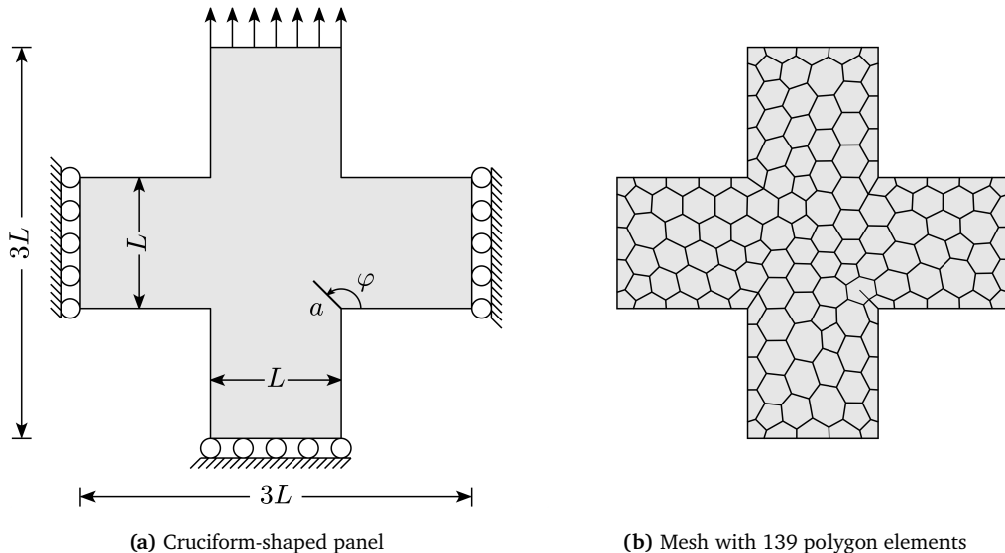


**Figure 7.14:** Physical model and discretization of a cruciform-shaped panel. (a) Geometry and boundary conditions. (b) Initial mesh with 139 polygon elements.

The panel's geometry is  $L = 1$  m, and the crack length  $a = 0.2$  m. The crack is at an angle of  $\varphi = 135^\circ$  from the horizontal axis. The panel's material properties are given as  $E = 218400$  Pa,  $\nu = 0.3$ ,  $\kappa = 1 \text{ W} (\text{m}^\circ\text{C})^{-1}$ , and  $\alpha = 1.67 \times 10^{-5} (\text{ }^\circ\text{C})^{-1}$ . The reference temperature of the panel is  $\theta_0 = 0$   $^\circ\text{C}$ . The right and left sides of the panel are constrained in the horizontal direction. The bottom side is constrained in the vertical direction. All the other sides are insulated except for the top, left, bottom, and right sides. The panel is in a plane strain state.

| BCs<br>Set | Temperature change in °C |      |        |       | Traction in Pa<br>Top |
|------------|--------------------------|------|--------|-------|-----------------------|
|            | Top                      | Left | Bottom | Right |                       |
| 1          | 10                       | 0    | -10    | 0     | 0                     |
| 2          | 0                        | 0    | 0      | 0     | 10                    |
| 3          | 10                       | 0    | -10    | 0     | 10                    |
| 4          | 20                       | 0    | -20    | 0     | 10                    |
| 5          | 10                       | -5   | -10    | -5    | 10                    |

**Table 7.11:** Sets of thermo-mechanical boundary conditions applied to a cruciform-shaped panel.

Five different sets of thermo-mechanical boundary conditions are applied, as listed in Table 7.11. Sets 1 and 2 of boundary conditions are purely thermal and mechanical, respectively. Sets 3-5 are mixed thermo-mechanical boundary conditions. Eleven quasi-static crack propagation steps with the incremental crack length of  $\Delta a = 0.3a$  are conducted for all five sets of boundary conditions. The stress intensity factors are normalized as  $\bar{K} = K/E\alpha\sqrt{\pi a}$ . The results of  $\bar{K}$  are compared with the reference solution of DBEM reported in [65]. Figures 7.15(a) and 7.15(b) present the normalized stress intensity factors  $\bar{K}_I$  and  $\bar{K}_{II}$ , respectively. Figure 7.16 shows the crack paths for all five sets of boundary conditions compared to the reference solution.

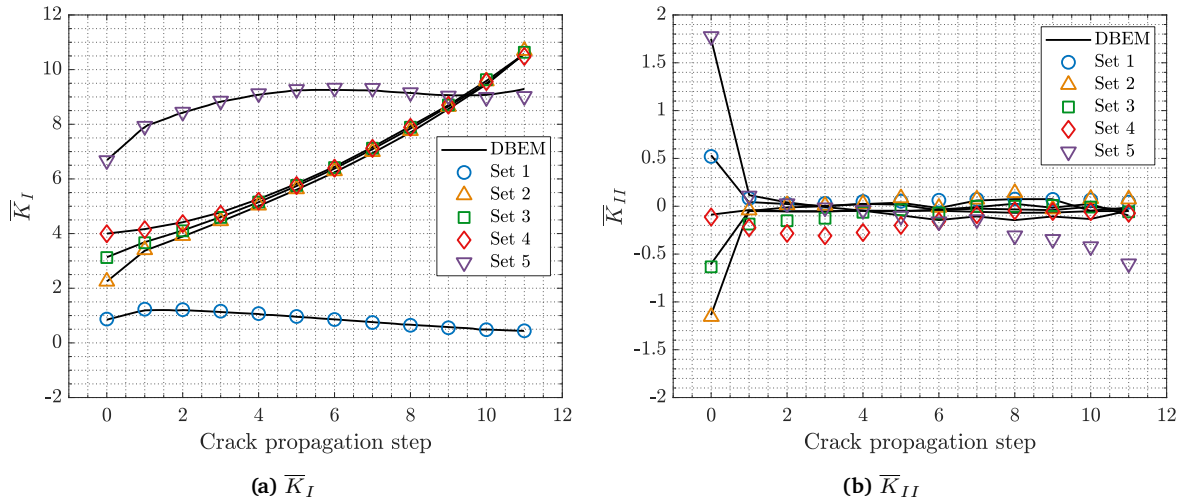


**Figure 7.15:** Normalized stress intensity factors of a cruciform-shaped panel for five sets of boundary conditions and 11 crack incremental steps compared with [65]. (a) Normalized mode-I stress intensity factors. (b) Normalized mode-II stress intensity factors.

It is observed that  $\bar{K}_I$  for sets 2-4 increases monotonically for each step of crack propagation. For set 5,  $\bar{K}_I$  becomes almost constant after the fourth crack propagation step. The crack will virtually arrest for set 1 after a few steps as  $\bar{K}_I \approx 0$ . Furthermore, it is noted that for sets 1-4,  $\bar{K}_{II} \approx 0$  after a few crack steps. The crack paths of mixed thermo-mechanical boundary conditions, i.e., 3-5, are between the crack paths of purely thermal and mechanical boundary conditions sets. Analyzing Eq. (2.87) reveals that the ratio  $K_{II}/K_I$  dictates the change in the direction of the crack path. Also, the crack path becomes a straight line if  $K_{II} \approx 0$ . As evident from Fig. 7.16, the crack paths for sets 1-4 are straight lines after a few crack propagation steps, which is justified as  $K_{II} \approx 0$  for these sets. The results of  $\bar{K}$  and crack paths agree with the reference solution of DBEM in [65].

Finally, Figs. 7.17(a) and 7.17(b) illustrate the temperature distributions at the initial and final

steps of crack propagation for the fifth set of boundary conditions. For all the sets of boundary conditions and 11 crack propagation steps, a maximum number of 79 additional polygon elements are generated during the localized remeshing of the domain.

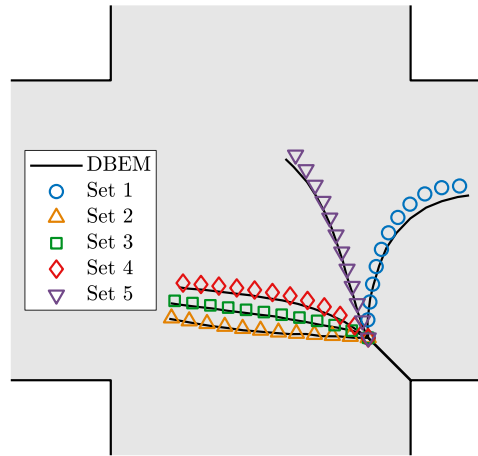


**Figure 7.16:** Crack paths in a cruciform-shaped panel for five sets of boundary conditions with  $\Delta a = 0.3a$  compared to [65].

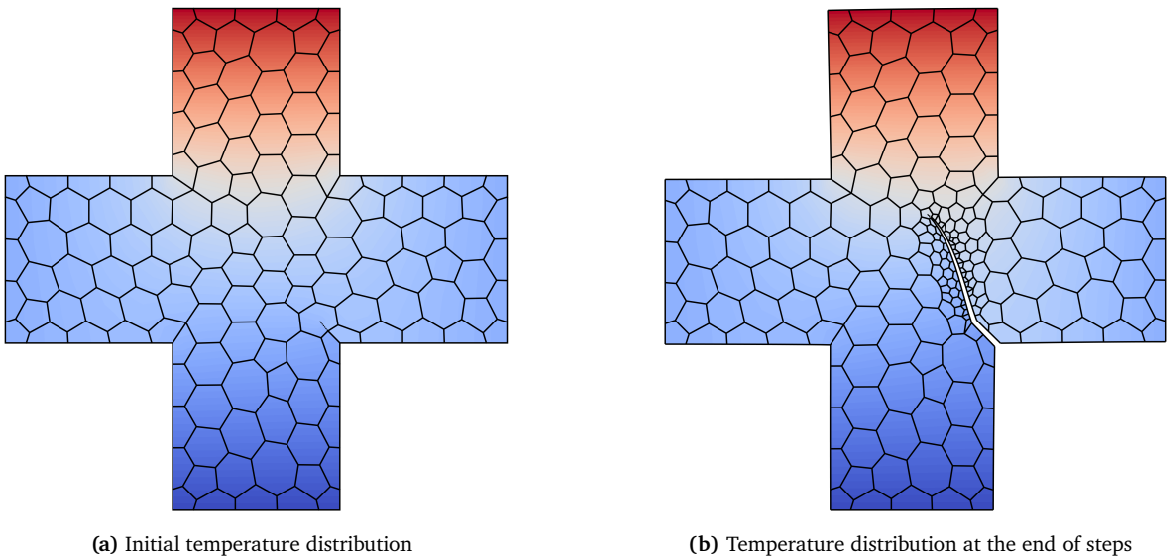


**Figure 7.17:** Initial and final temperature distribution for the fifth set of boundary conditions after 11 crack propagation steps.

### 7.3.2 Edge Crack in Perforated Plate

In this example, a perforated plate with an edge crack is analyzed. Two different cases of mechanical constraints are applied, and the thermal boundary conditions are kept identical for both cases. Figure 7.18(a) shows the geometry of the perforated plate. All the dimensions are in m, and the length of an edge crack is  $a = 0.15$  m. Figures 7.18(b) and 7.18(c) illustrate two different cases of mechanical constraints. In case one, the top and bottom sides are constrained vertically. The right corners of the top and bottom sides are also constrained in the horizontal direction. In case two, only the top and bottom sides are constrained in the vertical direction. The reference temperature of the plate is  $\theta_0 = 0^\circ\text{C}$ . The temperature changes of  $\theta_1 = -10^\circ\text{C}$  and  $\theta_2 = 10^\circ\text{C}$  are applied on the right and left sides of the plate, respectively. All the other sides are insulated.

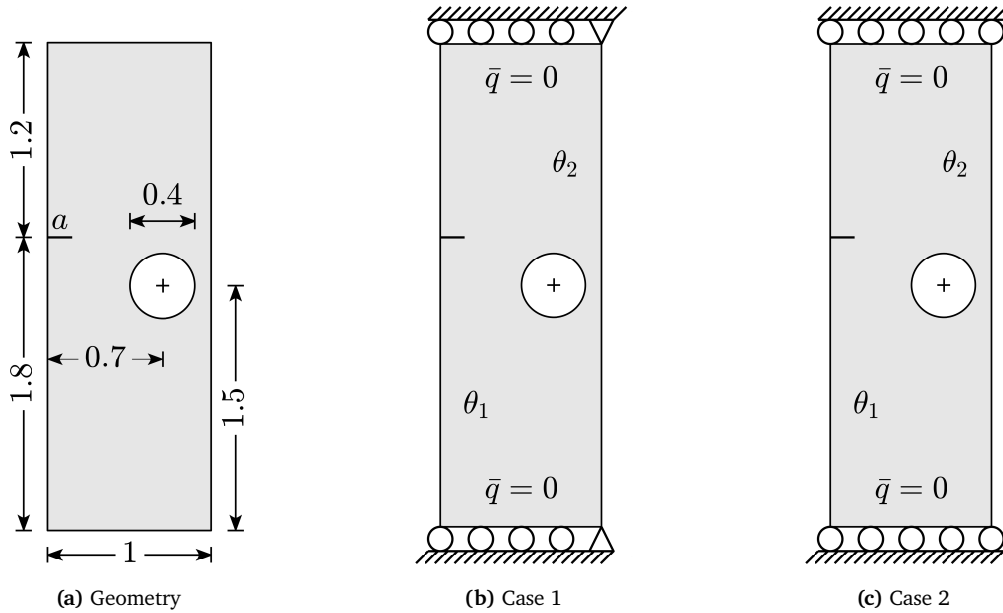


**Figure 7.18:** Geometry and boundary conditions of the perforated plate. (a) The geometry of the plate in m with a crack length of  $a = 0.15$  m. (b) Case 1 of mechanical constraints. (c) Case 2 of mechanical constraints.

The material properties of the plate are  $E = 30$  GPa,  $\nu = 0.2$ ,  $\kappa = 5 \text{ W}(\text{m}^\circ\text{C})^{-1}$ , and  $\alpha = 15 \times 10^{-6} (\text{ }^\circ\text{C})^{-1}$ . The plate is in a plane strain state. The crack propagation simulation is run for different crack incremental lengths  $\Delta a$ . Figures 7.19(a) and 7.19(b) show  $K$  of case 1 and 2 constraints for  $\Delta a = 0.05$  m. The crack path obtained for the case 1 constraints is compared with the reference solution of the extended four-node consecutive-interpolation quadrilateral element (XCQ4) [170]. For case 2 constraints, the result is compared with the meshless local Petrov-Galerkin method (MLPG) in [171]. Figures 7.20(a) and 7.20(b) present the crack paths for case 1 and 2 constraints, respectively.

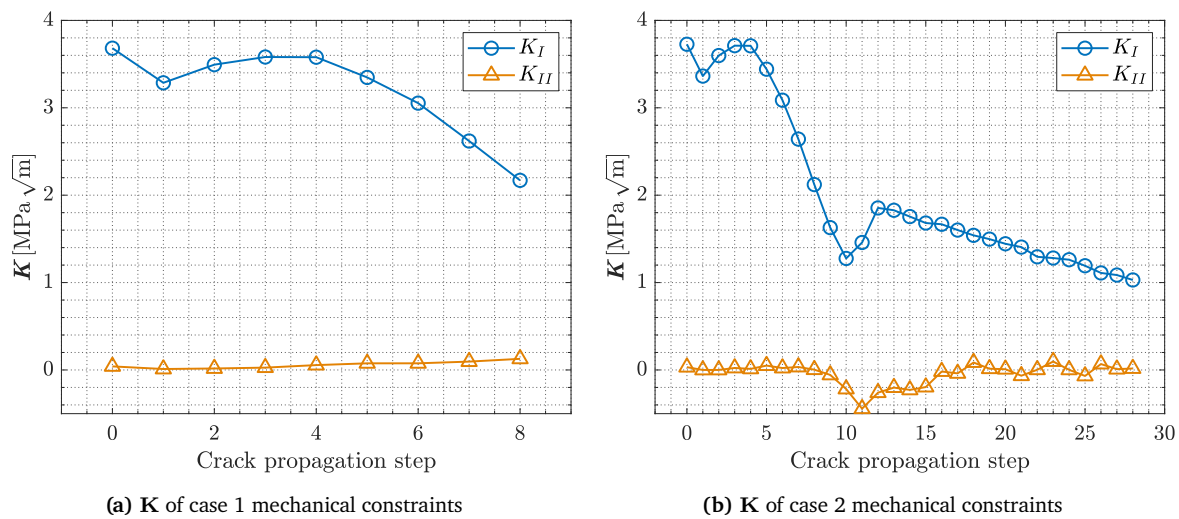


**Figure 7.19:** Stress intensity factors of a perforated plate for two cases of mechanical constraints with  $\Delta a = 0.05$  m. (a)  $K$  of case 1 mechanical constraints. (b)  $K$  of case 2 mechanical constraints.

It is noted that for case 1, the crack moves towards the perforation due to additional constraints. Initially,  $K_{II} \approx 0$  for a few steps indicates a straight crack path in Fig. 7.19(a). For case 2, the crack path follows a significantly different trajectory and bends towards the less constrained

region. Stress intensity factors also predict the curving of the crack path in case 2, as evident in Fig. 7.19(b). A sudden decrease in  $K_{II}$  is observed as the crack reaches near the perforation, where it starts moving towards the plate's upper corner. Figure 7.20(c) demonstrates the effects of  $\Delta a$  on the crack trajectory. The choice of  $\Delta a$  does not affect a straight crack path.

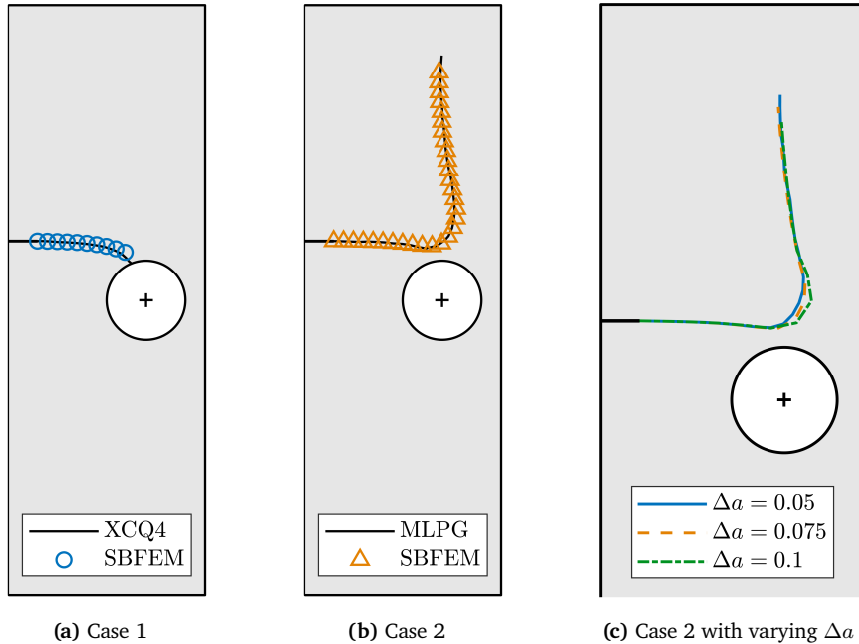


**Figure 7.20:** Crack paths in the perforated plate for case 1 and 2 mechanical constraints. (a) Case 1 constraints compared to [170] for  $\Delta a = 0.05$  m. (b) Case 2 constraints compared to [171] for  $\Delta a = 0.05$  m. (c) Case 2 with varying crack incremental lengths  $\Delta a$ .

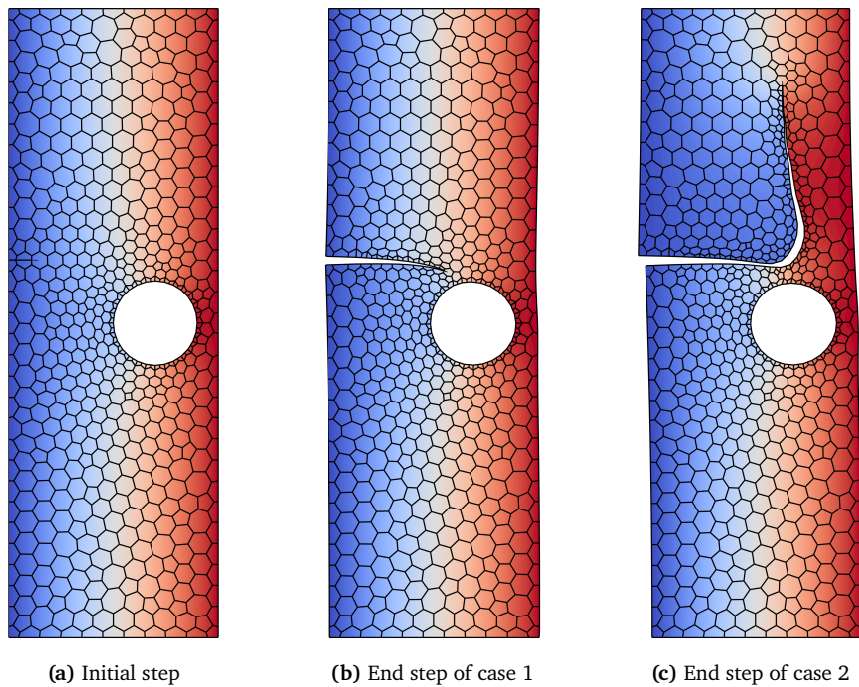
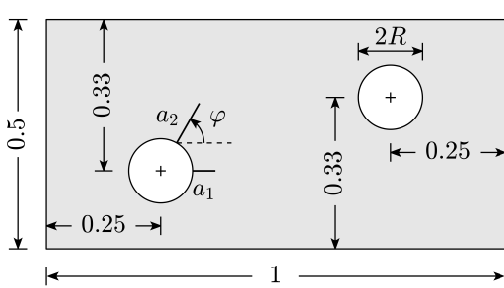


**Figure 7.21:** Mesh and temperature distributions of a perforated plate at the start and end of crack propagation steps. (a) Initial mesh with 577 polygons and temperature distribution. (b) Last step of case 1 with  $\Delta a = 0.05$ . (c) Last step of case 2 with  $\Delta a = 0.05$ .

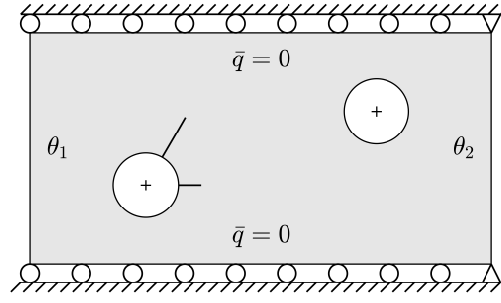
On the other hand, swerving cracks requires small crack incremental lengths to capture its path accurately. In Fig. 7.20(c), significant effects of  $\Delta a$  are noted when the crack path changes the direction towards a less constrained region. The results of crack paths are in excellent agreement with the reference solutions. Finally, Fig. 7.21(a) shows the initial temperature distribution and mesh with 577 polygon elements. Figures 7.21(b) and 7.21(c) illustrate the temperature distribution and mesh of case 1 and 2 constraints at the end of crack propagation steps for  $\Delta a = 0.05$ .

### 7.3.3 Multiple Cracks Emanating from Perforation

In the last example of this section, a plate with two perforations is considered. Additionally, two cracks are emanating from one of the perforations. The idea of this the problem is to demonstrate the propagation of multiple cracks simultaneously using the SBFEM. Figure 7.22(a) shows the geometry of the plate with all the dimensions in m. The lengths of ‘Crack-1’ and ‘Crack-2’, i.e.,  $a_1 = 0.05$  m and  $a_2 = 0.1$  m, respectively. The angle of Crack-2 from the horizontal axis is  $\varphi = 60^\circ$ . The radius of both perforations is  $R = 0.07$  m. The top and bottom sides of the plate are constrained in the vertical direction.



(a) Geometry of a plate with multiple cracks



(b) Physical model

**Figure 7.22:** Geometry and physical model of a perforated plate with multiple cracks. (a) Geometry of the plate in m. (b) A physical model of a plate with boundary conditions.

Moreover, the top and bottom corners of the left side are also constrained in the horizontal direction, as shown in Fig. 7.22(b). The material properties of the plate are  $E = 218.4$  MPa,  $\nu = 0.3$ ,  $\kappa = 205 \text{ W}(\text{m}^\circ\text{C})^{-1}$ , and  $\alpha = 1.67 \times 10^{-4} (\text{ }^\circ\text{C})^{-1}$ . The plate is in a plane strain state. Two sets of thermal boundary conditions and reference temperatures are considered, as listed in Table 7.12. In set 1, the left side of the plate is cooled by applying the temperature change  $\theta_1$ . In set 2, an additional temperature change of  $\theta_2$  is applied on the right side of the plate. All the other sides are assumed to be insulated.

| BCs set | Temperature in $^\circ\text{C}$ |            |            |
|---------|---------------------------------|------------|------------|
|         | $\theta_0$                      | $\theta_1$ | $\theta_2$ |
| Set 1   | 20                              | -20        | 0          |
| Set 2   | 0                               | -20        | 20         |

**Table 7.12:** Different sets of thermal boundary conditions and reference temperatures for a perforated plate with multiple cracks.

The crack incremental length  $\Delta a = 0.02$  m is chosen for crack propagation. Figures 7.23(a) and 7.23(b) show the  $\mathbf{K}$  for sets 1 and 2, respectively. Additionally, Figs. 7.24(a) and 7.24(b) describe the paths of both cracks for two sets of thermal boundary conditions. For set 1, it is observed that  $K_{II} \approx 0$  for both cracks after a few steps. Contrary to set 1,  $K_{II} \approx 0$  for a few initial steps for both cracks in set 2 boundary conditions.

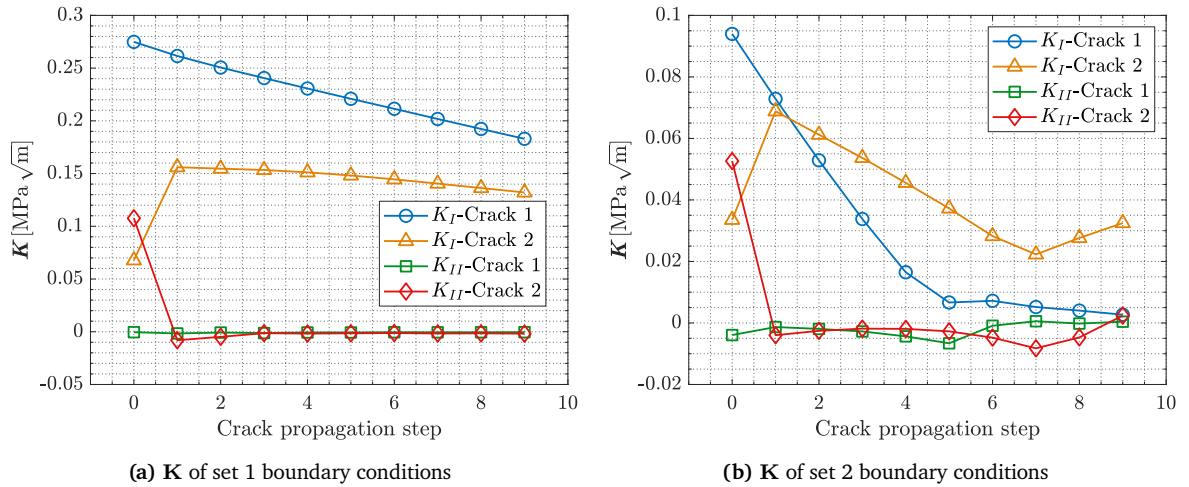


**Figure 7.23:** Stress intensity factors of multiple cracks emanating from perforation for two sets of boundary conditions with  $\Delta a = 0.02$  m. (a)  $K$  of set 1 boundary conditions. (b)  $K$  of set 2 boundary conditions.

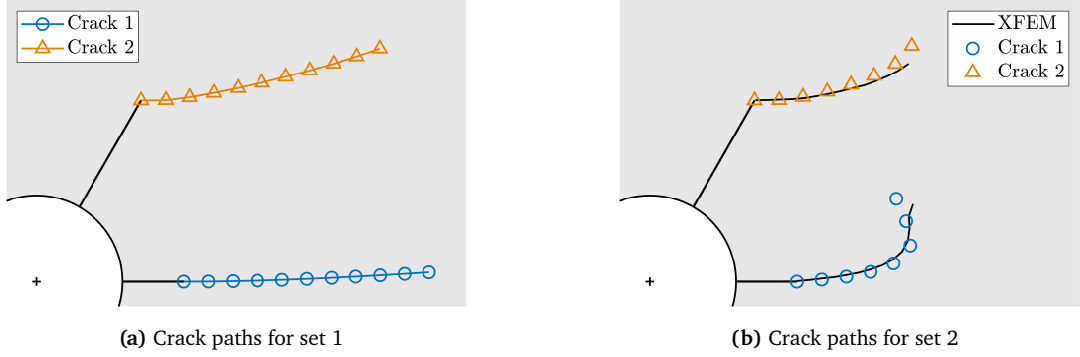


**Figure 7.24:** Multiple crack paths for different sets of thermal boundary conditions with  $\Delta a = 0.02$  m. (a) Set 1 thermal boundary conditions. (b) Set 2 thermal boundary conditions compared to [47].

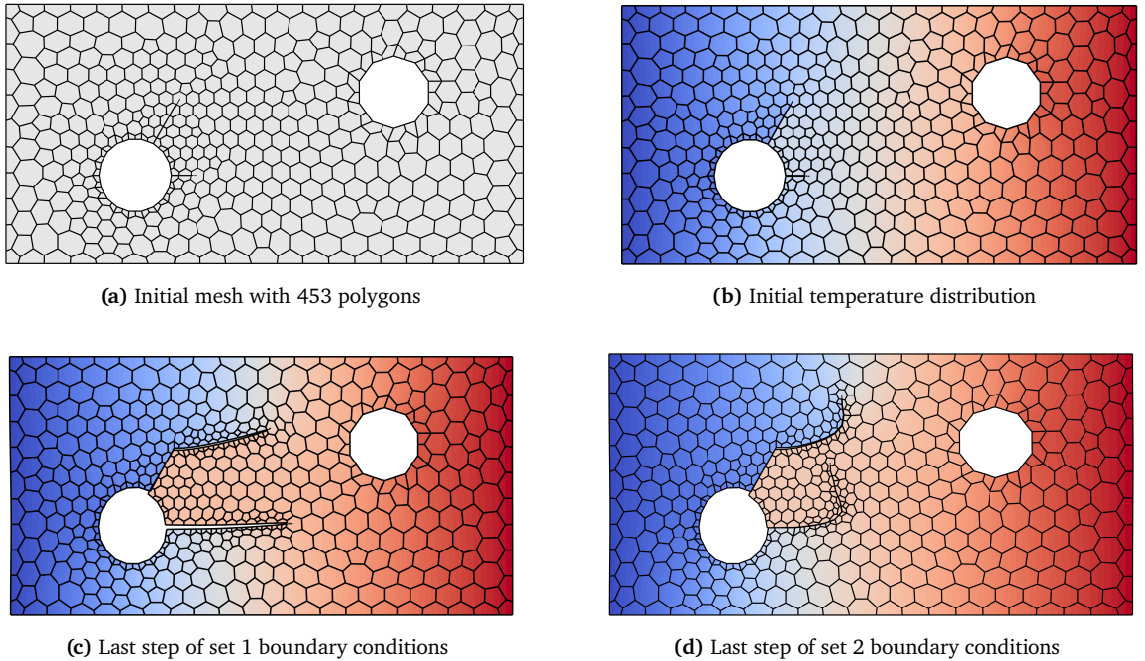


**Figure 7.25:** Mesh and temperature distribution of perforated plate with multiple cracks for  $\Delta a = 0.02$  m. (a) Initial mesh. (b) Initial temperature distribution. (c) Mesh and temperature distribution at the last step of set 1 boundary conditions. (d) Mesh and temperature distribution at the last step of set 2 boundary conditions.

Generally, higher values of  $\mathbf{K}$  are noted for set 1 boundary conditions. The paths of both cracks are almost a straight line for set 1 boundary conditions owing to small values of  $K_{II}$ . For set 2, both cracks propagate in a straight line for a few steps. Afterward, they bend in an upward direction. The results of both crack paths in set 2 boundary conditions are compared with the reference solution of XFEM in [47]. The results are in good agreement with the reference.

Finally, Figs. 7.25(a) and 7.25(b) show an initial mesh and temperature distribution of 453 polygon elements. Figures 7.25(c) and 7.25(d) illustrate the mesh and temperature distribution at the last crack propagation step for sets 1 and 2, respectively.

# Chapter 8

## Numerical Examples Part-II: Transient Coupling

This chapter presents the validation of the proposed method in modeling fully coupled thermoelastic fracture. To this end, the scaled boundary polygon and supplementary shape functions are utilized to discretize the governing equations of coupled thermoelasticity. The discretization of governing equations is presented in Section 4.4. The evaluation of thermoelastic fracture parameters, i.e., dynamic stress intensity factors, is discussed in Section 6.1.

Section 8.1 validates the calculations of dynamic SIFs for various thermal shock cases. Section 8.2 presents the calculations of dynamic thermoelastic fracture parameters in functionally graded materials. Section 8.3 showcases the results of fully coupled dynamic crack propagation caused by temperature shock. Furthermore, Section 8.3 outlines the choices of fracture parameters involving dynamic crack propagation problems, such as crack propagation velocity, equivalent dynamic SIFs, and crack accumulation length.

The scaled boundary polygon elements with quadratic (three-node) line elements are employed in all examples. Furthermore, each edge of the polygon element containing a crack is subdivided into four edges. The crack faces are assumed to be insulated in all examples. A standard Newmark implicit method is used to integrate the evolution of the state variables over time. In the case of dynamic crack propagation, the required re-meshing and mesh mapping techniques are discussed in Section 6.2.

### 8.1 Validation of Transient Stress Intensity Factors

In this section, three numerical examples are considered to analyze the efficacy of the SBFEM in capturing transient SIFs that occur in thermoelastic fracture. The first example considers a plate with an edge crack subjected to a temperature shock resulting in temperature variation parallel to a crack. This leads to a transient mode-I fracture. The second example considers an edge crack under thermal shock perpendicular to a crack, resulting in mode-II fracture. In the third example, an inclined edge crack is subjected to a flux shock, resulting in a mixed-mode fracture. All examples use polygons with quadratic (three-node) line elements. The results of all considered examples are already published in [153]. They are presented here for completeness.

#### 8.1.1 Mode-I Fracture – Temperature Shock

In this example, a plate with an edge crack is subjected to a temperature shock. Figure 8.1(a) shows the physical model of the plate. The geometry is defined by  $W = 10$  mm,  $L = 40$  mm, and the crack length ratio  $a/W = 0.5$ . The plate is made up of bismuth. Table 8.1 lists the material properties of bismuth. Initially, the plate is at a reference temperature of  $\theta_0 = 3.5$  K. The left side of the plate is subjected to a cooling temperature  $\theta(t) = -0.2 H(t)$  K at  $t = 0$ . Here,  $H(t)$  is the Heaviside function. All the other sides of the plate are assumed to be insulated. There are no mechanical boundary conditions present in the model. Applying cooling temperature shock results in a temperature variation parallel to a crack and, consequently, mode-I fracture. Furthermore, the plate is in a plane strain state. In this example, the inertial effects are also taken into consideration.

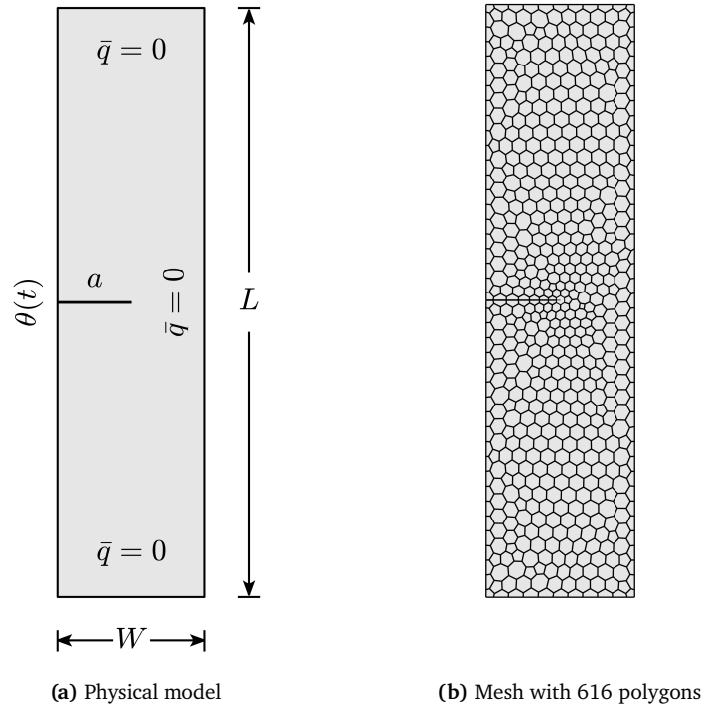


**Figure 8.1:** Physical model and mesh of a plate subjected to temperature shock result in a temperature variation parallel to a crack. (a) Geometry and boundary conditions. (b) Mesh with 616 polygon elements.

Figure 8.1(b) presents the discretized model of the plate with 616 polygon elements. Three different sets of mesh densities and time step sizes are considered to analyze the behavior of the mode-I stress intensity factor. The mesh characteristic length  $h$  is used to obtain different mesh densities. Table 8.2 shows the number of polygon elements and nodes obtained for various  $h$ . The simulations are run until  $t \approx 12 \mu\text{s}$  with  $\Delta t = 0.27 \mu\text{s}$ ,  $0.04 \mu\text{s}$ , and  $0.02 \mu\text{s}$ . The results of transient mode-I stress intensity factors are normalized, such that  $\bar{K}_I(t) = K_I(t)/K_0$  where  $K_0 = E\alpha\theta_0\sqrt{W}/(1 - 2\nu)$ . Moreover, the history of transient  $\bar{K}_I(t)$  is compared with the reference solution of XFEM where stress intensity factor are calculated using interaction integrals in [48].

| $E \text{ GPa}$ | $\nu$ | $\alpha (\text{K})^{-1}$ | $\kappa \text{ W} (\text{mK})^{-1}$ | $c \text{ J} (\text{kgK})^{-1}$ | $\rho \text{ kg} (\text{m})^{-3}$ |
|-----------------|-------|--------------------------|-------------------------------------|---------------------------------|-----------------------------------|
| 40              | 0.3   | $6.75 \times 10^{-6}$    | 875                                 | 0.052                           | 9780                              |

**Table 8.1:** Material properties of bismuth.

| $h$      | 2 mm | 1 mm | 0.5 mm |
|----------|------|------|--------|
| Polygons | 179  | 616  | 2334   |
| Nodes    | 1045 | 3342 | 12160  |

**Table 8.2:** The number of polygon elements used to model a plate subjected to temperature shock with different mesh characteristic lengths  $h$ .

First, the convergence of  $\bar{K}_I(t)$  over mesh densities is studied. Figure 8.2(a) illustrates the  $\bar{K}_I(t)$  for different mesh characteristic lengths  $h$  compared to the reference solution [48]. A significant difference is observed between the computed and reference values for mesh with  $h = 2 \text{ mm}$ , i.e., 179 polygon elements. Nevertheless, the curve still follows the path of the reference solution with a higher amplitude of oscillations. For  $h \leq 1 \text{ mm}$ , i.e., the number of polygons  $\geq 616$ , the results

are qualitatively the same compared to the reference solution. Note that for all  $h$ ,  $\Delta t = 0.02 \mu\text{s}$  is taken to compute  $\bar{K}_I(t)$ .

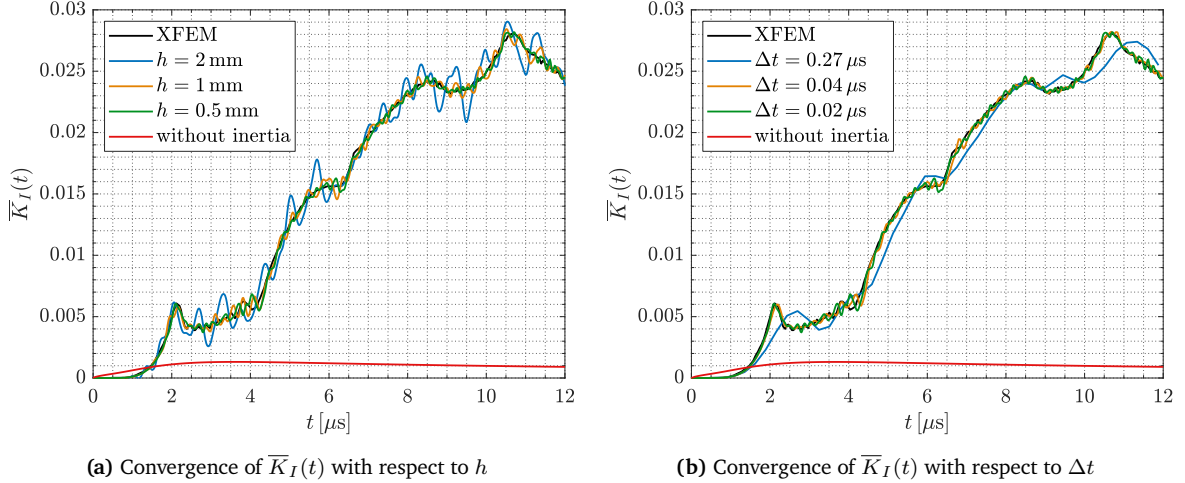


**Figure 8.2:** History of transient  $\bar{K}_I(t)$  of a plate subjected to temperature shock parallel to a crack compared to the reference solution of XFEM [48]. (a) Convergence of  $\bar{K}_I(t)$  for  $\Delta t = 0.02 \mu\text{s}$  with interial effects at different  $h$ , and  $\bar{K}_I(t)$  without inertial effects at  $h = 1 \text{ mm}$ . (b) Convergence of  $\bar{K}_I(t)$  for  $h = 0.5 \text{ mm}$  with interial effects at different time step size  $\Delta t$ , and  $\bar{K}_I(t)$  without inertial effects at  $\Delta t = 0.04 \mu\text{s}$ .

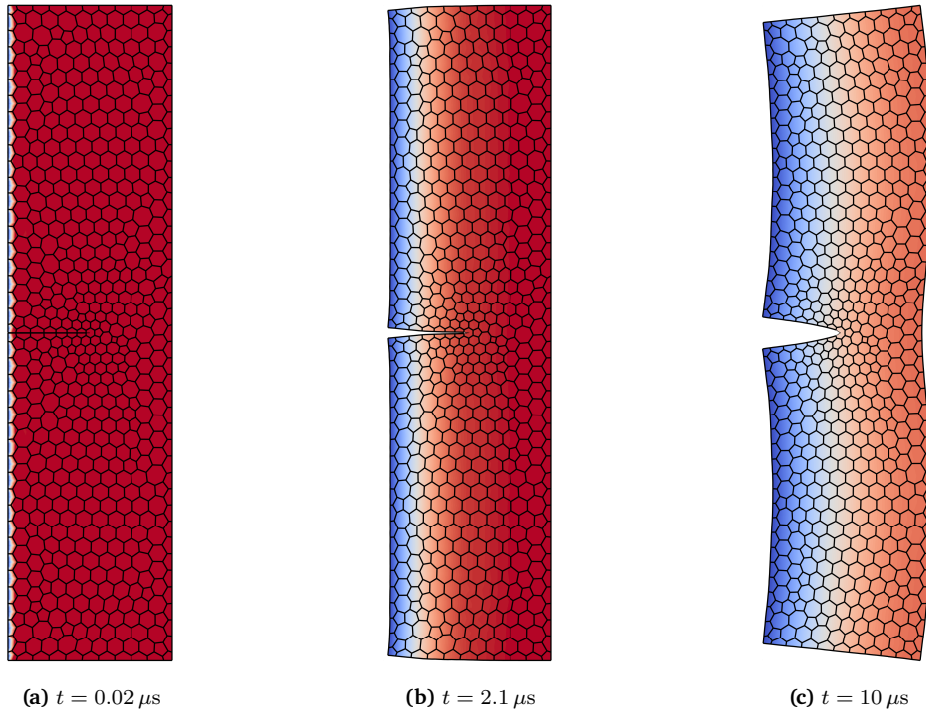


**Figure 8.3:** Temperature distribution and scaled deformation of a plate subjected to temperature shock parallel to a crack at different times with  $h = 1 \text{ mm}$  and  $\Delta t = 0.02 \mu\text{s}$ . (a) Temperature distribution at  $t = 0.02 \mu\text{s}$ . (b) Temperature distribution at  $t = 2.1 \mu\text{s}$ . (c) Temperature distribution at  $t = 10 \mu\text{s}$ .

Next, the effect of time step size  $\Delta t$  on transient  $\bar{K}_I(t)$  is considered. Figure 8.2(b) shows  $\bar{K}_I(t)$  results for different  $\Delta t$  with  $h = 0.5 \text{ mm}$ . It is observed that the stress wave reaches the crack tip at  $t \approx 2.1 \mu\text{s}$ , as indicated by a sudden dip in the value of  $\bar{K}_I(t)$ . To accurately model such behavior, smaller  $\Delta t$  values are required to accurately capture  $\bar{K}_I(t)$  oscillations. The results computed for the values of  $\Delta t \leq 0.04 \mu\text{s}$  agree with the reference solution. Moreover, it is noted

that the inertial effects have a significant influence on the values of  $\bar{K}_I(t)$  as illustrated in Fig. 8.2. Finally, Figs. 8.3(a–c) illustrate temperature distribution in a plate with scaled deformation for  $\Delta t = 0.02 \mu\text{s}$  and  $h = 0.5 \text{ mm}$ . Figure 8.3(a) shows the physical state of the plate at  $t = 0.02 \mu\text{s}$ . Figure 8.3(b) depicts the plate at  $t = 0.21 \mu\text{s}$  when stress wave reaches the crack tip. Temperature distribution at  $t = 10 \mu\text{s}$  is presented in Fig. 8.3(c).

### 8.1.2 Mode-II Fracture – Temperature Shock

In this example, a temperature shock perpendicular to a crack is considered. Figure 8.4(a) shows a physical model of a plate with an edge crack. The dimensions of the plate are  $W = 1 \text{ m}$  and  $L = 2 \text{ m}$  with changing  $a/W$  ratio. The material properties of the plate are  $E = 1 \text{ GPa}$ ,  $\nu = 0.3$ ,  $\alpha = 1 (\text{K})^{-1}$ ,  $\kappa = 1 \text{ W}(\text{mK})^{-1}$ ,  $c = 1 \text{ J}(\text{kgK})^{-1}$ , and  $\rho = 1 \text{ kg}(\text{m})^{-3}$ . The reference temperature of the plate is  $\theta_0 = 0 \text{ K}$ .

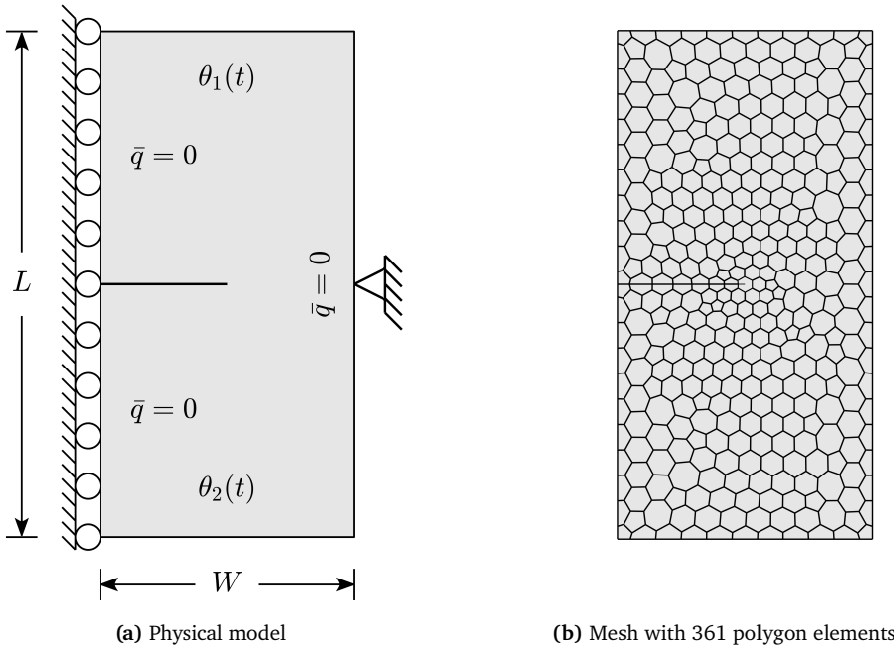


**Figure 8.4:** Physical model and mesh of a plate subjected to temperature shock perpendicular to a crack. (a) Geometry and boundary conditions. (b) Mesh with 361 polygon elements.

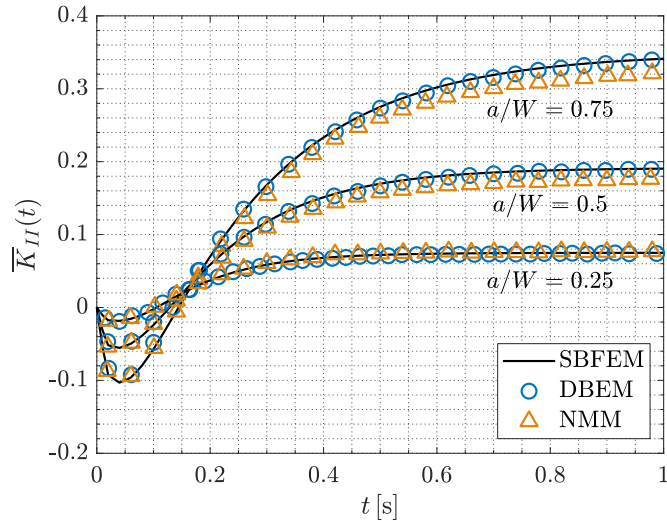
Afterwards plate is subjected to temperature shock by applying the temperature change at  $t = 0$  on the top and bottom sides, i.e.,  $\theta_1(t) = 1 H(t) \text{ K}$  and  $\theta_2(t) = -1 H(t) \text{ K}$ , respectively. All the other sides are insulated. The left side of the plate is constrained in the  $x$ -direction. The middle point of the right side is fixed in both directions. The state of plane strain is assumed. Moreover, inertial effects are neglected.

| $h$               | 0.2 m    | 0.1 m    | 0.05 m   | 0.035 m  | 0.025 m  |
|-------------------|----------|----------|----------|----------|----------|
| Polygons          | 113      | 361      | 1336     | 2739     | 5175     |
| Nodes             | 675      | 1987     | 7010     | 14157    | 26501    |
| $\bar{K}_{II}(t)$ | 0.027031 | 0.027068 | 0.027026 | 0.027013 | 0.027009 |

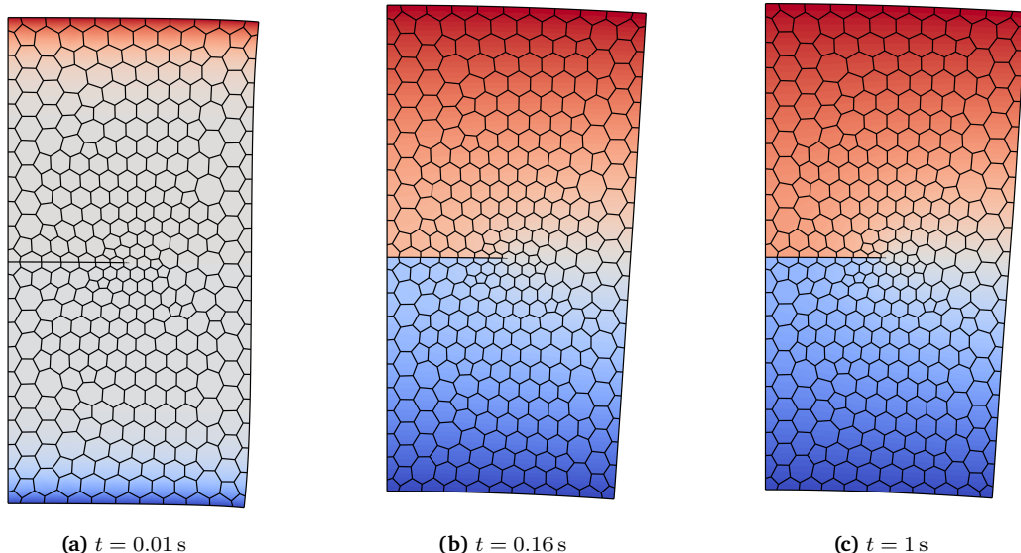
**Table 8.3:** Results of  $\bar{K}_{II}(t)$  for  $a/W = 0.5$  at  $t = 0.16 \text{ s}$  with  $\Delta t = 0.01 \text{ s}$  and different mesh densities.

Figure 8.4(b) shows a discretized model of the plate with 361 polygon elements for  $a/W = 0.5$ .

The simulations are run for  $t = 1$  s with  $\Delta t = 0.01$  s. The stress intensity factor are normalized as  $\bar{K}_{II}(t) = K_{II}(t)/(E\alpha\theta_1(t)\sqrt{W})$ . Table 8.3 lists the values of  $\bar{K}_{II}(t)$  with different mesh densities at  $t = 0.16$  s for  $a/W = 0.5$ . Convergent behavior of  $\bar{K}_{II}(t)$  is observed for increasing mesh densities. Furthermore, the results of mode-II transient stress intensity factor are compared with the reference solutions of the dual boundary element method (DBEM) [67] and the numerical manifold method (NMM) [172] for varying  $a/W$ .



**Figure 8.5:** History of transient  $\bar{K}_{II}(t)$  of a plate subjected to temperature shock perpendicular to a crack compared with the reference solutions of DBEM [67] and NMM [172].



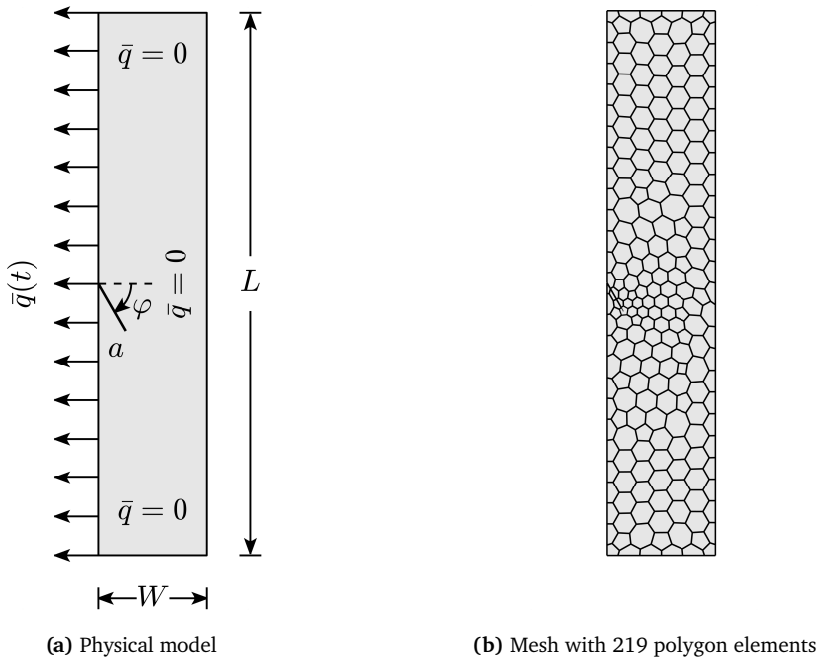
**Figure 8.6:** Temperature distribution and scaled deformation of a plate subjected to temperature shock perpendicular to a crack at different times with  $\Delta t = 0.01$  s,  $a/W = 0.5$ , and 361 polygon elements. (a) Temperature distribution at  $t = 0.01$  s. (b) Temperature distribution at  $t = 0.16$  s. (c) Temperature distribution at  $t = 1$  s.

Figure 8.5 presents the results of  $\bar{K}_{II}(t)$  for different  $a/W$  ratios compared to the reference solutions. For all  $a/W$ , the values of  $\bar{K}_{II}(t)$  decreases until  $t = 0.04$  s, then increases monotonically. Moreover, higher  $\bar{K}_{II}(t)$  values are observed with increasing  $a/W$ . The computed results are in excellent agreement with the reference solution of the DBEM. However, they only qualitatively agree with the reference solution of the NMM.

At the end, Fig. 8.6 shows temperature distribution in a plate with scaled deformation for  $a/W = 0.5$  with  $\Delta t = 0.01$  s and  $h = 0.1$  m. Figures 8.6(a–c) depict the physical state of the plate at  $t = 0.01$  s,  $t = 0.16$  s, and  $t = 1$  s, respectively.

### 8.1.3 Mixed-mode Fracture – Flux Shock on Inclined Crack

This example deals with a plate containing an inclined edge crack subjected to a flux shock. The aim of this example is to demonstrate the efficacy of the SBFEM in modeling transient mixed-mode fracture. Figure 8.7(a) shows the model of a plate whose dimensions are  $W = 10$  mm,  $L = 50$  mm,  $a/W = 0.3$ , and  $\varphi = 60^\circ$ . The plate is made of bismuth with material properties listed in Table 8.1. The reference temperature of the plate is  $\theta_0 = 3.5$  K. At  $t = 0$ , the left side of the plate is subjected to a flux shock of  $\bar{q}(t) = -10 \text{ kW(m)}^{-2}$  with the Heaviside function  $H(t)$ . All the other sides are insulated. Moreover, there are no mechanical boundary conditions present in the model. In this example, the inertial effects are considered. The state of plane strain is assumed.



**Figure 8.7:** Physical model and mesh of a plate with an inclined edge subjected to flux shock. (a) Geometry and boundary conditions. (b) Mesh with 219 polygon elements.

Figure 8.7(b) shows the mesh of the plate with 219 polygon elements. The transient stress intensity factors  $\mathbf{K}(t)$  are obtained until  $t = 7.5 \mu\text{s}$  with time step size  $\Delta t = 0.075 \mu\text{s}$ . The results of  $\mathbf{K}(t)$  are compared with the reference solution of the meshless local Petrov-Galerkin method (MLPG) [173]. Figure 8.8 presents the history of  $\mathbf{K}(t)$  for a mesh of 219 polygon elements compared to the reference solution. It is observed that the  $K_I(t)$  increases and  $K_{II}(t)$  decreases as time progresses. Both curves show more stable monotonous behavior compared to the reference solution. Nevertheless, qualitatively good agreement is observed compared to the solution of MLPG reported in [173]. Additionally, Figs. 8.9(a–c) illustrate the temperature distribution and scaled deformation at  $t = 0.075 \mu\text{s}$ ,  $t = 3.75 \mu\text{s}$ , and  $t = 7.5 \mu\text{s}$ , respectively.

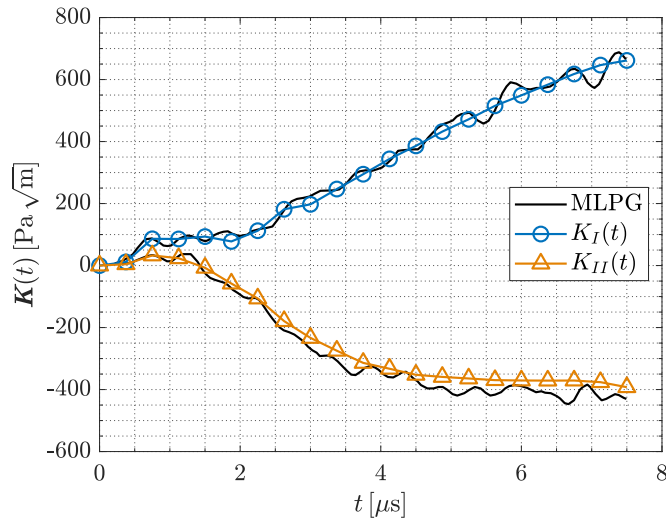


**Figure 8.8:** History of transient  $K(t)$  of a plate with an inclined edge crack subjected to flux shock compared with the reference solutions of MLPG [173] for  $\Delta t = 0.075 \mu s$ .

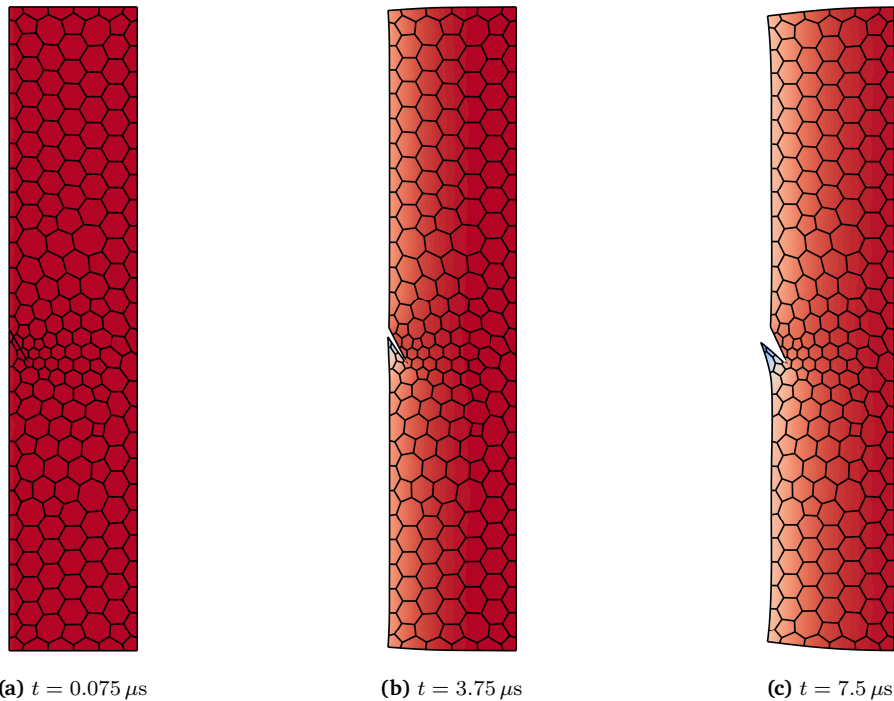


**Figure 8.9:** Temperature distribution and scaled deformation of a plate with an edge inclined crack subjected to flux shock at different times with  $\Delta t = 0.075 \mu s$  and 219 polygon elements. (a) Temperature distribution at  $t = 0.075 \mu s$ . (b) Temperature distribution at  $t = 3.75 \mu s$ . (c) Temperature distribution at  $t = 7.5 \mu s$ .

## 8.2 Dynamic Stress Intensity Factors in FGMs

In this section, three functionally graded plates with different material gradients are analyzed. In the first example, a plate with exponential material gradient under cooling temperature shock is considered. The second example presents a square plate with an inclined center crack. In this example, the material variation is defined by a power-law function. The last example of this section analyzes an orthotropic plate with an interface crack and exponential material gradient. The results of these examples are already published in [174] using the SBFEM.

In all examples, the polynomial order of material fitting is chosen as  $n = 2$  in Eq. (5.4). The discussion on the choice of material fitting order is presented in Section 5.2. Moreover, Section 7.2.1 validates that polynomial order of  $n = 2$  is sufficient to model any given material gradation as long as the size of polygon elements is sufficiently small. In this section, the polygons with quadratic (three-node) line elements are employed. Each edge of a polygon element containing a crack is subdivided into four edges. Similar to previous analyses, the crack faces are assumed to be insulated.

### 8.2.1 Exponential Material Gradient Parallel to Crack

This example considers a functionally graded plate with an exponential material gradient under temperature shock. Figure 8.10(a) shows a plate consisting of 100% ceramic ( $\text{ZrO}_2$ ) on the left side and 100% metal (Ti-6Al-4V) on the right side. The geometry of the plate is given as  $W = 1 \text{ m}$ ,  $L = 2 \text{ m}$ , and varying  $a/W$  ratio. Initially, the plate is at the reference temperature of  $\theta_0 = 1000 \text{ K}$ . At  $t = 0$ , the plate is subjected to a cooling temperature shock by applying temperature change with the Heaviside function  $H(t)$  at the left and right sides, i.e.,  $\theta_1(t) = -700 \text{ K}$  and  $\theta_2(t) = -600 \text{ K}$ , respectively. All the other sides are insulated. Additionally, the bottom side of the plate is constrained in the  $y$ -direction. The right corner point of the bottom plate is also constrained in the  $x$ -direction. The plate is assumed to be in a plane strain state. The effects of inertia are also considered in the analysis.

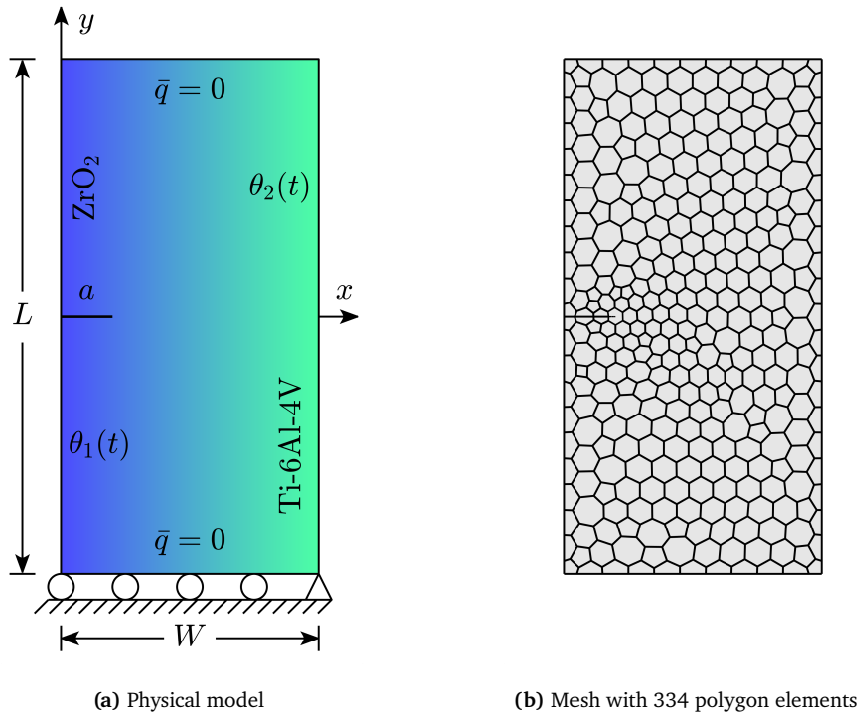


**Figure 8.10:** Physical model and mesh of a plate with an exponential material gradient parallel to a crack. (a) Geometry and boundary conditions. (b) Mesh with 334 polygon elements.

The functional grading of material is defined by an exponential function as follows

$$P(x) = P^c e^{\beta x}, \quad \text{with} \quad \beta W = \ln(P^m/P^c). \quad (8.1)$$

Here,  $P$  indicates the material parameters, i.e.,  $E$ ,  $\alpha$ ,  $\kappa$ ,  $\rho$ , and  $c$ . The symbols  $P^c$  and  $P^m$  denote the material properties of ceramic and metal, respectively. Table 8.4 lists the material properties of ceramic ( $\text{ZrO}_2$ ) and metal (Ti-6Al-4V).

| Material                   | $E$ GPa | $\nu$ | $\alpha$ (K) $^{-1}$ | $\kappa$ W (mK) $^{-1}$ | $c$ J (kgK) $^{-1}$ | $\rho$ kg(m) $^{-3}$ |
|----------------------------|---------|-------|----------------------|-------------------------|---------------------|----------------------|
| ZrO <sub>2</sub> ( $P^c$ ) | 151     | 0.33  | $10 \times 10^{-6}$  | 2.09                    | 456.7               | 5331                 |
| Ti-6Al-4V ( $P^m$ )        | 116.7   | 0.33  | $9.5 \times 10^{-6}$ | 7.5                     | 537                 | 4420                 |

Table 8.4: Material properties of ZrO<sub>2</sub> and Ti-6Al-4V.

Figure 8.10(b) illustrates the discretized model of the plate with 334 polygon elements. The subjugation of cooling temperature shock parallel to a crack results in mode-I fracture. The analysis is presented in non-dimensional form by normalizing the time as  $\tau = \kappa^c t / (c^c \rho^c W^2)$ . Moreover, the history of the transient mode-I stress intensity factor is normalized, such that  $\bar{K}_I(\tau) = K_I(\tau)/K_0$  with  $K_0 = |\theta_1(t)|\alpha^c E^c \sqrt{\pi a} / (1 - \nu^c)$ . Furthermore, the results of  $\bar{K}_I(\tau)$  are compared with the reference solution obtained analytically by the method of perturbation [175].

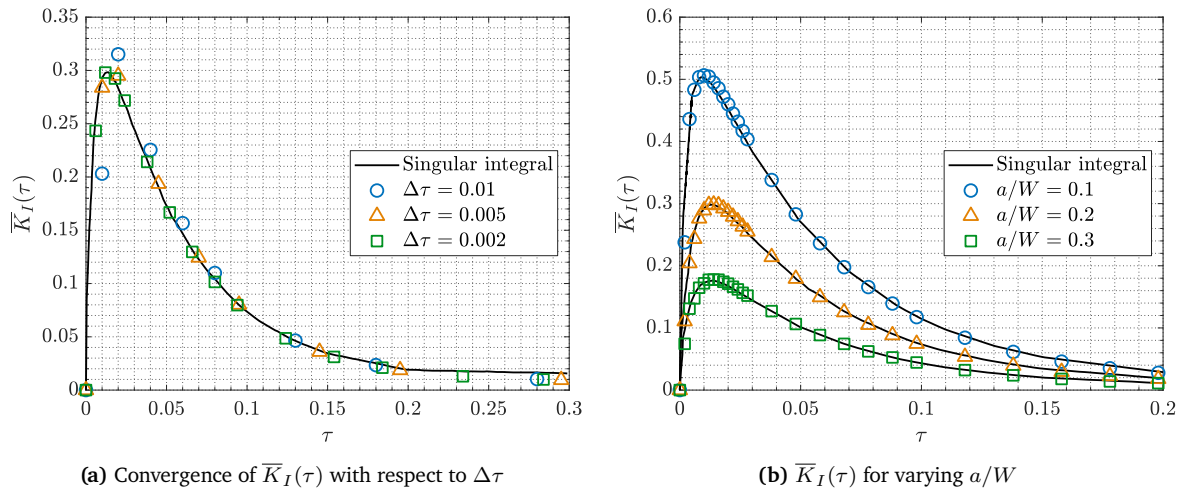


Figure 8.11: Convergence and history of transient  $\bar{K}_I(\tau)$  for varying  $a/W$  in FG plate with an exponential material gradient. (a) Convergence of  $\bar{K}_I(\tau)$  with respect to  $\Delta\tau$  for  $a/W = 0.2$ . (b)  $\bar{K}_I(\tau)$  at different  $a/W$  compared to the reference solution of singular integral equation in [175] for  $\Delta\tau = 0.002$ .

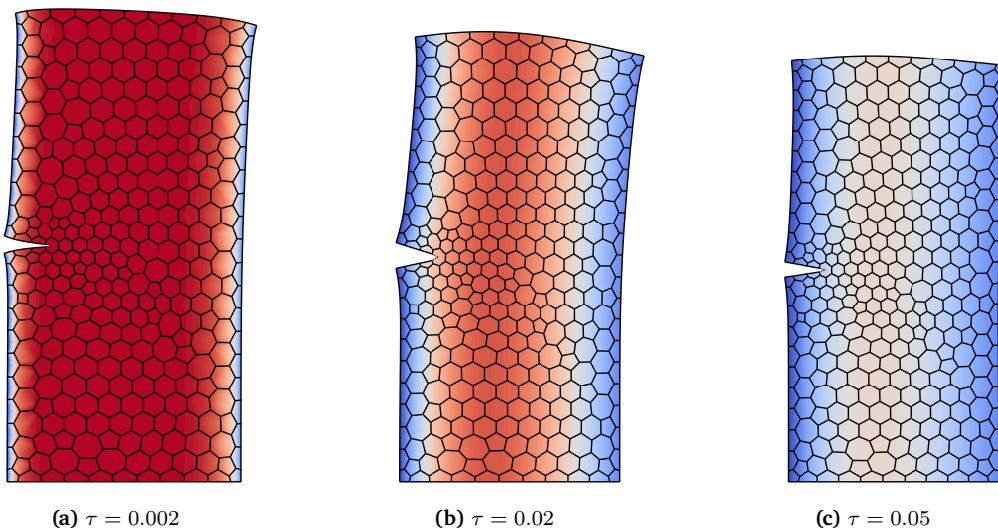


Figure 8.12: Temperature distribution and scaled deformation of a plate with an exponential material gradient at different normalized times for  $\Delta\tau = 0.002$ ,  $a/W = 0.2$ , and 334 polygon elements. (a) Temperature distribution at  $\tau = 0.002$ . (b) Temperature distribution at  $\tau = 0.02$ . (c) Temperature distribution at  $\tau = 0.05$ .

Note that  $\bar{K}_I(\tau)$  was calculated using a singular integral equation in [175]. Three different time step sizes are used to study the convergence behavior of  $\bar{K}_I(\tau)$ . The result of  $\bar{K}_I(\tau)$  for  $a/W = 0.2$  at different  $\Delta\tau$  comparing to the reference solution are presented in Fig. 8.11(a). It is observed that the larger  $\Delta\tau$  could not capture the sudden increase in  $\bar{K}_I(\tau)$  at  $\tau \approx 0.02$ . However, the history of  $\bar{K}_I(\tau)$  calculated with smaller  $\Delta\tau$  compares well with the reference solution.

Next, Fig. 8.11(b) presents the results of  $\bar{K}_I(\tau)$  for  $\Delta\tau = 0.002$  at different  $a/W$  compared with the reference solution [175]. Higher values of  $\bar{K}_I(\tau)$  are observed with increasing  $a/W$ . The results are in good agreement with the reference solution. Moreover, it is observed that the inertia does not affects the results of  $\bar{K}_I(\tau)$  in this example. For all the ratios of  $a/W$ , the maximum number of 350 polygon elements is used in the discretization.

Finally, Figs. 8.12(a–c) illustrate the resulting temperature distribution and scaled deformation of a FG plate with exponential material gradient subjected to cooling temperature shock at  $\tau = 0.002$ ,  $\tau = 0.02$ , and  $\tau = 0.05$ , respectively.

### 8.2.2 Plate with Inclined Crack and Power-law Material Gradient

This example analyzes a square plate with an inclined center crack. A power-law function defines the material gradient in a plate. Figure 8.13(a) shows the model of the plate with  $W = 1$  m and  $a = 0.25$  m. The crack inclination from the horizontal axis is expressed by  $\varphi$ . The right and left crack tips are A and B, respectively. The reference temperature of the plate is  $\theta_0 = 0^\circ\text{C}$ . At  $t = 0$ , the temperature changes of  $\theta_1(t) = 1^\circ\text{C}$  and  $\theta_2(t) = -1^\circ\text{C}$  are applied at the top and bottom sides of the plate. The Heaviside function  $H(t)$  defines the time dependency of the applied temperature change. Moreover, the bottom side is fixed in the  $x$ -direction, with its right and left corners fixed in both directions. The plate is in a plane strain state. The effects of inertia are neglected.

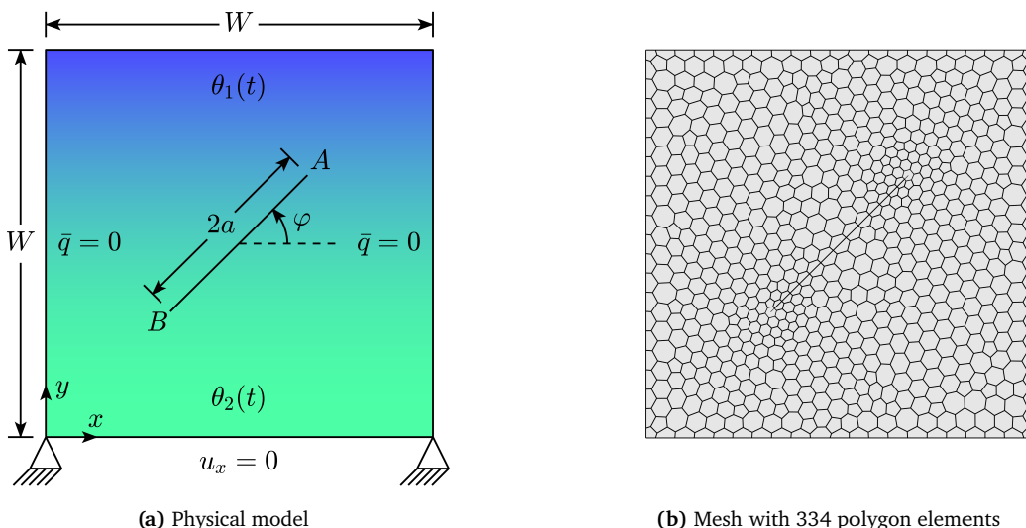


**Figure 8.13:** Physical model and mesh of a plate with a material gradient given by a power-law function. (a) Geometry and boundary conditions. (b) Mesh with 706 polygon elements.

The functional gradation of the material is expressed by a power-law function in  $y$ -direction as follows

$$P(y) = P^0 + (P^W - P^0)(y/W)^\beta, \quad (8.2)$$

where  $P$  indicates the material properties, i.e.,  $E$ ,  $\nu$ ,  $\alpha$ ,  $\kappa$ ,  $c$ , and  $\rho$ . The symbol  $\beta$  denotes the gradient index of the material variation. Table 8.5 lists the values of  $P^0$  and  $P^W$  that are the constant material properties at  $y = 0$  and  $y = W$ , respectively.

| $P(y)$       | $E$ GPa | $\nu$ | $\alpha$ (K) $^{-1}$ | $\kappa$ W (mK) $^{-1}$ | $c$ J (kgK) $^{-1}$ | $\rho$ kg(m) $^{-3}$ |
|--------------|---------|-------|----------------------|-------------------------|---------------------|----------------------|
| $P(0) = P^0$ | 1       | 0.3   | 0.01                 | 1                       | 1                   | 1                    |
| $P(W) = P^W$ | 10      | 0.4   | 0.1                  | 10                      | 10                  | 10                   |

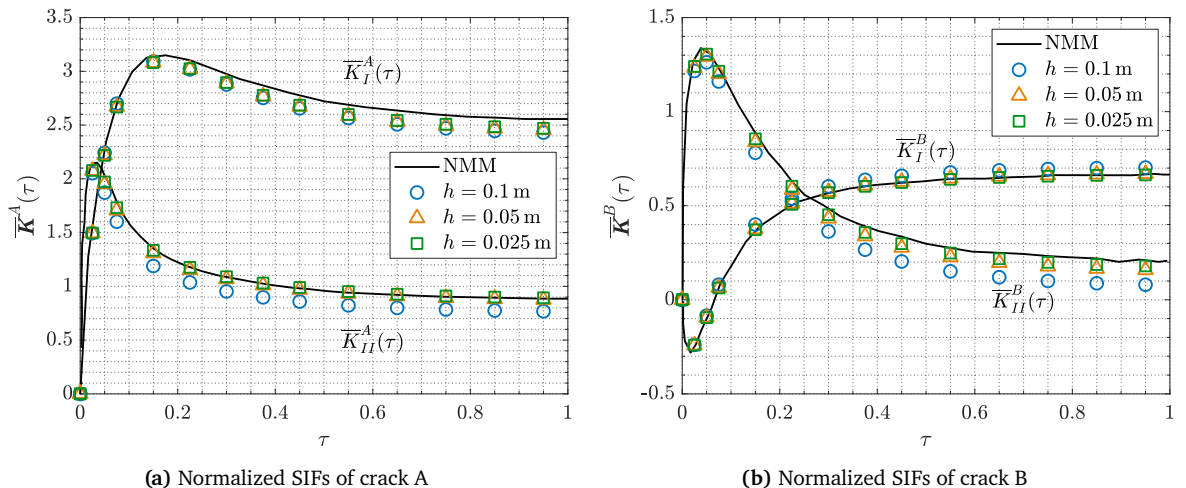
**Table 8.5:** Material properties  $P(y)$  defined by a power-law function at  $y = [0 \text{ } W]$ .

Figure 8.13(b) shows the discretized model of the plate with 706 polygon elements for  $\varphi = 45^\circ$ . The non-dimensional analysis is performed by normalizing the time as  $\tau = \kappa^0 t / \rho^0 c^0 W^2$ . Moreover, the transient stress intensity factors of both crack A and B are normalized as  $\bar{K}^A(\tau) = K^A(\tau)/K_0$  and  $\bar{K}^B(\tau) = K^B(\tau)/K_0$ , where  $K_0 = E^0 \alpha^0 \theta_1(t) \sqrt{W}$ . The time step size of  $\Delta\tau = 0.005$  is selected for all cases.

| $h$      | 0.1 m           |      |      | 0.05 m |      |      | 0.025 m |       |       |       |
|----------|-----------------|------|------|--------|------|------|---------|-------|-------|-------|
|          | $\varphi^\circ$ | 15   | 45   | 75     | 15   | 45   | 75      | 15    | 45    | 75    |
| Polygons |                 | 208  | 207  | 208    | 726  | 706  | 726     | 2676  | 2620  | 2684  |
| Nodes    |                 | 1230 | 1225 | 1230   | 3924 | 3824 | 3924    | 13890 | 13610 | 13930 |

**Table 8.6:** The number of polygon elements used to model a square plate with an inclined center crack for different mesh characteristic lengths  $h$  and inclination angles  $\varphi$ .

First, the convergence study of SIFs is performed over the mesh densities with gradient index  $\beta = 3$  and crack inclination angle  $\varphi = 45^\circ$ . Furthermore, the results are compared with the reference solution of the numerical manifold method (NMM) [176]. Figures 8.14(a) and 8.14(b) show the results of normalized SIFs of crack A and B, respectively, at different mesh densities. Table 8.6 presents the number of polygon elements and nodes obtained for various mesh characteristic lengths  $h$  and crack inclination angles  $\varphi$ . A convergent behavior of normalized SIFs is observed for increasing mesh densities. Also, a good qualitative agreement is noted between the computed and the reference solutions.



**Figure 8.14:** Convergence of  $\bar{K}(\tau)$  with respect to  $h$  compared with the reference solution of NMM [176] for  $\Delta\tau = 0.005$ ,  $\varphi = 45^\circ$ , and  $\beta = 3$ . (a) History of transient  $\bar{K}^A(\tau)$ . (b) History of transient  $\bar{K}^B(\tau)$ .

Next, the results of  $\bar{K}^A(\tau)$  and  $\bar{K}^B(\tau)$  for various  $\beta$  and  $\varphi$  are compared with the reference solution reported in [176]. To this end, the mesh characteristic length  $h = 0.05$  m and time step size  $\Delta\tau = 0.005$  are selected. Figure 8.15 presents the history of normalized SIFs for varying  $\beta$  at the crack inclination angle of  $\varphi = 45^\circ$ . In Fig. 8.15(a), it is observed that  $\bar{K}_I^A(\tau)$  decreases after

attaining its peak values. Similar behavior is observed for  $\bar{K}_{II}^A(\tau)$  except for  $\beta = 1$ , as shown in Fig. 8.15(b). For all  $\beta$  values,  $\bar{K}_I^B(\tau)$  increase gradually until they reach the steady-state, as illustrated in Fig. 8.15(c). Figure 8.15(d) shows the values of  $\bar{K}_{II}^B(\tau)$  decrease monotonically after achieving their peak values. Generally, higher steady-state values of  $\bar{K}(\tau)$  are observed with decreasing  $\beta$ . However,  $\bar{K}_{II}^B(\tau)$  exhibits the opposite behavior.

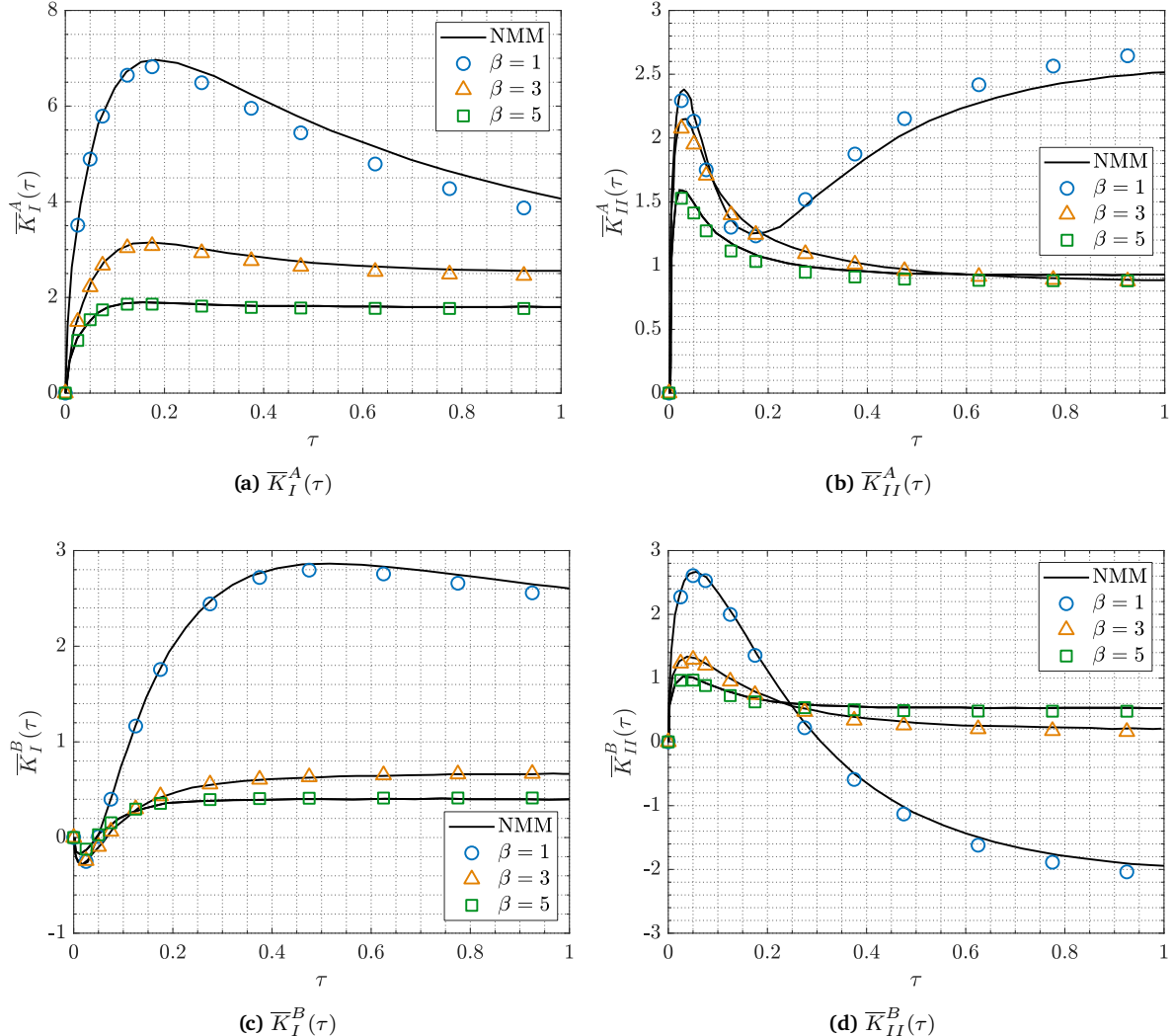


**Figure 8.15:** History of transient normalized SIFs compared with the reference solution in [176] for  $h = 0.05$  m,  $\Delta\tau = 0.005$ ,  $\varphi = 45^\circ$ , and varying material gradient index  $\beta$ . (a) Normalized mode-I SIF of crack A  $\bar{K}_I^A(\tau)$ . (b) Normalized mode-II SIF of crack A  $\bar{K}_{II}^A(\tau)$ . (c) Normalized mode-I SIF of crack B  $\bar{K}_I^B(\tau)$ . (d) Normalized mode-II SIF of crack B  $\bar{K}_{II}^B(\tau)$ .

The effects of crack inclination  $\varphi$  on  $\bar{K}(\tau)$  are analyzed by setting  $\beta = 1$ . Figure 8.16 shows the history of normalized SIFs at  $\varphi = 15^\circ$ ,  $45^\circ$ , and  $75^\circ$ . Figure 8.16(a) illustrates that  $\bar{K}_I^A(\tau)$  decreases monotonically after reaching peak values. In the case of  $\bar{K}_{II}^A(\tau)$ , a sudden dip is observed for  $\varphi = 45^\circ$  and  $75^\circ$  before raising. Moreover, increasing behaviour of  $\bar{K}_{II}^A(\tau)$  is observed for decreasing  $\varphi$ , as shown in Fig. 8.16(b).  $\bar{K}_I^B(\tau)$  exhibits similar behavior as  $\bar{K}_{II}^A(\tau)$ , except for even more sudden dip in their values for  $\varphi = 45^\circ$  and  $75^\circ$ , as depicted in Fig. 8.16(c). Fig. 8.16(d) shows that the values of  $\bar{K}_{II}^B(\tau)$  increase at first and then gradually decrease to their steady-state values.

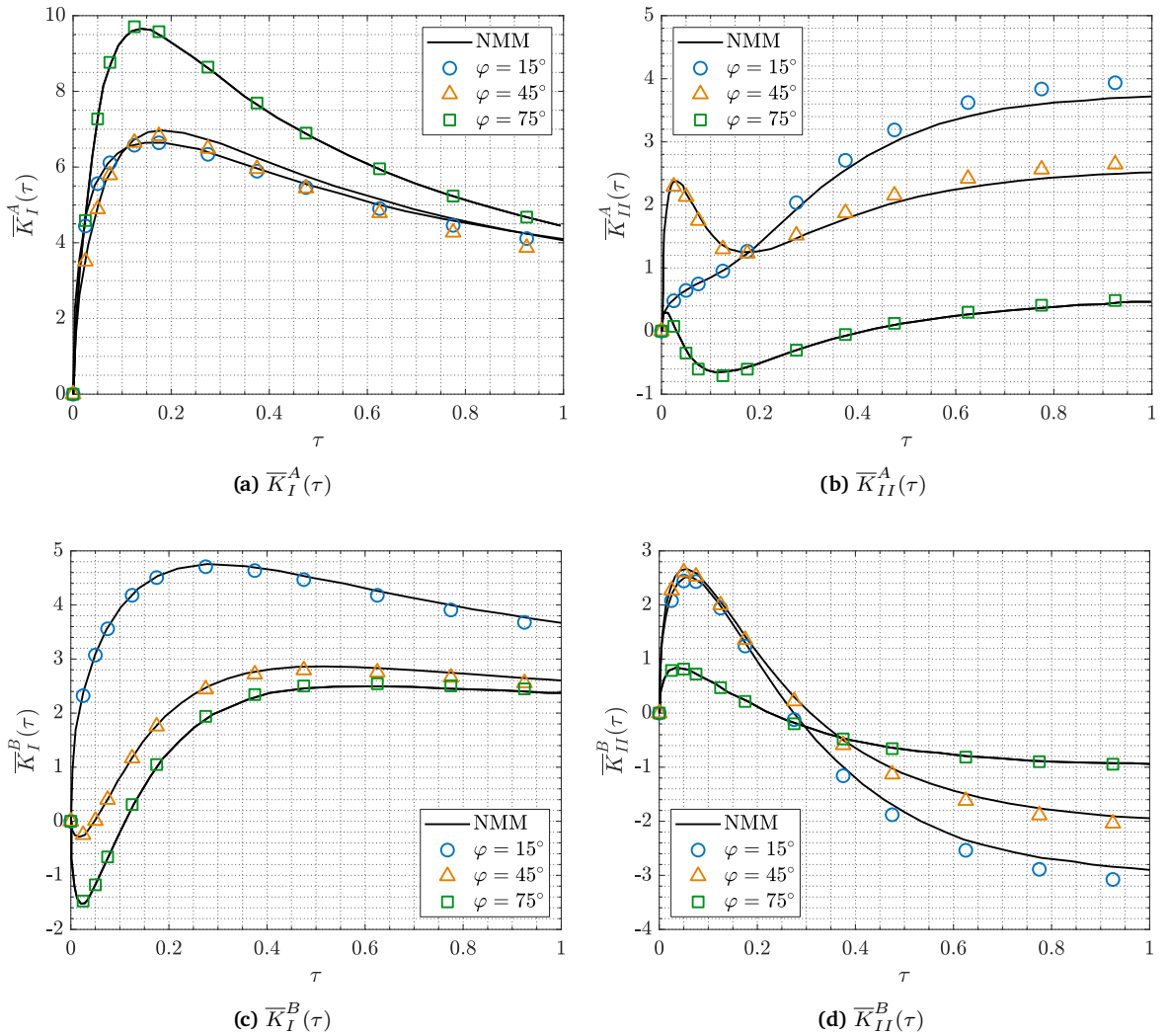


**Figure 8.16:** History of transient normalized SIFs compared with the reference solution in [176] for  $h = 0.05$  m,  $\Delta\tau = 0.005$ ,  $\beta = 1$ , and different crack inclination angles  $\varphi$ . (a) Normalized mode-I SIF of crack A  $\bar{K}_I^A(\tau)$ . (b) Normalized mode-II SIF of crack A  $\bar{K}_{II}^A(\tau)$ . (c) Normalized mode-I SIF of crack B  $\bar{K}_I^B(\tau)$ . (d) Normalized mode-II SIF of crack B  $\bar{K}_{II}^B(\tau)$ .

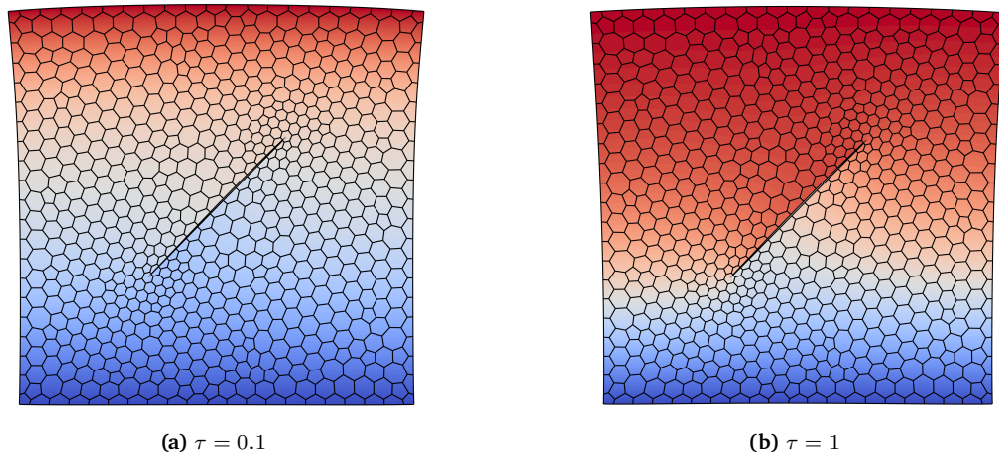


**Figure 8.17:** Temperature distribution and scaled deformation of a plate with material gradient defined by a power-law function at different normalized times with  $h = 0.05$  m,  $\Delta\tau = 0.005$ ,  $\beta = 3$ , and  $\varphi = 45^\circ$ . (b) Temperature distribution at  $\tau = 0.1$ . (c) Temperature distribution at  $\tau = 1$ .

Figures 8.17(a) and 8.17(b) show the temperature distribution and scaled deformation at  $\tau = 0.1$  and  $\tau = 1$ . Note that the resulting temperature distribution and scaled deformation in Fig. 8.17 are obtained using  $h = 0.05$  m,  $\Delta\tau = 0.005$ ,  $\beta = 3$ , and  $\varphi = 45^\circ$ . For all cases of gradient indices  $\beta$  and the crack inclination angles  $\varphi$ , a good qualitative agreement is noted compared to the reference solution of NMM [176].

### 8.2.3 Orthotropic Plate with Exponential Material Gradient

This example presents the analysis of an orthotropic plate with exponential material gradient. Figure 8.18 shows a plate with a crack at the material interface of homogeneous substrate and FGM region. The 1st and 2nd principal axes of orthotropy are aligned with  $x$  and  $y$  axes, respectively. The geometry of the plate is defined as  $b_1 = 1$  m,  $b_2 = 2$  m,  $W = 6(b_1 + b_2)$  m, and  $a = 1$  m. Initially, the orthotropic plate is at a reference temperature of  $\theta_0 = 0$  °C. The temperature changes of  $\theta_1(t) = 1$  °C and  $\theta_2(t) = -1$  °C are applied at the top and bottom sides, respectively. The temperature changes are applied with the Heaviside function at  $t = 0$ . All the other sides are insulated. The plate is in a state of plane stress.

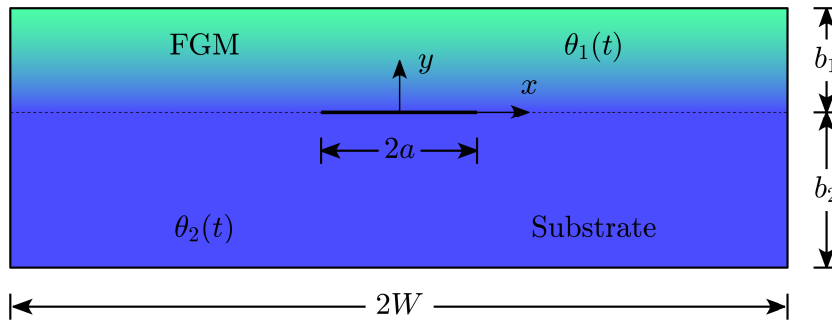


**Figure 8.18:** Physical model of an orthotropic plate with exponential material gradient and interface crack.

The material gradient is a function of  $y$  coordinate and given as

$$(E_1(y), E_2(y), G_{12}(y)) = (E_1^0, E_2^0, G_{12}^0) e^{(\beta y/b_1)}, \quad (8.3)$$

$$(\alpha_1(y), \alpha_2(y)) = (\alpha_1^0, \alpha_2^0) e^{(\gamma y/b_1)}, \quad (8.4)$$

$$(\kappa_1(y), \kappa_2(y)) = (\kappa_1^0, \kappa_2^0) e^{(\delta y/b_1)}, \quad (8.5)$$

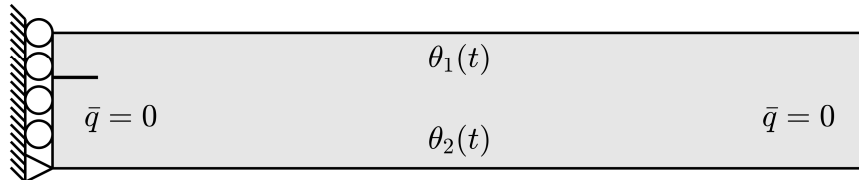
where all the coefficients  $(*)^0$  denote the homogeneous properties of the substrate and  $\beta$ ,  $\gamma$ , and  $\delta$  are the gradient indices. The substrate material is Tyrannohex, whose properties are listed in Table 8.7. The specific heat and density of the Tyrannohex are  $c = 1$  J (kgK) $^{-1}$  and  $\rho = 1$  kg(m) $^{-3}$ .

| Tyrannohex              |                                   |                                   |                 |
|-------------------------|-----------------------------------|-----------------------------------|-----------------|
| modulus GPa             | $E_1^0 = 135$                     | $E_2^0 = 87$                      | $G_{12}^0 = 50$ |
| $\alpha$ (K) $^{-1}$    | $\alpha_1^0 = 3.2 \times 10^{-6}$ | $\alpha_2^0 = 3.2 \times 10^{-6}$ |                 |
| $\kappa$ W (mK) $^{-1}$ | $\kappa_1^0 = 3.08$               | $\kappa_2^0 = 2.81$               |                 |
| $\nu$                   | $\nu_{12}^0 = 0.15$               | $\nu_{21}^0 = 0.0966$             |                 |

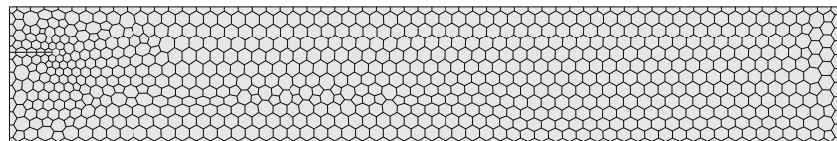
**Table 8.7:** Orthotropic material properties of Tyrannohex substrate.

The given boundary conditions and material gradient result in a symmetric model along the  $y$ -axis. Only half of the plate is modeled due to the symmetry, as shown in Fig. 8.19(a). Figure 8.19(b) illustrates the discretized model of the plate with 862 polygon elements. Furthermore, the left

side of the discretized plate is constrained in  $x$ -direction, while the bottom left corner is also constrained in  $y$ -direction.



(a) Physical model after exploiting the symmetry about  $y$ -axis

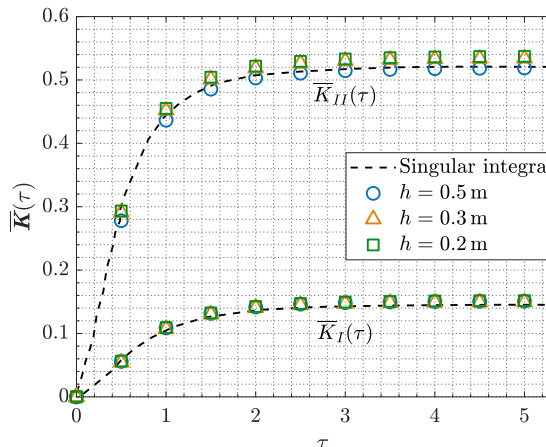


(b) Mesh with 862 polygon elements

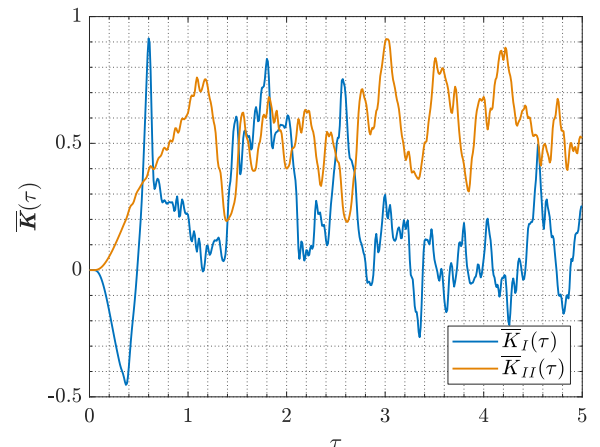
**Figure 8.19:** Physical model and mesh of an orthotropic plate with exponential material gradient. (a) Geometry and boundary conditions after using symmetry about  $y$ -axis. (b) Mesh with 862 polygon elements.

| $h$      | 0.5 m | 0.3 m | 0.2 m |
|----------|-------|-------|-------|
| Polygons | 334   | 862   | 1817  |
| Nodes    | 1884  | 4646  | 9567  |

**Table 8.8:** The number of polygon elements used to model an orthotropic plate after exploiting the symmetry for different mesh characteristic lengths  $h$ .



(a) Convergence of  $\bar{K}(\tau)$  with respect to  $h$



(b)  $\bar{K}(\tau)$  with inertial effects

**Figure 8.20:** Convergence and history of transient  $\bar{K}(\tau)$  of orthotropic FG plate with an exponential material gradient with and without inertial effects. (a) Convergence of  $\bar{K}(\tau)$  with respect to  $h$  compared to the reference solution in [177], neglecting inertial effects for  $\Delta\tau = 0.05$ . (b)  $\bar{K}(\tau)$  with inertial effects for  $h = 0.2$  m and  $\Delta\tau = 0.01$ .

Theoretically, the effects of various combinations of material gradient indices on fracture parameters can be analyzed. This example considers one such combination of  $\beta = -1$ ,  $\gamma = -1$ , and  $\delta = 0$ . This combination has opted to compare the results of transient stress intensity factors with

the reference solution of the singular integral equation reported in [177]. To this end, the time is normalized by  $\tau = \kappa_2^0 t / (\rho c a^2)$ . Moreover, the history of SIFs are normalized as  $\bar{\mathbf{K}}(\tau) = \mathbf{K}(\tau) / K_0$  with  $K_0 = E_1^0 \alpha_1^0 a^{1.5} \sqrt{\pi} / 2(b_1 + b_2)$ .

First, the convergence of  $\bar{\mathbf{K}}(\tau)$  over mesh densities is studied. For this purpose, three mesh characteristic lengths  $h$  are considered. Table 8.8 presents the number of polygon elements and nodes obtained for various  $h$ . Figure 8.20(a) shows the results of  $\bar{\mathbf{K}}(\tau)$  for different mesh densities with  $\Delta\tau = 0.05$  without consideration of inertial effects. The computed results of  $\bar{\mathbf{K}}(\tau)$  are compared with the reference solution [177]. It is observed that  $\bar{\mathbf{K}}(\tau)$  increases monotonically before attaining peak steady-state value. Higher values of  $\bar{K}_{II}(\tau)$  are noted compared to  $\bar{K}_I(\tau)$ . Furthermore,  $\bar{\mathbf{K}}(\tau)$  shows a convergent behavior with increasing mesh density. The results are in good agreement with the reference solution.

Next, the effects of inertia on  $\bar{\mathbf{K}}(\tau)$  are considered. The analysis is performed with the same gradient indices, i.e.,  $\beta = -1$ ,  $\gamma = -1$ , and  $\delta = 0$ . The time step size and mesh characteristic length are selected as  $\Delta\tau = 0.01$  and  $h = 0.2$  m. Figure 8.20(b) presents the results of  $\bar{\mathbf{K}}(\tau)$ . Considering inertial effects, significantly different behavior of  $\bar{\mathbf{K}}(\tau)$  is observed. The  $\bar{K}_I(\tau)$  value shows a sudden dip as the stress wave reaches the crack tip at  $\tau \approx 0.2$ . Highly modulated behavior of both  $\bar{K}_I(\tau)$  and  $\bar{K}_{II}(\tau)$  is noted. Similar to the case of neglected inertial effects, higher-value  $\bar{K}_{II}(\tau)$  is generally observed.

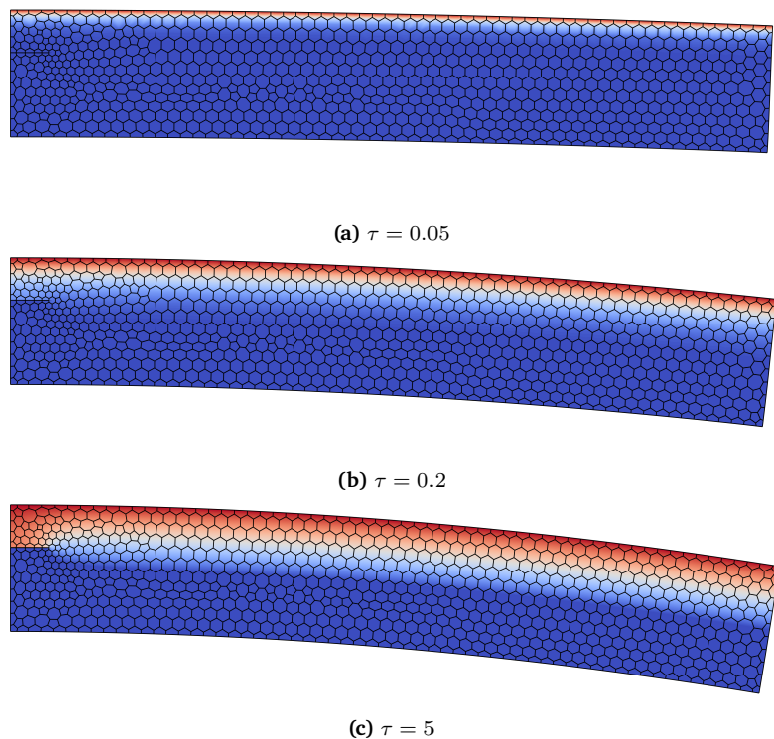


**Figure 8.21:** Temperature distribution and scaled deformation of an orthotropic plate with an exponential material gradient at different normalized times for  $\Delta\tau = 0.05$ ,  $h = 0.3$  m, and neglecting inertial effects. Temperature distribution at (a)  $\tau = 0.05$ , (b)  $\tau = 0.2$ , and (c)  $\tau = 5$ .

Finally, Figs. 8.21(a–c) illustrate the temperature distribution and scaled deformation at  $\tau = 0.05$ ,  $\tau = 0.2$ , and  $\tau = 5$ . Note that Fig. 8.21 presents the results without considering the inertial effects for  $\Delta\tau = 0.05$  and  $h = 0.3$ .

## 8.3 Fully Coupled Dynamic Crack Propagation

This section presents the preliminary results of coupled dynamic crack propagation modeling using SBFEM. The SBFEM modeling of coupled dynamic crack propagation is validated using two numerical examples, namely a notched plate with three holes Section 8.3.1 and a hollow disk with multiple cracks Section 8.3.2. Both examples consider a dynamic fracture caused by a temperature shock.

In a dynamic fracture, a crack propagates with a velocity of  $v$ . Thus, the dynamic stress intensity factors  $\mathbf{K}^{dyn}(\varphi)$  also depend on the crack velocity function, such that

$$\mathbf{K}^{dyn}(\varphi) = [k_1 \ k_2] \mathbf{K}(\varphi), \quad (8.6)$$

where  $k_1$  and  $k_2$  are the crack velocity functions, and  $\mathbf{K}(\varphi)$  denotes the SIFs at equilibrium given in Eq. (6.16). The crack velocity functions are given in [178] as

$$k_1 \approx \frac{1 - v/c_R}{\sqrt{1 - v/c_d}} \quad \text{and} \quad k_2 \approx \frac{1 - v/c_R}{\sqrt{1 - v/c_s}}. \quad (8.7)$$

Here, the symbols  $c_R$ ,  $c_d$ , and  $c_s$  denote the material's Rayleigh, dilatational, and shear wave speeds, respectively. Analysis of a moving crack in the time domain requires the information of crack velocity a priori. Crack velocity  $c$  can be obtained using dynamic fracture criteria based on material fracture toughness and limiting crack speed, i.e.,  $v_{lim} \approx 0.5 c_R$  [50, 51]. For both considered examples, crack propagation velocity is a user input taken from the corresponding reference of each example.

Once the crack velocity is known, the dynamic crack propagation angle  $\varphi_p^{dyn}$  is calculated by substituting the values of  $\mathbf{K}^{dyn}(\varphi)$  into Eq. (2.87) instead of  $\mathbf{K}(\varphi)$ . Next, the crack extension  $\Delta a_e$  is obtained using crack propagation velocity and time step size, i.e.,  $\Delta a_e = v \Delta t$ . Note that crack extension length can be accumulated over a series of time steps to avoid the re-meshing at each time step, as discussed in Section 6.2.

### 8.3.1 Temperature Shock in Notched Plate with Three Holes

This example considers a notched plate with three holes under temperature shock. The example is first studied in [51] using the XFEM. Figure 8.22(a) shows the plate's geometry with the holes' radii as  $R_s = 0.1$  and  $R_l = 0.15$ . The length of an edge crack is  $a = 0.3$ . The physical unit of dimension is described by the plate's characteristic length  $l_c = 2.82 \times 10^{-10}$  m, such that  $[x, y] = [\hat{x}, \hat{y}] l_c$ . The plate is at the reference temperature of  $\theta_0 = 1200$  K. The material properties of the plate are given in Table 8.9. The left side of the plate is subjected to a temperature shock of  $\theta = -0.2$  °C. All the other sides are assumed to be insulated. The plate is assumed to be in a plane strain state without mechanical constraints. Figure 8.22(b) presents a sample mesh of the plate with 654 polygon elements.

| $E$ GPa | $\nu$ | $\alpha$ (K) $^{-1}$   | $\kappa$ W (mK) $^{-1}$ | $c$ J (kgK) $^{-1}$ | $\rho$ kg(m) $^{-3}$ |
|---------|-------|------------------------|-------------------------|---------------------|----------------------|
| 26.62   | 0.333 | $8.918 \times 10^{-6}$ | 2.129                   | 632.128             | 3570.3               |

**Table 8.9:** Material properties of a notched plate with three holes.

The input velocity of the propagating crack dictates the criteria/speed of dynamic crack propagation. In [51], the velocity of crack propagation  $v$  is given as a ratio of Rayleigh wave speed  $c_R$  as illustrated in Fig. 8.23. Moreover, the characteristic velocity of this example is given as  $v_c = 3342$  m/s. The normalized time is defined as  $\tau = t v_c / l_c$ .

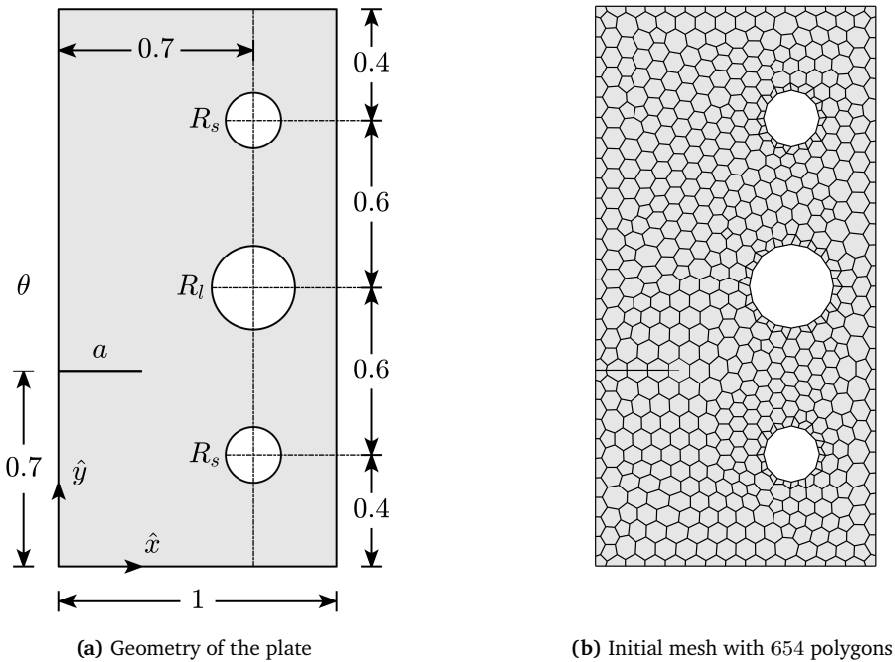


**Figure 8.22:** Geometry and sample mesh of a notched plate with three holes. (a) Model of the plate in normalized dimensions. (b) A sample mesh with 654 polygon elements.

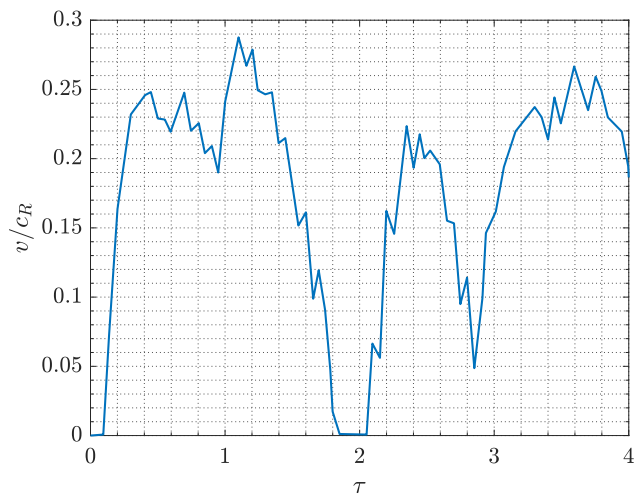


**Figure 8.23:** Normalized velocity  $v/c_R$  of propagating crack in a notched plate with three holes [51].

A set of three different initial meshes is utilized to study the example. Table 8.10 presents the number of polygon elements and nodes at three different normalized mesh characteristic lengths  $h$ . Additionally, the effects of crack accumulation length  $\Delta a$  and time step size  $\Delta \tau$  are also considered.

| $h$      | 0.075 | 0.05 | 0.025 |
|----------|-------|------|-------|
| Polygons | 654   | 1197 | 4095  |
| Nodes    | 3421  | 6194 | 20860 |

**Table 8.10:** The initial number of polygon elements used to model dynamic crack propagation in notched plate with three holes at different normalized mesh characteristic lengths  $h$ .

Figure 8.24 presents the results of crack paths at various normalized mesh characteristic lengths  $h$ , crack accumulation lengths  $\Delta a$ , and time step sizes  $\Delta\tau$ . In this example, it is observed that the choice of mesh densities does not affect the crack paths significantly, as illustrated in Fig. 8.24(a). However,  $\Delta a$  has a notable influence on the resulting crack paths, as depicted in Fig. 8.24(b).

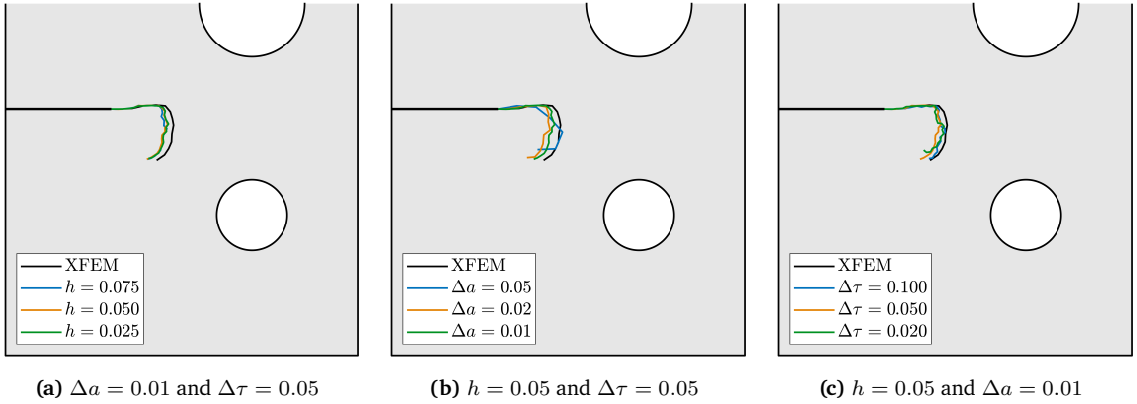


**Figure 8.24:** Resulting crack paths in a notched plate with three holes for varying  $h$ ,  $\Delta a$ , and  $\Delta\tau$ . (a) For varying  $h$  at  $\Delta a = 0.01$  and  $\Delta\tau = 0.05$ . (b) For varying  $\Delta a$  at  $h = 0.05$  and  $\Delta\tau = 0.05$ . (c) For varying  $\Delta\tau$  at  $h = 0.05$  and  $\Delta a = 0.01$ .

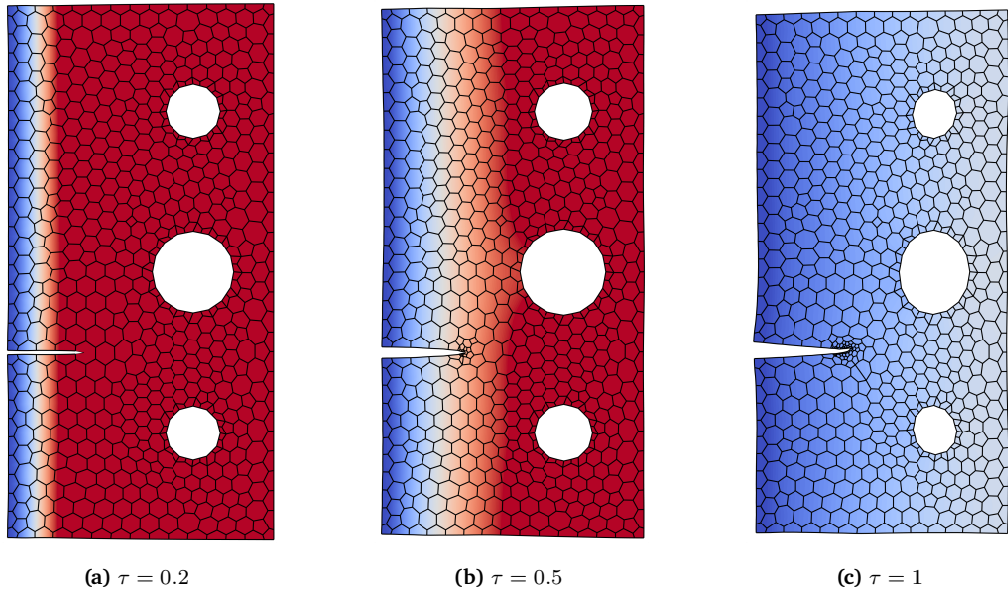


**Figure 8.25:** Temperature distribution and scaled deformation in a notched plate with three holes at different  $\tau$  for  $\Delta a = 0.01$ ,  $\Delta\tau = 0.05$ , and  $h = 0.075$ . Temperature distribution and scaled deformations at (a)  $\tau = 0.2$ , (b)  $\tau = 0.5$ , and (c)  $\tau = 1$ .

As expected, the longer crack accumulation length cannot accurately capture the swerving of the crack path. Fig. 8.24(c) shows the effects of  $\Delta\tau$  on crack paths. It is observed that the small  $\Delta\tau$  leads to more jagged paths compared to large  $\Delta\tau$ . Notably, the resulting crack paths simultaneously depend on the crack accumulation length and time step size. Thus, it is difficult and often unreasonable to study their effects independently. Nevertheless, in all studied cases of  $h$ ,  $\Delta a$ , and  $\Delta\tau$ , the crack traveled in a straight line, then swerved downwards and backward. The crack path results qualitatively agree with the reference solution of the XFEM reported in [51]. Additionally, Fig. 8.25 shows the temperature distribution and scaled deformation at different  $\tau$  for  $\Delta a = 0.01$ ,  $\Delta\tau = 0.05$ , and  $h = 0.075$ . Note that all the results of crack paths are obtained for

the crack opening case, i.e.,  $\bar{K}_I^{dyn} > 0$ . Thus, the absolute values of dynamic mode-I SIF  $|\bar{K}_I^{dyn}|$  are used to calculate the crack propagation angle in Eq. (2.87).

The results of crack paths in Fig. 8.24 are obtained using the SIFs. Therefore, it is relevant to analyze the behavior of SIFs and their effects on crack paths. Figures 8.26 and 8.27 present the results of normalized transient SIFs  $\bar{K}(\tau)$  for varying  $\Delta a$  and  $\Delta\tau$ , respectively. The SIFs are normalized as

$$\bar{K}(\tau) = \frac{\mathbf{K}(\tau) \times 10^3}{(\lambda + 2G) \alpha \theta_0 \sqrt{l_c}}. \quad (8.8)$$

Here,  $\lambda$  and  $G$  are Lamé constant and shear modulus, respectively.

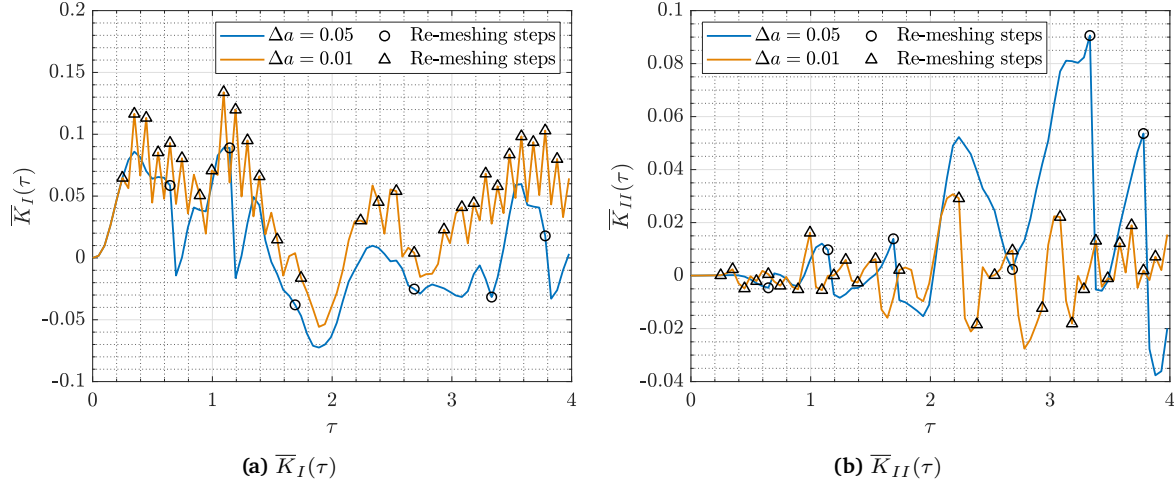


**Figure 8.26:** Normalized transient SIFs  $\bar{K}(\tau)$  in a notched plate for varying  $\Delta a$  at  $h = 0.05$  and  $\Delta\tau = 0.05$ . (a) Normalized mode-I SIF  $\bar{K}_I(\tau)$  and (b) normalized mode-II SIF  $\bar{K}_{II}(\tau)$ .

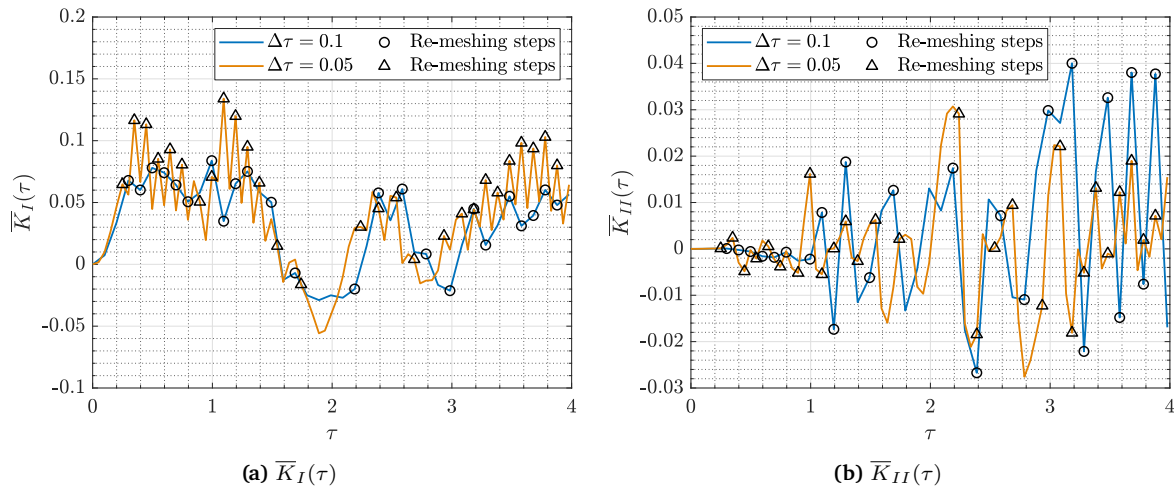


**Figure 8.27:** Normalized transient SIFs  $\bar{K}(\tau)$  in a notched plate for varying  $\Delta\tau$  at  $h = 0.05$  and  $\Delta a = 0.01$ . (a) Normalized mode-I SIF  $\bar{K}_I(\tau)$  and (b) normalized mode-II SIF  $\bar{K}_{II}(\tau)$ .

For all the cases of  $\Delta a$  and  $\Delta\tau$ , a jagged behavior of SIFs is observed. The accumulation of crack lengths over a series of time steps causes the stresses to build up at the crack tip. The geometry update through re-meshing releases built-up stresses, causing a sudden change in SIFs, as evident in Figs. 8.26 and 8.27. The sharp change in the SIFs value is observed for  $\bar{K}_I(\tau)$  and  $\bar{K}_{II}(\tau)$ . Therefore, these sudden changes do not necessarily affect the crack path as it depends on the  $\bar{K}_I(\tau)$  and  $\bar{K}_{II}(\tau)$  ratio, not their magnitude. For all the cases of  $\Delta a$  and  $\Delta\tau$ , the value

of  $\bar{K}_{II}(\tau) \approx 0$  until  $\tau = 0.8$ , as shown in Figs. 8.26b and 8.27b. Afterward, the  $\bar{K}_{II}(\tau)$  starts to change; this leads to the swerving of crack paths, as evident in Fig. 8.24. From  $\tau = 1.8$  to  $\tau = 2.1$ , the negative values of  $\bar{K}_I(\tau)$  are observed, resulting in the crack arrest as indicated by  $v \approx 0$  in Fig. 8.23.

Moreover, the frequency of abruptness in SIFs depends on the interplay of crack accumulation length and time step size. In Figs. 8.26 and 8.27, when  $\Delta a$  and  $\Delta\tau$  are smaller, i.e.,  $\Delta a = 0.01$  and  $\Delta\tau = 0.05$ , the re-meshing and crack accumulation steps occur more often, resulting in more abruptness in SIFs. In the case of larger  $\Delta a$  and smaller  $\Delta\tau$ , i.e.,  $\Delta a = 0.05$  and  $\Delta\tau = 0.05$ , a series of crack accumulation steps occur while the number of re-meshing steps remains relatively lower, leading to a lower number of sharp changes in SIFs, as shown in Fig. 8.26. Similarly, the smaller  $\Delta a$  and larger  $\Delta\tau$ , i.e.,  $\Delta a = 0.01$  and  $\Delta\tau = 0.1$ , leads to frequent re-meshing steps and lower crack accumulation steps, causing less frequent abruptness in SIFs, as illustrated in Fig. 8.27. It is important to note that the  $\Delta a$  and  $\Delta\tau$  are interlinked to each other through crack propagation velocity, which plays a vital role in determining the number of re-meshing and crack accumulation steps.

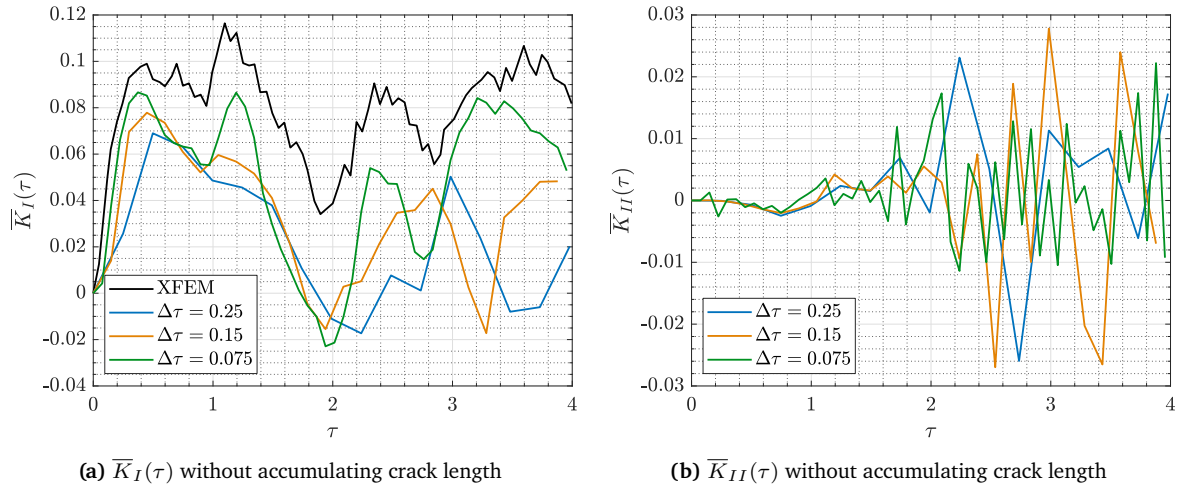


**Figure 8.28:** Normalized transient SIFs in a notched plate for varying  $\Delta\tau$  at  $h = 0.05$  without accumulating crack length. (a)  $\bar{K}_I(\tau)$  and (b)  $\bar{K}_{II}(\tau)$

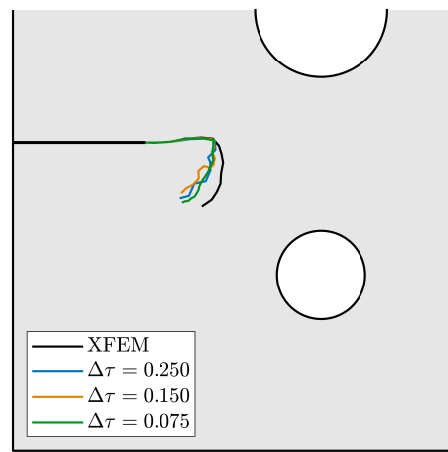


**Figure 8.29:** Crack paths in a notched plate at varying  $\Delta\tau$  without accumulating crack length.

The sharp change in SIFs can be circumvented by invoking the re-meshing algorithm at each time step. The geometry update at each time step alleviates the need for crack length accumulation. Thus, the building up of stresses can be avoided. Figure 8.28 presents the normalized SIFs at

various  $\Delta\tau$  for  $h = 0.05$  without accumulating crack length. In Figs. 8.28(a) and 8.28(b), the normalized SIFs  $\bar{K}_I(\tau)$  and  $\bar{K}_{II}(\tau)$  follow the same trend as in Figs. 8.26 and 8.27, except for the abrupt change in the SIFs. The results of  $\bar{K}_I(\tau)$  are compared with the reference solution of the XFEM reported in [51].  $\bar{K}_I(\tau)$  results follow a similar trend compared to the reference solution. However, they are not in a good agreement. It is important to note that the normalization of SIFs is not explicitly mentioned in the reference solution. Thus, the in-depth comparison of normalized SIFs is not possible. The results of  $\bar{K}_{II}(\tau)$  are not reported in the reference.

Finally, Fig. 8.29 presents the results of crack paths for varying  $\Delta\tau$  by updating the geometry at each time step without accumulating crack length. Similar to the results of SIFs presented in Fig. 8.28, the results of crack paths in Fig. 8.29 follow the same trend as illustrated in Fig. 8.24. However, they do not agree with the reference solution of the XFEM reported in [51]. The difference in crack paths can be alluded to larger  $\Delta\tau$ . In some cases, invoking the re-meshing at each time step is not a viable option due to very small resulting crack extensions, thus limiting the choice of  $\Delta\tau$ . The choice between the smaller time step sizes with an accumulation of crack length and invoking the re-meshing algorithm with larger time steps is mainly dependent on the problem. Choosing the re-meshing at each time step without crack length accumulation is recommended. However, if a problem requires a smaller time step size, it is better to accumulate the crack length with the acknowledgment of abrupt change in SIFs and avoid re-meshing at each time step.

### 8.3.2 Temperature Shock in Hollow Disk with Multiple Cracks

This example considers a hollow disk with multiple cracks under a temperature shock. The numerical example is first reported in [50] using the XFEM. Figure 8.30(a) describes the model of the disk. The two cracks  $a_1$  and  $a_2$  are labeled as crack-1 and crack-2, respectively. The normalized lengths of both cracks are equal to 0.2. Crack-1 is at an angle  $\varphi = 60^\circ$  from the negative  $\hat{x}$ -axis. The outer radius of the disk is  $R_o = 0.7$ , while the inner hole has a radius of  $R_i = 0.1$ . The semicircles on the outer surface have a radius of  $R_s = 0.15$ . The normalized dimension is described by the characteristic length  $l_c = 0.01$  m, such that,  $[\hat{x}, \hat{y}] = [x, y]/l_c$ .

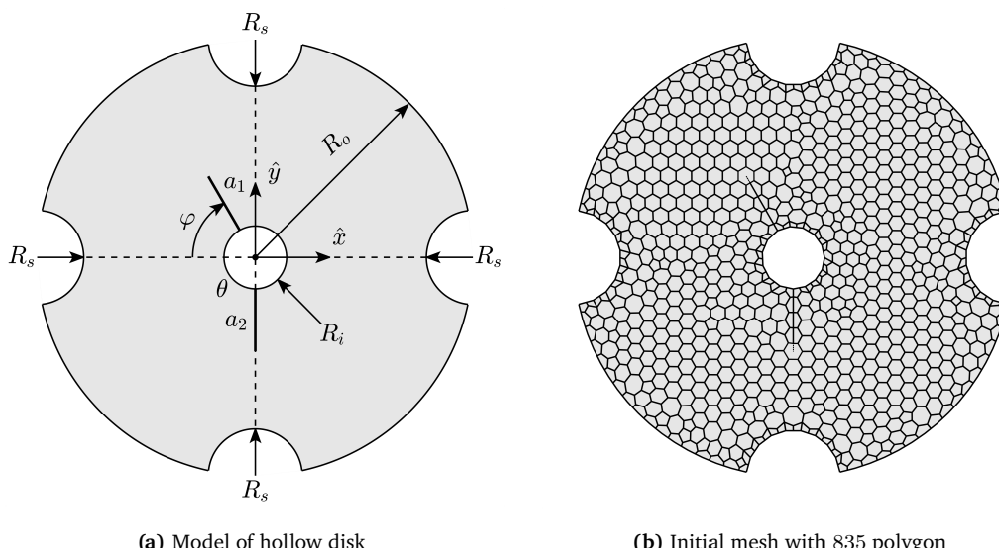


**Figure 8.30:** Model and initial mesh of a hollow disk. (a) Geometry of a hollow disk in normalized dimensions. (b) Initial mesh with 835 polygon elements.

The disk's material properties are listed in Table 8.11. The reference temperature of the disk is  $\theta_0 = 3.5$  K. The disk is subjected to a cooling thermal shock of  $\theta = -1$  °C at the inner hole.

The outer and crack surfaces are assumed to be insulated. A state of plane strain is considered. Figure 8.30(b) shows a sample mesh of the disk with 835 polygon elements.

| $E$ GPa | $\nu$ | $\alpha$ (K) $^{-1}$  | $\kappa$ W (mK) $^{-1}$ | $c$ J (kgK) $^{-1}$ | $\rho$ kg(m) $^{-3}$ |
|---------|-------|-----------------------|-------------------------|---------------------|----------------------|
| 40      | 0.3   | $6.75 \times 10^{-6}$ | 875                     | 0.052               | 9780                 |

Table 8.11: Material properties of a hollow disk.

The propagation velocities of both cracks are taken from [50], as shown in Fig. 8.31. For this example, the characteristic velocity  $v_c = 1000$  m/s is opted, and the time is normalized as  $\tau = t v_c / l_c$ . Three initial meshes described by normalized mesh characteristic length  $h$  are considered. Table 8.12 lists the number of polygon elements and nodes of each mesh. The dynamic crack propagation is studied using a set of three normalized time step sizes  $\Delta\tau$ . In this example, crack length is not accumulated. Thus, the geometry is updated at each time step based on crack extension within the one time step, i.e.,  $\Delta a = \Delta a_e = (v/v_c)\Delta\tau$ .

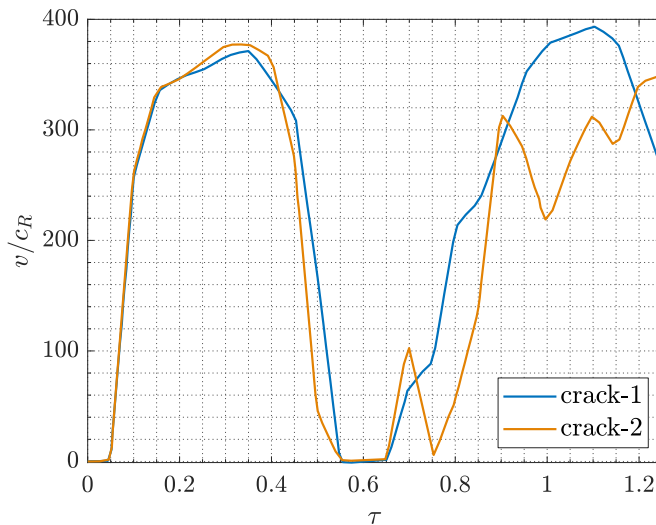


Figure 8.31: Normalized propagation velocities  $v/c_R$  of crack-1 and crack-2 in a hollow disk [50]

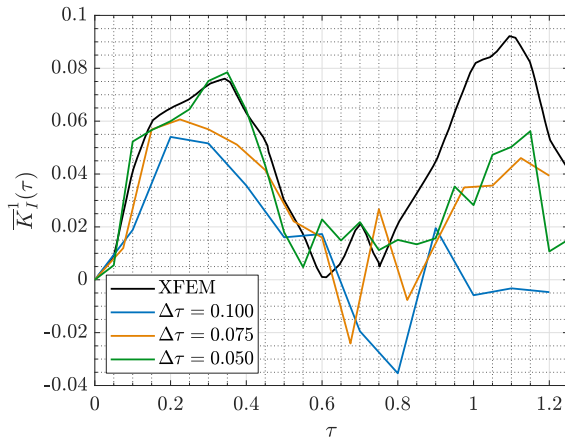
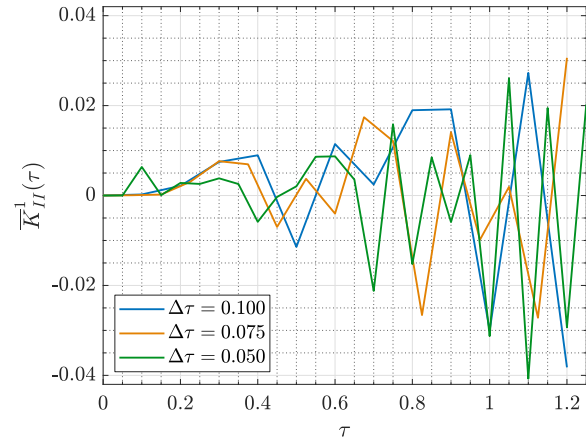
| $h$      | 0.075 | 0.05 | 0.025 |
|----------|-------|------|-------|
| Polygons | 432   | 835  | 2945  |
| Nodes    | 2306  | 4335 | 14949 |

Table 8.12: The initial number of polygon elements used to model dynamic crack propagation in a hollow disk at different mesh characteristic lengths  $h$ .

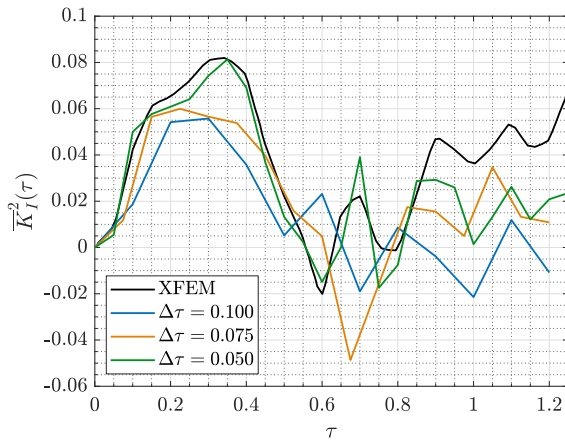
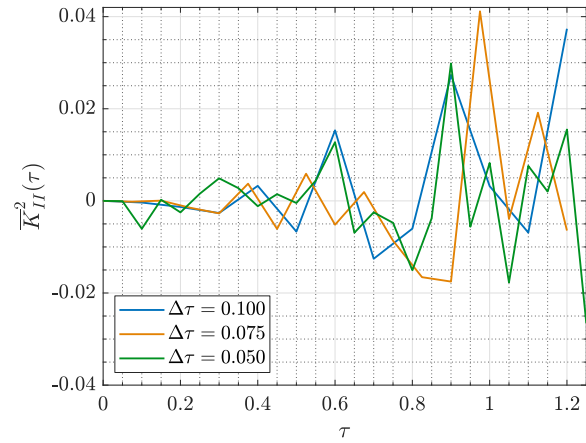
Figures 8.32 and 8.33 present the results of normalized SIFs of crack-1  $\bar{\mathbf{K}}^1(\tau)$  and crack-2  $\bar{\mathbf{K}}^2(\tau)$ , respectively. The normalization of SIFs is described as follows

$$\bar{\mathbf{K}}(\tau) = \frac{\mathbf{K}(\tau)}{(\lambda + 2G) \alpha \theta_0 \sqrt{l_c}}, \quad (8.9)$$

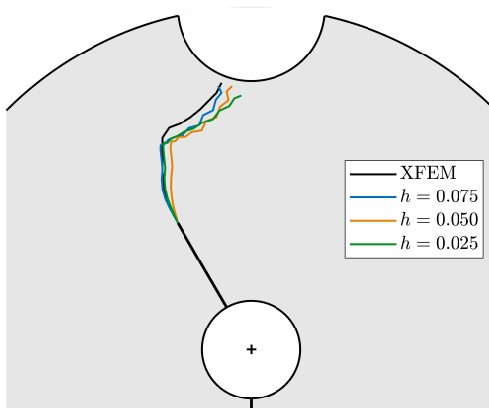
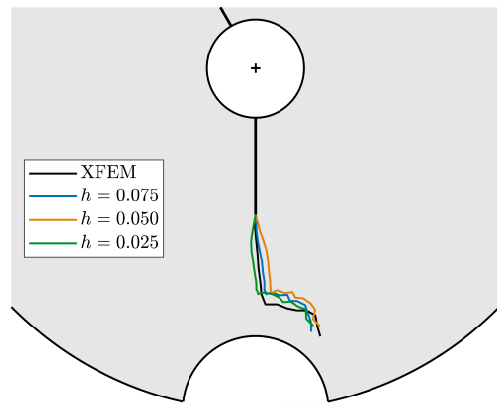
where  $\lambda$  and  $G$  are Lamé constant and shear modulus, respectively. Note that the normalization parameter of SIFs is not mentioned explicitly in the reference [50]. The normalized mode-I SIFs of both cracks are compared with the reference solution of the XFEM reported in [50].


 (a)  $\bar{K}_I(\tau)$  of crack-1

 (b)  $\bar{K}_{II}(\tau)$  of crack-1

**Figure 8.32:** Normalized SIFs of crack-1  $\bar{K}^1(\tau)$  for varying  $\Delta\tau$  at  $h = 0.05$  in a hollow disk. (a) Normalized mode-I SIF  $\bar{K}_I^1(\tau)$  and (b) normalized mode-II  $\bar{K}_{II}^1(\tau)$ .


 (a)  $\bar{K}_I(\tau)$  of crack-2

 (b)  $\bar{K}_{II}(\tau)$  of crack-2

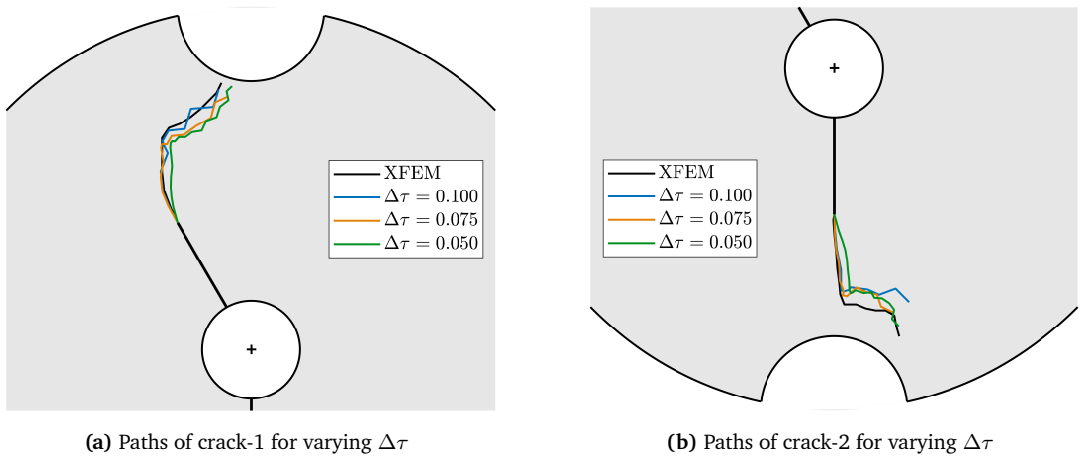
**Figure 8.33:** Normalized SIFs of crack-2  $\bar{K}^2(\tau)$  for varying  $\Delta\tau$  at  $h = 0.05$  in a hollow disk. (a) Normalized mode-I SIF  $\bar{K}_I^2(\tau)$  and (b) normalized mode-II  $\bar{K}_{II}^2(\tau)$ .


 (a) Paths of crack-1 for varying  $h$ 

 (b) Paths of crack-2 for varying  $h$ 

**Figure 8.34:** Crack paths in a hollow disk for varying  $h$  at  $\Delta\tau = 0.05$ . (a) Paths of crack-1, and (b) paths of crack-2.

Figures 8.32(a) and 8.33(a) depict the comparison of the  $\bar{K}_I(\tau)$  and  $\bar{K}_I^2(\tau)$  with the reference solution for varying  $\Delta\tau$  at  $h = 0.05$ . It is observed that for the smaller time step size, the results of  $\bar{K}_I(\tau)$  are in good agreement with the reference until the arrest of the cracks at  $\tau \approx 0.55$ . For  $\tau > 0.65$ , both cracks start propagating again, as evident by the crack propagation velocities (see Fig. 8.31). Lower values of  $\bar{K}_I(\tau)$  are noted for both cracks on resumption of crack propagation compared to the reference solution. In the case of  $\bar{K}_{II}(\tau)$ , it is observed that  $\bar{K}_{II}(\tau) \approx 0$  until  $\tau = 0.4$  for both cracks, then  $|\bar{K}_{II}(\tau)|$  started to rise, indicating swerving of the crack paths. Note that the reference [50] does not report  $\bar{K}_{II}(\tau)$  results.

Next, the results of crack paths are considered. Figs. 8.34 and 8.35 illustrate crack paths for varying  $h$  and  $\Delta\tau$ , respectively. It is noted that for both cracks, the paths do not differ significantly at different  $h$ , as depicted in Fig. 8.34. However,  $\Delta\tau$  has notable effects on the crack paths compared to  $h$ , as shown in Fig. 8.35.



**Figure 8.35:** Crack paths in a hollow disk for varying  $\Delta\tau$  at  $h = 0.05$ . (a) Paths of crack-1 and (b) paths of crack-2.

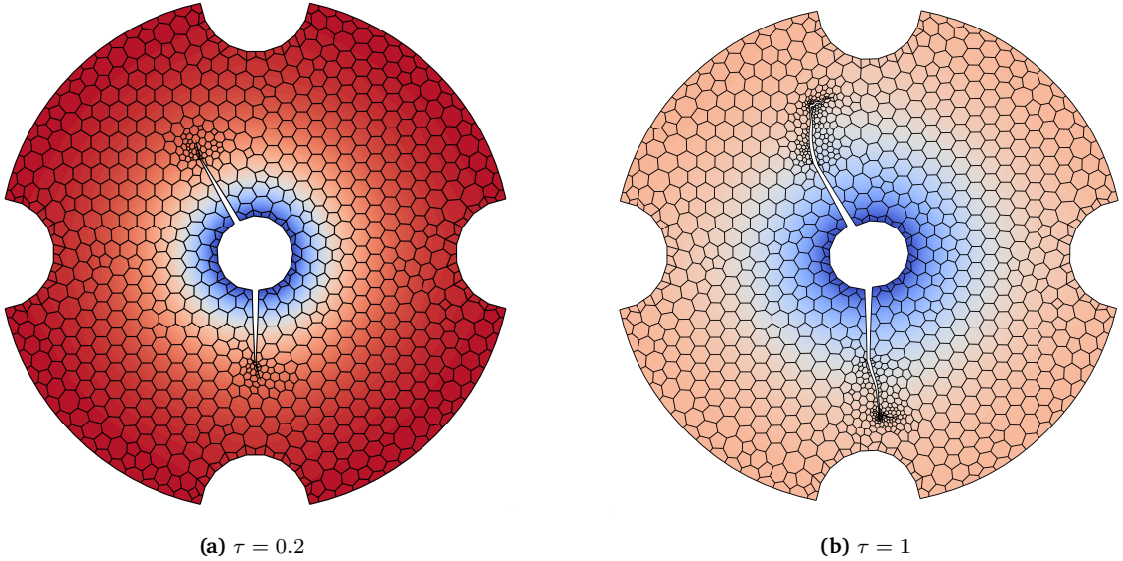


**Figure 8.36:** Temperature distribution and scaled deformation in a hollow disk at different  $\tau$  for  $\Delta\tau = 0.05$  and  $h = 0.05$ . Temperature distribution and scaled deformations at (a)  $\tau = 0.2$  and (b)  $\tau = 1$ .

The variation in  $\Delta\tau$  affects the smoothness of the crack paths. Such jagged behavior of crack paths is alluded to the crack extension at each time step. The amplitude of jaggedness depends on the length of crack extension, while the number of time steps affects the frequency of jaggedness.

Thus, smaller  $\Delta\tau$  causes more jagged crack paths, while the amplitude of jaggedness is greater when  $\Delta\tau$  is larger. In all the studied cases of  $h$  and  $\Delta\tau$ , both cracks travel in a straight line until  $\tau \approx 0.4$ , then start swerving towards the right, as  $\bar{K}_{II}(\tau)$  predicted in Figs. 8.32b and 8.33b. Additionally, Fig. 8.36 presents the temperature distribution and the scaled deformation in a hollow disk at  $\tau = 0.2$  and  $\tau = 1$  for  $h = 0.05$  and  $\Delta\tau = 0.05$ . The results of both crack paths are compared with the reference solution of the XFEM reported in [50]. The crack paths are in qualitative agreement with the reference solution. Similar to the previous example, all the results of crack paths are obtained for the crack opening case i.e.,  $\bar{K}_I^{dyn} > 0$ .

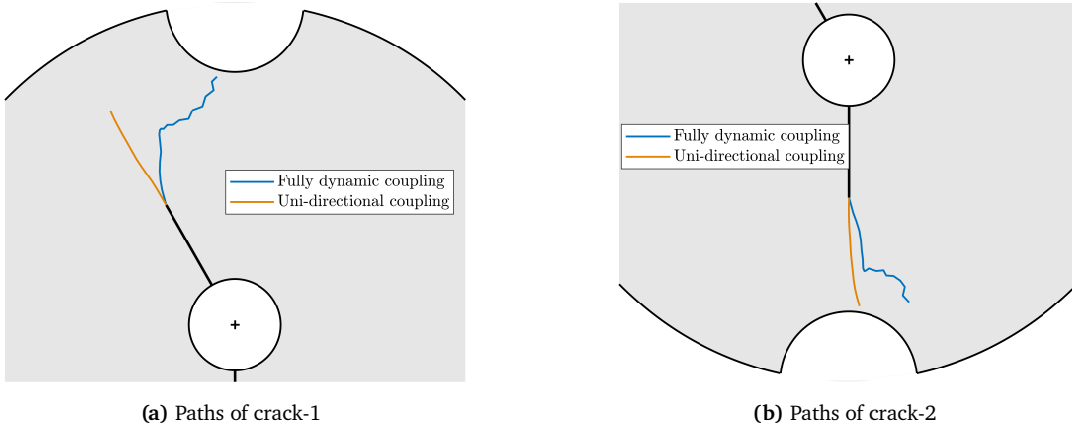


**Figure 8.37:** Comparison of crack paths in a hollow disk obtained using dynamic and uni-directional coupling. (a) Paths of crack-1 and (b) paths of crack-2.

Finally, the results of crack paths for the case of fully dynamic coupling are compared with the crack paths obtained using uni-directional coupling. Figure 8.37 shows the results of crack paths for both coupling types. For uni-directional coupling, the crack paths are obtained using the crack incremental length of  $\Delta a = 0.02$ . In the case of dynamic coupling, the time step size of  $\Delta\tau = 0.05$  is chosen. For both cases, the normalized mesh characteristic length is  $h = 0.05$ . In uni-directional coupling, both cracks travel in a straight line, completely different from the dynamic case.

# Chapter 9

## Concluding Remarks

In this work, a numerical technique based on the scaled boundary finite element method (SBFEM) is developed and applied to model thermoelastic fracture. Numerical modeling of thermoelastic fracture is highly relevant for the design and safety of engineering components in numerous applications. To the author's knowledge, the SBFEM has never been applied to model discrete crack propagation in the context of thermoelasticity prior to the presented work in this thesis. The first part of this work discusses the theoretical background of thermoelasticity and linear elastic fracture mechanics. Then, already existing concepts of the SBFEM in modeling heat conduction and linear elasticity problems are presented for completeness.

The predominant contribution of this thesis is to model thermoelastic fracture using the SBFEM. It has been shown that thermal load vectors for elastostatics problems can be integrated analytically, assuming uni-directional coupling of temperature and displacement fields. However, its application is limited to a specific case of known temperature distribution that varies as power functions of radial coordinate.

It has been demonstrated that the SBFEM formulation can be extended to model fully coupled thermoelasticity by enriching the SBFE shape functions of the displacement field with the supplementary shape functions. Also, the construction of supplementary shape functions does not require a prior solution of the temperature field. The SBFEM discretization of fully coupled thermoelasticity equations leads to a semi-analytical integration of mass-, damping-, and stiffness-like matrices with minimal addition of auxiliary degrees of freedom corresponding to supplementary shape functions. A novel procedure is presented to integrate material coefficient matrices semi-analytically for thermoelastic functionally graded materials.

Contrary to many other numerical methods, the scaled boundary open polygon elements have elegant built-in capabilities to capture stress singularities accurately, irrespective of the material's homogeneity and symmetry. Consequently, stress intensity factors (SIFs) are directly evaluated from their definitions without additional post-processing. It is demonstrated that the ability of the SBFEM to capture singular stress remains unchanged in the cases of uni-directional and full thermoelastic coupling. Thus, the calculation of SIFs also remains consistent. Furthermore, it has been shown that for discrete crack propagation modeling, only a localized patch needs to be re-meshed by employing polygon elements generated from background triangles. The proposed novel procedure of mapping auxiliary DOFs facilitates the modeling of discrete crack propagation in the case of fully coupled thermoelasticity. The simulated results with standard and functionally graded materials, stationary, and moving cracks have been validated by comparing them with results in the literature. In conclusion, it has been shown that the developed numerical technique based on the SBFEM can be applied to various thermoelastic fracture problems efficiently and accurately.

In the last part of this work, the numerical examples of fully coupled thermoelastic crack propagation modeling showed that the interplay of timestep size and user-defined crack accumulation length influences the results of crack paths. It is demonstrated that the crack extension at each timestep is desired. However, it is impractical in some cases due to the inherent limitation of discrete crack propagation, i.e., very small crack extension compared to the element size. An interesting future work could be the development of a new re-meshing approach. For example,

if the crack extension remains inside the same polygon element, only the scaling center of the cracked element needs to be moved to the new crack tip. This approach is applicable as the polygon element remains star-convex. The suggested approach requires only updating the cracked element, and the whole re-meshing procedure can be avoided. Another re-meshing approach could be a polytree-based mesh refinement that can rapidly transition from very refined mesh near the crack tip to coarse mesh away from the crack tip. A very small crack extension can then be captured with very fine mesh near the crack tip without needing overall mesh refinement. In this work, only two-dimensional thermoelastic fracture problems are addressed. The SBFEM has already been successfully applied to model elastic fracture in three dimensions. A logical addition to the work presented in this thesis is the modeling of thermoelastic fractures in three-dimensional space using the SBFEM. Recently, modeling generalized thermoelasticity based on Lord-Shulman [179], Green-Lindsay [180], and Green-Naghdi [181] models has become an active research topic. An interesting future extension of this work could be the modeling of fracture considering generalized thermoelasticity.

# Bibliography

- [1] Z. Chen and C. Butcher. *Micromechanics Modelling of Ductile Fracture*. Solid Mechanics and Its Applications 195. Springer, 2013.
- [2] A. A. Griffith. “The Phenomena of Rupture and Flow in Solids”. In: *Philosophical Transactions of the Royal Society of London. Series A, Containing Papers of a Mathematical or Physical Character* 221.582-593 (1921), pp. 163–198.
- [3] T. L. Anderson. *Fracture Mechanics: Fundamentals and Applications*. 3rd ed. Taylor & Francis, 2005.
- [4] S. Murakami. *Continuum Damage Mechanics: A Continuum Mechanics Approach to the Analysis of Damage and Fracture*. Solid Mechanics and Its Applications 185. Springer, 2012.
- [5] G. A. Francfort and J.-J. Marigo. “Revisiting Brittle Fracture as an Energy Minimization Problem”. In: *Journal of the Mechanics and Physics of Solids* 46.8 (1998), pp. 1319–1342.
- [6] B. Bourdin, G. A. Francfort, and J.-J. Marigo. “Numerical Experiments in Revisited Brittle Fracture”. In: *Journal of the Mechanics and Physics of Solids* 48.4 (2000), pp. 797–826.
- [7] C. Miehe, M. Hofacker, and F. Welschinger. “A Phase Field Model for Rate-Independent Crack Propagation: Robust Algorithmic Implementation Based on Operator Splits”. In: *Computer Methods in Applied Mechanics and Engineering* 199.45 (2010), pp. 2765–2778.
- [8] C. Miehe, F. Welschinger, and M. Hofacker. “Thermodynamically Consistent Phase-Field Models of Fracture: Variational Principles and Multi-Field FE Implementations”. In: *International Journal for Numerical Methods in Engineering* 83.10 (2010), pp. 1273–1311.
- [9] M. Ambati, T. Gerasimov, and L. De Lorenzis. “A Review on Phase-Field Models of Brittle Fracture and a New Fast Hybrid Formulation”. In: *Computational Mechanics* 55.2 (2015), pp. 383–405.
- [10] J. L. Bogdanoff. “Note on Thermal Stresses”. In: *Journal of Applied Mechanics* 21.1 (1954), pp. 88–88.
- [11] G. C. Sih. “On the Singular Character of Thermal Stresses near a Crack Tip”. In: *Journal of Applied Mechanics* 29.3 (1962), pp. 587–589.
- [12] V. Watwood. “The Finite Element Method for Prediction of Crack Behavior”. In: *Nuclear Engineering and Design* 11.2 (1970), pp. 323–332.
- [13] S. Chan, I. Tuba, and W. Wilson. “On the Finite Element Method in Linear Fracture Mechanics”. In: *Engineering Fracture Mechanics* 2.1 (1970), pp. 1–17.
- [14] G. P. Anderson, V. L. Ruggles, and G. S. Stibor. “Use of Finite Element Computer Programs in Fracture Mechanics”. In: *International Journal of Fracture Mechanics* 7.1 (1971), pp. 63–76.
- [15] D. J. Hayes. “A Practical Application of Buekner’s Formulation for Determining Stress Intensity Factors for Cracked Bodies”. In: *International Journal of Fracture Mechanics* 8.2 (1972), pp. 157–165.
- [16] E. Byskov. “The Calculation of Stress Intensity Factors Using the Finite Element Method with Cracked Elements”. In: *International Journal of Fracture Mechanics* 6.2 (1970), pp. 159–167.
- [17] D. M. Tracey. “Finite Elements for Determination of Crack Tip Elastic Stress Intensity Factors”. In: *Engineering Fracture Mechanics* 3.3 (1971), pp. 255–265.
- [18] S. E. Benzley. “Representation of Singularities with Isoparametric Finite Elements”. In: *International Journal for Numerical Methods in Engineering* 8.3 (1974), pp. 537–545.
- [19] J. E. Akin. “The Generation of Elements with Singularities”. In: *International Journal for Numerical Methods in Engineering* 10.6 (1976), pp. 1249–1259.
- [20] M. Nejati, A. Paluszny, and R. W. Zimmerman. “On the Use of Quarter-Point Tetrahedral Finite Elements in Linear Elastic Fracture Mechanics”. In: *Engineering Fracture Mechanics* 144 (2015), pp. 194–221.
- [21] R. S. Barsoum. “Application of Quadratic Isoparametric Finite Elements in Linear Fracture Mechanics”. In: *International Journal of Fracture* 10.4 (1974), pp. 603–605.
- [22] R. D. Henshell and K. G. Shaw. “Crack Tip Finite Elements Are Unnecessary”. In: *International Journal for Numerical Methods in Engineering* 9.3 (1975), pp. 495–507.

- [23] R. S. Barsoum. "On the Use of Isoparametric Finite Elements in Linear Fracture Mechanics". In: *International Journal for Numerical Methods in Engineering* 10.1 (1976), pp. 25–37.
- [24] M. Ortiz, Y. Leroy, and A. Needleman. "A Finite Element Method for Localized Failure Analysis". In: *Computer Methods in Applied Mechanics and Engineering* 61.2 (1987), pp. 189–214.
- [25] T. Belytschko, J. Fish, and B. E. Engelmann. "A Finite Element with Embedded Localization Zones". In: *Computer Methods in Applied Mechanics and Engineering* 70.1 (1988), pp. 59–89.
- [26] E. N. Dvorkin, A. M. Cuitiño, and G. Gioia. "Finite Elements with Displacement Interpolated Embedded Localization Lines Insensitive to Mesh Size and Distortions". In: *International Journal for Numerical Methods in Engineering* 30.3 (1990), pp. 541–564.
- [27] M. Jirásek. "Comparative Study on Finite Elements with Embedded Discontinuities". In: *Computer Methods in Applied Mechanics and Engineering* 188.1 (2000), pp. 307–330.
- [28] C. Linder and C. Miehe. "Effect of Electric Displacement Saturation on the Hysteretic Behavior of Ferroelectric Ceramics and the Initiation and Propagation of Cracks in Piezoelectric Ceramics". In: *Journal of the Mechanics and Physics of Solids* 60.5 (2012), pp. 882–903.
- [29] C. D. Foster, R. I. Borja, and R. A. Regueiro. "Embedded Strong Discontinuity Finite Elements for Fractured Geomaterials with Variable Friction". In: *International Journal for Numerical Methods in Engineering* 72.5 (2007), pp. 549–581.
- [30] C. Linder, D. Rosato, and C. Miehe. "New Finite Elements with Embedded Strong Discontinuities for the Modeling of Failure in Electromechanical Coupled Solids". In: *Computer Methods in Applied Mechanics and Engineering* 200.1 (2011), pp. 141–161.
- [31] F. Armero and C. Linder. "Numerical Simulation of Dynamic Fracture Using Finite Elements with Embedded Discontinuities". In: *International Journal of Fracture* 160.2 (2009), pp. 119–141.
- [32] J. Mosler and G. Meschke. "Embedded Crack vs. Smeared Crack Models: A Comparison of Elementwise Discontinuous Crack Path Approaches with Emphasis on Mesh Bias". In: *Computer Methods in Applied Mechanics and Engineering*. Computational Failure Mechanics 193.30 (2004), pp. 3351–3375.
- [33] N. Moës, J. Dolbow, and T. Belytschko. "A Finite Element Method for Crack Growth without Remeshing". In: *International Journal for Numerical Methods in Engineering* 46.1 (1999), pp. 131–150.
- [34] T. Belytschko and T. Black. "Elastic Crack Growth in Finite Elements with Minimal Remeshing". In: *International Journal for Numerical Methods in Engineering* 45.5 (1999), pp. 601–620.
- [35] N. Moës and T. Belytschko. "Extended Finite Element Method for Cohesive Crack Growth". In: *Engineering Fracture Mechanics* 69.7 (2002), pp. 813–833.
- [36] T. Strouboulis, I. Babuška, and K. Copps. "The Design and Analysis of the Generalized Finite Element Method". In: *Computer Methods in Applied Mechanics and Engineering* 181.1 (2000), pp. 43–69.
- [37] J. M. Melenk and I. Babuška. "The Partition of Unity Finite Element Method: Basic Theory and Applications". In: *Computer Methods in Applied Mechanics and Engineering* 139.1 (1996), pp. 289–314.
- [38] I. Babuška and J. M. Melenk. "The Partition of Unity Method". In: *International Journal for Numerical Methods in Engineering* 40.4 (1997), pp. 727–758.
- [39] J. Chessa and T. Belytschko. "An Enriched Finite Element Method and Level Sets for Axisymmetric Two-Phase Flow with Surface Tension". In: *International Journal for Numerical Methods in Engineering* 58.13 (2003), pp. 2041–2064.
- [40] J. Chessa and T. Belytschko. "An Extended Finite Element Method for Two-Phase Fluids". In: *Journal of Applied Mechanics* 70.1 (2003), pp. 10–17.
- [41] R. Duddu et al. "A Combined Extended Finite Element and Level Set Method for Biofilm Growth". In: *International Journal for Numerical Methods in Engineering* 74.5 (2008), pp. 848–870.
- [42] A. Zilian and A. Legay. "The Enriched Space-Time Finite Element Method (EST) for Simultaneous Solution of Fluid-Structure Interaction". In: *International Journal for Numerical Methods in Engineering* 75.3 (2008), pp. 305–334.
- [43] U. M. Mayer, A. Gerstenberger, and W. A. Wall. "Interface Handling for Three-Dimensional Higher-Order XFEM-computations in Fluid-Structure Interaction". In: *International Journal for Numerical Methods in Engineering* 79.7 (2009), pp. 846–869.
- [44] M. Duflot. "The Extended Finite Element Method in Thermoelastic Fracture Mechanics". In: *International Journal for Numerical Methods in Engineering* 74.5 (2008), pp. 827–847.

- [45] A. Zamani and M. R. Eslami. "Implementation of the Extended Finite Element Method for Dynamic Thermoelastic Fracture Initiation". In: *International Journal of Solids and Structures* 47.10 (2010), pp. 1392–1404.
- [46] V. Esmati, M. B. Nazari, and M. M. Rokhi. "Implementation of XFEM for Dynamic Thermoelastic Crack Analysis under Non-Classic Thermal Shock". In: *Theoretical and Applied Fracture Mechanics* 95 (2018), pp. 42–58.
- [47] F. Habib, L. Sorelli, and M. Fafard. "Full Thermo-Mechanical Coupling Using eXtended Finite Element Method in Quasi-Transient Crack Propagation". In: *Advanced Modeling and Simulation in Engineering Sciences* 5.1 (2018), p. 18.
- [48] M. Shahsavan, M. B. Nazari, and M. Mahdizadeh Rokhi. "Dynamic Analysis of Cracks under Thermal Shock Considering Thermoelasticity without Energy Dissipation". In: *Journal of Thermal Stresses* 42.5 (2019), pp. 607–628.
- [49] S. H. Bayat and M. B. Nazari. "Thermal Fracture Analysis in Orthotropic Materials by XFEM". In: *Theoretical and Applied Fracture Mechanics* 112 (2021), p. 102843.
- [50] S. H. Bayat and M. B. Nazari. "Dynamic Crack Propagation under Thermal Impact". In: *International Journal of Solids and Structures* 264 (2023), p. 112090.
- [51] S. H. Bayat and M. B. Nazari. "Thermally Nonlinear Analysis of Propagating Cracks under Generalized Thermal Shock". In: *International Journal of Non-Linear Mechanics* 157 (2023), p. 104522.
- [52] S. Bhattacharya et al. "Fatigue Crack Growth Simulations of Interfacial Cracks in Bi-Layered FGMs Using XFEM". In: *Computational Mechanics* 52.4 (2013), pp. 799–814.
- [53] H. Bayesteh and S. Mohammadi. "XFEM Fracture Analysis of Orthotropic Functionally Graded Materials". In: *Composites Part B: Engineering* 44.1 (2013), pp. 8–25.
- [54] S. Hosseini, H. Bayesteh, and S. Mohammadi. "Thermo-Mechanical XFEM Crack Propagation Analysis of Functionally Graded Materials". In: *Materials Science and Engineering: A* 561 (2013), pp. 285–302.
- [55] F. Guo et al. "An Interaction Energy Integral Method for T-stress Evaluation in Nonhomogeneous Materials under Thermal Loading". In: *Mechanics of Materials* 83 (2015), pp. 30–39.
- [56] Y. Zhang et al. "A Numerical Method for the Thermal-Shock Crack Problems of Nonhomogeneous Materials with Inclusions Based on an Interaction Energy Integral Method". In: *Engineering Fracture Mechanics* 190 (2018), pp. 159–174.
- [57] H. Pathak. "Crack Interaction Study in Functionally Graded Materials (FGMs) Using XFEM under Thermal and Mechanical Loading Environment". In: *Mechanics of Advanced Materials and Structures* 27.11 (2020), pp. 903–926.
- [58] T. Rabczuk. "Computational Methods for Fracture in Brittle and Quasi-Brittle Solids: State-of-the-Art Review and Future Perspectives". In: *ISRN Applied Mathematics* 2013 (2013), pp. 1–38.
- [59] V. P. Nguyen et al. "Meshless Methods: A Review and Computer Implementation Aspects". In: *Mathematics and Computers in Simulation* 79.3 (2008), pp. 763–813.
- [60] T. A. Cruse. "Numerical Solutions in Three Dimensional Elastostatics". In: *International Journal of Solids and Structures* 5.12 (1969), pp. 1259–1274.
- [61] T. A. Cruse. "Lateral Constraint in a Cracked, Three Dimensional Elastic Body". In: *International Journal of Fracture Mechanics* 6.3 (1970), pp. 326–328.
- [62] T. A. Cruse and W. Vanburen. "Three-Dimensional Elastic Stress Analysis of a Fracture Specimen with an Edge Crack". In: *International Journal of Fracture Mechanics* 7.1 (1971), pp. 1–15.
- [63] Kang Yong Lee and Youn Ho Cho. "Boundary Element Analysis of Thermal Stress Intensity Factors for Cusp Cracks". In: *Engineering Fracture Mechanics* 37.4 (1990), pp. 787–798.
- [64] J. Sladek and V. Sladek. "Computation of Strip Yield Lengths for a Crack in 2-d Stationary Thermoelasticity Using the BEM". In: *Engineering Analysis with Boundary Elements* 11.3 (1993), pp. 189–193.
- [65] N. N. V. Prasad, M. H. Aliabadi, and D. P. Rooke. "Incremental Crack Growth in Thermoelastic Problems". In: *International Journal of Fracture* 66.3 (1994), R45–R50.
- [66] N. N. V. Prasad, M. H. Aliabadi, and D. P. Rooke. "The Dual Boundary Element Method for Thermoelastic Crack Problems". In: *International Journal of Fracture* 66.3 (1994), pp. 255–272.
- [67] N. N. V. Prasad, M. H. Aliabadi, and D. P. Rooke. "The Dual Boundary Element Method for Transient Thermoelastic Crack Problems". In: *International Journal of Solids and Structures* 33.19 (1996), pp. 2695–2718.
- [68] A. Ekhlakov et al. "Thermoelastic Crack Analysis in Functionally Graded Materials and Structures by a BEM". In: *Fatigue & Fracture of Engineering Materials & Structures* 35.8 (2012), pp. 742–766.

- [69] A. Ekhlakov et al. "A BDEM for Transient Thermoelastic Crack Problems in Functionally Graded Materials under Thermal Shock". In: *Computational Materials Science* 57 (2012), pp. 30–37.
- [70] T. Belytschko, L. Gu, and Y. Y. Lu. "Fracture and Crack Growth by Element Free Galerkin Methods". In: *Modelling and Simulation in Materials Science and Engineering* 2.3A (1994), p. 519.
- [71] T. Belytschko, Y. Y. Lu, and L. Gu. "Element-Free Galerkin Methods". In: *International Journal for Numerical Methods in Engineering* 37.2 (1994), pp. 229–256.
- [72] Y. Y. Lu, T. Belytschko, and L. Gu. "A New Implementation of the Element Free Galerkin Method". In: *Computer Methods in Applied Mechanics and Engineering* 113.3 (1994), pp. 397–414.
- [73] S. Atluri and S. Shen. "The Meshless Local Petrov-Galerkin (MLPG) Method: A Simple & Less-Costly Alternative to the Finite Element and Boundary Element Methods". In: *Computer Modeling in Engineering & Sciences* 3.1 (1970), pp. 11–52.
- [74] S. N. Atluri and T. Zhu. "A New Meshless Local Petrov-Galerkin (MLPG) Approach in Computational Mechanics". In: *Computational Mechanics* 22.2 (1998), pp. 117–127.
- [75] S. N. Atluri and T. ... Zhu. "The Meshless Local Petrov-Galerkin (MLPG) Approach for Solving Problems in Elasto-Statics". In: *Computational Mechanics* 25.2 (2000), pp. 169–179.
- [76] N. K. Mukhopadhyay, S. K. Maiti, and A. Kakodkar. "A Review of SIF Evaluation and Modelling of Singularities in BEM". In: *Computational Mechanics* 25.4 (2000), pp. 358–375.
- [77] W. Zeng and G. R. Liu. "Smoothed Finite Element Methods (S-FEM): An Overview and Recent Developments". In: *Archives of Computational Methods in Engineering* 25.2 (2018), pp. 397–435.
- [78] A. Egger et al. "Discrete and Phase Field Methods for Linear Elastic Fracture Mechanics: A Comparative Study and State-of-the-Art Review". In: *Applied Sciences* 9.12 (2019), p. 2436.
- [79] M. Cervera et al. "A Comparative Review of XFEM, Mixed FEM and Phase-Field Models for Quasi-Brittle Cracking". In: *Archives of Computational Methods in Engineering* 29.2 (2022), pp. 1009–1083.
- [80] J. R. Rice. "A Path Independent Integral and the Approximate Analysis of Strain Concentration by Notches and Cracks". In: *Journal of Applied Mechanics* 35.2 (1968), pp. 379–386.
- [81] B. Budiansky and J. R. Rice. "Conservation Laws and Energy-Release Rates". In: *Journal of Applied Mechanics* 40.1 (1973), pp. 201–203.
- [82] M. Stern, E. B. Becker, and R. S. Dunham. "A Contour Integral Computation of Mixed-Mode Stress Intensity Factors". In: *International Journal of Fracture* 12.3 (1976), pp. 359–368.
- [83] B. N. Rao and S. Rahman. "An Interaction Integral Method for Analysis of Cracks in Orthotropic Functionally Graded Materials". In: *Computational Mechanics* 32.1 (2003), pp. 40–51.
- [84] B. N. Rao and S. Rahman. "Mesh-Free Analysis of Cracks in Isotropic Functionally Graded Materials". In: *Engineering Fracture Mechanics* 70.1 (2003), pp. 1–27.
- [85] B. N. Rao and S. Rahman. "Continuum Shape Sensitivity Analysis of a Mixed-Mode Fracture in Functionally Graded Materials". In: *Computer Methods in Applied Mechanics and Engineering* 194.18 (2005), pp. 1913–1946.
- [86] A. KC and J.-H. Kim. "Interaction Integrals for Thermal Fracture of Functionally Graded Materials". In: *Engineering Fracture Mechanics* 75.8 (2008), pp. 2542–2565.
- [87] J.-H. Kim and A. KC. "A Generalized Interaction Integral Method for the Evaluation of the T-stress in Orthotropic Functionally Graded Materials under Thermal Loading". In: *Journal of Applied Mechanics* 75.5 (2008), p. 051112.
- [88] H. Yu and M. Kuna. "Interaction Integral Method for Computation of Crack Parameters K-T – a Review". In: *Engineering Fracture Mechanics* 249 (2021), p. 107722.
- [89] C. Song and J. P. Wolf. "Consistent Infinitesimal Finite-Element Cell Method: Three-Dimensional Vector Wave Equation". In: *International Journal for Numerical Methods in Engineering* 39.13 (1996), pp. 2189–2208.
- [90] C. Song and J. P. Wolf. "The Scaled Boundary Finite-Element Method—Alias Consistent Infinitesimal Finite-Element Cell Method—for Elastodynamics". In: *Computer Methods in Applied Mechanics and Engineering* 147.3 (1997), pp. 329–355.
- [91] C. Song and J. P. Wolf. "The Scaled Boundary Finite-Element Method: Analytical Solution in Frequency Domain". In: *Computer Methods in Applied Mechanics and Engineering* 164.1 (1998), pp. 249–264.
- [92] C. Song. "The Scaled Boundary Finite Element Method in Structural Dynamics". In: *International Journal for Numerical Methods in Engineering* 77.8 (2009), pp. 1139–1171.
- [93] H. Gravenkamp et al. "The Simulation of Lamb Waves in a Cracked Plate Using the Scaled Boundary Finite Element Method". In: *The Journal of the Acoustical Society of America* 132.3 (2012), pp. 1358–1367.

- [94] H. Gravenkamp and S. Natarajan. "Scaled Boundary Polygons for Linear Elastodynamics". In: *Computer Methods in Applied Mechanics and Engineering* 333 (2018), pp. 238–256.
- [95] C. Birk and C. Song. "A Continued-Fraction Approach for Transient Diffusion in Unbounded Medium". In: *Computer Methods in Applied Mechanics and Engineering* 198.33 (2009), pp. 2576–2590.
- [96] H. Gravenkamp. "Efficient Simulation of Elastic Guided Waves Interacting with Notches, Adhesive Joints, Delaminations and Inclined Edges in Plate Structures". In: *Ultrasonics* 82 (2018), pp. 101–113.
- [97] D. Itner et al. "Efficient Semi-Analytical Simulation of Elastic Guided Waves in Cylinders Subject to Arbitrary Non-Symmetric Loads". In: *Ultrasonics* 114 (2021), p. 106389.
- [98] J. Liu and G. Lin. "A Scaled Boundary Finite Element Method Applied to Electrostatic Problems". In: *Engineering Analysis with Boundary Elements* 36.12 (2012), pp. 1721–1732.
- [99] G. Lin et al. "A Scaled Boundary Finite Element Approach for Sloshing Analysis of Liquid Storage Tanks". In: *Engineering Analysis with Boundary Elements* 56 (2015), pp. 70–80.
- [100] Y. Wang, G. Lin, and Z. Hu. "Novel Nonreflecting Boundary Condition for an Infinite Reservoir Based on the Scaled Boundary Finite-Element Method". In: *Journal of Engineering Mechanics* 141.5 (2015), p. 04014150.
- [101] L. Liu et al. "Automatic Three-Dimensional Acoustic-Structure Interaction Analysis Using the Scaled Boundary Finite Element Method". In: *Journal of Computational Physics* 395 (2019), pp. 432–460.
- [102] E. T. Ooi, C. Song, and S. Natarajan. "A Scaled Boundary Finite Element Formulation for Poroelasticity". In: *International Journal for Numerical Methods in Engineering* 114.8 (2018), pp. 905–929.
- [103] M. Wallner, C. Birk, and H. Gravenkamp. "A Scaled Boundary Finite Element Approach for Shell Analysis". In: *Computer Methods in Applied Mechanics and Engineering* 361 (2020), p. 112807.
- [104] S. Natarajan et al. "Isogeometric Analysis Enhanced by the Scaled Boundary Finite Element Method". In: *Computer Methods in Applied Mechanics and Engineering* 283 (2015), pp. 733–762.
- [105] S. Klinkel, L. Chen, and W. Dornisch. "A NURBS Based Hybrid Collocation–Galerkin Method for the Analysis of Boundary Represented Solids". In: *Computer Methods in Applied Mechanics and Engineering* 284 (2015), pp. 689–711.
- [106] A. J. Deeks and J. P. Wolf. "Stress Recovery and Error Estimation for the Scaled Boundary Finite-Element Method". In: *International Journal for Numerical Methods in Engineering* 54.4 (2002), pp. 557–583.
- [107] C. Song. "A Matrix Function Solution for the Scaled Boundary Finite-Element Equation in Statics". In: *Computer Methods in Applied Mechanics and Engineering* 193.23-26 (2004), pp. 2325–2356.
- [108] C. Song et al. "A Novel Error Indicator and an Adaptive Refinement Technique Using the Scaled Boundary Finite Element Method". In: *Engineering Analysis with Boundary Elements* 94 (2018), pp. 10–24.
- [109] H. Gravenkamp, C. Song, and J. Zhang. "On Mass Lumping and Explicit Dynamics in the Scaled Boundary Finite Element Method". In: *Computer Methods in Applied Mechanics and Engineering* 370 (2020), p. 113274.
- [110] Z. Yang and A. Deeks. "Fully-Automatic Modelling of Cohesive Crack Growth Using a Finite Element–Scaled Boundary Finite Element Coupled Method". In: *Engineering Fracture Mechanics* 74.16 (2007), pp. 2547–2573.
- [111] E. Ooi et al. "Automatic Modelling of Cohesive Crack Propagation in Concrete Using Polygon Scaled Boundary Finite Elements". In: *Engineering Fracture Mechanics* 93 (2012), pp. 13–33.
- [112] Hirshikesh et al. "Adaptive Phase-Field Modeling of Brittle Fracture Using the Scaled Boundary Finite Element Method". In: *Computer Methods in Applied Mechanics and Engineering* 355 (2019), pp. 284–307.
- [113] A. Ankit. "A Sideface Traction Approach for Cohesive and Frictional Crack Growth Problems Using SBFEM". In: *Computer Methods in Applied Mechanics and Engineering* 386 (2021), p. 114076.
- [114] R. Assaf et al. "Three-Dimensional Phase-Field Modeling of Brittle Fracture Using an Adaptive Octree-Based Scaled Boundary Finite Element Approach". In: *Computer Methods in Applied Mechanics and Engineering* 399 (2022), p. 115364.
- [115] S. Natarajan et al. "Adaptive Modelling of Dynamic Brittle Fracture - a Combined Phase Field Regularized Cohesive Zone Model and Scaled Boundary Finite Element Approach". In: *International Journal of Fracture* 236.1 (2022), pp. 87–108.
- [116] C. Song and J. P. Wolf. "Semi-Analytical Representation of Stress Singularities as Occurring in Cracks in Anisotropic Multi-Materials with the Scaled Boundary Finite-Element Method". In: *Computers & Structures* 80.2 (2002), pp. 183–197.
- [117] C. Song. "A Super-Element for Crack Analysis in the Time Domain". In: *International Journal for Numerical Methods in Engineering* 61.8 (2004), pp. 1332–1357.

## Bibliography

---

- [118] C. Song. "Evaluation of Power-Logarithmic Singularities, T-stresses and Higher Order Terms of in-Plane Singular Stress Fields at Cracks and Multi-Material Corners". In: *Engineering Fracture Mechanics* 72.10 (2005), pp. 1498–1530.
- [119] C. Song. "Analysis of Singular Stress Fields at Multi-Material Corners under Thermal Loading". In: *International Journal for Numerical Methods in Engineering* 65.5 (2006), pp. 620–652.
- [120] C. Song, F. Tin-Loi, and W. Gao. "A Definition and Evaluation Procedure of Generalized Stress Intensity Factors at Cracks and Multi-Material Wedges". In: *Engineering Fracture Mechanics* 77.12 (2010), pp. 2316–2336.
- [121] J. Bulling, H. Gravenkamp, and C. Birk. "A High-Order Finite Element Technique with Automatic Treatment of Stress Singularities by Semi-Analytical Enrichment". In: *Computer Methods in Applied Mechanics and Engineering* 355 (2019), pp. 135–156.
- [122] E. T. Ooi et al. "Polygon Scaled Boundary Finite Elements for Crack Propagation Modelling". In: *International Journal for Numerical Methods in Engineering* 91.3 (2012), pp. 319–342.
- [123] E. Ooi et al. "Dynamic Crack Propagation Simulation with Scaled Boundary Polygon Elements and Automatic Remeshing Technique". In: *Engineering Fracture Mechanics* 106 (2013), pp. 1–21.
- [124] I. Chiong et al. "Scaled Boundary Polygons with Application to Fracture Analysis of Functionally Graded Materials". In: *International Journal for Numerical Methods in Engineering* 98.8 (2014), pp. 562–589.
- [125] I. Chiong et al. "Computation of Dynamic Stress Intensity Factors in Cracked Functionally Graded Materials Using Scaled Boundary Polygons". In: *Engineering Fracture Mechanics* 131 (2014), pp. 210–231.
- [126] E. T. Ooi et al. "Crack Propagation Modelling in Functionally Graded Materials Using Scaled Boundary Polygons". In: *International Journal of Fracture* 192.1 (2015), pp. 87–105.
- [127] R. Behnke et al. "A Physically and Geometrically Nonlinear Scaled-Boundary-Based Finite Element Formulation for Fracture in Elastomers". In: *International Journal for Numerical Methods in Engineering* 99.13 (2014), pp. 966–999.
- [128] E. T. Ooi, C. Song, and F. Tin-Loi. "A Scaled Boundary Polygon Formulation for Elasto-Plastic Analyses". In: *Computer Methods in Applied Mechanics and Engineering* 268 (2014), pp. 905–937.
- [129] L. Chen, W. Dornisch, and S. Klinkel. "Hybrid Collocation-Galerkin Approach for the Analysis of Surface Represented 3D-solids Employing SB-FEM". In: *Computer Methods in Applied Mechanics and Engineering* 295 (2015), pp. 268–289.
- [130] M. Chasapi and S. Klinkel. "A Scaled Boundary Isogeometric Formulation for the Elasto-Plastic Analysis of Solids in Boundary Representation". In: *Computer Methods in Applied Mechanics and Engineering* 333 (2018), pp. 475–496.
- [131] S. Klinkel and R. Reichel. "A Finite Element Formulation in Boundary Representation for the Analysis of Nonlinear Problems in Solid Mechanics". In: *Computer Methods in Applied Mechanics and Engineering* 347 (2019), pp. 295–315.
- [132] M. Chasapi and S. Klinkel. "Geometrically Nonlinear Analysis of Solids Using an Isogeometric Formulation in Boundary Representation". In: *Computational Mechanics* 65.2 (2020), pp. 355–373.
- [133] M. Chasapi et al. "Isogeometric Analysis of 3D Solids in Boundary Representation for Problems in Nonlinear Solid Mechanics and Structural Dynamics". In: *International Journal for Numerical Methods in Engineering* 123.5 (2022), pp. 1228–1252.
- [134] M. E. Gurtin. *An Introduction to Continuum Mechanics*. Mathematics in Science and Engineering v. 158. Academic Press, 1981.
- [135] G. A. Holzapfel. *Nonlinear Solid Mechanics: A Continuum Approach for Engineering*. Wiley, 2000.
- [136] P. Wriggers. *Nonlinear Finite Element Methods*. Springer, 2010.
- [137] R. B. Hetnarski and M. R. Eslami. *Thermal Stresses—Advanced Theory and Applications*. Vol. 158. Solid Mechanics and Its Applications. Springer International Publishing, 2019.
- [138] S. K. Maiti. *Fracture Mechanics: Fundamentals and Applications*. Cambridge University Press, 2015.
- [139] D. Gross and T. Seelig. *Fracture Mechanics: With an Introduction to Micromechanics*. Mechanical Engineering Series. Springer International Publishing, 2018.
- [140] B. D. Coleman and M. E. Gurtin. "Thermodynamics with Internal State Variables". In: *The Journal of Chemical Physics* 47.2 (1967), pp. 597–613.
- [141] B. D. Coleman and W. Noll. "The Thermodynamics of Elastic Materials with Heat Conduction and Viscosity". In: *The Foundations of Mechanics and Thermodynamics*. Springer Berlin Heidelberg, 1974, pp. 145–156.

- [142] G. R. Irwin. "Analysis of Stresses and Strains near the End of a Crack Traversing a Plate". In: *Journal of Applied Mechanics* 24.3 (1957), pp. 361–364.
- [143] H. M. Westergaard. "Bearing Pressures and Cracks: Bearing Pressures through a Slightly Waved Surface or through a Nearly Flat Part of a Cylinder, and Related Problems of Cracks". In: *Journal of Applied Mechanics* 6.2 (1939), A49–A53.
- [144] F. Erdogan and G. C. Sih. "On the Crack Extension in Plates under Plane Loading and Transverse Shear". In: *Journal of Basic Engineering* 85.4 (1963), pp. 519–525.
- [145] G. C. Sih. "Strain-Energy-Density Factor Applied to Mixed Mode Crack Problems". In: *International Journal of Fracture* 10.3 (1974), pp. 305–321.
- [146] R. J. Nuismer. "An Energy Release Rate Criterion for Mixed Mode Fracture". In: *International Journal of Fracture* 11.2 (1975), pp. 245–250.
- [147] N. Sukumar and J.-H. Prévost. "Modeling Quasi-Static Crack Growth with the Extended Finite Element Method Part I: Computer Implementation". In: *International Journal of Solids and Structures* 40.26 (2003), pp. 7513–7537.
- [148] J. P. Wolf. *The Scaled Boundary Finite Element Method*. 1. edition. Wiley, 2003.
- [149] C. Song. *The Scaled Boundary Finite Element Method: Introduction to Theory and Implementation*. John Wiley & Sons, 2018.
- [150] M. G. Duffy. "Quadrature over a Pyramid or Cube of Integrands with a Singularity at a Vertex". In: *SIAM Journal on Numerical Analysis* 19.6 (1982), pp. 1260–1262.
- [151] C. Song and J. P. Wolf. "The Scaled Boundary Finite Element Method—Alias Consistent Infinitesimal Finite Element Cell Method—for Diffusion". In: *International Journal for Numerical Methods in Engineering* 45.10 (1999), pp. 1403–1431.
- [152] J. P. Wolf and C. Song. "The Scaled Boundary Finite-Element Method – a Primer: Derivations". In: *Computers & Structures* 78.1 (2000), pp. 191–210.
- [153] E. Ooi et al. "A Polygon Scaled Boundary Finite Element Formulation for Transient Coupled Thermoelastic Fracture Problems". In: *Engineering Fracture Mechanics* 240 (2020), p. 107300.
- [154] M. Iqbal et al. "Development of the Scaled Boundary Finite Element Method for Crack Propagation Modeling of Elastic Solids Subjected to Coupled Thermo-Mechanical Loads". In: *Computer Methods in Applied Mechanics and Engineering* 387 (2021), p. 114106.
- [155] M. Iqbal et al. "Thermoelastic Fracture Analysis of Functionally Graded Materials Using the Scaled Boundary Finite Element Method". In: *Engineering Fracture Mechanics* 264 (2022), p. 108305.
- [156] B. L. Karihaloo and Q. Z. Xiao. "Accurate Determination of the Coefficients of Elastic Crack Tip Asymptotic Field by a Hybrid Crack Element with P-Adaptivity". In: *Engineering Fracture Mechanics* 68.15 (2001), pp. 1609–1630.
- [157] B. Delaunay. "Sur La Sphere Vide". In: *Izv. Akad. Nauk SSSR, Otdelenie Matematicheskii i Estestvennyka Nauk* 7.793–800 (1934), pp. 1–2.
- [158] C. Geuzaine and J.-F. Remacle. "Gmsh: A 3-D Finite Element Mesh Generator with Built-in Pre- and Post-Processing Facilities". In: *International Journal for Numerical Methods in Engineering* 79.11 (2009), pp. 1309–1331.
- [159] E. H. Moore. "On the Reciprocal of the General Algebraic Matrix". In: *Bulletin of the american mathematical society* 26 (1920), pp. 294–295.
- [160] R. Penrose. "A Generalized Inverse for Matrices". In: *Mathematical Proceedings of the Cambridge Philosophical Society* 51.3 (1955), pp. 406–413.
- [161] H. Chen et al. "Simulation of Thermoelastic Crack Problems Using Singular Edge-Based Smoothed Finite Element Method". In: *International Journal of Mechanical Sciences* 115–116 (2016), pp. 123–134.
- [162] M. N. Nguyen et al. "Simulation of Dynamic and Static Thermoelastic Fracture Problems by Extended Nodal Gradient Finite Elements". In: *International Journal of Mechanical Sciences* 134 (2017), pp. 370–386.
- [163] Y. Murakami and N. Z. Gakkai. *Stress Intensity Factors Handbook, Volume 3*. Society of Materials Science, Japan, 1992.
- [164] S. Dag, E. Erhan Arman, and B. Yildirim. "Computation of Thermal Fracture Parameters for Orthotropic Functionally Graded Materials Using  $J_k$ -Integral". In: *International Journal of Solids and Structures* 47.25–26 (2010), pp. 3480–3488.
- [165] L. Bouhala, A. Makradi, and S. Belouettar. "Thermal and Thermo-Mechanical Influence on Crack Propagation Using an Extended Mesh Free Method". In: *Engineering Fracture Mechanics* 88 (2012), pp. 35–48.

## Bibliography

---

- [166] H. Wang. "A Meshfree Variational Multiscale Methods for Thermo-Mechanical Material Failure". In: *Theoretical and Applied Fracture Mechanics* 75 (2015), pp. 1–7.
- [167] W. Ai and C. E. Augarde. "Thermoelastic Fracture Modelling in 2D by an Adaptive Cracking Particle Method without Enrichment Functions". In: *International Journal of Mechanical Sciences* 160 (2019), pp. 343–357.
- [168] N. T. Nguyen et al. "Meshfree Thermomechanical Crack Growth Simulations with New Numerical Integration Scheme". In: *Engineering Fracture Mechanics* 235 (2020), p. 107121.
- [169] S. Sarkar, I. V. Singh, and B. K. Mishra. "A Thermo-Mechanical Gradient Enhanced Damage Method for Fracture". In: *Computational Mechanics* 66.6 (2020), pp. 1399–1426.
- [170] M. Nguyen et al. "Thermal-Mechanical Crack Propagation in Orthotropic Composite Materials by the Extended Four-Node Consecutive-Interpolation Element (XCQ4)". In: *Engineering Fracture Mechanics* 206 (2019), pp. 89–113.
- [171] A. Memari and H. Mohebalizadeh. "Quasi-Static Analysis of Mixed-Mode Crack Propagation Using the Meshless Local Petrov–Galerkin Method". In: *Engineering Analysis with Boundary Elements* 106 (2019), pp. 397–411.
- [172] H. Zhang, G. Ma, and L. Fan. "Thermal Shock Analysis of 2D Cracked Solids Using the Numerical Manifold Method and Precise Time Integration". In: *Engineering Analysis with Boundary Elements* 75 (2017), pp. 46–56.
- [173] A. Memari and M. R. Khoshravan Azar. "Thermo-Mechanical Shock Fracture Analysis by Meshless Method". In: *Theoretical and Applied Fracture Mechanics* 102 (2019), pp. 171–192.
- [174] M. D. Iqbal et al. "Transient Thermoelastic Fracture Analysis of Functionally Graded Materials Using the Scaled Boundary Finite Element Method". In: *Theoretical and Applied Fracture Mechanics* 127 (2023), p. 104056.
- [175] N. Noda and L.-C. Guo. "Thermal Shock Analysis for a Functionally Graded Plate with a Surface Crack". In: *Acta Mechanica* 195.1–4 (2008), pp. 157–166.
- [176] H. H. Zhang et al. "The Numerical Manifold Method for Crack Modeling of Two-Dimensional Functionally Graded Materials under Thermal Shocks". In: *Engineering Fracture Mechanics* 208 (2019), pp. 90–106.
- [177] W. Yang, A. Pourasghar, and Z. Chen. "Non-Fourier Thermal Fracture Analysis of a Griffith Interface Crack in Orthotropic Functionally Graded Coating/Substrate Structure". In: *Applied Mathematical Modelling* 104 (2022), pp. 548–566.
- [178] L. B. Freund. *Dynamic Fracture Mechanics: Cambridge Monographs on Mechanics and Applied Mathematics*. Cambridge University Press, 1998.
- [179] H. Lord and Y. Shulman. "A Generalized Dynamical Theory of Thermoelasticity". In: *Journal of the Mechanics and Physics of Solids* 15.5 (1967), pp. 299–309.
- [180] A. E. Green and K. A. Lindsay. "Thermoelasticity". In: *Journal of Elasticity* 2.1 (1972), pp. 1–7.
- [181] A. E. Green and P. M. Naghdi. "Thermoelasticity without Energy Dissipation". In: *Journal of Elasticity* 31.3 (1993), pp. 189–208.

# List of Figures

|      |   |    |
|------|---|----|
| 2.1  | Configurations of a body in continuum mechanics. . . . .  | 10 |
| 2.2  | Crack opening modes. . . . .  | 19 |
| 2.3  | A domain with a crack in polar and Cartesian coordinates. . . . .   | 20 |
| 2.4  | Variation of crack propagation angle with respect to SIF ratio. . . . .   | 21 |
| 3.1  | Geometric transformation of a two-dimensional domain $\Omega$ with a boundary $\Gamma$ into scaled boundary method. . . . .   | 23 |
| 3.2  | Two examples of star-convex polygons. . . . .   | 24 |
| 3.3  | One-dimensional shape functions of three-node line elements. . . . .  | 25 |
| 3.4  | Discretization of the $S^e$ subdomain with two-node line element and the formulation a scaled boundary finite element. . . . .  | 25 |
| 3.5  | Scaled boundary finite open-element with crack faces. . . . .   | 25 |
| 3.6  | Scaled boundary subdomain $S^e$ with coordinate curves $\Gamma^\xi, \Gamma^\eta$ and their tangential and normal vectors. . . . .   | 28 |
| 3.7  | Scaled boundary shape functions of a polygon element. . . . .   | 42 |
| 3.8  | Scaled boundary shape functions of an open-element. . . . .   | 42 |
| 4.1  | Supplementary shape functions $\hat{\chi}^{(p)}(\xi, \eta)$ of quadrilateral element. . . . .   | 51 |
| 4.2  | Supplementary shape functions $\hat{\chi}^{(p)}(\xi, \eta)$ of seven-node open-element. . . . .   | 52 |
| 5.1  | A few examples of functionally graded materials. . . . .  | 57 |
| 5.2  | Polygon meshes used for the fitting of a material variation in FGMs. . . . .  | 59 |
| 5.3  | Fitting of spatially varying material property in scaled boundary coordinates. . . . .  | 59 |
| 5.4  | Fitting of spatially varying material property in scaled boundary coordinates. . . . .  | 60 |
| 6.1  | Polygon mesh of a domain with an open SBFE at a crack tip. . . . .  | 64 |
| 6.2  | An open SBFE with $5^\circ$ crack opening angle and the effects of crack opening angle on $S^{(s)}$ . . . . .   | 65 |
| 6.3  | Convergence of singular modes $S^{(s)}$ with respect to number and order of line elements. . . . .  | 66 |
| 6.4  | A homogeneous isotropic domain with a crack, the same as an open scaled boundary finite polygon element in polar coordinates with the origin and scaling center at the crack tip. . . . . | 67 |
| 6.5  | Delaunay triangulation of a domain $\Omega$ with boundary $\Gamma$ at different mesh characteristic length $h$ . . . . .  | 70 |
| 6.6  | Polygon meshes obtained from the triangular meshes following the transformation. . . . .  | 70 |
| 6.7  | Sample polygon meshes of complex geometries. . . . .  | 71 |
| 6.8  | A localized re-meshing technique of polygon elements based on background triangular elements. . . . .   | 72 |
| 6.9  | Mapping of the global system after localized re-meshing with in patch. . . . .  | 73 |
| 6.10 | Additional mapping points to obtain the solution of supplementary DOFs. . . . .   | 75 |
| 7.1  | A plate with an edge crack under constant flux parallel to a crack. . . . .   | 78 |
| 7.2  | Convergence of mode-I stress intensity factors. . . . .   | 78 |
| 7.3  | A plate with a center crack under constant flux perpendicular to crack. . . . .   | 79 |

|      |  |     |
|------|--|-----|
| 7.4  | Convergence and results of $\bar{K}_{II}$ of a plate with center crack. . . . .  | 80  |
| 7.5  | A plate with an inclined center crack. . . . .   | 81  |
| 7.6  | $\bar{K}$ in a plate with an inclined center crack. . . . .  | 82  |
| 7.7  | A plate with an edge crack and linearly varying material properties. . . . .   | 83  |
| 7.8  | Covergence and results of $K_I$ for varying $a/W$ in FG plate with linear material gradient. . . . .   | 84  |
| 7.9  | A plate with an edge crack and hyperbolic tangent material gradient. . . . .   | 85  |
| 7.10 | Covergence and results of $K_I$ for varying $a/W$ in FG plate with hyperbolic tangent material gradient. . . . .                             | 86  |
| 7.11 | Model of an orthotropic FG plate with a center crack. . . . .  | 87  |
| 7.12 | Mesh and temperature distribution of the FG plate with orthotropic material gradient defined by power-law function. . . . .                  | 88  |
| 7.13 | Normalized stress intensity factors of an orthotropic FG plate for varying $b/W$ and $\omega_2$ . . . . .                                    | 88  |
| 7.14 | Physical model of a cruciform-shaped panel and initial mesh. . . . .   | 89  |
| 7.15 | Normalized stress intensity factors of a cruciform-shaped panel for five sets of boundary conditions and 11 crack incremental steps. . . . . | 90  |
| 7.16 | Crack paths in a cruciform-shaped panel for $\Delta a = 0.3a$ . . . . .  | 91  |
| 7.17 | Initial and final temperature distribution for the fifth set of boundary conditions. . . . .   | 91  |
| 7.18 | Geometry and boundary conditions of the perforated plate. . . . .  | 92  |
| 7.19 | Stress intensity factors of a perforated plate for two cases of mechanical constraints. . . . .  | 92  |
| 7.20 | Crack paths in the perforated plate for mechanical constraints. . . . .  | 93  |
| 7.21 | Mesh and temperature distributions of a perforated plate at the start and end of crack propagation steps. . . . .                            | 93  |
| 7.22 | Geometry and physical model of a perforated plate with multiple cracks. . . . .  | 94  |
| 7.23 | Stress intensity factors of multiple cracks emanating from perforation for two sets of boundary conditions. . . . .                          | 95  |
| 7.24 | Multiple crack paths for different sets of thermal boundary conditions. . . . .  | 95  |
| 7.25 | Mesh and temperature distribution of perforated plate with multiple cracks. . . . .  | 95  |
| 8.1  | The physical model and mesh of a plate subjected to temperature shock result in a temperature variation parallel to a crack. . . . .         | 98  |
| 8.2  | History of transient $\bar{K}_I(t)$ of a plate subjected to temperature shock parallel to a crack. . . . .                                   | 99  |
| 8.3  | Temperature distribution and scaled deformation of a plate subjected to temperature shock parallel to a crack. . . . .                       | 99  |
| 8.4  | Physical model and mesh of a plate subjected to temperature shock perpendicular to a crack. . . . .  | 100 |
| 8.5  | History of transient $\bar{K}_{II}(t)$ of a plate subjected to temperature shock perpendicular to a crack. . . . .                           | 101 |
| 8.6  | Temperature distribution and scaled deformation of a plate subjected to temperature shock perpendicular to a crack. . . . .                  | 101 |
| 8.7  | Physical model and mesh of a plate with an inclined edge crack subjected to flux shock. . . . .  | 102 |
| 8.8  | History of transient stress intensity factors of a plate with an inclined edge crack subjected to flux shock. . . . .                        | 103 |
| 8.9  | Temperature distribution and scaled deformation of a plate with an inclined edge crack subjected to flux shock. . . . .                      | 103 |
| 8.10 | Physical model and mesh of a plate with an exponential material gradient parallel to a crack. . . . .  | 104 |

---

|      |  |     |
|------|--|-----|
| 8.11 | Convergence and results of $\bar{K}_I(\tau)$ for varying $a/W$ in FG plate with an exponential material gradient. . . . .      | 105 |
| 8.12 | Temperature distribution and scaled deformation of a plate with an exponential material gradient. . . . .                      | 105 |
| 8.13 | Physical model and mesh of a plate with a material gradient given by a power-law function. . . . .                             | 106 |
| 8.14 | Convergence of $\bar{K}(\tau)$ of a plate with a material gradient defined by a power-law function. . . . .                    | 107 |
| 8.15 | History of transient normalized SIFs with varying material gradient index $\beta$ . . . . .                                    | 108 |
| 8.16 | Normalized transient SIFs at different crack inclination angles $\varphi$ . . . . .  | 109 |
| 8.17 | Temperature distribution and scaled deformation of a plate with material gradient given by a power-law function. . . . .       | 109 |
| 8.18 | Physical model of an orthotropic plate with an exponential material gradient. . . . .  | 110 |
| 8.19 | Physical model and mesh of an orthotropic plate with exponential material gradient. . . . .                                    | 111 |
| 8.20 | Convergence and results of $\bar{K}(\tau)$ of orthotropic FG plate with an exponential material gradient. . . . .              | 111 |
| 8.21 | Temperature distribution and scaled deformation of an orthotropic plate with an exponential material gradient. . . . .         | 112 |
| 8.22 | Geometry and sample mesh of a notched plate with three holes. . . . .  | 114 |
| 8.23 | Normalized velocity of propagating crack in a notched plate [51]. . . . .  | 114 |
| 8.24 | Resulting crack paths in a notched plate with three holes for varying $h$ , $\Delta a$ , and $\Delta\tau$ . . . . .            | 115 |
| 8.25 | Temperature distribution and scaled deformation in a notched plate with three holes at different $\tau$ . . . . .              | 115 |
| 8.26 | Normalized transient SIFs in a notched plate for $h = 0.05$ , $\Delta\tau = 0.02$ , and varying $\Delta a$ . . . . .           | 116 |
| 8.27 | Normalized transient SIFs in a notched plate for $h = 0.05$ , $\Delta a = 0.01$ , and varying $\Delta\tau$ . . . . .           | 116 |
| 8.28 | Normalized transient SIFs in a notched plate for varying $\Delta\tau$ at $h = 0.05$ without accumulating crack length. . . . . | 117 |
| 8.29 | Crack paths in a notched plate at varying $\Delta\tau$ without accumulating crack length. . . . .                              | 117 |
| 8.30 | Model and initial mesh of a hollow disk. . . . .   | 118 |
| 8.31 | Normalized velocities of propagating cracks in a hollow disk [50]. . . . .   | 119 |
| 8.32 | Normalized SIFs of crack-1 $\bar{K}^1(\tau)$ for varying $\Delta\tau$ in a hollow disk. . . . .                                | 120 |
| 8.33 | Normalized SIFs of crack-2 $\bar{K}^2(\tau)$ for varying $\Delta\tau$ in a hollow disk. . . . .                                | 120 |
| 8.34 | Crack paths in a hollow disk for varying $h$ . . . . .   | 120 |
| 8.35 | Crack paths in a hollow disk for varying $\Delta\tau$ . . . . .  | 121 |
| 8.36 | Temperature distribution and scaled deformation in a hollow disk at different $\tau$ . . . . .                                 | 121 |
| 8.37 | Comparison of crack paths in a hollow disk obtained using dynamic and unidirectional coupling. . . . .                         | 122 |



# List of Tables

|      |  |     |
|------|--|-----|
| 5.1  | Maximum error percentage in the fitting of exponential material variation. . . . .   | 60  |
| 5.2  | Maximum error percentage in the fitting of material variation defined by a power-law function. . . . .                                       | 60  |
| 7.1  | Normalized mode-I stress intensity factors. . . . .  | 79  |
| 7.2  | Number of polygon and nodes used for different $a/W$ . . . . .   | 80  |
| 7.3  | Results of $\bar{K}_{II}$ for a plate with a center crack for different $a/W$ . . . . .  | 80  |
| 7.4  | Material properties at the left and right sides of a FG plate. . . . .   | 83  |
| 7.5  | Number of nodes and polygon elements used to discretize the FG plate with linearly varying material. . . . .                                 | 84  |
| 7.6  | $K_I$ for varying $a/W$ in FG plate with linear material gradient. . . . .   | 84  |
| 7.7  | Material parameters of hyperbolic tangent gradation. . . . .   | 85  |
| 7.8  | Number of nodes and polygon elements used to discretize the FG plate with hyperbolic tangent material variation. . . . .                     | 86  |
| 7.9  | $K_I$ for varying $a/W$ in FG plate with hyperbolic tangent material gradient. . . . .   | 86  |
| 7.10 | Thermal and mechanical material properties of nickel (Ni) and alumina ( $Al_2O_3$ ). .   | 88  |
| 7.11 | Sets of thermo-mechanical boundary conditions applied to a cruciform-shaped panel.   | 90  |
| 7.12 | Different sets of thermal boundary conditions and reference temperatures for a perforated plate with multiple cracks. . . . .                | 94  |
| 8.1  | Material properties of bismuth. . . . .  | 98  |
| 8.2  | The number of polygon elements used to model a plate subjected to temperature shock parallel to a crack. . . . .                             | 98  |
| 8.3  | Results of transient mode-II SIF for $a/W = 0.5$ with different mesh densities. . . .  | 100 |
| 8.4  | Material properties of $ZrO_2$ and Ti-6Al-4V. . . . .  | 105 |
| 8.5  | Material properties of defined by a power-law function. . . . .  | 107 |
| 8.6  | The number of polygon elements used to model a square plate with an inclined center crack for different mesh characteristic lengths. . . . . | 107 |
| 8.7  | Othotropic material properties of Tyrannohex substrate. . . . .  | 110 |
| 8.8  | The number of polygon elements used to model an orthotropic plate. . . . .   | 111 |
| 8.9  | Material properties of a notched plate with three holes. . . . .   | 113 |
| 8.10 | The initial number of polygon elements used to model dynamic crack propagation in notched plate with three holes. . . . .                    | 114 |
| 8.11 | Material properties of a hollow disk. . . . .  | 119 |
| 8.12 | The initial number of polygon elements used to model dynamic crack propagation in a hollow disk. . . . .                                     | 119 |